Imperial College London

Vortex-lattice-based nonlinear aeroservoelastic modelling and analysis of large floating wind turbines

Arturo Muñoz-Simón
Supervisors: Rafael Palacios, Andrew Wynn

Imperial College London
Department of Aeronautics

This dissertation is submitted for the degree of Doctor of Philosophy

October 2021

Declaration

I hereby declare that this dissertation is the product of my own work except from fully acknowledged references. This thesis has not been submitted, totally or partially, for the consideration for another degree.

Acknowledgements

I would like to start acknowledging the great supervision I have had from Rafael Palacios and Andrew Wynn. Thank you Rafa for giving me the space and time required to develop my research and for pushing my limits when it has been needed to pursue our objectives and their perfection. Thank you Andy for your patience, support and particular point of view that has significantly improved this work.

I would also like to thank all the members of the Load Control and Aeroelastics Lab at Imperial College London for supporting me, teaching me and sharing with me the hard work of these years. Thank you also for the crucial good times together.

I also want to thank the warm welcome at my secondments at the Technical University of Munich (TUM) and the National Renewable Energy Centre in Spain (CENER) where I spend a great time and where I got essential insights for my work. Thank you to the Conflex project members, it has been very enriching seeing the Control of Flexible Strucures and fluid-structure interaction from such a wide range of points of view.

It would have been impossible for me to go through this project without my friends in Spain and London and my family. Thank you for believing in me, encouraging me and supporting me in the bad times.

This project has received funding from the European Research Council (ERC) under the European Union's Horizon 2020 research and innovation programme (grant agreement number 765579).

Abstract

Wind turbine blades have significantly increased in length over the last few decades and are being operated in increasingly complex inflows such as the wake of other wind turbines or on floating platforms. This is increasing the unsteady and three-dimensional aerodynamic effects and the nonlinear structural dynamics that are neglected by the industry-standard Blade-Element Momentum and linear structural theories, respectively. In this dissertation, we employ Unsteady Vortex-Lattice Method for the aerodynamics and nonlinear Geometrically-Exact Beam Theory for the structural dynamics computations to describe these phenomena and their role on wind turbine aeroelasticity. We show that, Unsteady Vortex-Lattice Method fails to provide accurate drag estimation that we overcome with a semiempirical correction to include drag from steady-state tabulated data. We also show that, in cases of yaw, Blade-Element Momentum theory predicts accurate root-bending moments and rotor coefficients up to about ten degrees of yaw, for larger yaw angles, it over estimates the loads decay with the yaw angle. Furthermore, the interaction between radial sections of the blade under turbulent inflow is significant but not accounted for by Blade-Element Momentum theory so we study this phenomenon with Unsteady Vortex-Lattice Method and propose a correction to include the interaction between blade sections in Blade-Element Momentum theory that improves the prediction of loads along the span. We also reduce the computational cost of the Unsteady Vortex-Lattice Method by proposing a new wake discretisation scheme of the wake convection equation. We study the change in aerodynamic surface orientation in long flexible blades and conclude that capturing the twist degree of freedom is important for loads and power estimation. Moreover, we describe the influence of the platform pitch and roll motions in the unsteady character of the aerodynamic loads. Finally, we redesign the controller of the blade pitch to account for nonlinear structural dynamics and unsteady aerodynamics showing a reduction in the fluctuations of the main platform motions and energy production around the equilibrium position.

Contents

List of Figures

List of Tables

Nomenclature

Abbreviations

AC	Aerodynamic Centre
AD	Actuator Disk
AL	Actuator Line
BEM	Blade Element Momentum theory
BTC	Bend-Twist Coupling
CFD	Computational Fluid Dynamics
CL	Closed Loop
CRV	Cartesian Rotation Vector
DAE	Differential-Algebraic system of Equations
FSI	Fluid-Structure Interaction
GEBT	Geometrically-Exact Beam Theory
IPC	Individual Pitch Control
LCoE	Levelised cost of energy
LES	Large-Eddy Simulation
ODE	Ordinary Differential Equation
OL	Open Loop
PID	Proportional Integral Derivative controller
RANS	Reynolds Averaged Navier-Stokes
ROM	Reduced Order Model

SVD Singular Value Decomposition

SWL Sea Water Level

TLP Tension Leg Platform

UVLM Unsteady Vortex-Lattice Method

Symbols

$\overline{k}_{\mathrm{c}}$ Upper reduced frequency limit for the integration of the controllability Gramian

$\overline{k}_{\mathrm{o}}$ Upper reduced frequency limit for the integration of the observability Gramian

$\overline{S}$ Strain rate tensor

$\tilde{c}_{L_{2D}}$ Filtered section lift force coefficient

$A(\omega_{\mathrm{p}})$ Added-mass matrix of the platform associated to radiation

A Gust amplitude

a Axial induction factor

A_{∞} Infinitely upstream area of the streamtube that includes the rotor

A_{a} State-space matrix for linear UVLM

A_{cs} Cross-sectional area

A_{m} Mooring line cross-sectional area

A_{p} Panel area

a_{s} Straight axis location behind the leading edge

a_{w} Wave amplitude

A_d Rotor sweep area

A_s Platform area perpendicular to the relative velocity between the platform and the water

A_w Infinitely downstream area of the streamtube that includes the rotor

B Damping matrix of the platform associated to radiation

b Semispan

B_{a} State-space matrix for linear UVLM

B_{h}	Matrix that contains the derivatives of the holonomic constraints
B_{n}	Matrix that contains the derivatives of the non-holonomic constraints
B_d	Added damping matrix
C	Courant number
c	Airfoil chord
C^t	Tangent damping matrix
$C^{\bullet\bullet}$	Rotation matrix from the A to the B frame of reference
C_{a}	State-space matrix for linear UVLM
c_{in}	Blade section in-plane force coefficient
c_{out}	Blade section out-of-plane force coefficient
C_{s}	Buoyancy restoring matrix
C_B	Drag coefficient between the mooring line and the seabed
c_D	Section drag force coefficient
c_d	Platform drag force coefficient
c_L	Section lift force coefficient
c_M	Section pitching moment coefficient
c_m	Platform apparent-mass force coefficient
C_P	Wind turbine power coefficient
C_s	Constant of the Smagorinsky LES model
c_s	Section spanwise force coefficient
C_T	Rotor thrust coefficient
c_z	Yaw moment proportional constant
c_{L_α}	Lift vs angle of attack curve slope
$c_{L_{ss}}$	Steady-state section lift coefficient
D	Blade section drag force
D_{a}	State-space matrix for linear UVLM

E	Electric power generated by the wind turbine
E_0	Nominal power
E_{m}	Mooring line Young modulus
F_{in}	In-plane force
F_{out}	Out-of-plane force
f_{p}	Prescribed frequency
F_h	Horizontal mooring force
F_v	Vertical mooring force
G	Gearbox ratio
g	Gravity value
H	Transfer function
H_{r}	Transfer function between platform velocities and radiation forces
H_c	Rational transfer function to account for spanwise section interaction
h_s	Wave characteristic height
I	Platform moment of inertia
I_{D}	Drive-train inertia
I_{L}	Platform lumped mass moment of inertia
I_T	Turbulence intensity
J	Cross-section inertia matrix
$J(\omega_{\mathrm{w}})$	Frequency-domain representation of the sea waves
K	Radiation impulse response function
k	Reduced frequency
K^t	Tangent stiffness matrix
k_{L}	Scaling parameter of the Lagrange multipliers method
k_{N}	Nyquist circular frequency
K_D	Derivative gain of the PID controller

K_I	Integral gain of the PID controller
K_P	Proportional gain of the PID controller
L	Blade section lift force
L_{m}	Mooring line unstretched length
L_{T}	Largest characteristic length scale for turbulence generation
L_B	Length of the mooring line laying on the seabed
L_b	Wind turbine base height
L_s	Spar platform length
L_{e_x}	Length of the empty box in the x direction
$L_{x,y,z}$	Length of the LES box in the x, y and z directions
M	Number of chordwise panels in the UVLM grid
M	System mass matrix
m	Mass per unit length
M_{in}	In-plane root bending moment
M_{L}	Platform lumped mass
M_{out}	Out-of-plane root bending moment
M_{p}	Platform total mass
m_{s}	Spar mass per unit length
m_{T}	Tower base mass per unit length
M_{w}	Ballast mass
M_{w}	Number of panels in the flow direction in the UVLM grid
M_z	Yaw moment from the mooring system
N	Finite-element shape functions
N	Number of spanwise panels in the UVLM grid
N_{bl}	Number of blades
N_{w}	Number of panels in the UVLM wake

N_b	Number of bound panels in the UVLM grid
n_b	Number of bodies in a multibody system
n_c	Number of constraints in a multibody system
n_q	Number of generalised coordinates in a multibody system
N_w	Number of wake panels in the UVLM grid
$N_{x,y,z}$	Number of nodes in the x, y and z directions
p	Air pressure
p_d^+	Pressure of the air stream immediately upstream the rotor
p_d^-	Pressure of the air stream immediately downstream the rotor
R	Wind turbine radius
r	Radial coordinate
r_{G_x}	Platform surge displacement
S	System action
S_1	1-sided power spectral density of the sea waves
S_2	2-sided power spectral density of the sea waves
T	Balanced transformation matrix
$T(\mathbf{\Psi})$	Tangential operator
t^*	Non-dimensional time
T_g	Generator torque
T_r	Rotor torque
T_p	Wave peak period
U	Matrix from the Singular Value Decomposition of the Gramians
U_1, U_2	Random variables with values between 0 and 1
U_∞	Wind mean velocity infinitely upstream the wind turbine
u_r	Relative flow-solid velocity
U_d	Mean wind velocity at rotor plane

U_w	Wind mean velocity infinitely downstream the wind turbine
V	Matrix from the Singular Value Decomposition of the Gramians
V_0	Initial submerged platform volume
W	Frequency-domain representation of white noise
W_c	Controllability Gramian
W_o	Observability Gramian
x_fa	Tower-top fore-aft displacement
x_in	In-plane displacement
x_out	Out-of-plane displacement
X_w	Wave force excitation coefficient matrix
x_G	Global horizontal position of the first beam tip in the double pendulum
x_h	Horizontal coordinate of a mooring line fairlead with respect to the anchor
x_v	Vertical coordinate of a mooring line fairlead with respect to the anchor
Z_c	Low-rank controllability factor
z_g	Centre of mass below SWL
Z_o	Low-rank observability factor
z_w	Ballast depth below SWL
z_{A_0}	Local bending displacement of the first beam tip in the double pendulum
z_{A_1}	Local bending displacement of the second beam tip in the double pendulum
r_{G_z}	Platform heave displacement
α	Angle of attack
α_0	Initial or mean angle of attack
α_F	Parameter of the generalized-α time integration scheme
α_M	Parameter of the generalized-α time integration scheme
α_N	Parameter of the Newmark-β time integration scheme
α_T	Empirical constant for the generation of turbulence

α_{L_0}	Angle of attack of zero lift
β_0	Parameter for the numerical computation of the time derivative
β_1	Parameter for the numerical computation of the time derivative
β_{T}	Parameter of the time integration schemes
β_{t}	Blade local twist
β_{w}	Wave incidence angle
β_{-1}	Parameter for the numerical computation of the time derivative
χ	LES Gaussian kernel
Δt	Time step
Δ_g	LES grid characteristic size
$\Delta_{x,y,z}$	Grid size in the x, y and z directions
ϵ_{T}	Wind specific turbulence dissipation rate
ϵ_g	Smearing strength
η	Spanwise coordinate
Γ	Flow circulation of the bound vorticity
γ	Yaw angle
Γ_{T}	Stretching parameter
γ_{T}	Parameter of the time integration schemes
Γ_{w}	Flow circulation of the wake vorticity
γ_J	Peak shape parameter
κ	Wave number
Λ	Sideslip angle
λ	Wavelength
λ_{t}	Tip-speed ratio
μ_{G}	Doublet intensity
μ_{m}	Mooring line apparent weight

Ω	Flow domain
ω	Circular frequency
ω_{c}	Corner frequency of the low pass filter
ω_{g}	Generator velocity
ω_{g}^{*}	Filterred generator velocity
ω_{p}	Platform oscillation frequency
ω_{r}	Rotor velocity
ω_{w}	Wave circular frequency
$\partial\Omega_{\infty}$	Infinite boundary of the flow domain
$\partial\Omega_{s}$	Solid boundary of the flow domain
ϕ	Potential air flow field
ϕ_{c}	Controllability transfer function
ϕ_{o}	Observability transfer function
ϕ_{W}	Wagner function
ϕ_{w}	Potential of the water velocity field
ϕ_{f}	Flow angle
ψ_{K}	Küssner function
ρ	Air density
ρ_{∞}	spectral radius at high frequencies of the generalized-α time integration scheme
ρ_{m}	Mooring line density
ρ_{r}	spectral radius of the generalized-α time integration scheme
ρ_{w}	Water density
Σ	Matrix from the Singular Value Decomposition of the Gramians
σ_{G}	Source intensity
σ_{J}	Scaling factor for sea waves spectrum
τ	Stress tensor

θ	Azimuthal rotor angle
θ_{p}	Blade pitch angle
φ_0	Rotation of the first node of the first beam in the double pendulum
φ_1	Rotation of the first node of the second beam in the double pendulum
φ_x	Platform roll rotation
φ_y	Platform pitch rotation
φ_z	Platform yaw rotation
ϑ	Air kinematic viscosity
ϑ_t	Air turbulent kinematic viscosity
ζ	Coordinate parallel to the relative flow-solid velocity
ζ_{b}	Chordwise direction
f_{w}	Wave frequency
$\hat{\boldsymbol{u}}$	Flow velocity induced by the vorticity field
$\boldsymbol{b}$	Position of the solid nodes in the B frame of reference
$\boldsymbol{b}_B^{\mathrm{cg}}$	Position of the centre of gravity of a cross-section
$\boldsymbol{F}_{\mathrm{a}}$	Additional damping forces on the wind turbine platform
$\boldsymbol{F}_{\mathrm{mf}}$	Mooring forces at the fairleads
$\boldsymbol{F}_{\mathrm{m}}$	Mooring forces on the wind turbine platform
$\boldsymbol{F}_{\mathrm{p}}$	Resultant forces on the wind turbine platform
$\boldsymbol{F}_{\mathrm{q}}$	Quasi-steady aerodynamic force
$\boldsymbol{F}_{\mathrm{r}}$	Radiation forces on the wind turbine platform
$\boldsymbol{F}_{\mathrm{s}}$	Buoyancy static forces on the wind turbine platform
$\boldsymbol{F}_{\mathrm{u}}$	Unsteady aerodynamic force
$\boldsymbol{F}_{\mathrm{v}}$	Viscous drag forces on the wind turbine platform
$\boldsymbol{F}_{\mathrm{w}}$	Wave forces on the wind turbine platform
$\boldsymbol{F}_B$	Internal forces

$\boldsymbol{f}_B$	Resultant external forces in a cross-section
$\boldsymbol{g}$	Multibody constraints
$\boldsymbol{g}_{\mathrm{h}}$	Multibody holonomic constraints
$\boldsymbol{g}_{\mathrm{n}}$	Multibody non-holonomic constraints
$\boldsymbol{H}_B$	Angular momenta
$\boldsymbol{K}_B$	Auxiliary vector in Equation (2.12)
$\boldsymbol{M}_B$	Internal moments
$\boldsymbol{m}_B$	Resultant external moments in a cross-section
$\boldsymbol{n}$	Normal vector to solid surfaces
$\boldsymbol{p}$	Degrees of freedom of the wind turbine platform ($\boldsymbol{r}_G$, $\boldsymbol{\vartheta}$)
$\boldsymbol{P}_B$	Transitional momenta
$\boldsymbol{Q}$	Forces
$\boldsymbol{q}$	Generalised coordinates
$\boldsymbol{Q}_e$	External forces
$\boldsymbol{Q}_g$	Gyroscopic forces
$\boldsymbol{Q}_s$	Stiffness forces
$\boldsymbol{r}$	Residual vector
$\boldsymbol{R}_A$	Position vector of the reference line
$\boldsymbol{r}_G$	Position vector of the A frame of reference (tower base)
$\boldsymbol{u}$	Flow velocity
$\boldsymbol{U}^{\infty}$	Free-stream flow velocity
$\boldsymbol{u}_{\mathrm{w}}$	Water velocity field
$\boldsymbol{v}_{\mathrm{a}}$	Input vector for linear UVLM
$\boldsymbol{v}_A$	Linear velocity of the A frame of reference (tower base)
$\boldsymbol{V}_B$	Linear velocity of the reference line
$\boldsymbol{x}_{\mathrm{a}}$	State vector for linear UVLM

$\boldsymbol{x}_b$	Balanced states of the linear UVLM
$\boldsymbol{X}_G$	Position vector of the reference line in the G frame of reference
$\boldsymbol{y}_\mathrm{a}$	Output vector for linear UVLM
$\boldsymbol{\beta}$	Vector of linear and angular velocities of the A frame of reference $(\boldsymbol{v}_A, \boldsymbol{\omega}_A)$
$\boldsymbol{\chi}$	Quaternion (orientation of the A frame of reference)
$\boldsymbol{\eta}$	Vector with the nodes degrees of freedom ($\boldsymbol{R}_A$ and $\boldsymbol{\Psi}$)
$\boldsymbol{\gamma}$	Generalised strains
$\boldsymbol{\kappa}$	Generalised curvatures
$\boldsymbol{\lambda}$	Lagrange multipliers
$\boldsymbol{\mu}_G$	External forces
$\boldsymbol{\omega}_A$	Angular velocity of the A frame of reference (tower base)
$\boldsymbol{\Omega}_B$	Angular velocity of the reference line
$\boldsymbol{\omega}^*_{A_1}$	Relative velocity between tower-top and blade root
$\boldsymbol{\phi}$	Orientation of the reference line
$\boldsymbol{\Psi}$	Cartesian rotation vector (Parametrisation of $\boldsymbol{\Phi}$)
$\boldsymbol{\varphi}$	Orientation of the A frame of reference (tower base)
$\boldsymbol{\xi}$	Aerodynamic grid vertices coordinates
AR	Aspect ratio
$\boldsymbol{\mathcal{F}}_A$	Resultant external forces in the system
$\boldsymbol{\mathcal{H}}^R_A$	System angular momenta
$\boldsymbol{\mathcal{M}}_A$	Resultant external moments in the system
$\boldsymbol{\mathcal{P}}^R_A$	System transitional momenta
$\mathcal{A}$	Influence matrix of the bound vorticity on solid surfaces velocities (linear UVLM)
$\mathcal{A}_\mathrm{w}$	Influence matrix of the wake vorticity on solid surfaces velocities (linear UVLM)
$\mathcal{A}_s$	Mapping between trailing edge and wake panels circulation for steady state cases
$\mathcal{B}$	Influence matrix of the inputs to the solid velocities (linear UVLM)

$\mathcal{C}_\Gamma$	Shedding vorticity matrix
$\mathcal{C}_{\Gamma_\mathrm{w}}$	Wake convection matrix
$\mathcal{F}$	Fourier transform
$\mathcal{H}_\infty$	$\mathcal{H}_\infty$ norm
$\mathcal{L}$	Lagrangian
$\mathcal{L}^*$	Augmented Lagrangian
$\mathcal{M}_\mathrm{cs}$	Cross-sectional mass matrix
$\mathcal{S}_\mathrm{cs}$	Cross-sectional stiffness matrix
$\mathcal{T}$	Kinetic energy
$\mathcal{U}$	Internal energy
$\mathcal{W}$	Work of external forces
$\mathcal{W}_\mathrm{cv}$	Interpolation matrix from vortex corners to panel centres
$\mathcal{W}_\mathrm{vc}$	Interpolation matrix from panel centres to vortex corners
$\mathcal{W}_\mathrm{vs}$	Interpolation matrix from vortex segments midpoint to vortex corners
$\mathfrak{c}_L$	Spanwise Fourier transform of the lift force coefficient

Chapter 1

Introduction

A long history of developments has transformed wind energy from the agricultural use of windmills to one of the main stakeholders in the electricity market [1]. Wind energy for electricity generation has its origins at the end of the nineteenth century in remote regions without electricity access and its surge at the end of the twentieth century as a result of a significant increase in oil prices and Governmental subsidies [2, 3]. Until this point, the large-scale deployment of wind energy was delayed due to the cheap and easy electricity generation with fossil fuels. Wind turbines have significantly increased in size from blades of the order of 10 m in the 1950s to current prototypes of more than 100 m to increase the rotor swept area and, thus, the energy production of each wind turbine [4] (Figure 1.1). With the same objective, towers have also become higher to avoid the low-speed wind near the ground. All these improvements, have reduced the levelised cost of energy (LCoE) and have created conditions under which onshore wind energy generation has increased from 30 TWh in 2000 to 1300 TWh in 2019 (out of 25000 TWh electricity consumption in the world). In Europe, wind energy currently provides 10% of the electricity generation [5].

The development of wind energy science started with the study of ship propellers by Rankine and Froude at the end of the nineteenth century. They set the basis of rotor aerodynamics [2] with the idealisation of the propellers as a permeable infinitely thin disc covering the rotor sweep area on which the propeller force is uniformly distributed (actuator disc). The flow velocity at the rotor plane and the propeller thrust are obtained through mass, axial momentum and energy balances. At the beginning of the twentieth century, Betz and Joukowsky proved that the maximum efficiency of this idealised rotor is 16/27. Wind turbines work by extracting kinetic energy from wind and, unavoidably, slowing it down, thus, maximum efficiency is obtained at an optimum balance where as much energy as possible is

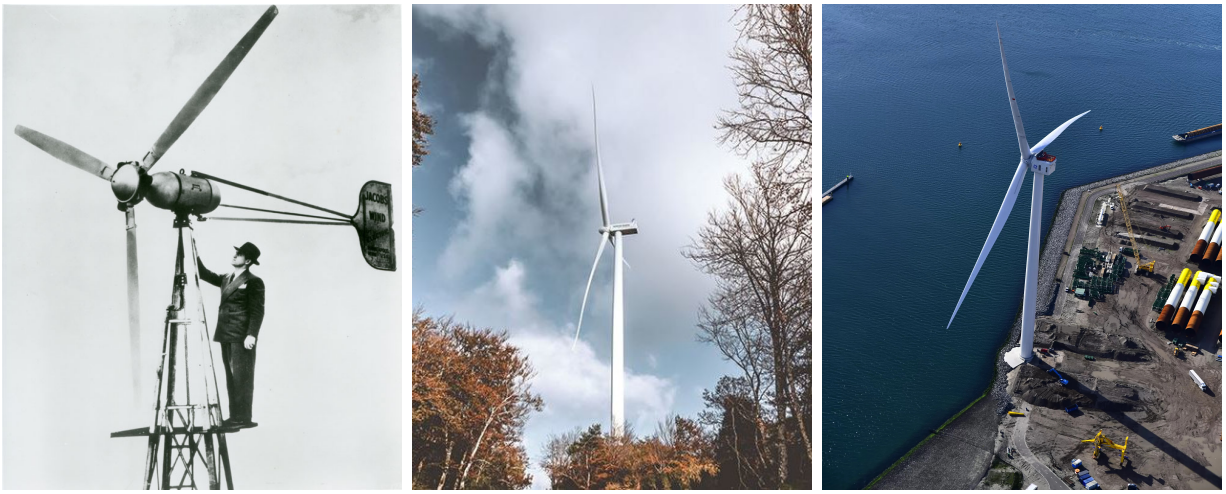

(a) 2.5kW Jakobs turbine (1940s).

(b) Current 3 MW Siemens-Gamesa wind turbine. 132 m rotor diameter.

(c) 14 MW Haliade-X wind turbine prototype. 220 m rotor diameter.

Figure 1.1: Wind turbine designs from the 1940s to the current prototypes*.

taken out from the flow, yet, it is left with enough momentum to move downstream. The previous one-dimensional rotor model was improved by including a tangential momentum balance, which provides information about the azimuthal force that generates rotor torque and the associated rotation of the fluid in the wake. The ratio between blade tip and freestream velocities (also known as tip-speed ratio) is a measure of the wake rotation and is associated with a reduction of the maximum efficiency estimated by Betz and Joukowsky: a rotor with zero velocity has zero efficiency which increases asymptotically with the tip-speed ratio towards the 16/27 limit [2].

These theories were not useful for rotor design because they did not provide local information at blade level. At the same time, Joukowsky in Russia and Prandtl and Betz in Germany developed two idealised rotor models (Figure 1.2) based on vortex theory [6]. The former assumes constant circulation along the span while the latter allows spanwise varying circulation based on Prandtl's lifting line theory. Analytical solutions were only available for an infinite number of blades and were useful to corroborate momentum theory and to set the basis for the study of rotors with finite number of blades that would be significantly

*Image 1.1a from Jacobs Wind Electric `https://www.jacobswind.net/history`. Accessed on October 4^{th}, 2021.
Image 1.1b from Siemens-Gamesa `https://www.siemensgamesa.com/es-es/products-and-services/onshore/aerogenerador-sg-5-0-132`. Accessed on October 4^{th}, 2021.
Image 1.1c from General Electric. `https://www.ge.com/renewableenergy/wind-energy/offshore-wind/haliade-x-offshore-turbine`. Accessed on October 4^{th}, 2021.

simplified with the increase in computational power.

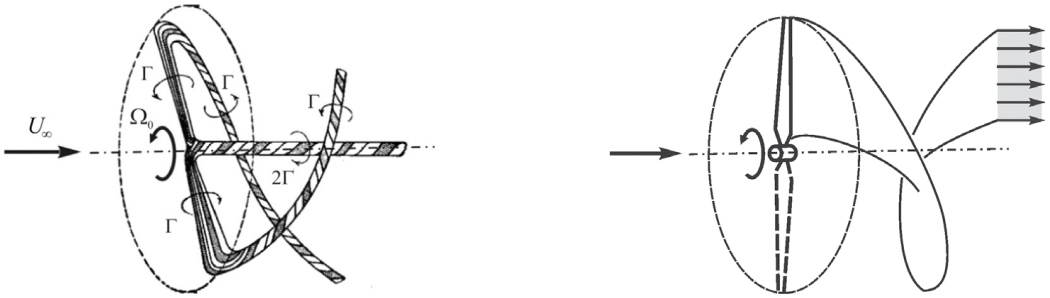

(a) Joukowski. Image from van Kuik et al. [2]. (b) Betz. Image from Okulov et al. [7].

Figure 1.2: Sketches of two early rotor models.

Blade-element theory appeared at the end of the nineteenth century in the work of Drzewiecki but it only became sufficiently accurate when the concept of induced velocity from momentum and vortex theories was included [6]. The combination of the blade-element and momentum theories is known as Blade-Element Momentum (BEM) theory and its accuracy has been improved with vortex methods studies, such as, the vortex solution of a cascade of semi-infinite sheets that gave rise to the Prandtl tip-loss correction [4]. Modern versions of BEM theory include semi-empirical corrections to improve the results in cases outside the original steady uniform wind perpendicular to the rotor plane such as yaw and dynamic cases [4]. Nowadays, this theory constitutes the industry standard and has been the main driver of the evolution of numerical models for wind energy for electricity production. Recently, the applicability of BEM theory has been compromised due to the intensified aerodynamic unsteadiness and three-dimensional effects associated to the increased blade length and flexibility and the larger sweep rotor areas operating in turbulent inflows. Other computational methods provide insights about aerodynamic effects that are outside the range of applicability of BEM theory [8] and target smaller or larger spatial scales. On the one hand, Reynolds Averaged Navier-Stokes (RANS) solutions are usually employed to accurately describe fluid phenomena with relevant scales up to wind turbine size including rotation effects on the flow, boundary layer transition and separation. Thus, they have been used for the specific design of high-lift airfoils for wind energy, as opposed to aeronautical shapes, that have enabled more slender and lighter blades (90% lighter than the first designs in the 1980s [9]). The baseline blade design has also been improved with other local add-ons like flat-back airfoils, vortex generators or gurney flaps and with increasing tip-speed ratios to reduce torque and, thus, drivetrain loading [9] (Figure 1.3). On the other hand, Large-Eddy Simulation with

Actuator Line (LES-AL) captures the large turbulent structures that contain most of the energy in the flow and models wind turbines as distributed forces in the flow. Therefore it is suitable to describe wind farm aerodynamics and the interaction between wind turbines.

Aerodynamics is only the first step for the characterisation of wind turbine mechanics because it provides the wind forces on the blades and tower that generate power, displace the wind turbine platform and bend the structure. Consequently, the complete mechanical characterisation of onshore wind turbines requires other physical models, some of which are relevant for this project: multibody structural dynamics to study aeroelastic couplings and control to improve the behaviour of the wind turbine through power production optimisation and load reduction. Traditionally linear structural methods that assume small displacements have been used for wind turbine design [10]. However, they are being pushed outside their range of applicability due to the previously described increase in length of blades and tower and the use of composite materials, which generate more flexible blades that undergo larger deformations [9]. Moreover, they require an adequate characterisation of composite anisotropic material including complex couplings such as bend-twist coupling. Thus, composite nonlinear beam theories are gaining importance. Control design requires accurate computational methods that account for all the relevant physics of the system but simple and inexpensive to run due to the large number of computations that are typically required by the design process. Aerodynamics, structural dynamics and control interact with each other and should be studied concurrently (aeroservoelasticity) to accurately describe wind turbine behaviour.

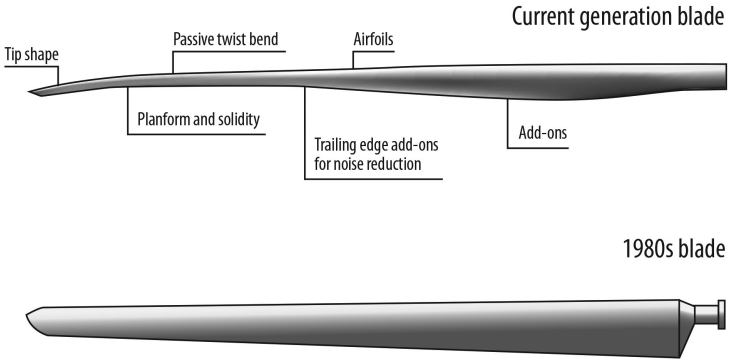

Figure 1.3: Current and 1980s blade designs. Image from Veers et al. [9].

The future of wind energy is very promising with onshore expecting to triple its generation in the next ten years by placing wind turbines in more complex terrains and in more dense layouts within wind farms forcing them to operate in the wake of other wind turbines and

more complicated inflow conditions [5, 9]. Moreover, there is a need of cost reduction due to competition. Offshore wind energy, that started only in the late 1990s with bottom-fixed wind turbines, is expected to grow from 70 TWh in 2018 to 600 TWh in 2030 [5]. In shallow waters, foundations to the seabed include monopile for depths up to 30 m and jackets for depths up to 60 m. Bottom-fixed wind energy is very expensive compared to onshore wind energy due to the large foundations needed, the manufacturing cost and the scarce availability of shallow water that is, in addition, more exposed to visual impact [8]. For water depths larger than 60 m, floating platforms are considered as support structures for wind turbines. In onshore wind energy, the wind turbine itself is the main contributor to the life-cycle cost, however, in offshore wind energy, the platform and the operation and maintenance costs due to the extreme weather conditions [9] exceed those of the wind turbine, thus, an accurate and robust design of the system is very critical [11].

The operation in floating platforms and the need of accurate prediction of robust designs will make unsteady and three-dimensional aerodynamic effects and nonlinear structural deformation even more relevant. Moreover, experimental campaigns are very expensive, for example, blades are structurally tested at full scale in very expensive destructive experiments, however, all aerodynamic tests are performed on scaled down models in wind tunnels that sometimes need to be pressurised to match as closely as possible the Reynolds and Mach numbers between reality and experiments. Scaling down a floating wind turbine maintaining the relative importance of aerodynamic, structural and hydrodynamic effects is almost impossible.

In summary, computational methods, specially low-fidelity, have massively transformed wind turbines in the last decades together with advances in other engineering fields. Moreover, higher-fidelity methods and experiments have been used to validate low-fidelity methods, get insights into wind turbine's physics and for very detailed designs of wind turbine blades but they are extremely expensive and difficult to scale. Thus, having accurate and efficient numerical methods for design is critical.

1.1 Literature review

Wind energy has evolved and changed during the last one hundred years as we described in the preface of this chapter and the current knowledge about their mechanical behaviour is vast. In this section, we aim to describe some previous work to characterise the important physics in offshore wind turbine aeroservoelasticity with special attention to computational

methods, their ranges of applicability and relevant uses in wind energy.

1.1.1 Aerodynamics

Wind turbine aerodynamics studies the forces generated by the wind on the wind turbine. A wide range of physical phenomena is needed to explain rotor aerodynamics, which are qualitatively well understood [4] when analysed separately such as wake-skewness in yaw cases and unsteadiness. However, numerical methods are needed to quantify them, especially under complex scenarios [8] such as complicated geometries or combination of phenomena. Aerodynamics is the most resource-consuming physical process to model of all those involved in wind turbine aeroservoelasticity, thus, there are different theories available that are classified according to their accuracy and computational cost [12]. This section uses previous work to highlight existing knowledge concerning wind turbine aerodynamics with especial attention to the computational methods employed describing their limitations and some efforts to overcome them.

Uniform inflow perpendicular to the rotor plane

Momentum theory is based on a momentum balance (Figure 1.4a) of the flow in control volumes that extend far upstream and downstream in annular sections of the rotor. The momentum loss of the flow is equivalent to the force exerted on the rotor. This force is computed with blade-element theory (Figure 1.4b) that obtains the forces at blade sections from steady-state look-up tables based on the angle of attack. The simplest case for wind turbine aerodynamics is the operation at constant rotation speed under steady uniform wind perpendicular to the rotor plane. In this situation, incoming velocities do not vary azimuthally and, thus, neither do blade forces. This is a steady-state situation in a frame of reference rotating with the rotor and, typically, the optimum for power production and loading. In this scenario all BEM hypotheses hold making this method very accurate [13, 14].

Vortex theory [15] constitutes a medium fidelity approximation at an intermediate computational cost in its different variations [16]. In general, it is based on the solution of the potential inviscid flow equations through Green's theorem to compute singularity fields on the fluid domain boundaries. However, it has also been applied to viscous flows [17]. The type of singularity used in the boundaries (source, doublet or vortex) defines the model. In this work, we pay special attention to the Unsteady Vortex Lattice Method (UVLM) in

which solid surfaces and wakes are discretised with vortex rings [18] (Figure 1.4c) . The most important simplification of UVLM is the assumption of potential flow, which neglects the effect of viscosity. As an example, in the computation of 2D airfoil properties with vortex methods and Computational Fluid Dynamics (CFD) [19], the former cannot predict friction drag or flow separation. The effect of drag has been proved considerable in the estimation of wind turbine loads and power but not so critical in the prediction of wake velocities [20]. For this reason, different drag corrections have been proposed in the past for vortex methods such as employing the integral boundary layer equations [18] which consist of: first, inviscid vortex methods simulate the flow outside boundary layers according to Laplace equations; second, Navier-Stokes equations are simplified in the boundary layer, assuming small thickness and two-dimensional flow. The velocity at the interface of these two domains (the edge of the boundary layer) should match, thus, the coupled solution through different schemes [18] provide solutions for the whole flow field. The 2D implementation of Drela in XFOIL [15] is the most popular one and it has also been applied to 3D wind turbines by some authors [16, 20].

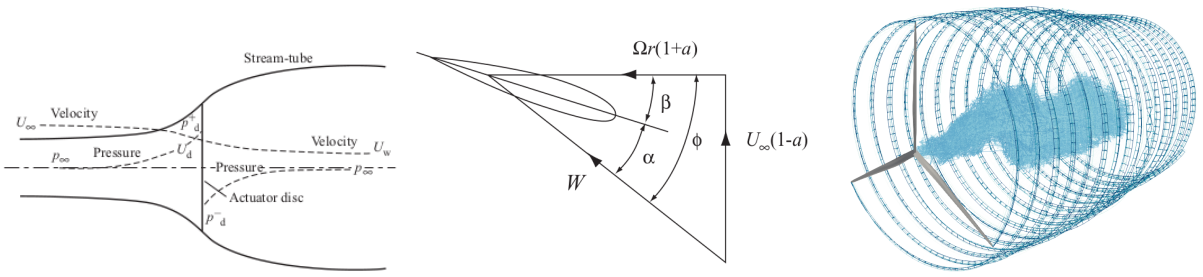

(a) Momentum theory. (b) Blade-Element theory. (c) UVLM.

Figure 1.4: Sketches of three aerodynamic theories. Images (a) and (b) from Burton et al. [4].

In ordinary power-production operation, separation only affects the blade root which is not a critical contributor to blade loads or power generation. The basic implementation of vortex methods has also been successfully modified to account for stall in wind turbines [21, 22] which requires knowing the separation point and assuming a pressure distribution along the separated airfoil. This effect is even more complicated in dynamic cases of pitching airfoils at high angles of attack [23]. With the same purpose, some strip vortex methods use a decambering approach [24] to change the airfoil camber such that the viscous lift-angle of attack curve is tracked throughout the vortex simulation. Moreover, some vortex methods are able to account for body thickness [15] capturing the associated increase in slope of the

lift curve and drag up to a certain extent. Finally, the effect of compressibility based on Karman-Tsien correction [25] has been shown to be relevant and adequately captured by corrected vortex methods [15].

It is important to notice that some vortex methods impose strong constraints on domain discretisation [26] that, together with free wake approximations to accurately model aerodynamic loads, can result in significant computational cost [27]. For example, in the UVLM implementation of vortex theory, the size of the vortex shed at each time step has to be equal to the last trailing edge panel [28] which links and tightly constrains spatial and time discretisations. This requirement arises from the stability limitations of the first order upwind scheme used to discretise the convection equation. There are attempts to discretise a non-uniform wake with simple geometries using Galerkin approximation [29]. Multiple strategies to reduce the UVLM's computational burden exist [16] such as transforming vortex rings into vortex blobs far away from solid surfaces [30] or using mathematical approximations like the fast multipole method [31]. The former requires the numerical treatment of a new kind of singularity and the latter constitutes a numerical approximation to the problem so they are complex methods that do not completely solve the problem of computational cost in vortex methods.

Yawed inflow

Uniform steady wind perpendicular to the rotor is not the usual operating state of wind turbines because incoming flows are not uniform (shear and turbulence), steady (turbulence) or perpendicular to the rotor plane (yaw). In the presence of wind shear, the largest incoming velocity and induction occur when blades are at the upper position, giving rise to the largest loads [32]. In the presence of yaw (Figure 1.5), two effects differentiate wind turbine aerodynamics from the reference case of zero-yaw [33]. The first one is the advancing/retreating effect and accounts for the change in angle of attack along a revolution due to the change in relative orientation between the blade and the inflow. For example, for positive yaw angles (wind comes from the right hand side according to an observer at the wind turbine position looking upwind), when the blade is at the top position, the blade rotation is in the opposite direction to the in-plane component of the incoming wind which increases the angle of attack with respect to the zero-yaw case. This effect does not create a net out-of-plane loading along one complete rotation. This effect is less noticeable near the tip because the velocity of the blade due to rotation is dominant there. The second effect is known as the skewed-wake effect and accounts for the different distances from the blade to the shed vorticity in

the wake along a revolution. The blade and the vorticity will be closer when the blade is in the downwind position and further away when it is in the upwind position. This effect generates a net yaw moment that tends to orient the wind turbine perpendicular to the wind with minimum and maximum when the blade is at one of the two horizontal positions and stronger near the tips.

The azimuthal variation of incoming speed in shear cases and in the advancing/retracting effect of yaw cases contradict the basic hypothesis of BEM. The corrections implemented to overcome this drawback perform one axisymmetric computation for each blade based on the real conditions seen by that blade at each location. However, there is no agreement in the particular details of the implementation [32] which leads to slightly different solutions. The skewed-wake effect requires another model (originally related to Glauert theory of autogyro [34]) that includes a theoretical equation for the azimuthal variations of axial induction up to some unknown parameters. Those parameters were initially estimated according to vortex theory [35] and improved [36], afterwards, based on some reviews and comparisons with experiments [33]. Other corrections for BEM based on high fidelity computations [37] include root vortex, yaw, tip-speed ratio, azimuthal and radial variations.

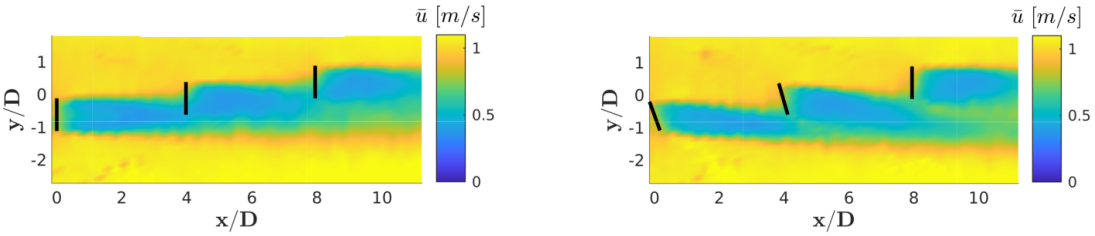

(a) Wind turbines at zero yaw

(b) Yawed wind turbines

Figure 1.5: Two wind tunnel tests of a wind farm. Top view of horizontal velocity contours at a horizontal plane at hub height. Image from Wang et al. [38].

Turbulent inflow

The numerical characterisation of wind turbine loads under turbulent wind conditions requires sufficiently accurate descriptions of both the turbulence field and the unsteady and three dimensional aerodynamic effects on blades [8]. Moreover, the stochastic nature of turbulence implies that very long experiments or computations are needed to provide statistically converged results for fundamental metrics such as mean power or equivalent fatigue loads.

The characterisation of turbulence in wind farms is challenging due to the numerous physical phenomena and wide range of temporal and spatial scales [39] from boundary layer turbulence to atmospheric weather. Moreover, experimental campaigns to evaluate wind turbine loads under these turbulent conditions are extremely expensive and, thus, only a small number of studies are available. For example, in wind tunnels, active grids have been created to generate controlled turbulence [40] to test wind turbine airfoils under turbulent flows with prescribed statistics [41], while some in-field campaigns have provided relevant validation data [42].

Computational techniques offer an alternative to full-scale experimental campaigns but the challenge in this setting is to ensure simulation accuracy. First, the generation of a representative turbulence field is a challenging task. One approach is to generate a box of turbulence to feed as inflow conditions to a wind turbine computational model through Taylor's frozen turbulence hypothesis which relates the spatial coordinates in the box with the time scale using the mean wind velocity. Statistical (Turbsim [43]) and physical models based on linearised Navier-Stokes equations (Mann boxes [44]) can be used, but a more accurate approach is to generate turbulence with Large Eddy Simulations (LES) of the boundary layer as a precursor simulation [45].

The simulation of turbulent flows is outside the range of applicability of vortex methods [27] because these flows have inherent vorticity which is in conflict with the basic assumptions of vortex theory. However, vortex methods have been employed for that purpose, for example, in [46] variations on the lateral wind conditions with a vortex method and an indicial response method show very good agreement in the estimation of yaw moment coefficient.

Advantages of vortex methods

The greatest advantage of vortex methods is their intrinsic capability to account for three-dimensional and unsteady aerodynamic phenomena. To highlight the importance of this capability, we describe next the corrections needed by lower fidelity models to attempt to provide acceptable predictions under these scenarios: three-dimensional effects, unsteadiness and azimuthal variations. Despite all the semi-empirical corrections created for BEM methods, they should be put into perspective as long as they are restricted to the operation conditions under which they were designed and they do not account for interaction between effects but apply corrections on top of each other. Thus, even after all these corrections, BEM still cannot predict yaw as well as CFD does [47].

Conventional BEM does not account for unsteadiness because it is based on steady equi-

librium. For that reason, when sudden changes occur in the system that go beyond the quasi-steady approximation a correction needs to be applied. In this case, it is based on the indicial response of Beddoes-Leishman theory of airfoils [48] which was later revisited by [23] for three dimensional effects and inclusion into BEM codes. These models are usually referred to as Unsteady BEM and are being used for load design cases with significant unsteady and three-dimensional flows, such as, sudden pitch changes [49] and gusts even if they are not within their applicability limits.

The induction changes along the azimuthal direction in rotors with a finite number of blades because the flow slows down more in front of the blades than in the space between them. This three-dimensional effect is against the basic hypothesis of BEM of constant induction along the azimuthal direction forcing the use of the tip-loss correction. The correction name comes from the fact that this effect is important near the tip and the root of the blade. Another correction for the change of induction in the azimuthal (and radial) direction is the accelerated-potential method that assumes an a-priori distribution for the induction within the rotor plane. The well-known Prandtl tip-loss correction and the accelerated-potential method have been developed based on vortex theory [4]. The second three-dimensional effect is the interaction between blade sections which has long been of interest in aeronautics for complex wing geometries [50, 51]. For wind turbines, near wake models have been developed to account for the induction change along the blade span that is disregarded in BEM. They make use of vortex theory to define this interaction between radial sections by assuming, for example, that the trail vorticity (associated to vortices perpendicular to the trailing edge and responsible for the three-dimensional effects) stays in the rotor plane and that its influence is negligible after a certain amount of time [52]. The complexity of this method is to combine the near wake model with the far wake model of BEM that is required to define the steady-state response.

Higher-fidelity methods

CFD is usually considered a very high fidelity method for aerodynamic computations which would be extremely expensive [8] to analyse all the load cases in the design process. However, CFD is very useful for particular analysis such as the design of blades add-ons [9]. They require a fluid domain discretisation to solve the Navier-Stokes equations, and, these equations are solved filtered in time or space which are known as RANS and LES, respectively [53]. The largest Mach numbers are found at the blade tip due to the rotation velocity, when they are small, the incompressible version of the equations are solved to

reduce the computational cost [54]. There is no agreement in the literature concerning the performance of BEM, UVLM and CFD under turbulent inflow conditions. BEM has previously been found to provide good agreement with measurements and CFD simulations [55]. However, it has also been found to overestimate fluctuations with respect to blade resolved and vortex simulations and experiments [56, 57]. Even within the blade resolved simulations, the results arising from different turbulence models have not been found to be consistent [58, 59].

In three-dimensional cases, such as, complex inflow [60], the qualitative trends of forces and rotor power and thrust coefficients between CFD and vortex methods are generally in good agreement, but the mean values are not. Moreover, CFD methods provide results closer to experiments for wind turbines under yaw and tower effect [61]. As a consequence, CFD has been used for very detailed analysis of specific phenomena like aeroelasticity [62], flap performance [63] and cases involving deep stall such as parked or standstill conditions [61]. In the case of comparing flow field velocities against experiments, both CFD codes and vortex methods have been found to provide accurate results [64, 65, 66]. Some complex scenarios, like the influence of the ground, can be equally computed with CFD and vortex methods [67].

Analysing wind farms with CFD codes is very expensive due to the large range of scales present from the blade boundary layer to atmospheric flows. To overcome this problem, actuator disc (AD) or actuator line (AL) models embedded in LES have become fashionable [68]. They solve forces on blades with the same approach as BEM methods but retrieving the velocity from the LES simulation which constitutes a high fidelity representation of the turbulent field [69]. At the same time, the previously-estimated forces are introduced into the LES flow through momentum sources. The main difficulties of these simulations are retrieving the velocity from the LES simulation, computing the force based on two-dimensional information and feeding back the force. AL combined with LES has been extensively validated against experimental wind turbine wake velocity profiles [70]. However, more discrepancies appear when blade loads are estimated [71, 32].

1.1.2 Structural dynamics

Understanding and modelling wind turbine structural dynamics is important to accurately estimate displacements, loads and assess stability [4, 72]. Extreme loads are usually large and occur in the event of extreme inflow conditions and/or exceptional machine states such as emergency stops or grid loss. These are experienced only a very limited number of

times during a turbine's life cycle. On the other hand, fatigue loads are smaller in amplitude but are time-varying and affect the structure in a continuous manner even during normal operation of a wind turbine [4].

Fully three-dimensional models provide very detailed information about local deformations which is needed to analyse problems such as buckling or propagation of cracks [73]. These models have a very large computational cost that can be reduced taking advantage of the slenderness of wind turbine blades and tower through the simplification of the structure as a collection of one-dimensional beams [74]. Good agreement between one-dimensional beam models and three-dimensional shell models has been confirmed unless local effects like buckling occur [75], which is usually associated to edgewise bending moments and it softens the structure. Generating a one-dimensional beam model of a three-dimensional structure requires a step of cross-sectional properties homogenisation [74] to quantify the stress-strain relationship of the cross section. It consists of approximating the strain energy of the three-dimensional beam as a function of the reference line properties by means of an asymptotic analysis based on the assumption that the blade length is much larger than the other two [76, 77].

Linear beam theory assumes small rotations, displacements and curvatures [78] and linear relationships between stresses and strains. Euler-Bernoulli theory provides the simplest model, while Timoshenko beam models include shear, account for cross-sectional rotation with respect to the reference line and centrifugal stiffening which is important in rotating systems [79]. The number of degrees of freedom of the system can be further reduced by using the modal approximation in which the deformed shape is approximated by a set of appropriately chosen basis functions, selected to efficiently capture realistic deformations [12]. Theoretically, the exact deformation can be recovered with a large number of independent functions but the solution is usually approximated by choosing only the shape functions associated to the lowest eigenvalues of the structure. Most computational codes for wind turbine certification originally used modal approximation [10], however, most of them have implemented nonlinear approximations in the recent years because geometrically nonlinear deformations are expected in new blades with increasing flexibility and length, [80] can occur.

Geometrically-Exact Beam Theory (GEBT) is an exact representation of the equilibrium of forces and moments in one-dimensional beams under small strains (linear stress-strain relation) but large displacements and rotations [81, 82, 83] which introduce nonlinearities in the theory. The representation of the rotations constitutes a critical point of this theory that is tackled through the definition of a set of parameters for the invariants of the rotation

field [84, 85]. One option for these parameters is using Euler angles that are intuitively defined as the rotation around cartesian axis. Rotations can also be parametrised with the cartesian rotation vector (CRV) that has the direction of the rotation axis and the module equal to the rotation amplitude. The CRV is an adequate choice because it requires the minimum number of parameters (three) and provides good linearisation properties. Third, quaternions are a representation of rotations in space through a set of four parameters and the particular algebraic operations associated to them. They remove the singularity present in Euler parameters and CRV. Nevertheless, quaternions do not perform as well as cartesian rotation vector upon linearisation. The beam dynamics equations are obtained from the principle of least action and displacements and rotations or beam strains (intrinsic formulation) [86] can be chosen as independent variables. The former has the advantage of directly providing the beam geometry, which facilitates the coupling with aerodynamic models that rely on displacements and rotations and the disadvantage of increased numerical cost of treating the rotations. The latter has the advantage of reduced computational cost but the disadvantage of requiring postprocessing of the independent variables to obtain the beam geometry. There are also hybrid approaches with increased computational cost but enhanced numerical stability [87]. This theory is usually implemented through finite elements [80, 88] and, sometimes, with multibody approximations [89].

In GEBT, global rigid body motions of the structure are tracked by means of a non-inertial frame of reference moving with the structure with respect to a ground-fixed inertial frame of reference [90]. Moreover, deformations and rotations with respect to the undeformed configuration are measured on the non-inertial frame of reference that moves with the structure (Figure 1.6a). This approach is commonly referred to as floating frame of reference [91]. Geometrically nonlinear deformations are usually associated with large deformations and rotations of the flexible structure when measured with respect to the non-inertial frame of reference moving with the structure [89]. If the body is divided into enough substructures, each of which has its own non-inertial frame of reference, deformations become small when measured on the substructure's own frame of reference [92], such that, they can be considered linear (Figure 1.6b). Multibody dynamics are employed to impose constraints between all the non-inertial frames of reference associated to the substructures. It allows a simple implementation of geometrically nonlinear deformations in multibody linear software packages [89]. For nonlinear benchmark cases, GEBT provides extremely accurate results and good agreement is also achieved with the multibody approach [93]. Moreover, results for common wind turbine loading cases are very similar between the two models [94]. However,

the multibody approximation shows small discrepancies in the computation of very nonlinear structural couplings [93].

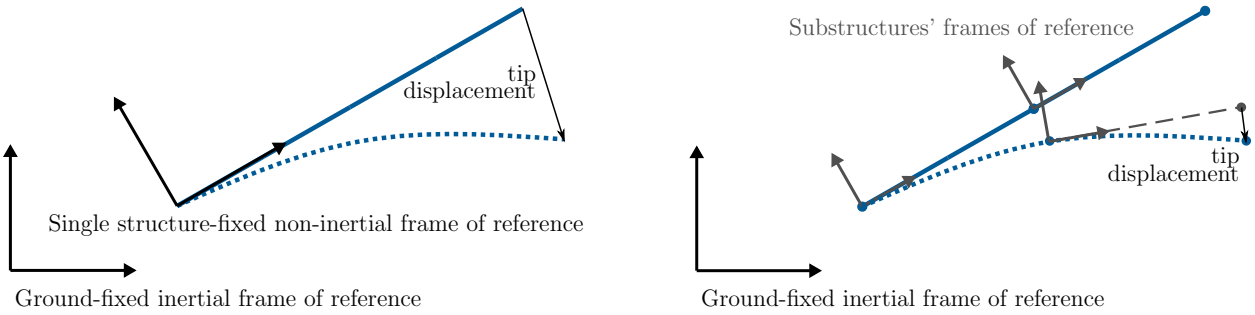

(a) Single floating. (b) Several substructures.

Figure 1.6: Frames of reference in nonlinear multibody dynamics.

GEBT can represent initially pre-bent, pre-swept and pretwisted blades that constitute the current design trends of wind turbine blades. It also accounts for large deformations that were not important in old stiff blades [88] but are gaining importance in current ones [95] due to their increasing flexibility (Figure 1.7). Moreover, it includes fully-populated stiffness matrices characteristic of anisotropic composite materials [75] and it has the capability to track the true deformation of the beam and apply the forces on it instead of using the undeformed geometry [10]. This feature makes GEBT more suitable for systems whose forces depend on the orientation of the surfaces such as wind turbine blades and to study aeroelastic problems. In particular, vortex methods can be easily integrated with beam dynamics through the assumption of rigid cross sections for flight dynamics [96, 97] or wind turbine applications [67, 98, 99, 100, 101, 102].

Composite anisotropic wind turbine blades exhibit couplings between different modes of deformation, for example, under a bending deformation the blade will also twist. This particular example is known as bend-twist coupling (BTC) and can be achieved through composite layout modification (introducing material couplings) or through geometric sweep (modifying the relative position of the aerodynamic centre, the pitch axis and the elastic centre of the cross section). Thus, it is important to accurately estimate the position of the shear and geometric centre when the one-dimensional model is created to avoid unrealistic torsion-bending couplings [75]. This coupling mechanism is more efficient under large bending deformations [94], therefore, it is mainly observed at below-rated conditions when large out-of-plane deformations occur due to the relatively low stiffness in the flapwise direction. BTC is accurately modelled by GEBT and a promising mechanism for passive load allevia-

Figure 1.7: Wind turbine blade test. Image from Renewable Energy World `https://www.renewableenergyworld.com/storage/substructure-testing-paving-the-way-to-longer-blades/`. Accessed October 5^{th}, 2021.

tion [103, 104]. As a consequence of the load reduction in critical cases, the rotor radius, and hence the energy yield, can be increased [105]. This optimisation process requires concurrent optimisation of the blade aerodynamic surface and structure [104].

The assessment of the aeroelastic system stability concerns the study of resonance and self-excited instabilities. Resonance is the linear growth of the structure motion due to an external force that interacts with the natural frequencies of the system. Given that it occurs at the structure's natural frequencies, it is relatively easily predicted and avoided at the initial design stage by separating the characteristic vibration frequencies of the structure from the operational regimes of the rotor and other external forcing. This is done, for example, by restricting the rotor velocities equal to the system natural frequencies. Self-excited instabilities do not require external forcing at natural frequencies but appear when a dynamic feedback loop is established between, for example, aerodynamic loading and structural deformation (flutter) [106] or between a static force and displacement (divergence). In linear systems, displacements grow exponentially at the beginning and, in nonlinear systems, might exhibit limit-cycle oscillation. Some authors claim future designs will be stability-driven instead of loads-driven due to the increasing appearance of this effects on very flexible blades and associated with floating dynamics [107]. The combination of a vortex method with a nonlinear beam theory provides more accurate predictions of the damping values of the edgewise

vibrations than those of the BEM theory with linear beam dynamics when compared against experiments [99]. However, the damping of the tower fore-aft movement is overestimated by free wake vortex methods due to the overly large lift-to-angle-of-attack slope [99].

Low aerodynamic damping in the edgewise direction causes very high frequency in-plane vibrations that strongly influence the drivetrain and tower dynamics [107]. Instabilities are not usually experienced at design operating conditions because they are avoided during design. However, they can arise in parked and idling conditions in both onshore and offshore configurations [107]. Some studies on flutter instability on wind turbine blades [72, 106] suggest that such instabilities would only occur at much higher frequencies than those experienced in current operational regimes. However, they could be reached for future wind turbines.

Finally, the time integration of second order beam dynamics is characterised by the wide range of characteristic frequencies (stiff system) which makes unconditional stability desirable. In nonlinear systems, a certain level of numerical damping to high frequencies [85] is usually required. Two common algorithms are the Newmark-β [85] and the generalized-α [108] which are second-order accurate for linear systems, stable under certain constraints of their parameters and permit the inclusion of dissipation controlled by the user.

1.1.3 Multibody dynamics

In previous Section 1.1.2 we described the structural behaviour of continuous elements in the system, known as elastic bodies. Complex systems, such as wind turbines, are composed of several bodies connected through a wide variety of joints, for example, hinges or sliding joints. In the finite element method, each body is divided into elements with a certain number of nodes to solve the structural dynamics equations and joints are just a description of the constrained movements between the nodes at both sides of the joint. Very rarely, these constraints are explicit on the degrees of freedom of the nodes. They are more commonly described by an implicit algebraic equation involving several degrees of freedom or their derivatives. When these equations are a function of the generalised coordinates only, the constraint is called "holonomic" and "non-holonomic" in all other cases, such as cases involving the time derivative of the generalised coordinates [85].

Additional constraints to describe joints generate a system with more equations than unknowns. In some simple cases, these systems can be solved by removing the constrained degrees of freedom, for example, when a node is clamped, all its degrees of freedom need to be removed. Another approach is, first, to compute for each body independently, second,

obtaining the reaction forces at the joints, applying those forces to the other bodies and iterate until convergence [109]. Generating universal procedures to solve constrained systems with the previous approaches is very difficult because each set of bodies and constraints has to be solved differently. Thus, the implementation of these approaches in general purpose computational codes is not feasible [110].

The application of Newton's laws and the principle of least action are two alternatives to compute the equations of motion of a system. The former requires a procedure that is very system-dependent and, thus, only convenient for simple systems. However, for more complex systems, the principle of least action provides a very general procedure in which the equations of motion are obtained by minimising the action of the system. The action of a system is the integral of its Lagrangian which consists of expressions for potential and kinetic energies and work of external forces on the system as a function of the system degrees of freedom. We use the principle of virtual work to obtain the equations of the GEBT in Section 2.1. To account for the constraints in multibody systems, we employ the *Lagrange multipliers* method which is a mathematical tool to compute maxima and minima of a function (in this case the system Lagrangian) under constraints (in this case the multibody constraints) [111]. There are subtle variations of the *Lagrange multipliers* method for flexible multibody systems [85] that aim to improve the numerical characteristics such as stability and convergence [91]. First, the *penalty function* variation proposes to substitute the evaluation of the constraints by the introduction of a penalty term into the Lagrangian that will automatically force the boundary conditions. Second, the *perturbed Lagrangian* variation aims to improve the computational properties of the Lagrange multipliers method through an additional term. These two variations cannot provide the exact solution of the problem. Finally, the *augmented Lagrangian* variation is a modification of the Lagrange multipliers approach that also includes a penalty function to improve the computational properties such as the condition number but it retains the constraints to achieve the exact solution.

The combination of the differential equations of motion of bodies with the algebraic equations of the constraints generates a differential-algebraic system of equations (DAE) that requires specific treatment for the solution. One of the approaches to solve DAE systems (known as constraint regularisation) is transforming them into a second order ODE by differentiating the constraint equations. Enforcing accelerations removes constant terms in velocities and first order terms in coordinates and controlling this numerical drift requires introducing a stabilisation term which leads to not satisfying the constraints exactly. An-

other option is to transform the structural differential equations and the constraints into a first order system [112]. For nonlinear flexible multibody systems, specific studies have shown the importance of time integration algorithms [113]. Some authors have shown that the conditioning and sensitivity of the DAE systems get worse with decreasing time step requiring more complex methods for their solution [114, 115].

In wind turbine dynamics, the most common approach to structural dynamics is to use the finite element method or modal approximation. Wind turbines require joint modelling, for example, in the hub-nacelle joint and this is almost always done through the Lagrange multipliers approach. Some examples of the use of multibody dynamcis in wind energy include CFD, drivetrain dynamics and control [116], others implement the floating frame of reference concept [103] and others have been coupled with vortex methods [117]. The use of multibody dynamics is also required in the study of wind turbine control [118, 119] because the yaw and blade pitch control mechanisms effectively constitute joints between wind turbine parts.

1.1.4 Floating platform dynamics

Floating platform dynamics include all physics associated with the interaction between the floating platform [120] and the sea. Hydrostatics is the application of Archimedes' principle to submerged bodies that results in a vertical buoyancy force to keep the wind turbine afloat through integration of the hydrostatic pressure on the platform wetted surface. Hydrostatic force (and moments) depend on the platform location and orientation. Usually, this dependency is linearised, which is accurate when the displacements are small compared to the platform characteristic length [121]. On the other hand, nonlinear effects are typically only important when the platform undergoes large amplitude motions or operates in complex sea states. In those cases, a complete integration of forces over the instantaneous wetted surface is needed. Most of the knowledge on marine dynamics has been transferred from the oil and gas industry. The knowledge directly associated to wind turbines comes from the laboratory conditions because of the few available floating wind turbines. For example, [122] presents an analysis on mooring lines, [123] studies hydrodynamics and [124] wave impact loads.

It is very common to separate hydrodynamic effects into two different contributions. Radiation explains the dissipative forces generated on a submerged body that oscillates in a fluid initially at rest as a result of the waves radiated by the body. In general, these forces are linearised and identified as damping and added-mass forces that depend on the

platform velocity and acceleration, respectively [120]. Added-mass forces can be applied to the forcing term of the wind turbine's dynamical equations but the convergence of numerical algorithms is significantly deteriorated because, in reality, these forces depend on the system acceleration. It is usually a better approach to include these forces on the mass matrix of the system [125, 123].

The diffraction phenomenon describes the wave forces on solid bodies. In particular, Airy theory studies the sea surface elevation under single amplitude and single frequency waves, and the forces they generate on solid surfaces. Again, a linearisation of this problem allows the superposition of different frequencies and amplitudes to simulate sea-states characterised by a complex spectrum of waves [126]. Second-order effects appear as a result of quadratic interactions in a situation with an irregular wave spectrum [127]. There is a non-zero-average force acting on solid bodies that displaces them from the equilibrium position known as mean-drift. There are also slow-varying loads associated with terms of frequency differences and, similarly, associated with the addition of two frequencies. The former can interact with the slow platform motions and the latter with vibration modes of the structure [128].

The study of hydrodynamics with CFD is very complex and expensive, particularly, if the air-water interface is accounted for [129]. In general, lower order methods like potential flow theory [130] are applied and, in particular, slender structures are of interest due to their abundance in offshore applications. There is a wide theory about slender structures (i.e. their characteristic length is small compared to the wave length) [120] that is usually simplified through Morison's equation [123] which just separates forces on drag and inertia and computes them through a coefficient times kinematic properties of the system. This formulation can be corrected [131] for more complex structures. The Cummings equation [121] computes the platform dynamics from a convolution integral of a retardation function matrix.

Different levels of approximation for mooring lines are available [132]. The quasi-steady approach proposes to solve the catenary equation to obtain the forces accounting for mooring line weight, buoyancy, axial stiffness and friction with the seabed [133, 134]. Quasi-steady models can be assumed in the estimation of blade loads although they introduce a small-to-significant error in tower-base loads and clearly fail to predict dynamic loads on the mooring lines [122]. Quasi-steady approximation neglects the added-mass, damping and drag effects that are only captured by dynamic models based on finite element representations of the mooring lines. The force-displacement theory is a finite element solution that takes into account similar effects to the quasi-steady approach. Lastly, dynamic models include inertia,

added mass and hydrodynamic drag to the previous effects. Usually, they employ Morison's equation due to the slender shape of mooring lines. These effects might be important in deep waters where mooring lines undergo large and quick movements [135].

There are several designs for wind turbine floating platforms [11] whose main objective is to provide buoyancy and stability to the system at a minimum cost such as spar buoy, barge, tension leg platform (TLP) and hybrid designs. They are usually classified as a function of their main stabilisation mechanism. Spar buoy (Figure 1.8a) is a vertical deep-draft structure with an underwater ballast that acts as a pendulum to provide stability and increases the material cost. The links of the mooring system provide some yaw stability. Barge (Figure 1.8b) is a shallow-draft structure with a relatively large water plane area to provide stability. It usually results in simple but heavy platforms which are self-stable making their shipping easier and cheaper. Ideally, platforms should be placed at a certain depth underwater (draft) to avoid excessive wave interaction, this is especially critical in the barge-type because this is the most exposed to wave motions and air and water exposure enhancing corrosion. The tension leg platform (Figure 1.8c) consists of a small platform linked to the seabed by mooring lines in tension which provide the stability to the wind turbine. It is the most complex in design and installation of the platforms presented here but it provides the most stable system and, thus, the least impact on turbine dynamics. The spar buoy and the barge use mooring lines to avoid platform drifting but they do not significantly provide stabilisation. Thus, the mooring lines are longer, simpler and less loaded in the spar buoy and barge platforms than in the TLP. In practice, most designs are hybrid among the previous ones, such as the Dutch tri-floater (Figure 1.8d).

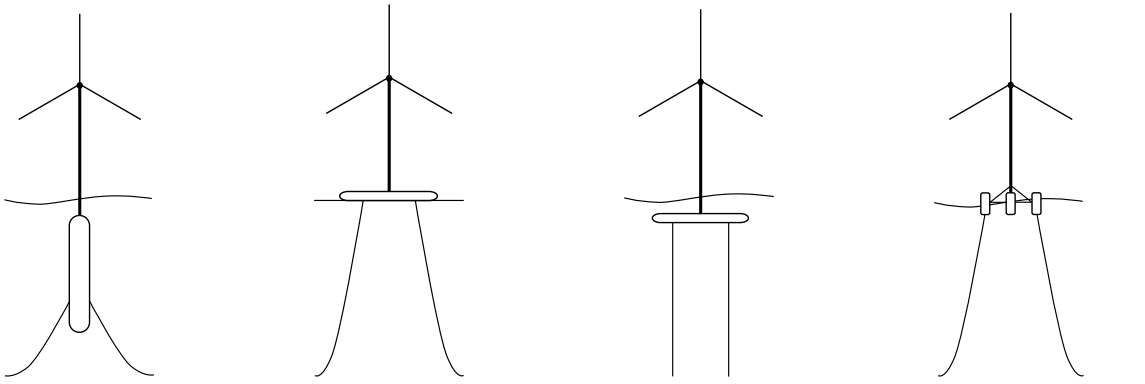

(a) Spar (b) Barge. (c) Tension leg. (d) Dutch tri-floater.

Figure 1.8: Floating platform designs.

A particular numerical study [136] involving the three platform concepts shows that the

barge design is very influenced by the waves and leads to excessive pitch and roll motions generating the largest fatigue and ultimate loads. The TLP concept shows much less platform motion than the barge, which slightly increases the loads with respect to the land based turbine. The controller for the spar buoy design was changed generating results that are difficult to compare against the land based turbine but it exhibits intermediate movements and loads than the other two. Experimental studies have shown significant changes in the dynamics of the three concepts [137], and have evidenced the need to design specific controllers for offshore wind turbines mainly for displacement and load reduction due to the influence on the pitch damping [138].

The rotor mean and dynamic displacements in pitch significantly influence the power production [139]. The average pitch displacement reduces the power generation more in the spar configuration than the semisubmersible platform studied. The semisubmersible shows power increases with respect to the fixed base wind turbine due to dynamic motions of the rotor upwind/downwind which increase/decrease the relative velocity of the wind and the rotor. The rest of the platform displacements show insignificant effects on the power generation in the studied setup. For high pitching frequencies equal to half of the rotation frequency, huge differences in power and thrust with respect to the fixed base turbine can be found [140]. In these cases, aerodynamic states out of the range of application of BEM can be found such as vortex ring state.

1.1.5 Control

Wind turbines operate with a feedback control in which the state of the system is measured and modified through a series of actuators to satisfy a user input. Control systems seek to achieve optimal operation, stabilisation and load reduction. Some examples have already been introduced in the previous Section 1.1.4 where we described the problem of establishing and optimising the pitching motion of floating wind turbines.

Nowadays, the most common wind turbine configuration is variable rotor speed and variable pitch. It has relatively high complexity but allows optimal operation of the wind turbine at a wider range of wind speeds as compared to other concepts, such as, fixed speed or fixed-pitch wind turbines. At low wind speeds, wind turbines operate at maximum efficiency extracting all the possible power from wind. At a certain wind speed, which depends on the wind turbine design, nominal power generation is reached such that for higher wind speeds the wind turbine does not operate at maximum efficiency but at constant rated power. The reason to limit the efficiency and power generation is avoiding excessive structural loads

that would increase the wind turbine cost. These two regimes are named "below-rated" and "above-rated", respectively. The main objective of the wind turbine controller below rated power is operating the wind turbine in optimal conditions such that the maximum power generation is achieved. Above rated power, the objective is maintaining a constant power generation and rotational speed [4]. A traditional control scheme of a variable-pitch variable-velocity wind turbine is included in Figure 1.9.

The main control actuator in current wind turbines is the pitch actuator (rotation of the blade around its longitudinal axis) through a proportional-integral feedback controller. A change in the pitch angle modifies the aerodynamic forces and consequently the power production and loading of the wind turbine. Positive and negative pitch angles rotate the blade such that its chord aligns with the incoming wind speed or the rotation velocity, respectively. These pitch motions are usually referred to as "pitch-to-feather" and "pitch-to-stall", respectively. Above rated power, pitch is typically operated towards feather. The pitch angle is increased to reduce the angle of attack and, thus, decrease the power generation with respect to the maximum production to reduce the design loads. Another option is the pitch-to-stall, which generates less pitch actuation and smoother control [141] but it is not commonly employed because stall loads are not very desirable on wind turbines due to the uncertainty in their estimation and unsteadiness. If the three blades are operated at the same pitch angle we call it "collective pitch" control. Individual pitch control (IPC) allows the definition of the pitch angle of each blade independently achieving even better results at the cost of increased control complexity and the availability of other sensors [141]. There is a second important actuator (yaw) used to align the rotor to the wind through the rotation of the nacelle and rotor around the longitudinal axis of the tower. The need of rotating the large mass and inertia of the rotor and the nacelle makes this mechanism very slow (it is usually actuated every ten minutes) and not suitable for load reduction during the operation of individual wind turbines. However, it can be used to reduce the influence of one wind turbine in the downstream one optimising the whole wind farm behaviour [142].

We now present a series of problems in wind energy that can be tackled just through controller design. A first problem is to minimise deterministic loads (associated to shear and tower shadow) which can be tackled by just measuring the rotor azimuthal angle [144]. If the individual loading of the blades can be measured, for example with strain gauges at blade roots, shaft or yaw bearing sensors, more complex designs could be generated for example through linear–quadratic–gaussian control design techniques, which represents the simplest modern technique for multiple input and output controller design. IPC can be especially

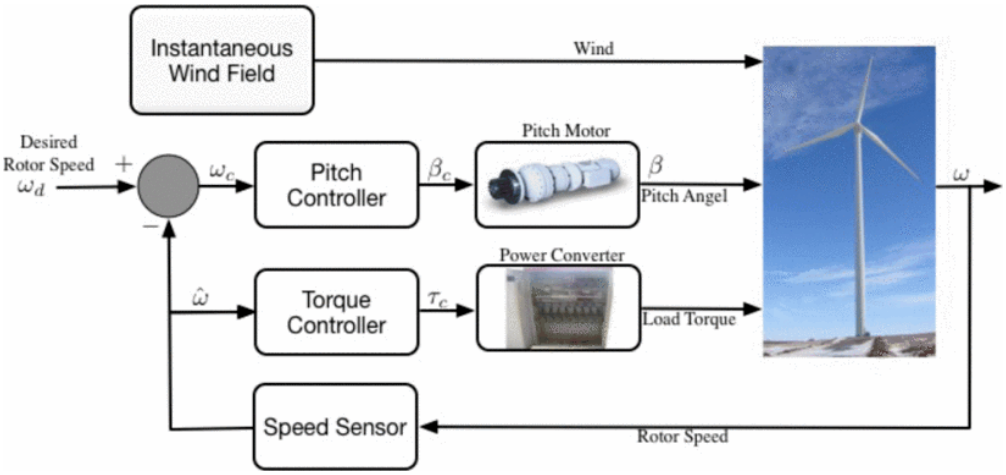

Figure 1.9: Control scheme of a variable-pitch variable-velocity wind turbine. Image from Mughal et al. [143].

useful to reduce the peak in the root-bending moment spectrum at rotation frequency, the shaft bending moment or the yaw moment on the bearing [141].

A second problem is the non-desirable tower fore-aft movement that causes fatigue loads at the tower base. Rotor thrust is the main excitation to tower fore-aft movement and it is significantly influenced by the blade pitch angle. The quantification of pitch-to-thrust sensitivity and the measurement of the tower-top acceleration enables the generation of control logic that attempts to reduce the tower-top movement. This effect is aggravated in floating wind turbines in which large rotor excursions imply a significant change of the relative velocity between the wind and the rotor. This affects the rotor loads and the aerodynamic damping of the platform pitching motion, and, consequently, the system stability. Some authors [145] have run experiments that use this philosophy to reduce the tower vibrations. However, some computations [146] and experiments [138] have shown that it was not possible to reduce the platform motions because the two objectives of the controller require opposite operation of the pitch actuation. This is, in an event of a forward movement of the platform, the relative wind velocity increases, the controller would try to, first, maintain the rotor velocity by increasing the pitch and, second, to increase damping to reduce the forward movement by reducing the pitch. The assumption of constant damping coefficient with frequency leads to an underestimation of the system displacements. However, accounting for the changes of the pitch-to-thrust sensitivity with frequency is not enough to keep the platform displacements in adequate ranges [147].

Torque oscillations in the drivetrain of variable speed wind turbines are also of concern

because they generate life-limitting fatigue loads. The most efficient way of reducing these fatigue loads is by avoiding excessive operation around the drivetrain resonant frequencies. With this objective, a band-rejection filter around the drivetrain resonant frequency is applied to the generator velocity measurement such that the pitch actuation at the resonant frequencies is reduced [141].

Smart rotors include a series of distributed sensors, such as accelerometers and strain gauges, and actuators, such as flaps or plasma actuators. These actuators provide a local mechanism to control loads with higher frequencies than the achievable by the pitch actuator [148]. Some modern control techniques like model predictive control, that estimate the current and future state of the system base on an internal model of the wind turbine, have been used to study the performance of flaps showing promising load reduction at the cost of complex system identification techniques [149]. This method has been validated in experimental wind turbines [144] showing root bending moment reduction. Flaps, in particular, have also been tested in collaboration with passive control mechanisms such as bend-twist coupling based on a explicit linearisation of the system and a $\mathcal{H}_\infty$ controller [150]. Smart rotors are being studied in the research community but they require new sensors and actuators that are not currently available in commercial wind turbines and improvements in computational methods to match experimental results.

The control design process should be informed by all the relevant phenomena involved in the system behaviour. For example, the tower fore-aft movement, the blade pitching rotation and the blade flapwise and torsional deformations generate unsteady aerodynamic phenomena that should be accounted for in the control design process to avoid the large overshoot of aerodynamic forces [151].

1.1.6 Some software packages for wind turbine aeroelasticity

This section presents a review of the state of the art for aeroelastic simulation code developed in both industry and academia. We pay special attention to the similarities and differences with `SHARPy` which is the software package in which we have implemented all the required capabilities to enable the simulation of floating wind turbines from the baseline code thought for aircraft simulation.

- `SHARPy` (Simulation of High-Aspect Ratio Planes in Python) is the open-source [152, 153, 154] aeroelastic code from Imperial College London for the simulation of flexible aircraft [155, 156] and wind turbines. It is based on UVLM and GEBT for the aero-

dynamics and the structural dynamics, respectively. It includes multibody dynamics based on Lagrange multipliers, floating dynamics with added-mass and damping radiation matrices, Airy theory for waves and quasi-steady mooring dynamics. It also has collective blade pitch control capabilities through PID. It includes explicit linearisation and model order reduction (balanced truncation and Krylov methods).

- `OpenFAST` (Open Fatigue, Aerodynamics, Structures and Turbulence) [157] is the aeroelastic code of National Renewable Energy Laboratory (NREL). It is built in a modular framework in which different modules compute different physics. It has traditionally used BEM for the aerodynamics with the usual corrections (Section 1.1.1) but the latest versions include also a free vortex wake method [158] based on actuator-line theory. It includes structural solution based on linear modal analysis with two flap and one edgewise modes and nonlinear approaches. It has interfaces with external hydrodynamic and control libraries. It also implements internal simple models for control and linearisation capabilities to aid the control design. As a part of the distribution `TurbSim` [43] generates 3D turbulent velocity fields.

- `HAWC2` (Horizontal Axis Wind turbine simulation Code 2nd generation) is the aeroelastic code from Danmarks Tekniske Universitet (DTU) Wind Energy [159]. It is based on BEM with the usual corrections (Section 1.1.1), multibody formulation and structural dynamics with Timoshenko beam theory with a fully populated stiffness matrix. It has interfacing capabilities with other solvers such as the CFD code `EllipSys3D` [160] and control libraries. It has also interesting preprocessing open-source tools like a Mann box turbulence generator [44, 161].

- `Bladed` is the commercial software from DNV-GL [162]. It uses BEM with the usual corrections and a multibody approach for nonlinear beam dynamics [89]. It includes hydrodynamics and interfaces with other software for complex scenarios and control libraries.

- In the National Technical University of Athens (NTUA) they have several modules that can be combined for wind turbine aeroelasticity. `hGAST` is the linear and nonlinear structural solver and `GenUVP` (GENeral Unsteady Vortex Particle) is the aerodynamic one. It discretises solid surfaces with panels and it sheds free vorticity to the fluid in form of vortex blobs. It uses a particle-mesh method to reduce the computational cost [59, 163, 99].

- Energy Research Centre of the Netherlands (ECN), now part of TNO, has the aeroelastic code `PHATAS` (Program for Horizontal Axis wind Turbine Analysis and Simulation). The aero-module includes BEM and free vortex wake modules (`AWSM`). And the structural dynamics are managed by FOCUS-Phatas [27].

- `WAMIT` is not an aeroelastic code but a hydrodynamic inviscid panel method used to compute the platform frequency response [130, 164] for the radiation and diffraction problems. It is used as preprocessing tool for some of the above aeroelastic codes.

Some implementations use vortex methods for the aerodynamics (`GenUVP` and `AWSM`) but most of them employ BEM methods (`OpenFAST`, `HAWC2`, `Bladed` and `PHATAS`). In the past, they employed linear models but most of them offer the possibility to compute nonlinear structural dynamics through traditional (`OpenFAST` and `hGAST`) or multibody (`Bladed` and `HAWC2`) approaches. The hydrodynamics and control are always included as an interface with a dedicated library. `SHARPy` is a state-of-the-art software package for the computation of offshore wind turbine aeroelasticity which is the only one that combines UVLM with GEBT and the advantage of being open-source. In this dissertation, we also analyse the capabilities of LES-AL theory to capture wind turbine dynamics. LES-AL theory is usually employed for wind farm simulation and has been implemented, for example, in the following packages

- `WInc3D` is a LES-AL wind farm simulator previously developed at Imperial College London to study the flow structure and turbulence in wind farms [45]. It includes several LES implicit and explicit models (such as the constant Smagorinsky explicit LES) with a sixth-order finite difference discretisation. The AL model is an in-house implementation based on rigid blades and tower.

- `SOWFA` (Simulator fOr Wind Farm Applications) combines `OpenFOAM` as the flow solver and `FAST` as the actuator-line model. `SOWFA` includes the capabilities of both software packages, being of particular interest, the applications for wind energy such as the simulation of atmospheric boundary layer or the use of precursor simulations as input.

In this thesis, we compare the accuracy of BEM, UVLM and LES-AL with their implementations in `OpenFAST`, `SHARPy` and `WInc3D`, respectively.

1.2 Motivation and research questions

We have identified some phenomena that are or might be of concern in wind energy including unsteady and three-dimensional aerodynamics and anisotropic nonlinear structural dynamics and that might require more complex numerical methods for their estimation. This idea motivates the study of several operating conditions (yaw, turbulent and floating cases) of wind turbines with several modelling fidelities (BEM, UVLM, LES-AL) to identify whether these phenomena are relevant or negligible, to establish ranges of validity for these methods and to improve them when possible. This analysis is based on the collaboration between modelling fidelities due to the lack of access to experiments or higher-accuracy numerical methods. This motivation leads to the following research questions (**RQ**):

Research Question 1: When are vortex methods sufficiently accurate for the analysis of wind turbines? The main drawback of UVLM is the assumption of negligible flow viscosity which prevents the modelling of viscous drag and flow separation (Section 1.1.1) which are effects occurring in wind turbines. This reduces the accuracy on the estimation of blade loads and flow velocities in the wake.

Research Question 2 : When are unsteady and three-dimensional aerodynamic effects relevant in wind turbine aerodynamics and can vortex methods help understanding them? Unsteady and three-dimensional aerodynamic effects come from the operation of wind turbines in complex inflows (e.g., arising from uneven terrain or the wake of upstream turbines), blade vibrations and rotor excursions associated with tower flexibility and, more importantly, platform displacement. They are inherently captured by UVLM but not by BEM.

Research Question 3: Can we define the accuracy of BEM computations in cases of yaw using vortex methods? When a wind turbine operates in yaw, BEM hypotheses fail because there is not uniform induction in the radial and azimuthal directions. To include this effect in BEM, skewed-wake models have long been proposed (Section 1.1.1). Vortex methods inherently account for unsteady and three-dimensional aerodynamic effects that are characteristics in cases of yaw so they are a suitable tool to evaluate the accuracy of the skewed-wake models for BEM.

Research Question 4: When are nonlinear structural deformations and platform displacements relevant and how do they interact with aerodynamics? New wind turbine designs with longer and more flexible blades are increasing the structural

deformations. This has an effect on structural dynamics but also on aerodynamics due to the change in aerodynamic surface orientation. Moreover, the platform movements generates rotor excursions and might interact with the rotor structural dynamics and aerodynamics causing unsteady effects that could lead to a load increase or a performance decrease

Research Question 5: Is the combination of vortex methods with nonlinear beam theory sufficiently efficient for design purposes? One of the main advantages of BEM is the low computational cost that makes it more suitable to run the large number of computations required in the design phase. The increase in accuracy expected from the use of vortex methods and nonlinear beam theories cannot come at the expenses of a privative computational cost. Another desirable characteristic of the numerical implementation is being open-source to achieve an impact on industry and academia.

Research Question 6: Can the improved modelling features be used to improve the controller design towards load reduction? The previous questions are oriented towards increasing the knowledge about aeroelasticity of offshore wind turbines and describe the accuracy and efficiency of numerical tools. Both the increased knowledge and the availability of an accurate numerical tool for testing provide a suitable environment to propose controllers with increased performance that could achieve loads reduction or performance increase.

1.3 Dissertation outline

Chapter 2 describes the numerical methods employed during this thesis for the computation of floating wind turbine aeroservoelasticity. First, nonlinear multibody structural dynamics are described together with the Newmark-β and the generalized-α time integration schemes. Then, BEM, UVLM and LES-AL are described as the three fidelities to capture the aerodynamics. Then, the simple models chosen for floating dynamics are outlined. Finally, the integration of all the different physics fields is illustrated together with the wind turbine controller. The advantages and drawbacks of each numerical method stems from their theoretical basis, thus, this chapter is important to understand the suitability of each method for each scenario.

Chapter 3 includes validation cases for the numerical implementations performed during this thesis. First, multibody dynamics and time integration schemes. Second, unsteady

and three dimensional capabilities of UVLM. Third, a mesh convergence study on a wind turbine rotor is performed for UVLM together with the analysis of the different wake models. Finally, floating dynamics and the control implementations are validated against literature results. This chapter provides certainty about the numerical implementations used in the following ones.

Chapter 4 describes our efforts to include a drag estimation in UVLM (**RQ 1**), to reduce the computational cost of UVLM through a new discretisation of the wake convection equation (**RQ 5**) and the improvement of BEM to account for the interaction between spanwise sections based on a UVLM analysis of this phenomenon (**RQ 2**). Then, the three aerodynamic fidelities are benchmarked for traditional flows such as steady uniform, yawed (**RQ 3**) and turbulent inflows (**RQ 2**) to critically describe the suitability of each one of them in each case including ranges of applicability.

Chapter 5 presents the effect of twist deformation on wind turbine aerodynamic loading and the unsteady contribution of the platform pitch and roll motions (**RQ 4**) to the aeroelastic behaviour of the blades. It is shown that accounting for the twist deformation significantly modifies the sensitivity of the generated power to a change in blade pitch angle. Thus, we redefine the baseline controller based on our UVLM and GEBT computations that achieves a reduction of the fluctuations of platform displacements and rotor velocity with respect to the baseline controller (**RQ 6**).

Chapter 6 presents a summary of this dissertation together with the main conclusions, contributions and guidelines for future work.

1.4 Publications

Part of the work compiled in this dissertation has also been disseminated in the following conference and journal papers:

- A. Muñoz-Simón, A. Wynn, and R. Palacios. "Unsteady and three-dimensional aerodynamic effects on wind turbine rotor loads". AIAA Scitech 2020 Forum (Jan. 2020). DOI:10.2514/6.2020-0991

- A. Muñoz-Simón, R. Palacios, and A. Wynn. "Benchmarking different fidelities in wind turbine aerodynamics under yaw". Journal of Physics: Conference Series 1618 (Sept. 2020), p.042017. DOI:10.1088/1742-6596/1618/4/042017

- C. Wang, A. Muñoz-Simón, G. Deskos, S. Laizet, R. Palacios, F. Campagnolo, and C.L. Bottasso. "Code-to-code-to-experiment validation of LES-ALM wind farm simulators". Journal of Physics: Conference Series 1618 (Sept. 2020), p.062041. DOI:10.1088/1742-6596/1618/6/062041

- A. del Carre, A. Muñoz-Simón, N. Goizueta, and R. Palacios. "SHARPy: A dynamic aeroelastic simulation toolbox for very flexible aircraft and wind turbines". Journal of Open Source Software 4.44 (Dec. 2019), p. 1885. DOI:10.21105/joss.01885

- A. Muñoz-Simón, R. Palacios and A. Wynn. "Some modelling improvements for prediction of wind turbine rotor loads in turbulent wind". Wind Energy, Wiley, 2021. DOI:10.1002/we.2675

Chapter 2

Numerical methods

Wind turbine blades with increasing length and flexibility are the current design trends to increase the power generation and reduce the cost. First, the increasing blade length and flexibility is leading to larger and possibly nonlinear deformations that are not captured by linear structural theories, thus, we describe nonlinear Geometrically-Exact Beam Theory (GEBT) that is adequate for the simulation of nonlinear deformation in anisotropic composite materials. This theory needs to be generalised for multibody systems that use joints between the different bodies (nacelle and blades) and to be equipped with time integration schemes to capture the system dynamics. The GEBT expanded with multibody dynamics and time integration schemes constitutes the structural dynamics of the system described in Section 2.1.

Moreover, increasing blade length and flexibility together with the operation of the wind turbine in more complex inflows (i.e. from the wake of other turbines, platform motions or complex terrain) is increasing the unsteady and three-dimensional aerodynamic effects. We describe three different aerodynamic fidelities for the computation of the wind forces on the wind turbine blades (Section 2.2). Blade-Element Momentum (BEM) theory is the industry standard for aerodynamic computations and it is extremely efficient. However, it does not intrinsically account for unsteady (sudden pitch changes, gusts and blade vibrations) and three-dimensional (skewed-wake in yaw cases and quick changes of circulation along the span) aerodynamic effects because it is based on steady theories and two-dimensional force data. The Unsteady Vortex-Lattice Method (UVLM) inherently captures these effects at the expense of increased computational cost with respect to BEM theory and assuming potential inviscid flow. Finally, Large-Eddy Simulation with Actuator-Line (LES-AL) is gaining relevance in the computation of wind-farm scale flows accounting for flow unsteadiness

and three-dimensionality but relying on two-dimensional information for the computation of forces at an extremely high cost.

Future wind turbines will be mounted on floating platforms in the sea as opposed to current onshore wind turbines. This will significantly increase the rotor excursions and requires more complex simulations described in Section 2.3. It includes a quasi-steady model for the mooring dynamics that accounts for mooring forces as a function of the platform displacements but disregards dynamic effects. The hydrostatics are described though a linear method suitable for small displacements and rotations. The hydrodynamics are divided into radiation and wave diffraction forces for which we also describe linear models suitable for small platform displacements and small amplitude wakes. These models are completed with a viscous drag estimation from the Morison's equation. Morison's equation can be considered accurate for the structures employed in this dissertation, whose characteristic length is smaller than the wave length [120, 165].

Finally, we describe the interactions between the structural dynamics, aerodynamics, mooring dynamics and hydrodynamics and the control system in Section 2.4 because the concurrent simulation of all of them is vital for the adequate prediction of wind turbine aeroelasticity.

2.1 Structural dynamics

Originally, `SHARPy` included single-body geometrically nonlinear beam theory GEBT (Section 2.1.1) with a Newmark-β time integration scheme (Section 2.1.2). Nevertheless, understanding the underlying theory was needed by the author for code debugging and developing the author's own contributions, thus, a brief theory description is presented next. Moreover, the code has been extended by the author with multibody dynamics (Section 2.1.3) to account for the tower-rotor joint and the generalized-α time integration scheme (Section 2.1.2).

2.1.1 Nonlinear geometrically-exact beam theory

Each wind turbine blade and the tower are considered as beams and modelled by defining a reference line with rigid cross sections [74]. The reference line geometry along time is tracked with a displacement-based approach using Cartesian coordinates and cross-sectional rotations. GEBT [87] does not assume infinitesimal displacements and rotations as opposed to linear theories of elasticity. This implies acknowledging the differences between the initial

and the deformed reference lines, the effect it has on the system mass and stiffness distribution and the direction of application of aerodynamic forces. This constitutes a geometrically nonlinear theory which uses linear stress-strain relationships of the material.

Three different frames of references (Figure 2.1) are defined to characterise the geometry of the structure [80]. A non-inertial body-fixed frame of reference A (also referred to as the *global* frame) is placed at the wind turbine base or the rotor hub position. The kinematics of this frame of reference with respect to a global inertial frame of reference G corresponds to the rigid body motions of the structure. The inertial G frame of reference is also used as a reference for gravity loads. Finally, a local frame of reference B (also referred to as the *material* frame) is defined at each position along the reference line. Reference line displacements and rotations associated with the structure flexibility are tracked through the motion of the B frame of reference with respect to the A frame of reference. In this way, displacements and rotations associated to rigid-body motions and flexibility, which are usually of different orders of magnitude, are tracked with different variables increasing computational accuracy and speed [90].

Subindices are added to variables according to the frame of reference they refer to. Lower-case variables track rigid-body motions: position $\boldsymbol{r}_A$, rotation $\boldsymbol{\varphi}$, linear $\boldsymbol{v}_A$ and angular $\boldsymbol{\omega}_A$ velocities of the A frame of reference. Upper-case variables represent flexible beam deformation: position $\boldsymbol{R}_A$, rotation $\boldsymbol{\Phi}$, linear $\boldsymbol{V}_B$ and angular $\boldsymbol{\Omega}_B$ velocities of the B frames of reference which are fixed at each position of the reference line. Lastly, the position of points outside the reference line is given by $\boldsymbol{b}$ with respect to the B frame of reference. The representation of large rotations ($\boldsymbol{\varphi}$ and $\boldsymbol{\Phi}$) in space requires further discussion which is given next.

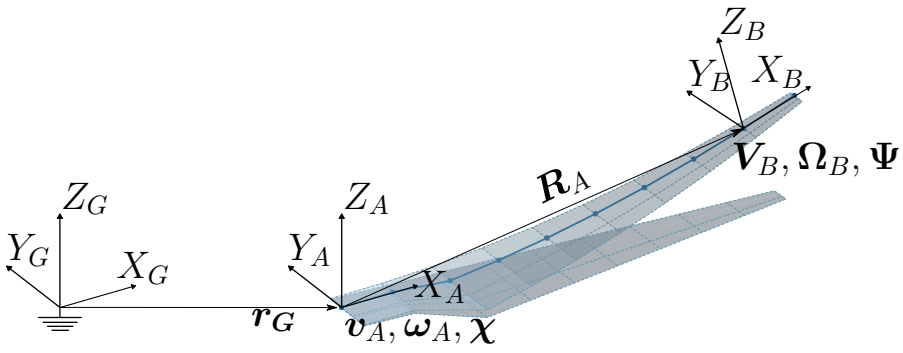

Figure 2.1: Scheme of the structural problem nomenclature.

Parametrisation of rotations

To represent rotations, we follow an algebraic approach [85] based on parametrising the invariants of rotation [84] with two different sets of parameters: one for the flexible ($\boldsymbol{\Phi}$) and one for the rigid body ($\boldsymbol{\chi}$) rotations. Moreover, the mathematical tools required in the following section to obtain the equations of motion are also discussed.

First, the rotations of the beam cross sections associated with the flexible deformation of the beam (denoted by $\boldsymbol{\Phi}$ in general) are parametrised with the cartesian rotation vector (CRV, $\boldsymbol{\Psi}$). This approach provides a minimum set of parameters and are easy to interpolate in the finite-element model described next in Section 2.1.1. The coordinate transformation matrix between the A and B frames of reference, C^{BA}, can be computed from the CRV ($\boldsymbol{\Psi}$)

$$C^{BA}(\boldsymbol{\Psi}) = I_{3\times3} + \frac{\sin\left(\|\boldsymbol{\Psi}\|\right)}{\|\boldsymbol{\Psi}\|}\tilde{\boldsymbol{\Psi}} + \frac{1-\cos\left(\|\boldsymbol{\Psi}\|\right)}{\|\boldsymbol{\Psi}\|^2}\tilde{\boldsymbol{\Psi}}^2 = \sum_{k=0}^{\infty}\frac{1}{k!}\tilde{\boldsymbol{\Psi}}^k, \tag{2.1}$$

where the $\tilde{\bullet}$ operator [87] is defined as

$$\tilde{\boldsymbol{\Psi}} = \begin{bmatrix} 0 & -\Psi_3 & \Psi_2 \\ \Psi_3 & 0 & -\Psi_1 \\ -\Psi_2 & \Psi_1 & 0 \end{bmatrix}, \tag{2.2}$$

where Ψ_i represents the i^{th} component of the $\boldsymbol{\Psi}$ vector. Eventually, this operator will be useful to express the cross product of two vectors $\boldsymbol{a}_1$ and $\boldsymbol{a}_2$ as $\boldsymbol{a}_1 \times \boldsymbol{a}_2 = \tilde{\boldsymbol{a}}_1\boldsymbol{a}_2$.

The angular velocities $\boldsymbol{\Omega}_B$ of the material frame of reference are computed as the time derivative of the CRV $\boldsymbol{\Psi}$:

$$\boldsymbol{\Omega}_B = T(\boldsymbol{\Psi})\dot{\boldsymbol{\Psi}} + C^{BA}(\boldsymbol{\Psi})\boldsymbol{\omega}_A. \tag{2.3}$$

with the tangential operator T defined as

$$T(\boldsymbol{\Psi}) = I_{3\times3} + \frac{\cos\left(\|\boldsymbol{\Psi}\|\right)-1}{\|\boldsymbol{\Psi}\|^2}\tilde{\boldsymbol{\Psi}} + \left(1-\frac{\sin\left(\|\boldsymbol{\Psi}\|\right)}{\|\boldsymbol{\Psi}\|}\right)\frac{\tilde{\boldsymbol{\Psi}}^2}{\|\boldsymbol{\Psi}\|^2} = \sum_{k=0}^{\infty}\frac{(-1)^k}{(k+1)!}\tilde{\boldsymbol{\Psi}}^k. \tag{2.4}$$

Two expressions are given for the rotation matrix (Equation 2.1) and the tangential operator (Equation 2.4) because the exact expression generates numerical problems for small norms of the CRV and the series expression is easily truncated to a certain accuracy in numerical methods.

Second, the rotation of the body-fixed frame of reference is parametrised with quater-

nions ($\boldsymbol{\chi} = [\chi_0 \quad \boldsymbol{\chi}_v^T]^T$) which require four parameters instead of the three employed by the CRV but are more robust in the characterisation of large rotations because they have no singularities. The rotation matrix between the frames of reference G and A is computed as:

$$C^{GA}(\boldsymbol{\chi}) = (2\chi_0^2 - 1)I_{3\times3} + 2(\boldsymbol{\chi}_v\boldsymbol{\chi}_v^\top + \chi_0\tilde{\chi}_v). \tag{2.5}$$

Moreover, the time evolution of the quaternion is described by the following equation [166]:

$$\dot{\boldsymbol{\chi}} = \frac{1}{2}\begin{bmatrix} 0 & -\boldsymbol{\omega}_A^\top \\ \boldsymbol{\omega}_A & -\tilde{\boldsymbol{\omega}}_A \end{bmatrix}\boldsymbol{\chi}. \tag{2.6}$$

Continuous beam equations of motion

The action of a flexible system S between two time instants t_1 and t_2 is defined as:

$$S = \int_{t_1}^{t_2}\int_0^L (\mathcal{L} + \mathcal{W})\ \mathrm{d}s\,\mathrm{d}t, \tag{2.7}$$

with s a variable along the beam of length L, $\mathcal{L}$ the Lagrangian per unit length of the system equivalent to the difference between the kinetic $\mathcal{T}$ and potential $\mathcal{U}$ energies and the work $\mathcal{W}$ of externally applied forces. The kinetic energy is

$$\mathcal{T} = \frac{1}{2}[\boldsymbol{V}_B^\top \quad \boldsymbol{\Omega}_B^\top]\mathcal{M}_{\mathrm{cs}}[\boldsymbol{V}_B^\top \quad \boldsymbol{\Omega}_B^\top]^\top = [\boldsymbol{V}_B^\top \quad \boldsymbol{\Omega}_B^\top][\boldsymbol{P}_B^\top \quad \boldsymbol{H}_B^\top]^\top, \tag{2.8}$$

with $\boldsymbol{P}_B$ and $\boldsymbol{H}_B$ the local transitional and angular momenta, respectively, and $\mathcal{M}_{\mathrm{cs}}$ the cross-sectional mass matrix. The mass matrix relates forces and accelerations and, under the assumption of non-deformable cross sections ($\partial\boldsymbol{b}_B/\partial t = 0$), is obtained from rigid body properties: the mass per unit length m, the cross-sectional inertia matrix J, and the distance between the reference line and the centre of mass of the cross section $\boldsymbol{b}_B^{\mathrm{cg}}$:

$$\mathcal{M}_{cs} = \begin{bmatrix} mI_{3\times3} & -m\tilde{\boldsymbol{b}}_B^{\mathrm{cg}} \\ m\tilde{\boldsymbol{b}}_B^{\mathrm{cg}} & J \end{bmatrix}. \tag{2.9}$$

The potential energy is

$$\mathcal{U} = \frac{1}{2}[\boldsymbol{\gamma}^\top \quad \boldsymbol{\kappa}^\top]\mathcal{S}_{\mathrm{cs}}[\boldsymbol{\gamma}^\top \quad \boldsymbol{\kappa}^\top]^\top = [\boldsymbol{\gamma}^\top \quad \boldsymbol{\kappa}^\top][\boldsymbol{F}_B^\top \quad \boldsymbol{M}_B^\top]^\top, \tag{2.10}$$

with $\boldsymbol{\gamma}$ and $\boldsymbol{\kappa}$ the generalised strains and curvatures, respectively, $\boldsymbol{F}_B$ and $\boldsymbol{M}_B$ are the internal forces and moments, respectively, and $\mathcal{S}_{\text{cs}}$ the cross-sectional stiffness matrix. The stiffness matrix relates strains and stresses in the cross section and is obtained from the constitutive relations of the material. It depends on the elastic properties of the material such as elastic modulus, shear modulus and Poisson coefficient and on the geometric properties of the cross section such as area, shear area and moments of inertia. Anisotropic properties of wind turbine blades are represented through the definition of the full mass and stiffness matrices of each cross section. Strains $\boldsymbol{\gamma}$ and curvatures $\boldsymbol{\kappa}$ are obtained from the geometrical description of the system:

$$\boldsymbol{\gamma}(s,t) = C^{BA}(s,t)\boldsymbol{R}'_A(s,t) - C^{BA}(s,0)\boldsymbol{R}'_A(s,0), \tag{2.11a}$$

$$\boldsymbol{\kappa}(s,t) = \boldsymbol{K}_B(s,t) - \boldsymbol{K}_B(s,0), \tag{2.11b}$$

where $\bullet'$ denotes the derivative with respect to the arc length s and $\tilde{\boldsymbol{K}}_B$ is defined [167] as $\tilde{\boldsymbol{K}}_B = C^{BA}\left(C^{AB}\right)'$. In particular, for the CRV parametrisation of the rotations,

$$\boldsymbol{K}_B(s,t) = T(\boldsymbol{\Psi}(s,t))\boldsymbol{\Psi}'(s,t) - T(\boldsymbol{\Psi}(s,0))\boldsymbol{\Psi}'(s,0). \tag{2.12}$$

Finally, the work $\mathcal{W}$ performed by external forces $\boldsymbol{\mu}$ is

$$\mathcal{W} = \int_{A_{\text{cs}}} \boldsymbol{X}_G^{\top}\boldsymbol{\mu}_G \,\mathrm{d}\sigma, \tag{2.13}$$

with $\boldsymbol{X}_G$ the coordinates of the application point of the force $\boldsymbol{\mu}_G$, σ a differential area element in the cross-sectional area A_{cs}.

Equation (2.7) describes the action of the system. The evolution of the system follows the minimum action path according Hamilton's principle [80]. Thus, differentiating Equation (2.7) with respect to the degrees of freedom of the system ($\boldsymbol{R}_A$, $\boldsymbol{\Phi}$, $\boldsymbol{r}_G$ and $\boldsymbol{\varphi}$) and integrating

by parts, the weak formulation of the equations of motion is obtained [87, 80]

$$\int_{t_1}^{t_2}\Bigg\{\int_L\Big\{\delta\boldsymbol{R}_A^\top C^{AB}\left(\dot{\boldsymbol{P}}_B+\tilde{\boldsymbol{\Omega}}_B\boldsymbol{P}_B-\boldsymbol{f}_B-\tilde{\boldsymbol{K}}_B\boldsymbol{F}-\boldsymbol{F}'_B\right)+ \\ \delta\boldsymbol{\Phi}^\top\left(\dot{\boldsymbol{H}}_B+\tilde{\boldsymbol{\Omega}}_B\boldsymbol{H}_B+\tilde{\boldsymbol{V}}_B\boldsymbol{P}_B-\tilde{\boldsymbol{K}}_B\boldsymbol{M}_B-\boldsymbol{M}'_B-\tilde{\boldsymbol{R}}'_A\boldsymbol{F}_B-\boldsymbol{m}_B\right)+\delta\boldsymbol{\Phi}'^\top\boldsymbol{M}_B\Big\}\,\mathrm{d}s+ \\ \delta\boldsymbol{r}_G^\top C^{GA}\left(\dot{\boldsymbol{\mathcal{P}}}_A^R+\tilde{\boldsymbol{\omega}}_A\boldsymbol{\mathcal{P}}_A^R-\boldsymbol{\mathcal{F}}_A\right)+\delta\boldsymbol{\varphi}^\top\left(\dot{\boldsymbol{\mathcal{H}}}_A^R+\tilde{\boldsymbol{\omega}}_A\boldsymbol{\mathcal{H}}_A^R-\boldsymbol{\mathcal{M}}_A^R\right)\Big\}\,\mathrm{d}t= \\ \int_L\left[\delta\boldsymbol{R}_A^\top C^{AB}\boldsymbol{P}_B+\delta\boldsymbol{\Phi}^\top\boldsymbol{H}_B\right]_{t_1}^{t_2}\mathrm{d}s+\left[\delta\boldsymbol{r}_G^\top C^{GA}\boldsymbol{\mathcal{P}}_A^R+\delta\boldsymbol{\varphi}^\top\boldsymbol{\mathcal{H}}_A^R\right]_{t_1}^{t_2}-\int_{t_1}^{t_2}\left[\delta\boldsymbol{R}_A C^{AB}\boldsymbol{F}_B+\delta\boldsymbol{\Phi}^\top\boldsymbol{M}_B\right]_L\mathrm{d}t, \tag{2.14}$$

where $\boldsymbol{f}_B$ and $\boldsymbol{m}_B$ are integration in the cross section area of the externally applied forces ($\boldsymbol{\mu}_B$) and moments ($\boldsymbol{b}_B\times\boldsymbol{\mu}_B$). Moreover, $\boldsymbol{\mathcal{F}}_A$, $\boldsymbol{\mathcal{M}}_A$, $\boldsymbol{\mathcal{P}}_A^R$ and $\boldsymbol{\mathcal{H}}_A^R$ are the integration of the externally applied forces and moments and the local transitional and angular momenta, respectively, and expressed in the A as required by the rigid-body equations. This system has as many equations as generalised coordinates, thus, to satisfy the previous equations each term accompanying the variation of one generalised coordinate ($\delta\boldsymbol{R}_A,\delta\boldsymbol{\Phi},\delta\boldsymbol{r}_G,\delta\boldsymbol{\varphi}$) needs to be independently zero (which follows from the fundamental lemma of calculus of variations) leading to the associated strong formulation or Euler-Lagrange equations:

$$\dot{\boldsymbol{P}}_B+\tilde{\boldsymbol{\Omega}}_B\boldsymbol{P}_B=\boldsymbol{f}_B+\tilde{\boldsymbol{K}}_B\boldsymbol{F}+\boldsymbol{F}'_B, \tag{2.15a}$$

$$\dot{\boldsymbol{H}}_B+\tilde{\boldsymbol{\Omega}}_B\boldsymbol{H}_B+\tilde{\boldsymbol{V}}_B\boldsymbol{P}_B=\tilde{\boldsymbol{K}}_B\boldsymbol{M}_B+\boldsymbol{M}'_B+\tilde{\boldsymbol{R}}'_A\boldsymbol{F}_B+\boldsymbol{m}_B, \tag{2.15b}$$

$$\dot{\boldsymbol{\mathcal{P}}}_A^R+\tilde{\boldsymbol{\omega}}_A\boldsymbol{\mathcal{P}}_A^R=\boldsymbol{\mathcal{F}}_A, \tag{2.15c}$$

$$\dot{\boldsymbol{\mathcal{H}}}_A^R+\tilde{\boldsymbol{\omega}}_A\boldsymbol{\mathcal{H}}_A^R=\boldsymbol{\mathcal{M}}_A^R. \tag{2.15d}$$

For Equation (2.14) to hold, the terms on the right hand side of the equation should also vanish, which happens under compatible boundary and initial conditions to the problem. Finally, the evolution of the quaternion with time in Equation (2.6) should be added to the previous set of equations to capture effects that depend on the orientation global orientation of the system such as gravity forces.

Discretised equations of motion

The Equations of motion (2.15) are solved through the finite-element method. In the present work, the structure is divided into elements composed of three nodes (quadratic elements). The spatial distribution of the unknown variables is approximated through the

shape functions N which depend on the value of these variables at the nodes $\overline{\bullet}$:

$$\boldsymbol{R}_A(s) = \sum_{i=1}^{3} N_i(s)\overline{\boldsymbol{R}}_A(s_i), \tag{2.16a}$$

$$\boldsymbol{\Psi}(s) = \sum_{i=1}^{3} N_i(s)\overline{\boldsymbol{\Psi}}(s_i). \tag{2.16b}$$

For simplicity, the vector of generalised coordinates $\boldsymbol{q}$ is created joining $\overline{\boldsymbol{R}}_A$ and $\overline{\boldsymbol{\Psi}}$ at each one of the N_n nodes, the A frame of reference linear and angular velocities ($\boldsymbol{\beta} = \left[\boldsymbol{v}_A^\top; \boldsymbol{\omega}_A^\top\right]^\top$) and the quaternion $\boldsymbol{\chi}$:

$$\boldsymbol{q} = \left[\overline{\boldsymbol{R}}_{A_i}^\top; \overline{\boldsymbol{\Psi}}_i^\top; \boldsymbol{v}_A^\top; \boldsymbol{\omega}_A^\top; \boldsymbol{\chi}\right]^\top \quad 1 \leq i \leq N_n. \tag{2.17}$$

Upon discretisation of Equation (2.15) we obtain:

$$M\ddot{\boldsymbol{q}} + \boldsymbol{Q}_g + \boldsymbol{Q}_s = \boldsymbol{Q}_e, \tag{2.18}$$

where, M is the global mass matrix and $\boldsymbol{Q}_\bullet$ are the different forces that appear in the system [80]: gyroscopic ($\boldsymbol{Q}_g$), stiffness ($\boldsymbol{Q}_s$) or externally applied ($\boldsymbol{Q}_e$). Only gyroscopic and external effects influence the rigid body dynamics meanwhile the three of them influence the flexible movements of the structure. The problem is closed with the time evolution Equation (2.6) for the quaternion.

At each time step, Equation (2.18) is solved through a fixed-point iteration based on the following analytical linearisation [80]:

$$\underbrace{\begin{bmatrix} M_{\eta\eta} & M_{\eta\beta} & 0 \\ M_{\beta\eta} & M_{\beta\beta} & 0 \\ 0 & 0 & I_{4\text{x }4} \end{bmatrix}}_{M} \begin{Bmatrix} \Delta\ddot{\boldsymbol{\eta}} \\ \Delta\dot{\boldsymbol{\beta}} \\ \Delta\dot{\boldsymbol{\chi}} \end{Bmatrix} + \underbrace{\begin{bmatrix} C^t_{\eta\eta} & C^t_{\eta\beta} & 0 \\ C^t_{\beta\eta} & C^t_{\beta\beta} & 0 \\ 0 & C^t_{\chi\beta} & C^t_{\chi\chi} \end{bmatrix}}_{C^t} \begin{Bmatrix} \Delta\dot{\boldsymbol{\eta}} \\ \Delta\boldsymbol{\beta} \\ \Delta\boldsymbol{\chi} \end{Bmatrix} + \underbrace{\begin{bmatrix} K^t_{\eta\eta} & 0 & 0 \\ K^t_{\beta\eta} & 0 & 0 \\ 0 & 0 & 0 \end{bmatrix}}_{K^t} \begin{Bmatrix} \Delta\boldsymbol{\eta} \\ 0 \\ 0 \end{Bmatrix} = \underbrace{\begin{Bmatrix} \boldsymbol{r}_\eta \\ \boldsymbol{r}_\beta \\ \boldsymbol{r}_\chi \end{Bmatrix}}_{\boldsymbol{r}}, \tag{2.19}$$

where M are mass , C^t tangent damping and K^t tangent stiffness matrices, I is the identity matrix and 0 represents a zero matrix of the appropriate size. The first subscript shows the equations the matrix refer to and the second one the variables increments. The matrices and vectors in the previous equations will be renamed M, C^t, K^t, $\Delta\boldsymbol{q}$ and $\boldsymbol{r}$ for convencience:

$$M\Delta\ddot{\boldsymbol{q}} + C^t\Delta\dot{\boldsymbol{q}} + K^t\Delta\boldsymbol{q} = \boldsymbol{r}. \tag{2.20}$$

The solution of Equation (2.20) at each time step needs to be accompanied by a time marching scheme (Section 2.1.2).

2.1.2 Time integration

Time discretisation of the Equations of motion (2.20) requires the definition of relationships between generalised displacements $\Delta \boldsymbol{q}$, velocities $\Delta \dot{\boldsymbol{q}}$ and accelerations $\Delta \ddot{\boldsymbol{q}}$. The different possible relationships constitute the different time integration schemes, two of which are widely applied to multibody systems [85] and presented next: the Newmark-β and the generalized-α. In general, the requirements of time marching schemes is a balance between accuracy, computational cost and stability. Ideally, the scheme should be unconditionally stable with respect to the time step. Moreover, numerical methods usually require the introduction of a certain degree of dissipation for the higher frequencies that, otherwise, would require a prohibitively small time step. This dissipation should not affect the low frequencies that are usually the most important ones for the system dynamics.

Newmark-beta

The Taylor expansion of the velocities and accelerations is:

$$\boldsymbol{q}_{n+1} = \boldsymbol{q}_n + \dot{\boldsymbol{q}}_n \Delta t + \frac{1}{2} \ddot{\boldsymbol{q}}_n \Delta t^2 + \mathcal{O}(\Delta t^3), \tag{2.21a}$$

$$\dot{\boldsymbol{q}}_{n+1} = \dot{\boldsymbol{q}}_n + \ddot{\boldsymbol{q}}_n \Delta t + \mathcal{O}(\Delta t^3). \tag{2.21b}$$

Based on these expansions, the Newmark-β approximation [85, 168] proposes a weighted average between the beginning n and the end $n+1$ of the time step Δt for the accelerations that lead to:

$$\boldsymbol{q}_{n+1} = \boldsymbol{q}_n + \dot{\boldsymbol{q}}_n \Delta t + (\frac{1}{2} - \beta_{\mathrm{T}}) \ddot{\boldsymbol{q}}_n \Delta t^2 + \beta_{\mathrm{T}} \ddot{\boldsymbol{q}}_{n+1} \Delta t^2 + \mathcal{O}(\Delta t^3), \tag{2.22a}$$

$$\dot{\boldsymbol{q}}_{n+1} = \dot{\boldsymbol{q}}_n + (1 - \gamma_{\mathrm{T}}) \ddot{\boldsymbol{q}}_n \Delta t + \gamma_{\mathrm{T}} \ddot{\boldsymbol{q}}_{n+1} \Delta t + \mathcal{O}(\Delta t^3), \tag{2.22b}$$

where γ_{T} and β_{T} are the model parameters.

Neglecting the higher order terms and rearranging the formulas, the increments in the velocities and accelerations of the generalised coordinates are obtained from the increments

in the generalised coordinates themselves:

$$\boldsymbol{\Delta q} = \boldsymbol{q}_{n+1} - \boldsymbol{q}_n = \beta_{\mathrm{T}} \Delta t^2 \ddot{\boldsymbol{q}}_{n+1}, \tag{2.23a}$$

$$\boldsymbol{\Delta \dot{q}}_{n+1} = \dot{\boldsymbol{q}}_{n+1} - \dot{\boldsymbol{q}}_{n+1} = \gamma_{\mathrm{T}} \Delta t \ddot{\boldsymbol{q}}_{n+1} = \frac{\gamma_{\mathrm{T}}}{\beta_{\mathrm{T}} \Delta t} \boldsymbol{\Delta q}_{n+1}. \tag{2.23b}$$

Substituting these relations in Equation (2.20):

$$\underbrace{\left(\frac{1}{\beta_{\mathrm{T}} \Delta t^2} M + \frac{\gamma_{\mathrm{T}}}{\beta_{\mathrm{T}} \Delta t} C^t + K^t \right)^k}_{M^*} \boldsymbol{\Delta q}_{n+1}^{k+1} = \boldsymbol{r}_{n+1}^k. \tag{2.24}$$

This equation should be solved iteratively (loop denoted by k) given the non-linearity of the problem through a conventional predictor-corrector step. At the beginning of the time-step iteration, the increments with respect to the previous time step in generalised coordinates and velocities are estimated through Equation (2.22) assuming zero-acceleration at $n+1$ (predictor step). These values are used to compute M^* and $\boldsymbol{r}$ in Equation (2.24) which provides the values of $\boldsymbol{\Delta q}_{n+1}^{k+1}$ that are used to correct the previous guess for the generalised coordinates and velocities (corrector step).

The β_{T} and the γ_{T} values are parameters of the time stepping scheme which is stable [85] for:

$$\gamma_{\mathrm{T}} \geq \frac{1}{2} \quad \text{and} \quad \beta_{\mathrm{T}} \geq \frac{1}{4} \left(\gamma_{\mathrm{T}} + \frac{1}{2} \right)^2. \tag{2.25}$$

Moreover, for $\gamma_{\mathrm{T}} = 1/2$ and $\beta_{\mathrm{T}} = 1/4$, the scheme reaches maximum (second order) accuracy. The numerical damping of high frequencies is introduced with the α_{N} parameter around the maximum-accuracy unconditionally-stable point defined before:

$$\gamma_{\mathrm{T}} = \frac{1}{2} + \alpha_{\mathrm{N}} \quad \text{and} \quad \beta_{\mathrm{T}} = \frac{1}{4} \left(\gamma_{\mathrm{T}} + \frac{1}{2} \right)^2. \tag{2.26}$$

Generalized-α

Several time integration schemes with high frequency dissipation (like the Newmark-β algorithm) are unified in the generalized-α algorithm [108]. The relations between coordinates, velocities and accelerations in Equation (2.22) still hold. Moreover, this algorithm enforces the equilibrium Equation (2.20) not only at the beginning n and the end $n+1$ of the discrete time steps but also at intermediate points $t_{n+1-\alpha_F} = (1-\alpha_F) t_{n+1} + \alpha_F t_n$ computed as a weighted average between n and $n+1$ with the α_F and α_M parameters [108].

The study of the algorithm accuracy through the amplification matrix and the truncation error [108] concludes that the generalized-α method is second order accurate if

$$\gamma_{\mathrm{T}} = \frac{1}{2} - \alpha_M + \alpha_F. \tag{2.27}$$

Moreover, algorithms are unconditionally stable for linear systems if the spectral radius $\rho_{\mathrm{r}} \leq 1$. In particular, the generalized-α is unconditionally stable if

$$\alpha_M \leq \alpha_F \leq 0.5 \quad \text{and} \quad \beta_{\mathrm{T}} \geq 0.25 + 0.5\left(\alpha_F - \alpha_M\right). \tag{2.28}$$

The dissipation at high frequencies is quantified by the algorithm spectral radius at high frequencies ρ_∞. This property is desirable and maximised if

$$\beta_{\mathrm{T}} = \frac{1}{4}\left(1 - \alpha_M + \alpha_F\right)^2. \tag{2.29}$$

It is also desirable to minimise the low-frequency dissipation which leads to the expression of the α_M and α_F coefficients as a function of the spectral radius at high frequencies

$$\alpha_M = \frac{2\rho_\infty - 1}{\rho_\infty + 1} \quad \text{and} \quad \alpha_F = \frac{\rho_\infty}{\rho_\infty + 1}. \tag{2.30}$$

These expressions guarantee that the algorithm will be stable and second order accurate for linear systems with adequate low and high frequency limits for the dissipation that is easily controlled by the user through the ρ_∞ parameter. In particular, $\rho_\infty = 1$ provides no dissipation and $\rho_\infty = 0$ completely annihilates the oscillations.

The M^* matrix used in Equation (2.24) is computed [111] as:

$$M^* = \frac{1 - \alpha_M}{\beta_{\mathrm{T}}\Delta t^2} M + \frac{\gamma_{\mathrm{T}}\left(1 - \alpha_F\right)}{\beta_{\mathrm{T}}\Delta t} C^t + \left(1 - \alpha_F\right) K^t. \tag{2.31}$$

2.1.3 Multibody dynamics

Section 2.1.1 describes the dynamics of single bodies. Consider a multibody system with n_b bodies, the vector of generalised coordinates for the whole system is generated by stacking the generalised coordinates of each body described by Equation (2.17): $\boldsymbol{q} = \left[\boldsymbol{q}_1^\top; \boldsymbol{q}_2^\top; \ldots; \boldsymbol{q}_k^\top; \ldots; \boldsymbol{q}_{n_b}^\top\right]^\top$ with $1 \leq k \leq n_b$ leading to n_q generalised coordinates. Equivalently, we define the system generalised velocities $\dot{\boldsymbol{q}}$. The action of a multibody system S

includes the contribution of every body

$$S = \sum_{i=0}^{n_b} S_i, \tag{2.32}$$

where S_i is the action of each body described in Equation (2.7). The minimisation of the system action (Hamilton's principle) that lead to the Euler-Lagrange Equations (2.15) in previous section becomes a minimisation problem under the constraints between the bodies that are expressed by n_c equations $\boldsymbol{g}$

$$\begin{cases} \min\ S(\boldsymbol{q}, \dot{\boldsymbol{q}}, t), \\ \text{subjected to } \boldsymbol{g}(\boldsymbol{q}, \dot{\boldsymbol{q}}, t) = 0. \end{cases} \tag{2.33}$$

This Equation (2.33) is a system with more equations ($n_q + n_c$) than unknowns (n_q). Minimisation problems under constraints are usually solved with the Lagrange multipliers method which introduces a series of unknowns (the Lagrange multipliers, $\boldsymbol{\lambda}$) equal to the number of constraints that are physically associated to the forces generated in the joints to satisfy the constrain equations. The solving procedure is different for holonomic and non-holonomic constraints and is detailed next.

Holonomic constraints

Holonomic constraints $\boldsymbol{g}_\mathrm{h}(\boldsymbol{q}, t) = 0$ can be stated as a function of the generalised coordinates and, possibly, time. If they depend explicitly on time, they are called rheonomic and are called scleronomic otherwise. If we apply variations to the constraint Equation (2.33) in system:

$$\delta \boldsymbol{g}_\mathrm{h} = \sum_{i=0}^{n_q} \frac{\partial \boldsymbol{g}_\mathrm{h}}{\partial q_i} \delta q_i = 0, \tag{2.34}$$

where q_i are each one of the generalised coordinates of the system. Multiplying by the n_c Lagrange multipliers $\boldsymbol{\lambda}$ and rearranging the equation

$$\sum_{i=0}^{n_q} \sum_{j=0}^{n_c} k_{\mathrm{L}_j} \frac{\partial \boldsymbol{g}_\mathrm{h}}{\partial q_i} \boldsymbol{\lambda}_j \delta q_i = 0, \tag{2.35}$$

where k_{L_j} is just a constant factor which relevance is shown below. Equation (2.35) can be included into the variational description of the system action

$$\delta S = \int_{t_1}^{t_2} \sum_{i=0}^{n_q} \left(\frac{\delta L}{\delta q_i} + \sum_{j=0}^{n_c} k_{\mathrm{L}_j} \boldsymbol{\lambda}_j \frac{\partial \boldsymbol{g}_{\mathrm{h}}}{\partial q_i} \right) \delta q_i \, \mathrm{d}t = 0, \tag{2.36}$$

which suggest the definition of an augmented Lagrangian of the system

$$\mathcal{L}^*(\boldsymbol{q}, \dot{\boldsymbol{q}}, t, \boldsymbol{\lambda}) = \mathcal{L} - k_{\mathrm{L}} \boldsymbol{\lambda}^\top \boldsymbol{g}_{\mathrm{h}}. \tag{2.37}$$

The matrix containing the derivative of the constraints with the generalised coordinates is

$$B_{\mathrm{h}} = \frac{\partial \boldsymbol{g}_{\mathrm{h}}}{\partial \boldsymbol{q}}. \tag{2.38}$$

Which leads to the full definition of the problem

$$\begin{cases} M(\boldsymbol{q})\ddot{\boldsymbol{q}} + B_{\mathrm{h}}^\top(\boldsymbol{q}, t) k_{\mathrm{L}} \boldsymbol{\lambda} = \boldsymbol{Q}\left(\boldsymbol{q}, \dot{\boldsymbol{q}}, t\right), \\ k_{\mathrm{L}} \boldsymbol{g}_{\mathrm{h}}\left(\boldsymbol{q}, t\right) = 0, \end{cases} \tag{2.39}$$

where $\boldsymbol{Q}$ are the forces on the system generated by concatenating the forces of each body as per Equation (2.18). In incremental form:

$$\begin{bmatrix} M & 0 \\ 0 & 0 \end{bmatrix} \begin{Bmatrix} \boldsymbol{\Delta}\ddot{\boldsymbol{q}} \\ 0 \end{Bmatrix} + \begin{bmatrix} C^t & 0 \\ 0 & 0 \end{bmatrix} \begin{Bmatrix} \boldsymbol{\Delta}\dot{\boldsymbol{q}} \\ 0 \end{Bmatrix} + \begin{bmatrix} K^t & k_{\mathrm{L}} B_{\mathrm{h}}^\top \\ k_{\mathrm{L}} B_{\mathrm{h}} & 0 \end{bmatrix} \begin{Bmatrix} \Delta \boldsymbol{q} \\ \Delta \boldsymbol{\lambda} \end{Bmatrix} = \begin{Bmatrix} \boldsymbol{r^*} \\ -\boldsymbol{g}_{\mathrm{h}}^* \end{Bmatrix} + \mathcal{O}(\Delta^2) \tag{2.40}$$

using the following definitions:

$$\boldsymbol{r}^* = \boldsymbol{Q} - M\ddot{\boldsymbol{q}} - B_{\mathrm{h}}^\top k_{\mathrm{L}} \boldsymbol{\lambda}, \quad C^t = -\frac{\partial \boldsymbol{Q}}{\partial \dot{\boldsymbol{q}}} \quad \text{and} \quad K^t = -\frac{\partial \boldsymbol{r}}{\partial \boldsymbol{q}} + \frac{\partial (M\ddot{\boldsymbol{q}})}{\partial \boldsymbol{q}} - \frac{\partial (B_{\mathrm{h}}^T k_{\mathrm{L}} \boldsymbol{\lambda})}{\partial \boldsymbol{q}}. \tag{2.41}$$

These equations are the multibody equivalent of Equation (2.20) in single body system. The terms in the system mass M, tangent damping C^t and tangent stiffness K^t matrices are usually several orders of magnitude larger than those in the B_{h} matrix, thus, the k_{L} scaling parameter is used to scale the constraint equations such that the condition number of the matrices is kept in reasonable bounds to enable numerical operations.

Non-holonomic constraints

A non-holonomic constraint is any constraint that can be writen as $\boldsymbol{g}_{\mathrm{n}}(\dot{\boldsymbol{q}}, \boldsymbol{q}, t) = 0$. There is a particular subset in this wide group of constraints that is of interest in this work which are those that depend linearly on the generalised velocities:

$$\boldsymbol{g}_{\mathrm{n}}(\dot{\boldsymbol{q}}, \boldsymbol{q}, t) = B_{\mathrm{n}}(\boldsymbol{q}, t) \cdot \dot{\boldsymbol{q}} + \boldsymbol{g}_0 = 0. \tag{2.42}$$

This type of non-holonomic constraint can be transformed through a procedure [169] similar to the explained in previous section to the following set of equations

$$\begin{cases} M(\boldsymbol{q})\ddot{\boldsymbol{q}} + B_{\mathrm{n}}^{\top}(\dot{\boldsymbol{q}}, t) k_{\mathrm{L}} \dot{\boldsymbol{\lambda}} = \boldsymbol{Q} \\ k_{\mathrm{L}} \boldsymbol{g}_{\mathrm{n}}(\boldsymbol{q}, \dot{\boldsymbol{q}}, t) = 0 \end{cases} \tag{2.43}$$

with the incremental equations:

$$\begin{bmatrix} M & 0 \\ 0 & 0 \end{bmatrix} \begin{Bmatrix} \boldsymbol{\Delta}\ddot{\boldsymbol{q}} \\ 0 \end{Bmatrix} + \begin{bmatrix} C^t & k_{\mathrm{L}} B_n^{\top} \\ k_{\mathrm{L}} B_n & 0 \end{bmatrix} \begin{Bmatrix} \boldsymbol{\Delta}\dot{\boldsymbol{q}} \\ \boldsymbol{\Delta}\boldsymbol{\lambda} \end{Bmatrix} + \begin{bmatrix} K^t & 0 \\ 0 & 0 \end{bmatrix} \begin{Bmatrix} \boldsymbol{\Delta}\boldsymbol{q} \\ 0 \end{Bmatrix} = \begin{Bmatrix} \boldsymbol{r}^* \\ -\boldsymbol{g}_{\mathrm{n}}^* \end{Bmatrix} + \mathcal{O}(\Delta^2) \tag{2.44}$$

using the following definitions:

$$\boldsymbol{r} = \boldsymbol{Q} - M\ddot{\boldsymbol{q}} - B_n^{\top} k_{\mathrm{L}} \dot{\boldsymbol{\lambda}}, \quad C^t = -\frac{\partial \boldsymbol{Q}}{\partial \dot{\boldsymbol{q}}} \quad \text{and} \quad K^t = -\frac{\partial \boldsymbol{r}}{\partial \boldsymbol{q}}. \tag{2.45}$$

The derivatives of the term B_{n} required are computed analytically. For each joint, the constraint equations $\boldsymbol{g}_{\mathrm{n}}$, and, thus, the derivatives with the degrees of freedom B_{n} are different. This description and the implementation in `SHARPy` is general in the sense that it allows the addition of any new constraint. At the moment of writing, the author has implemented spherical, hinge, rigid joint as well as the possibility to define linear and angular velocities in nodes. Next, we present some examples that are useful for the computation of Chapters 3 and 5.

Nacelle-rotor joint

Figure 2.2 shows a scheme of a simplified joint between the nacelle (left hand side of the image) and the rotor (right hand side the image) that is described in this section. The frame of reference at the tower base position A_0 captures the platform motions. On one side of the joint there is a tower node $\bullet^p$ and, on the other, a frame of reference A_1 that rotates together

with the rotor. Actually, the present description allows the use of one frame of reference at the root of each blade if needed. Moreover, $\boldsymbol{R}^p_{A_0}$ will be the position of the last node of the tower.

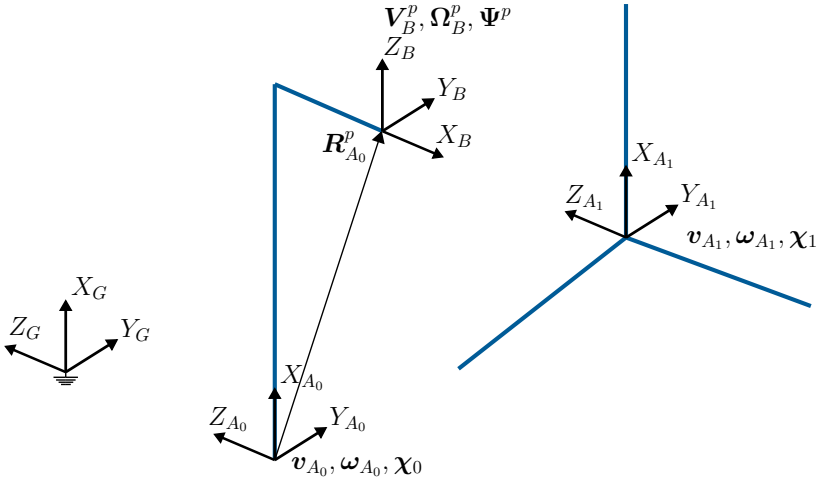

Figure 2.2: Scheme of the multibody nacelle-rotor joint.

First, equal linear velocity between the node $\bullet^p$ and the frame of reference A_1 should be imposed. The velocity of the tower top node is a composition of the velocities of the A_0 frame of reference plus the velocity due to flexible deformation of the tower. The rotor velocity is directly a generalised velocity of the system $\boldsymbol{v}_{A_1}$

$$\boldsymbol{g}_{n1} = C^{GA_1} \cdot \boldsymbol{v}_{A_1} - C^{GA_0} \cdot \left(\dot{\boldsymbol{R}}^p_{A_0} + \boldsymbol{v}_{A_0} + \boldsymbol{\omega}_{A_0} \times \boldsymbol{R}^p_{A_0} \right) = 0. \tag{2.46}$$

The easiest way to include these equations in Equation (2.44) is to put them in matrix notation showing the function dependencies to facilitate the analytical computation of the B_n matrices

$$\boldsymbol{g}_{\mathrm{n}1} = \underbrace{\begin{bmatrix} C^{GA_1}(\boldsymbol{\chi}_1) & - C^{GA_0}(\boldsymbol{\chi}_0) & - C^{GA_0}(\boldsymbol{\chi}_0) & + C^{GA_0}(\boldsymbol{\chi}_0)\tilde{\boldsymbol{R}}^p_{A_0} \end{bmatrix}}_{B_{\mathrm{n}1}} \begin{bmatrix} \boldsymbol{v}_{A_1} \\ \dot{\boldsymbol{R}}^p_{A_0} \\ \boldsymbol{v}_{A_0} \\ \boldsymbol{\omega}_{A_0} \end{bmatrix} = 0. \tag{2.47}$$

Second, the relative angular velocities between the tower top and the rotor hub $\boldsymbol{\omega}^*_{A_1}$ is composed of the rotor velocity ω_r and the blade pitch velocity $\dot{\theta}_\mathrm{p}$ which is assumed to be

prescribed although not necessarily constant

$$\boldsymbol{g}_{\mathrm{n2}} = C^{BA_0} C^{A_0 G} C^{GA_1} \boldsymbol{\omega}_{A_1} - T\dot{\boldsymbol{\Psi}} - C^{BA_0} \boldsymbol{\omega}_{A_0} - C^{BA_1} \boldsymbol{\omega}^*_{A_1} = 0, \tag{2.48}$$

In matrix form

$$\boldsymbol{g}_{\mathrm{n2}} = \underbrace{\begin{bmatrix} C^{BA_0}(\boldsymbol{\Psi}) C^{A_0 G}(\boldsymbol{\chi}_0) C^{GA_1}(\boldsymbol{\chi}_1) & -T(\boldsymbol{\Psi}) & -C^{BA_0}(\boldsymbol{\Psi}) \end{bmatrix}}_{B_{\mathrm{n2}}} \begin{bmatrix} \boldsymbol{\omega}_{A_1} & \dot{\boldsymbol{\Psi}} & \boldsymbol{\omega}_{A_0} \end{bmatrix}^\top - C^{BA_1} \boldsymbol{\omega}^*_{A_1} = 0. \tag{2.49}$$

Double pendulum joints

A double pendulum system is used for validation purposes in Chapter 3. This system (Figure 2.3) has two joints to be modelled.

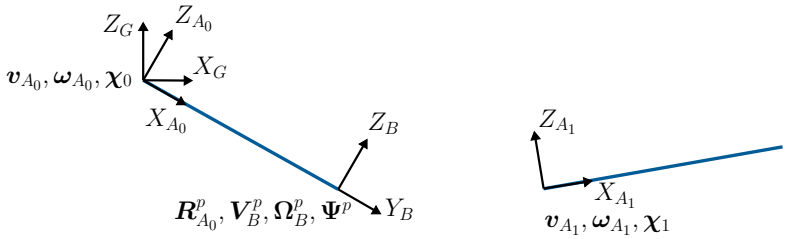

Figure 2.3: Scheme of the multibody double pendulum.

In the first joint, only the rotation around Y_G is allowed, thus, the linear velocities of the A_0 frame of reference should be zero

$$\boldsymbol{g}_{\mathrm{n3}} \equiv \boldsymbol{v}_{A_0} = 0. \tag{2.50}$$

Moreover, the rotations around X_{A_0} and Z_{A_0} should also be zero to avoid the rotation of beam 0 around itself and to keep it in the plane of Figure 2.3, respectively,

$$\boldsymbol{g}_{\mathrm{n4}} \equiv Z\boldsymbol{\omega}_{A_0} = 0, \tag{2.51}$$

where Z is used to choose the two components of $\boldsymbol{\omega}_{A_0}$ that are zero, in this particular case:

$$Z = \begin{bmatrix} 1 & 0 & 0 \\ 0 & 0 & 1 \end{bmatrix}. \tag{2.52}$$

In the second joint, the two beams have equal linear velocities which is equivalent to

Equation (2.46). Moreover, the relative rotation velocity of body 1 with respect to body 0 has to be zero in two components: the X_{A_1} component to avoid rotation of the beam 1 around itself and the rotation around Z_{A_1} so the beam stays in the plane of the image in Figure 2.3

$$\boldsymbol{g}_{\mathrm{n5}} \equiv ZC^{BA_0}C^{A_0G}C^{GA_1}\boldsymbol{\omega}_{A_1} - ZT\dot{\boldsymbol{\Psi}} - ZC^{BA_0}\boldsymbol{\omega}_{A_0} = 0. \tag{2.53}$$

This constraint is equivalent to the joint between the tower top and the rotor Equation (2.49) with zero relative velocity ($\boldsymbol{\omega}^*_{A_1} = 0$) between them. Thus, it constitutes a simpler case than the nacelle-rotor joint suitable for validation purposes.

Coordinate changes between frames of reference

Each one of the n_b bodies that compose a multibody system has an associated A_i frame of reference in which the structural dynamic equations are solved. Sometimes it is convenient to describe the whole system in the same frame of reference, for example, to interact with other physical fields that do not have multibody models such as aerodynamics (Section 2.2) or hydrodynamics (Section 2.3). This requires the change of coordinates between frames of reference. In this work, we consider A_0 as the main frame of reference and the rest A_i frames of reference are considered secondary.

First, the position of a generic node in the A_0 frame of reference $\boldsymbol{R}_{A_0}$ is computed from its position in the A_1 frame of reference $\boldsymbol{R}_{A_1}$ as

$$\boldsymbol{R}_{A_0} = C^{A_0A_1}\boldsymbol{R}_{A_1} + C^{A_0G}\left(\boldsymbol{r}_1 - \boldsymbol{r}_0\right), \tag{2.54}$$

where $C^{\bullet\bullet}$ are rotation matrices and $\boldsymbol{r}_i$ is the location of the origin of the i^{th} frame of reference with respect to G. The time derivative of the previous expression leads to the relationship between node velocities:

$$\dot{\boldsymbol{R}}_{A_0} = C^{A_0A_1}\left(\dot{\boldsymbol{R}}_{A_1} + \boldsymbol{v}_{A_1} + \boldsymbol{\omega}_{A_1}\times\boldsymbol{R}_{A_1}\right) - \boldsymbol{v}_{A_0} - \boldsymbol{\omega}_{A_0}\times\boldsymbol{R}_{A_0}, \tag{2.55}$$

where $\boldsymbol{v}_{A_i}$ and $\boldsymbol{\omega}_{A_i}$ are the linear and angular velocities of the i-th A frame of reference.

Second, rotations are referred to a different frame of reference by successive rotation matrix multiplication

$$C^{A_0B}\left(\boldsymbol{\Psi}_{A_0}\right) = C^{A_0G}\left(\boldsymbol{\chi}_{A_0}\right)C^{GA_1}\left(\boldsymbol{\chi}_{A_1}\right)C^{A_1B}\left(\boldsymbol{\Psi}_{A_1}\right). \tag{2.56}$$

The angular velocity of a cross section with respect to a generic A frame of reference is

$$\boldsymbol{\Omega}_B = T(\boldsymbol{\Psi})\dot{\boldsymbol{\Psi}} + C^{BA}(\boldsymbol{\Psi})\boldsymbol{\omega}_A. \tag{2.3 revisited}$$

The angular velocity $\boldsymbol{\Omega}_B$ is expressed in its own B frame of reference (thus, the subindex B), then, the value of $\boldsymbol{\Omega}_B$ is the same regardless of the A frame of reference

$$T(\boldsymbol{\Psi}_{A_0})\dot{\boldsymbol{\Psi}}_{A_0} + C^{BA}(\boldsymbol{\Psi}_{A_0})\boldsymbol{\omega}_{A_0} = T(\boldsymbol{\Psi}_{A_1})\dot{\boldsymbol{\Psi}}_{A_1} + C^{BA}(\boldsymbol{\Psi}_{A_1})\boldsymbol{\omega}_{A_1}, \tag{2.57}$$

rearranging we obtain the expression for the change in frame of reference of the CRV time derivative

$$\dot{\boldsymbol{\Psi}}_{A_1} = T^{-1}(\boldsymbol{\Psi}_{A_1})\left(T(\boldsymbol{\Psi}_{A_0})\dot{\boldsymbol{\Psi}}_{A_0} + C^{BA}(\boldsymbol{\Psi}_{A_0})\boldsymbol{\omega}_{A_0} - C^{BA}(\boldsymbol{\Psi}_{A_1})\boldsymbol{\omega}_{A_1}\right). \tag{2.58}$$

2.2 Aerodynamics

One of the main objectives of this dissertation is to analyse the unsteady and three-dimensional effects on wind turbine aerodynamics. UVLM is a suitable theory to capture these effects at a reasonable cost and is described in Section 2.2.1. Moreover, its performance is compared against traditional BEM theory (Section 2.2.2) and LES-AL (Section 2.2.3), therefore, short summaries are included. These theories were already implemented at the beginning of this dissertation but a description is included next because the basic theory behind each method defines the physical phenomena that it is able to describe and the possible drawbacks. Additionally, the author has also implemented a new discretisation scheme for the wake convection equation (Section 4.1.2). In Chapter 4, we use the knowledge on the phenomena that each method is able to describe, to evaluate the performance of each method. Moreover, we propose improvements on their drawbacks. We use the implementations of BEM, UVLM and LES-AL in `OpenFAST v2.1.0`, `SHARPy v1.2` and `WInc3D`, respectively, which are further described in Section 1.1.6.

2.2.1 Unsteady Vortex-Lattice Method

The flow equations are solved under the assumptions of inviscid, incompressible and irrotational flow in a fluid domain $\Omega \subset \mathbb{R}^3$. In this case, the continuity equation is enough

to define the velocity field

$$\nabla \cdot \boldsymbol{u} = 0 \quad \text{on } \Omega, \tag{2.59a}$$

$$(\boldsymbol{u} - \dot{\boldsymbol{\xi}}) \cdot \boldsymbol{n} = 0 \quad \text{on } \partial\Omega_s, \tag{2.59b}$$

$$\boldsymbol{u} = \boldsymbol{U}^{\infty} \quad \text{on } \partial\Omega_{\infty}. \tag{2.59c}$$

where, $\partial\Omega_s$ represent solid boundaries with $\dot{\boldsymbol{\xi}}$ velocity and $\boldsymbol{n}$ unit normal where a non-penetrating condition applies. Infinitely far away from solid boundaries $||\boldsymbol{x}|| \to \infty$, $\partial\Omega_{\infty}$ is the other boundary of the problem where the free-stream flow velocity $\boldsymbol{U}^{\infty}$ is imposed. The free-stream flow is assumed irrotational, thus, in absence of rotation forces, the velocity field remains irrotational (Helmholtz's third theorem) in Ω. However, rotation, i.e. vorticity $\nabla \times \boldsymbol{u}$, is generated in the boundary layer of solid surfaces [25], is shed into the flow at the trailing edges of lifting surfaces by means of the Kutta condition, and is convected downstream giving rise to a wake $\partial\Omega_w$. This wake constitutes a further boundary of the irrotational flow field in Ω. The wake and the boundary layers on solid surfaces are not irrotational. Using Green's first identity [18], the velocity field in the domain can be computed from two fields on the boundaries:

$$\boldsymbol{u} = -\frac{1}{4\pi}\int_{\partial\Omega_s} \sigma_{\mathrm{G}} \nabla\left(\frac{1}{r}\right) \mathrm{d}\sigma + \frac{1}{4\pi}\int_{\partial\Omega} \mu_{\mathrm{G}} \nabla\left(\frac{\partial}{\partial n}\left(\frac{1}{r}\right)\right) \mathrm{d}\sigma + \boldsymbol{U}^{\infty}, \tag{2.60}$$

where the source σ_{G} and doublet μ_{G} singularity fields are associated with the divergence and the curl of the velocity field, respectively [18, 15], and $\mathrm{d}\sigma$ a differential element of area. The divergence of the velocity field in Ω is zero according to Equation (2.59a), thus, the source field should be zero in this region, however, it could be non-zero outside of the flow field (for example, inside solid boundaries). Wind turbine blade thickness is considerably smaller than blades chord and span. Thus, in the present work, wind turbine blades are assumed to have zero thickness (strip theory) and the source field will be zero in the whole domain. Equation (2.60) shows that the flow velocity $\boldsymbol{u}$ is composed of a velocity induced by the singularity field $\hat{\boldsymbol{u}}$ plus the free-stream velocity $\boldsymbol{U}^{\infty}$:

$$\boldsymbol{u} = \hat{\boldsymbol{u}} + \boldsymbol{U}^{\infty}. \tag{2.61}$$

Numerical solution of the vortex problem

The singularity terms on the right-hand side of Equation (2.60) satisfy the continuity Equation (2.59a) and the boundary condition in Equation (2.59c). Thus, the solution process is reduced to find the value of the doublet field μ_{G} on the boundaries such that the non-penetrating boundary condition in Equation (2.59b) is satisfied [18].

The numerical solution requires dividing the boundaries into polygonal regions (usually with four sides) called panels (Figure 2.4). Within each panel the value of the doublet field is constant. Moreover, a vortex along the perimeter $\partial\Sigma$ of the panel can be defined such that its strength Γ is related with the doublet value and the fluid vorticity enclosed

$$\Gamma = -\mu_{\mathrm{G}} = \int_{\partial\Sigma} \boldsymbol{u} \cdot \mathrm{d}\boldsymbol{l} = \int_{\Sigma} \nabla \times \boldsymbol{u} \, \mathrm{d}S. \tag{2.62}$$

Each one of the sides of the vortex is a called a vortex segment. Vortices associated with the solid surfaces and wakes are usually called "bound vortices" and "wake vortices", respectively.

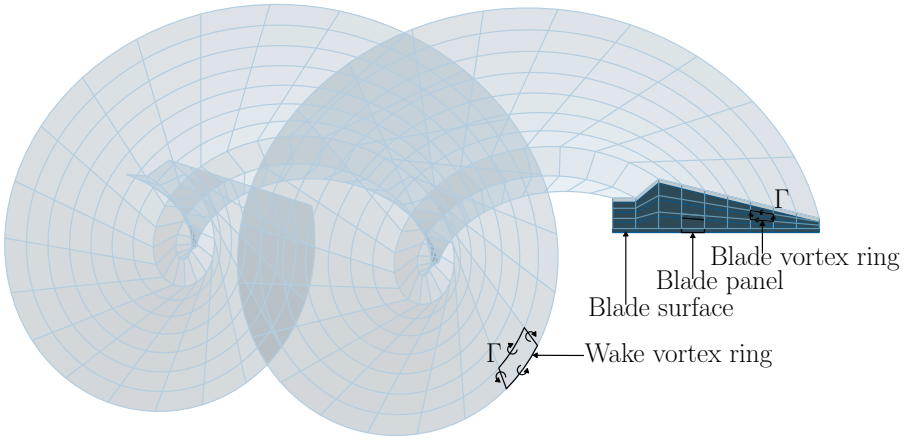

Figure 2.4: Aerodynamic discretisation nomenclature.

The velocity field induced by each vortex segment is computed through the Biot-Savart law [25]

$$\hat{\boldsymbol{u}}_{ij} = \frac{\Gamma_j}{4\pi} \sum_{k=1}^{4} \frac{\boldsymbol{l}_k \times \boldsymbol{r}_{ik}}{|\boldsymbol{r}_{ik}|^3} \tag{2.63}$$

where i indexes the point where the velocity is being induced, j indexes the vortex ring and k indexes the segments within the vortex ring. Γ is the strength of the vortex ring, $\boldsymbol{l}_k$ is the length of the segment, $\boldsymbol{r}_{ik}$ is the distance between the point and the segment centre and $\hat{\boldsymbol{u}}_{ij}$ is the velocity induced by the j^{th} vortex ring on the i^{th} collocation point. The linear character

of the flow Equations (2.59) allows the use of the superposition principle to compute the velocity induced at a collocation point as the sum of the contribution of each bound and wake vortex segment

$$\hat{\boldsymbol{u}}_i \cdot \boldsymbol{n}_i = \sum_{j=1}^{N_b} \mathcal{A}_{ij}\Gamma_j + \sum_{j=1}^{N_w} \mathcal{A}_{\mathrm{w}_{ij}}\Gamma_{w_j}, \tag{2.64}$$

where Γ and Γ_w is the circulation at each bound or wake vortex ring, respectively, $\mathcal{A}$ and $\mathcal{A}_\mathrm{w}$ are the bound and wake vortices influence coefficient matrices, respectively.

The bound Γ and wake Γ_w circulation of each vortex ring can be gathered into the vectors $\boldsymbol{\Gamma}$ and $\boldsymbol{\Gamma}_\mathrm{w}$, respectively, through the mapping

$$J(\eta, \zeta) \mapsto j, \tag{2.65}$$

where η and ζ are the spanwise and streamwise coordinates and j is the j^{th} position in the $\boldsymbol{\Gamma}$ or $\boldsymbol{\Gamma}_\mathrm{w}$ vectors (Figure 2.5). In general, the notation $\boldsymbol{\Gamma}_{\mathrm{w}J(\eta,\zeta)}$ is omitted in this work to avoid excessive notation but it is recovered whenever it clarifies the explanation. Together with Equations (2.61) and (2.64) the mapping J permits the expression of Equation (2.59b) in matrix form

$$\mathcal{A}\boldsymbol{\Gamma} = \left(\dot{\boldsymbol{\xi}} + \boldsymbol{U}^\infty\right) \cdot \boldsymbol{n} - \mathcal{A}_w\boldsymbol{\Gamma}_w. \tag{2.66}$$

This condition is enforced at the centre of each bound vortex (collocation point) where the solid velocity $\dot{\boldsymbol{\xi}}$ and the boundary normal vector $\boldsymbol{n}$ are known. This system of equation includes N_b unknowns (the circulation at bounder vortices) and equations (the non-penetrating condition at collocation points).

In a steady-state case, the circulation associated to all the wake panels in a particular row η^p is the same and equal to the value at the last bound panel $\zeta = M$, this is,

$$\boldsymbol{\Gamma}_{\mathrm{w}J(\eta^\mathrm{p},\zeta)} = \boldsymbol{\Gamma}_{J(\eta^\mathrm{p},M)} \quad \text{for} \quad 1 < \zeta \leq M_\mathrm{w}. \tag{2.67}$$

Applying this equation to every row η^p, the matrix $\mathcal{A}_s$ can be generated such that $\boldsymbol{\Gamma}_\mathrm{w} = \mathcal{A}_s\boldsymbol{\Gamma}$. Together with Equation (2.66) the steady-state solution can be obtained solving for $\boldsymbol{\Gamma}$:

$$\left(\mathcal{A} + \mathcal{A}_\mathrm{w}\mathcal{A}_s\right)\boldsymbol{\Gamma} = \left(\dot{\boldsymbol{\xi}} + \boldsymbol{U}^\infty\right) \cdot \boldsymbol{n}. \tag{2.68}$$

For unsteady cases, an additional description of the wake convection is needed and included next.

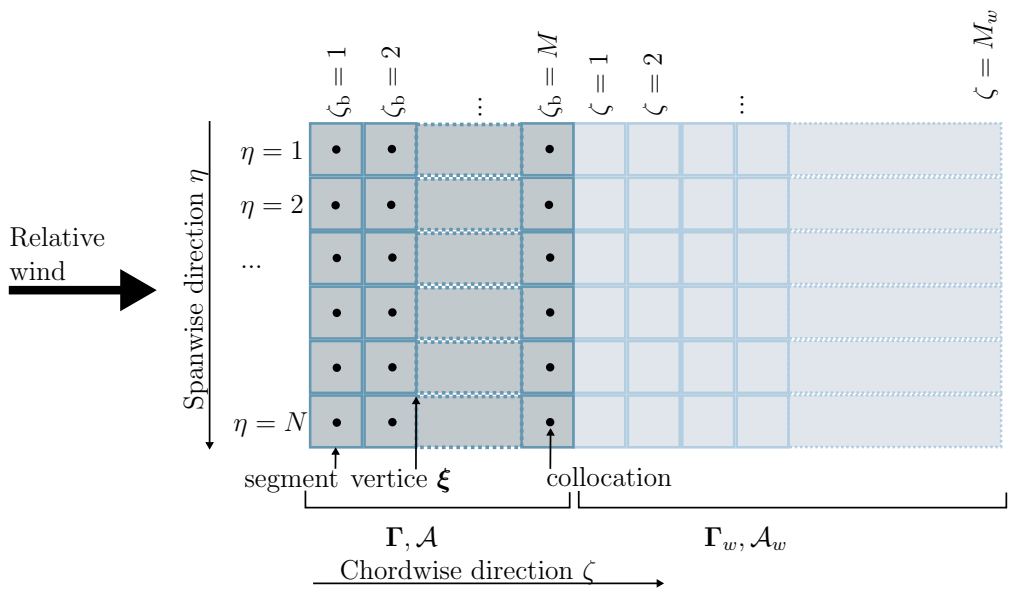

Figure 2.5: Detail of the aerodynamic problem nomenclature.

Wake convection

The wake moves and changes shape with time, in particular, it convects together with the flow such that a generic point $\boldsymbol{x} \in \partial\Omega_w$ initially located at $\boldsymbol{x}_0$ moves following the flow velocity $\boldsymbol{u}$ as

$$\boldsymbol{x}(t) = \boldsymbol{x}_0 + \int_0^t \boldsymbol{u}(\boldsymbol{x}(s), s)\, \mathrm{d}s. \tag{2.69}$$

A free wake model moves the wake with the flow velocity in Equation (2.61). However, the flow velocity can also be approximated by the unperturbed upstream velocity $\boldsymbol{U}^\infty$ such that the wake shape is known a-priori (prescribed wake approximation) which significantly reduces the computational cost at the expense of reduced accuracy on the axial induction and aerodynamic forces computation in wind turbine rotors.

The relative wind velocity is the responsible for the convection of the circulation in the wake and, for convenience, the wake discretisation is generated aligned with the relative wind (Figure 2.5) such that the circulation convection only occurs along panels indexed with ζ, that is, rows (indexed with η) in Figure 2.5 are independent. We describe the convection for one particular row (constant η^p) by defining $\Gamma_{\mathrm{w},\zeta} = \boldsymbol{\Gamma}_{\mathrm{w}J(\eta^p,\zeta)}$ the circulation of the η^p and ζ^{th} panel of the wake. The first order upwind discretisation of Equation (2.69) along one particular η^p row is

$$\frac{\Gamma_{\mathrm{w}\zeta}^{t+1} - \Gamma_{\mathrm{w}\zeta}^{t}}{\Delta t} + u_r \frac{\Gamma_{\mathrm{w}\zeta}^{t} - \Gamma_{\mathrm{w}\zeta-1}^{t}}{\Delta \zeta} = 0, \tag{2.70}$$

with $\Delta\zeta$ the vortex size in the ζ direction, u_r the relative wind velocity and t the time index. In most UVLM implementations [18], the wake discretisation is generated such that $u_r \Delta t = \Delta\zeta$, simplifying Equation (2.70) as

$$\Gamma^{t+1}_{\mathrm{w}\zeta} = \Gamma^{t}_{\mathrm{w}\zeta-1} \quad \text{for} \quad 1 < \zeta \leq M_{\mathrm{w}}, \tag{2.71}$$

which represents a shift of circulation from one panel to the following one in the ζ direction at every time step. This complies with Kelvin's theorem that states that, in inviscid flow, each vortex moves according to Equation (2.69) and keeps its strength. In particular, the circulation of the first wake vortex $\Gamma_{\mathrm{w}1}$ is obtained from the last bound vortex $\zeta_{\mathrm{b}} = M$ in the previous time step:

$$\Gamma^{t+1}_{\mathrm{w}1} = \Gamma^{t}_{M}, \tag{2.72}$$

which represents the Kutta condition for vorticity shedding. By applying Equations (2.71) and (2.72) to all the η rows and applying, again, the J mapping in Equation (2.65) to organise Γ and Γ_{w} into $\boldsymbol{\Gamma}$ and $\boldsymbol{\Gamma}_{\mathrm{w}}$, respectively, the wake convection equation for the whole system is [98]

$$\boldsymbol{\Gamma}^{n+1}_{\mathrm{w}} = \mathcal{C}_{\Gamma}\boldsymbol{\Gamma}^{n} + \mathcal{C}_{\Gamma_{\mathrm{w}}}\boldsymbol{\Gamma}^{n}_{\mathrm{w}}, \tag{2.73}$$

where the $\mathcal{C}_{\Gamma}$ matrices are sparse matrices.

Forces

The momentum conservation equation reduces to the unsteady Bernoulli equation under the previous hypothesis of inviscid, incompressible flow without relevant buoyancy forces [25]

$$\rho\frac{\partial\phi}{\partial t} + p + \frac{1}{2}\rho\|\boldsymbol{u}\|^2 = \text{constant}, \tag{2.74}$$

where ρ is the flow velocity, ϕ is the potential field from which the velocity field can be obtained ($\boldsymbol{u} = \nabla\phi$) and p is the fluid pressure. This equation is used to compute the unsteady term of the forces at the vortex collocation point

$$\boldsymbol{F}_{\mathrm{u}} = \rho A_{\mathrm{p}}\frac{\partial\phi}{\partial t}\cdot\boldsymbol{n} = \rho A_{\mathrm{p}}\dot{\Gamma}\boldsymbol{n}, \tag{2.75}$$

where A is the panel surface. The steady term is more easily calculated through the Kutta-Joukowsky theorem [18] that defines the force that a vortex filament with strength Γ and

length $\boldsymbol{l}$ experiences in steady conditions applied at its centre:

$$\boldsymbol{F}_{\mathrm{q}} = \rho\Gamma\boldsymbol{u} \times \boldsymbol{l}. \tag{2.76}$$

Linearisation

UVLM can be analytically linearised around a steady-state reference to generate a very efficient model with the only assumption of the wake geometry not changing with time [170]

$$\frac{\partial \bullet}{\partial \boldsymbol{\xi}_{\mathrm{w}}} = 0, \tag{2.77}$$

where $\boldsymbol{\xi}_{\mathrm{w}}$ describes the wake geometry through the vertex locations. The linearisation process assumes small perturbations δ around the steady-state reference $\bullet_0$ for the bound circulation $\boldsymbol{\Gamma} = \boldsymbol{\Gamma}_0 + \delta\boldsymbol{\Gamma}$ but also for its time derivative $\dot{\boldsymbol{\Gamma}}$, the wake circulation $\boldsymbol{\Gamma}_{\mathrm{w}}$, the bound vortex corners coordinates $\boldsymbol{\xi}$ and velocities $\dot{\boldsymbol{\xi}}$, the inflow velocities $\boldsymbol{U}^{\infty}$ and the forces $\boldsymbol{F}_{\mathrm{u}}$ and $\boldsymbol{F}_{\mathrm{q}}$.

Freestream flow velocities $\boldsymbol{U}^{\infty}$ in Equation (2.66) are required at the collocation points $\bullet_{\mathrm{c}}$. Meanwhile, in Equation (2.76) they are required at segment mid points $\bullet_{\mathrm{s}}$. In the linear system, linear mappings are required to interpolate variables between these grid notable points including, also, the vertices of the vortices $\bullet_{\mathrm{v}}$ (Figure 2.5). These mappings $\mathcal{W}$ are indicated with the relevant subindices: $\bullet_{\mathrm{c}}$, $\bullet_{\mathrm{s}}$ and $\bullet_{\mathrm{v}}$. For example, the interpolation of a variable defined at a vertex onto a collocation points is:

$$\bullet_{\mathrm{c}} = \mathcal{W}_{\mathrm{cv}} \bullet_{\mathrm{v}} . \tag{2.78}$$

With this notation and showing the variable dependency, Equation (2.66) is rewritten:

$$\mathcal{A}(\xi^{n+1}) + \mathcal{A}_{\mathrm{w}}(\xi^{n+1}, \xi_{\mathrm{w}}^{n+1})\boldsymbol{\Gamma}_{\mathrm{w}}^{n+1} + \mathcal{W}_{\mathrm{cv}}(\xi^{n+1}) \left(\boldsymbol{u}^{n+1} - \dot{\boldsymbol{\xi}}^{n+1}\right) = 0 \tag{2.79}$$

The perturbation around equilibrium is

$$\frac{\partial \mathcal{A}}{\partial \boldsymbol{\xi}}\boldsymbol{\Gamma}_0^{n+1} + \mathcal{A}_0\delta\boldsymbol{\Gamma}^{n+1} + \frac{\partial \mathcal{A}_{\mathrm{w}}}{\partial \boldsymbol{\xi}}\boldsymbol{\Gamma}_{\mathrm{w}0}^{n+1} + \mathcal{A}_{\mathrm{w}0}\delta\boldsymbol{\Gamma}_{\mathrm{w}}^{n+1} + \frac{\partial \mathcal{W}_{\mathrm{cv}}}{\partial \boldsymbol{\xi}} \left(\boldsymbol{\vartheta}_0^{n+1} - \dot{\boldsymbol{\xi}}_0^{n+1}\right) + \mathcal{W}_{\mathrm{cv}0} \left(\delta\boldsymbol{\vartheta}_0^{n+1} - \delta\dot{\boldsymbol{\xi}}_0^{n+1}\right) = 0. \tag{2.80}$$

For convenience in the next sections, we rewrite:

$$\mathcal{A}_0\delta\boldsymbol{\Gamma}^{n+1} + \mathcal{A}_{\mathrm{w}0}\delta\boldsymbol{\Gamma}_{\mathrm{w}}^{n+1} = \mathcal{B}\boldsymbol{v}_{\mathrm{a}}, \tag{2.81}$$

where $\boldsymbol{v}_\mathrm{a}$ is a vector generated by staggering the inputs $\left[\delta\boldsymbol{\xi}; \delta\dot{\boldsymbol{\xi}}; \delta\boldsymbol{U}^\infty\right]$. The wake convection Equation (2.73) is already linear, the perturbation of the unsteady forces in Equation (2.75) is

$$\delta\boldsymbol{F}_\mathrm{u} = -\rho A_{\mathrm{p}_0}\boldsymbol{n}\delta\dot{\Gamma} - \rho\dot{\Gamma}_0\frac{\partial A_\mathrm{p}\boldsymbol{n}}{\partial\boldsymbol{\xi}}\delta\boldsymbol{\xi}, \tag{2.82}$$

and the quasisteady component in Equation (2.76) is

$$\delta\boldsymbol{F}_\mathrm{q} = \rho\delta\Gamma\boldsymbol{u}_0 \times \boldsymbol{l}_0 + \rho\Gamma_0\delta\boldsymbol{u} \times \boldsymbol{l}_0 + \rho\Gamma_0\delta\boldsymbol{u}_0 \times \delta\boldsymbol{l}, \tag{2.83}$$

that should be linearly interpolated on the grid vertices:

$$\boldsymbol{F} = \mathcal{W}_\mathrm{vc}\boldsymbol{F}_\mathrm{u} + \mathcal{W}_\mathrm{vs}\boldsymbol{F}_\mathrm{q}. \tag{2.84}$$

Finally, the time derivative in Equation (2.82) is approximated with a second-order backwards scheme:

$$\Delta t\dot{\boldsymbol{\Gamma}}^{n+1} = \frac{3}{2}\boldsymbol{\Gamma}^{n+1} - \frac{4}{2}\boldsymbol{\Gamma}^n + \frac{1}{2}\boldsymbol{\Gamma}^{n-1}, \tag{2.85}$$

where the factors are renamed as $\beta_1 = 3/2$, $\beta_0 = -2$ and $\beta_{-1} = 1/2$.

Substituting the perturbation of Equation (2.73) in (2.80) and the result into (2.85), the system can be written in standard state-space form [170]:

$$\begin{cases} \boldsymbol{x}_a^{n+1} = A_\mathrm{a}\boldsymbol{x}_a^n + B_\mathrm{a}\boldsymbol{v}_a^{n+1} \\ \boldsymbol{y}_a^{n+1} = C_\mathrm{a}\boldsymbol{x}_a^n + D_\mathrm{a}\boldsymbol{v}_a^n \end{cases} \tag{2.86}$$

where the $\boldsymbol{x}_a$ column vector gathers the system states $\left[\delta\boldsymbol{\Gamma}^n; \delta\boldsymbol{\Gamma}_\mathrm{w}^n; \Delta t\delta\dot{\boldsymbol{\Gamma}}^n; \delta\boldsymbol{\Gamma}^{n-1}\right]$, $\boldsymbol{v}_a$ the inputs $\left[\delta\boldsymbol{\xi}; \delta\dot{\boldsymbol{\xi}}; \delta\boldsymbol{U}^\infty\right]$ and $\boldsymbol{y}$ the forces $\delta\boldsymbol{F}$. The use of Δt in the state associated with $\delta\dot{\boldsymbol{\Gamma}}$ makes the A_a matrix independent of the time step. The term $\delta\boldsymbol{\Gamma}^{n-1}$ in the state vector is required only for the second-order approximation of the time derivative in Equation (2.85). Moreover, the system has a delay (input defined at $n+1$) that can be removed through the change of state definition $\hat{\boldsymbol{x}}_a^n = \boldsymbol{x}_a^n - B_\mathrm{a}\boldsymbol{v}_a^n$ if required.

Reduced order models

We partially reproduce here the work in [171] to give the basis for a small contribution we make in Section 4.1.2 and a numerical example we show in Section 4.2.3. Balanced truncation is a method to find reduced order models of discrete linear time invariant (DLTI)

systems such as Equation (2.86). It consists of eliminating from the state-space equations those states that are less controllable and observable. The controllability and observability properties are quantified through the controllability W_{c} and observability W_{o} Gramians, respectively. In general, both Gramians are different such that the truncation criteria is not obvious. However, for stable systems with controllable and observable states, there exists a state transformation

$$\boldsymbol{x}_{\mathrm{b}} = T^{-1}\boldsymbol{x}_{\mathrm{a}}, \tag{2.87}$$

the so-called balanced transformation, such that the controllability and observability Gramians are equal and equal to a positive-definite diagonal matrix.

The computation of the balancing transformation requires the solution of the Lyapunov equations to obtain the system Gramians, the computation of their Cholesky factorisation and their singular value decomposition (SVD). These operations are unaffordable for UVLM Equations (2.86) because they require hundreds of thousands of states, inputs and outputs for wind turbine simulation. Thus, a bespoke methodology [171] is described and employed here exploiting the particular structure of the system (2.86) for the direct integration of the controllability and observability Gramians in a limited-frequency range $0 \leq k \leq \overline{k}_c$ and $0 \leq k \leq \overline{k}_o$, respectively:

$$W_c = \frac{1}{2k_N}\int_{-\overline{k}_c}^{\overline{k}_c} H_b(k)B_{\mathrm{a}}B_{\mathrm{a}}^{\top}H_b^*(k)\,\mathrm{d}k = \int_{-\overline{k}_c}^{\overline{k}_c} \phi_c(k)\phi_c^*(k)\,\mathrm{d}k, \tag{2.88a}$$

$$W_o = \frac{1}{2k_N}\int_{-\overline{k}_o}^{\overline{k}_o} H_b^*(k)C_{\mathrm{a}}^{\top}C_{\mathrm{a}}^{\top}H_b(k)\,\mathrm{d}k = \int_{-\overline{k}_o}^{\overline{k}_o} \phi_o(k)\phi_o^*(k)\,\mathrm{d}k, \tag{2.88b}$$

where $k_N = \pi/\Delta t$ is the reduced Nyquist frequency, ϕ_c and ϕ_o are transfer functions and $H_b(k)$ is defined as

$$H_b(k) = \left(e^{jk\Delta t}I_{Nx} - A_{\mathrm{a}}\right)^{-1}, \tag{2.89}$$

with I_{Nx} an identity matrix with number of rows and columns equal to the system states N_x. We use the subindices $\bullet_{c,o}$ to indicate that an expression applies to the controllability and observability Gramians. The approximation of the integrals in Equation (2.88) by finite sums and the symmetry of transfer functions $\phi_{c,o}(k) = \phi_{c,o}^*(-k)$ leads to the expression of the Gramians as a function of the $Z_{c,o}$ factors:

$$W_{c,o} \approx Z_{c,o}Z_{c,o}^{\top}. \tag{2.90}$$

The singular value decomposition of $Z_o^\top Z_c = U\Sigma V^\top$ provides the transformation $T = Z_c V \Sigma^{-1/2}$ that balances the system (2.87).

The complex factor $\phi_c(z) = \overline{x}_\mathrm{a}(z)$ requires to solve for the system states in the frequency domain. This is easily obtained by applying the z-transform to the UVLM Equations (2.81), (2.73) and (2.85):

$$\mathcal{A}\overline{\mathbf{\Gamma}} + \mathcal{A}_\mathrm{w}\overline{\mathbf{\Gamma}}_\mathrm{w} = \mathcal{B}\overline{\boldsymbol{u}}, \tag{2.91a}$$

$$z\overline{\mathbf{\Gamma}}_\mathrm{w} = \mathcal{C}_\Gamma\overline{\mathbf{\Gamma}} + \mathcal{C}_{\Gamma_\mathrm{w}}\overline{\mathbf{\Gamma}}_\mathrm{w}, \tag{2.91b}$$

$$z\Delta\overline{\dot{\mathbf{\Gamma}}} = \sum_{i=-1}^{1} \beta_i z^i \overline{\mathbf{\Gamma}}, \tag{2.91c}$$

where $\overline{\bullet}$ represents the z-transform and the frequency domain is obtained by setting $z = e^{jk\Delta t}$. According to Equations (2.71) and (2.72), the circulation at a wake panel can be computed from the circulation at the trailing edge ζ time steps before, being ζ the panel number in the chordwise direction. In the z-domain:

$$\overline{\mathbf{\Gamma}}_w = z^{-\zeta}\overline{\mathbf{\Gamma}}, \tag{2.92}$$

from which a closed form solution can be found for Equation (2.91a)

$$\overline{\mathbf{\Gamma}} = \left[\mathcal{A} + \mathcal{A}_\mathrm{w}\overline{\mathcal{C}}_\mathrm{w}(z)\right]^{-1} \mathcal{B}\overline{\boldsymbol{u}}_\mathrm{a}, \tag{2.93}$$

where $\overline{\mathcal{C}}_\mathrm{w}(z)$ comes from applying (2.92) to every row and expressing it in matrix form.

2.2.2 Blade-Element Momentum

We have described in previous Section 2.2.1 the UVLM which is suitable for the computation of unsteady and three-dimensional aerodynamic effects. However, it does not account for viscous effects that lead to flow separation and viscous drag in wind turbine aerodynamics. BEM theory is widely used due to its accuracy under steady uniform inflow perpendicular to the rotor plane and high computational efficiency. However, as we explain next, BEM is based on steady theory and two-dimensional data. In Chapter 4, we benchmark these methods under uniform, yawed and turbulent inflows and we propose improvements for them.

BEM theory [4] connects momentum theory with rotor blade theory. Momentum theory idealises the rotor as a porous disc such that the mass conservation along a streamtube that

includes the rotor is

$$\rho A_\infty U_\infty = \rho A_d U_d = \rho A_w U_w, \tag{2.94}$$

where U_∞, U_d and U_w are the flow velocities infinitely upstream of the rotor, at the rotor plane and in the wake, respectively. Similarly, A_∞, A_d and A_w are the cross-sectional area of the streamtube at these positions and ρ is the flow density. Traditionally, the axial induction a is defined as $U_d = U_\infty(1-a)$ and measures, in average terms, the velocity reduction experienced by the wind upstream of a rotor. Moreover, the force on the porous disc can be related to the momentum loss of the flow across the disc

$$(p_d^+ - p_d^-)A_d = (U_\infty - U_w)\rho A_d U_\infty(1-a), \tag{2.95}$$

where p_d^+ and p_d^- are the pressure immediately upstream and downstream the rotor. The flow pressures and velocities are also related by the Bernoulli equation that should be applied separately upstream and downstream the rotor

$$\frac{1}{2}\rho U_\infty^2 + p_\infty = \frac{1}{2}\rho U_d^2 + p_d^+ \quad \text{and} \quad \frac{1}{2}\rho U_w^2 + p_\infty = \frac{1}{2}\rho U_d^2 + p_d^-, \tag{2.96}$$

where p_∞ is the flow pressure infinitely away from the rotor.

Under the assumption of independent radial sections of the rotor, the momentum theory described above can be applied separately to each radial annulus such that it can be related with the rotor blade theory. This theory defines the aerodynamic lift δL and drag δD forces per unit length in each annulus via

$$\delta L \cos\phi_f + \delta D \sin\phi_f = \frac{1}{2}\rho u_r^2 N_{\text{bl}} c(c_L \cos\phi_f + c_D \sin\phi_f)\delta r, \tag{2.97}$$

where u_r is the local relative flow velocity, c_L and c_D are two-dimensional aerodynamic force coefficients typically obtained from tabulated values, r is the radial coordinate, ϕ_f the flow angle at a section with chord c and N_{bl} is the number of rotor blades. The combination of the two previous theories and the appropriate geometrical relationships between velocities give rise to a system of equations that can be iteratively solved to obtain velocities and forces.

There are some further details needed to complete the method such as the angular momentum equation [4]. Moreover, important three-dimensional and unsteady effects are missing, forcing this method to use semi-empirical corrections [172] for rotation, tip and root ends. There are two more semi-empirical corrections of relevance for this dissertation. First, the Unsteady BEM [4] employs indicial responses from the theory of airfoils [48] to model

unsteady effects. Second, the Pitt and Peters [4] model assumes sinusoidal variation of induction along a revolution to account for the skewed-wake effect. Usually, these corrections are adjusted for the most simple cases leading to miscalculations in the most complex ones [61] such as unsteady inflow or large yaw angles.

2.2.3 Large-Eddy Simulation with Actuator-Line

LES-AL is currently gaining importance to capture wind farm aerodynamics. In Chapter 4, we benchmark it against UVLM and BEM to describe its accuracy in the computation of aerodynamic loads on the wind turbine. We also use it to generate a realistic turbulent field to estimate aerodynamic loads with BEM, UVLM and LES-AL in Section 4.1.4.

The LES-AL technique combines two theories. First, incompressible Navier-Stokes equations are solved subjected to the forces generated on the flow. Second, the forces on the wind turbine are computed from an actuator line (AL) theory [173].

LES solves the incompressible flow equations for the largest scales of turbulence which represent the largest energy content in the flow. Meanwhile, the small scales of turbulence are modelled. This decomposition of every field ψ into a filtered component $\bar{\psi}$ and a sub-filtered component ψ' is achieved by a low-pass filter. This procedure applied to the Navier-Stokes equations (in Einstein notation) gives

$$\frac{\partial \bar{u}_i}{\partial x_i} = 0, \tag{2.98a}$$

$$\frac{\partial \bar{u}_i}{\partial t} + \bar{u}_j \frac{\partial \bar{u}_i}{\partial x_j} = -\frac{1}{\rho}\frac{\partial \bar{p}}{\partial x_i} + \nu \frac{\partial^2 \bar{u}_i}{\partial x_j \partial x_j} - \frac{\partial \tau_{ij}}{\partial x_j}, \tag{2.98b}$$

with ν the kinematic viscosity and $\tau_{ij} = \overline{u_i u_j} - \bar{u}_i \bar{u}_j$ the stress tensor which is modelled through a turbulent viscosity ν_t approximation as

$$\tau_{ij} - \frac{1}{3}\tau_{kk}\delta_{ij} = 2\nu_t \bar{S}_{ij} = 2\nu_t \frac{1}{2}\left(\frac{\partial \bar{u}_i}{\partial x_j} + \frac{\partial \bar{u}_j}{\partial x_i}\right), \tag{2.99}$$

with $\bar{S}_{ij}$ the strain rate tensor and δ_{ij} the Kronecker delta. The turbulent viscosity is estimated with the subgrid-scale model of Smagorinsky based on a model constant, C_s, and the grid characteristic size, Δ_g , as

$$\nu_t = (C_s \Delta_g)^2 \sqrt{2\bar{S}_{ij}\bar{S}_{ij}}. \tag{2.100}$$

AL theory is very similar to BEM theory explained in Section 2.2.2. Instead of establishing a balance between induced velocities and forces on the wind turbine, the velocities are known because they are sampled from the LES velocity field at blade locations. Thus, the forces can be directly computed from Equation (2.97) at the discrete actuator line locations. These forces are distributed onto the LES nodes according to a Gaussian kernel

$$\chi_{ij}(r) = \frac{1}{\epsilon_g^3 \pi^{3/2}} e^{-(r/\epsilon_g)^2}, \tag{2.101}$$

where χ is the fraction of the actuator line force at node i that is applied onto the LES node j, r is the distance between these nodes and ϵ_g measures the strength of the smearing and is computed as twice the characteristic grid size Δ_g. Unlike BEM, LES-AL inherently accounts for the azimuthal change in induction and, thus, it does not require tip and root semi-empirical corrections for the aerodynamic forces.

During the course of the project that is summarised in this dissertation, we performed a preliminary code-to-code-to-experiments validation of the wind farm aerodynamics under large yaw angles. It was a collaborative work with the Technical University of Munich that was published in [38].

2.3 Floating platform dynamics

Wind turbine platform is just an extension of the multibody system formed by tower and rotor that was described in Section 2.1.3. This section aims to compute the forces generated on the platform to completely simulate floating wind turbine behaviour. The platform displacements (surge, sway and heave) and rotations (roll, pitch and yaw) are illustrated in Figure 2.6 and grouped in a vector for simplicity $\boldsymbol{p} = [\boldsymbol{r}_G; \boldsymbol{\varphi}]^\top$. The resultant forces and moments generated on the platform $\boldsymbol{F}_\mathrm{p}$ referred to the tower base

$$\boldsymbol{F}_\mathrm{p} = \boldsymbol{F}_\mathrm{m} + \boldsymbol{F}_\mathrm{s} + \boldsymbol{F}_\mathrm{r} + \boldsymbol{F}_\mathrm{a} + \boldsymbol{F}_\mathrm{w} + \boldsymbol{F}_\mathrm{v}, \tag{2.102}$$

with contributions from the mooring system $\boldsymbol{F}_\mathrm{m}$, buoyancy of the submerged part $\boldsymbol{F}_\mathrm{s}$, water reaction to platform movements associated to radiation $\boldsymbol{F}_\mathrm{r}$, additional damping forces $\boldsymbol{F}_\mathrm{a}$, waves' excitation $\boldsymbol{F}_\mathrm{w}$ and viscous drag $\boldsymbol{F}_\mathrm{v}$ that are detailed later in this section. The description below is as general as possible following [174] but modelling details change between different solutions. In the rest of this dissertation we use the NREL5 MW wind turbine with the OC3 spar platform [133] because of the detailed definition [175] and data available for

validation [176]. A spar platform consist of a submerged cylinder that provides the required buoyancy to the system to keep the wind turbine afloat and a ballast to stabilise it (Figure 2.6). The implementation of floating dynamics on `SHARPy` is one of the author's main contributions. Thus, we choose the simplest platform model (Section 1.1.4) to facilitate the validation. While the implementation is general, some limitations of the method are described below because it might not be suitable for all platforms. For example, Morison's equation cannot be used to accurately simulate semi-submersible platforms (Section 1.1.4).

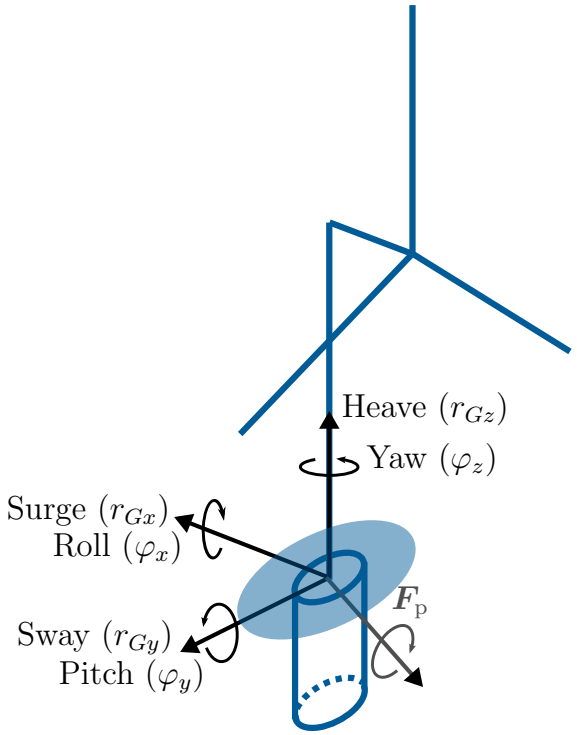

Figure 2.6: Floating platform movements and forces nomenclature.

2.3.1 Mooring forces

Mooring lines are modelled as a set of cable structures without bending stiffness extending from seabed anchors to the wind turbine attachment points (fairleads). Here we use a quasi-steady approximation that neglects the added-mass, damping and drag effects that are only captured by dynamic models based on finite element representations of the mooring lines. Dynamic effects might be important in deep waters where mooring lines undergo large and quick movements [135]. They are also typically important for the computation of loads on the mooring lines but not so for the computation of blade loads [122].

First, we consider the case of a free-hanging line, namely, the anchor is the only point of contact between the seabed and the mooring line which deforms in the shape of a catenary curve under the action of gravity. Using the equations to describe the catenary shape, Hooke's law for the elongation-force relationship and assuming quasi-steady approximation, the horizontal x_h and vertical x_v coordinates of the fairlead location with respect to the anchor position satisfy the following equations [133]:

$$x_h = \frac{F_h}{\mu_\mathrm{m}}\left[\ln\left(\frac{F_v}{F_h}+\sqrt{1+\left(\frac{F_v}{F_h}\right)^2}\right)-\ln\left(\frac{F_v-\mu_\mathrm{m}L_\mathrm{m}}{F_h}+\sqrt{1+\left(\frac{F_v-\mu_\mathrm{m}L_\mathrm{m}}{F_h}\right)^2}\right)\right]+\frac{F_hF_l}{E_\mathrm{m}A_\mathrm{m}}, \tag{2.103a}$$

$$x_v = \frac{F_h}{\mu_\mathrm{m}}\left[\sqrt{1+\left(\frac{F_v}{F_h}\right)^2}-\sqrt{1+\left(\frac{F_v-\mu_\mathrm{m}L_\mathrm{m}}{F_h}\right)^2}\right]+\frac{1}{E_\mathrm{m}A_\mathrm{m}}\left(F_vL_\mathrm{m}-\frac{\mu_\mathrm{m}L_\mathrm{m}^2}{2}\right), \tag{2.103b}$$

where F_v and F_h are, respectively, the vertical and horizontal forces at the fairlead, g is gravity, ρ_w is the water density and the mooring line properties are: unstretched length L_m, area A_m, density ρ_m and Young modulus E_m. For convenience, $\mu_\mathrm{m} = gA_\mathrm{m}\left(\rho_m - \rho_w\right)$ is the apparent weight per unit length of the mooring line in water.

In our simulations with `SHARPy`, the fairlead coordinates (x_h and x_v) are known from the simulation and the force values (F_h and F_v) are sought. Thus, these equations are solved through a Newton-Raphson iteration based on an analytical computation of the Jacobian. The iteration is initialised with the value at the previous time step.

Second, we consider the possibility to have part of the mooring line laying on the seabed L_B which generates an additional horizontal force based on the seabed drag coefficient C_B. The rest of the line follows a catenary shape and contributes with its apparent weight to the vertical force on the fairlead [133]

$$\begin{aligned} x_h =& L_B + \left(\frac{F_h}{\mu_\mathrm{m}}\right)\ln\left[\frac{F_v}{F_h}+\sqrt{1+\left(\frac{F_v}{F_h}\right)^2}\right]+\frac{F_hL_\mathrm{m}}{EA_\mathrm{m}}+ \\ & \frac{C_B\mu_\mathrm{m}}{2E_\mathrm{m}A_\mathrm{m}}\left[-L_B^2+(L_B-\frac{F_h}{C_B\mu_\mathrm{m}})\max(L_B-\frac{F_h}{C_B\mu_\mathrm{m}},0)\right], \end{aligned} \tag{2.104a}$$

$$x_v = \frac{F_h}{\mu_\mathrm{m}}\left[\sqrt{1+\left(\frac{F_v}{F_h}\right)^2}-1\right]+\frac{F_v^2}{2E_\mathrm{m}A_\mathrm{m}\mu_\mathrm{m}}, \tag{2.104b}$$

$$L_B = L_\mathrm{m} - F_v/\mu_\mathrm{m}. \tag{2.104c}$$

The total mooring force acting on the platform fairleads $\boldsymbol{F}_{\mathrm{mf}}$ is

$$\boldsymbol{F}_{\mathrm{mf}} = F_v \boldsymbol{n}_v + F_h \boldsymbol{n}_h, \tag{2.105}$$

where $\boldsymbol{n}_v$ and $\boldsymbol{n}_h$ are the vertical and horizontal components of the anchor-fairlead direction. The mooring forces applied at tower base $\boldsymbol{F}_{\mathrm{m}}$ are computed from $\boldsymbol{F}_{\mathrm{mf}}$ assuming rigid platform structure.

Figure 2.7 shows the solution of the Equations (2.103) and (2.104) for the OC3 platform mooring lines [175]. For $x_h < 858.5\,\mathrm{m}$ the behaviour is dominated by the apparent weight of the mooring line that partially lies on the seabed, thus, the suspended length is smaller than the unstretched length (902.2 m). For $x_h > 858.5\,\mathrm{m}$ the mooring line does not lie on the seabed and there is a very quick increase of the tension with the distance dominated by the mooring line stiffness. In the intermediate region, there is a balance between both effects. Finally, the mooring system has a small resistance against yaw rotation which is

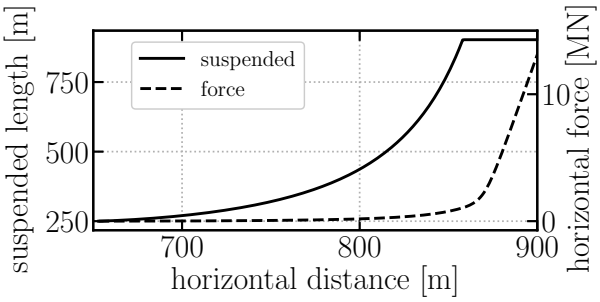

Figure 2.7: Mooring line tension and suspended length as a function of the distance between anchor and fairlead.

implemented as a torsion spring

$$M_z = c_z \cdot \varphi_z, \tag{2.106}$$

being M_z the yaw moment generated by the mooring system, c_z the spring proportional constant and φ_z the rotation around the yaw axis.

2.3.2 Hydrostatics

Archimedes principle defines the buoyancy force and moments generated on the platform due to the submerged part. In particular, only a vertical force appears on vertical spar structures with value $\rho_w g V_0$ being ρ_w the water density, g the gravity and V_0 the initial volume submerged. When the platform displaces or rotates, this force changes. Under a

linear assumption, these changes in forces and moments $\boldsymbol{F}_{\mathrm{s}}$ can be related to the (small) displacements and rotations of the structure $\boldsymbol{p}$ through the buoyancy restoring matrix C_{s}:

$$\boldsymbol{F}_{\mathrm{s}} = C_{\mathrm{s}}\boldsymbol{p}. \tag{2.107}$$

The i^{th} j^{th} element of the C_{s} matrix is the i^{th} force (or moment) per unit j^{th} displacement (or rotation). In a spar platform, due to symmetry, only the terms associated to heave-heave, pitch-pitch and roll-roll in C_{s} are different from zero.

2.3.3 Potential hydrodynamics

Hydrodynamics study the forces on solid bodies due to the relative motion between solids and fluids coming from platform motions, currents and waves. These effects interact nonlinearly with the platform, however, in the present work we will consider a linear approximation to these interactions which allows the analysis of each effect separately and their combination through superposition principle. This assumption requires small platform displacements and rotations, for example, in the realistic operation case in Section 5.3, the surge displacement and the pitch rotation with respect to the equilibrium position are below 10 m and 8 deg respectively. The heave and sway displacements and the yaw and roll rotations are below 2 m and 2 deg, respectively.

Panel methods (similar to the one described in Section 2.2.1) are suitable to compute the forces on structures interacting with water in cases where inertia forces are significantly larger than viscous forces, in particular, when no separation occurs in the flow. For the spar OC3 platform, separation occurs only for extreme sea states (long wave periods and high waves) [175], which are not of interest in this work. Potential panel methods do not account for viscous effects which are of relevance for the cases studied in this dissertation, thus, they are computed through Morison's equation in Section 2.3.4. Roughly, inviscid, incompressible and irrotational flow assumptions lead to flow dynamics governed by the Laplace equation. On the platform wetted surface and the seabed (for swallow water assumption), non-penetrating boundary conditions are applied. The free surface also has boundary conditions

$$\frac{\partial \phi_{\mathrm{w}}}{\partial z} - \kappa\phi_{\mathrm{w}} = 0, \tag{2.108}$$

with ϕ_{w} the water velocity potential, z the main direction perpendicular to the surface and κ the wave number. This boundary condition transforms into Newman and Dirichlet boundary

conditions in the zero and infinite frequency limits. Once the water velocity field $\boldsymbol{u}_w = \nabla\phi_{\mathrm{w}}$ is obtained, the forces on the solid surface are computed with Bernoulli equation. The radiation and diffraction phenomena described next can be quantified with this theory.

Radiation

A solid body (in this case the wind turbine platform) oscillating in water radiates waves and generates a pressure field in the surrounding water. The integration of this pressure field on the solid boundary in contact with the water results in the reaction force generated on the solid body $\boldsymbol{F}_r$ that is applied in this work to the tower base. Under the assumption of a linear system, the forces on the platform can be computed from the platform velocities $\dot{\boldsymbol{p}}$

$$\boldsymbol{F}_r(t) = \int_0^t K(t-\tau)\dot{\boldsymbol{p}}(\tau)d\tau, \tag{2.109}$$

where $K(t)$ is the impulse response function [177]. In the particular case of the OC3 spar platform, the non-zero terms of the impulse response function are shown in Figure 2.8.

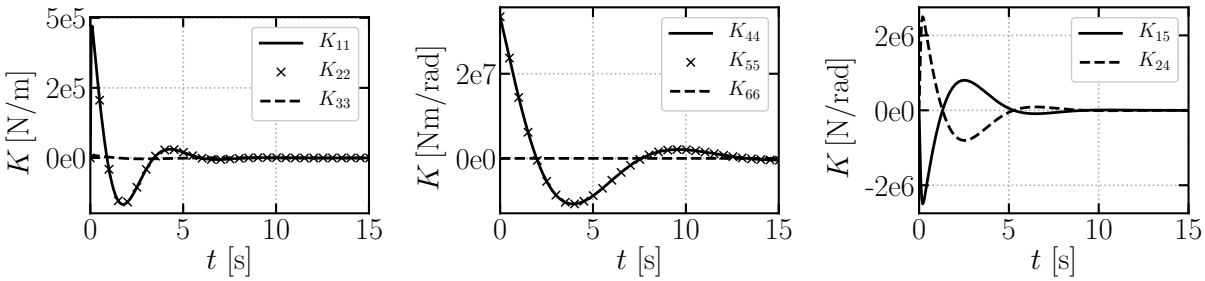

(a) K_{11}, K_{22}, K_{33} terms. (b) K_{44}, K_{55}, K_{66} terms. (c) K_{15}, K_{24} terms.

Figure 2.8: Radiation impulse response function. OC3 platform.

The radiation process is usually studied in the frequency domain as a function of the platform oscillation frequency ω_{p}. Computer codes like `WAMIT` (Section 1.1.6) numerically solve Equation (2.108) upon discretisation of the platform shape to obtain K. In particular, `WAMIT` provides the platform added-mass $A(\omega_{\mathrm{p}})$ and damping $B(\omega_{\mathrm{p}})$ matrices that are the Fourier sine and cosine transformations of the impulse response function K, respectively

$$A(\omega_{\mathrm{p}}) = A(\infty) - \frac{1}{\omega_{\mathrm{p}}}\int_0^\infty K(t)\sin(\omega_{\mathrm{p}}t)\,\mathrm{d}t, \tag{2.110}$$

and

$$B(\omega_{\mathrm{p}}) = \int_0^\infty K(t)\cos(\omega_{\mathrm{p}} t)\,\mathrm{d}t. \tag{2.111}$$

Figure 2.9 shows the non-zero terms of the added-mass matrix of the OC3 platform which present almost constant values across the frequencies. Similarly, the damping values are shown in Figure 2.10 which decay very quickly for frequencies beyond 5 rad/s and show a peak around 1 rad/s.

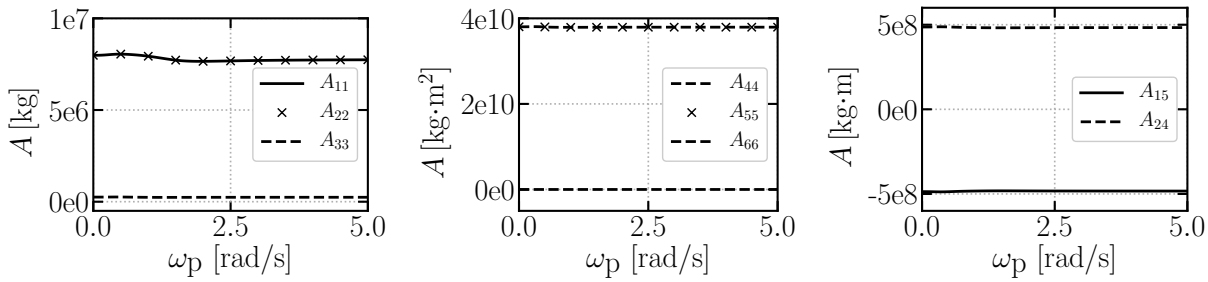

(a) A_{11}, A_{22}, A_{33} terms. (b) A_{44}, A_{55}, A_{66} terms. (c) A_{15}, A_{24} terms.

Figure 2.9: Added-mass force excitation coefficients. OC3 platform.

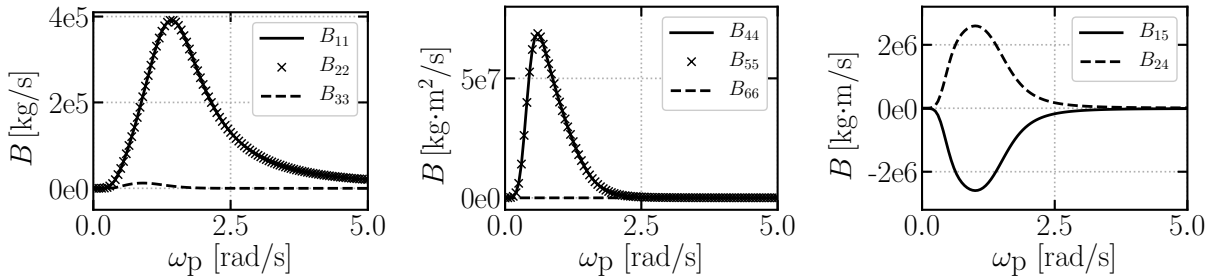

(a) B_{11}, B_{22}, B_{33} terms. (b) B_{44}, B_{55}, B_{66} terms. (c) B_{15}, B_{24} terms.

Figure 2.10: Damping force excitation coefficients. OC3 platform.

It is convenient for the numerical computation of forces on the platform to define a transfer function H_{r} from the impulse response function K:

$$H_{\mathrm{r}}(\omega_{\mathrm{p}}) = B(\omega_{\mathrm{p}}) + (A(\infty) - A(\omega_{\mathrm{p}}))\, i\omega_{\mathrm{p}}. \tag{2.112}$$

Our contribution to this method is to generate a rational function approximation (RFA) of the solution of the potential flow Equation (2.108) at a discrete set of frequencies for the OC3 platform that was computed in [175]. For numerical simulation, we generate a RFA

for each term of the previous matrix for the range of frequencies of relevance. Then, we use the transfer function H_r in Equation (2.112) to create MIMO state space representation that uses platform velocities $\dot{\boldsymbol{p}}$ as input and generates forces $\boldsymbol{F}_\mathrm{p}$ on the platform as the output.

Figure 2.11 shows the RFA of the non-zero terms in the H_r function for the particular case of the OC3 platform. All terms in H_r tend to zero for $\omega_\mathrm{p} \to 0$ and $\omega_\mathrm{p} \to \infty$, thus, the numerator of the RFA is forced to have zero independent term and the degree of the denominator polynomial is forced to be higher than the numerator. All functions show a maximum between 0 rad/s and 2 rad/s. The heave-heave RFA (Figure 2.11a) has degree-one and degree-four polynomials in the numerator and denominator, respectively. Due to symmetry, the RFA that relates a surge input with a surge output is the same as the sway-sway RFA and has been fitted with a RFA with degree-one and degree-four polynomials in the numerator and denominator, respectively. Similarly, the roll-roll term is equal to the pitch-pitch (RFA numerator polynominal degree one and denominator of degree two), and the surge-pitch is equal to the sway-roll (RFA numerator polynomial degree one and denominator polynomial degree four). Moreover, the term pitch-surge term (and the roll-sway) are opposite to surge-pitch (and sway-roll). Finally, the yaw-yaw term has been approximated to zero. The maximum errors of the heave-heave (Figure 2.11a), surge-surge (Figure 2.11b), pitch-pitch (Figure 2.11c) and sway-roll (Figure 2.11d) RFA are: 30%, 16%, 28% and 33%, respectively.

The damping force coefficients vanish at both $\omega_\mathrm{p} \to 0$ and $\omega_\mathrm{p} \to \infty$ limits. However, the added-mass coefficients do not. $A(\infty)$ can be seen as an added mass force to the platform which are known to be problematic [125], thus, in our implementation in `SHARPy`, we prefer to include this term as a constant lumped mass in our model and keep $A(\omega_\mathrm{p})$ as a time-varying exciting force[1].

In some cases, additional damping is required to match real life experiments. It is included, again, through a matrix of coefficients relating platform motion velocities to forces:

$$\boldsymbol{F}_a = -B_a \dot{\boldsymbol{p}}. \tag{2.113}$$

In the OC3 platform, additional damping is advised [175] in surge-surge, sway-sway, heave-heave and yaw-yaw terms.

[1]The $A(\infty)$ lumped mass should not be affected by gravity, thus, we include a force equivalent to $-A(\infty)\boldsymbol{g}$ as the structural library does not distinguishes between regular and added masses in the computation of gravity forces.

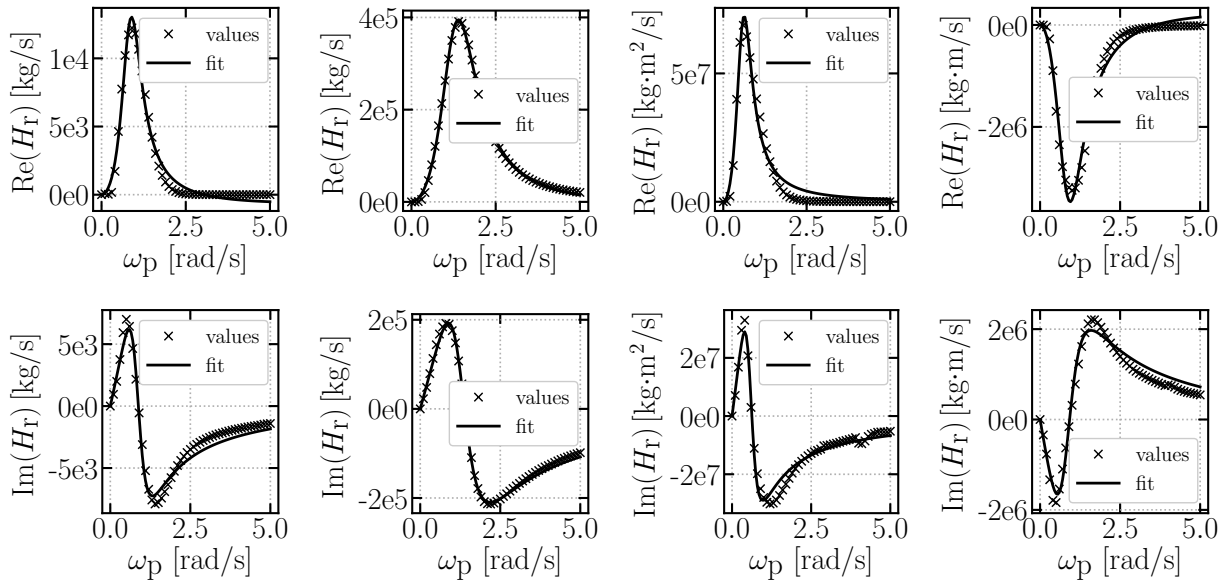

(a) Heave-heave. (b) Surge-surge. (c) Pitch-pitch. (d) Sway-roll.

Figure 2.11: Radiation coefficient values and rational function approximation. OC3 platform.

Waves

Another type of loading that floating wind turbine platforms are subjected to comes from the sea waves. Airy linear theory describes the sea elevation with sinusoidal waves of a single amplitude a_w and frequency ω_w. The forces on the support platform are closely related with the wave elevation through the diffraction problem which is a function of the platform geometry, wave frequency and incidence angle (β_w). The solution of Equation (2.108) in this case generates the force excitation coefficients (X_w) that now relate the sea elevation $\mathrm{Re}\left(a_w e^{j\omega_w t}\right)$ at the platform location with the forces generated on it. For single frequency wave, the force generated on the platform $\boldsymbol{F}_w$ is

$$\boldsymbol{F}_w(t, \beta_w) = \mathrm{Re}\left(a_w e^{j\omega t} X_w(\omega_w, \beta_w)\right). \tag{2.114}$$

For negative ω_w values, the force excitation coefficients are the complex conjugate $\bullet^*$ of the coefficient at positive ω_w: $X_w(-\omega_w, \beta_w) = X_w^*(\omega_w, \beta_w)$. For the OC3 platform, the force excitation coefficients for waves of different frequencies have been computed in [175, 176] and are shown in Figure 2.12. Forces in surge, heave and pitch show a maximum around 0.5 rad/s and decay to zero at high frequencies. The rest of the coefficients are negligible. Superposition can be used to account for sea states with multiple wave components with

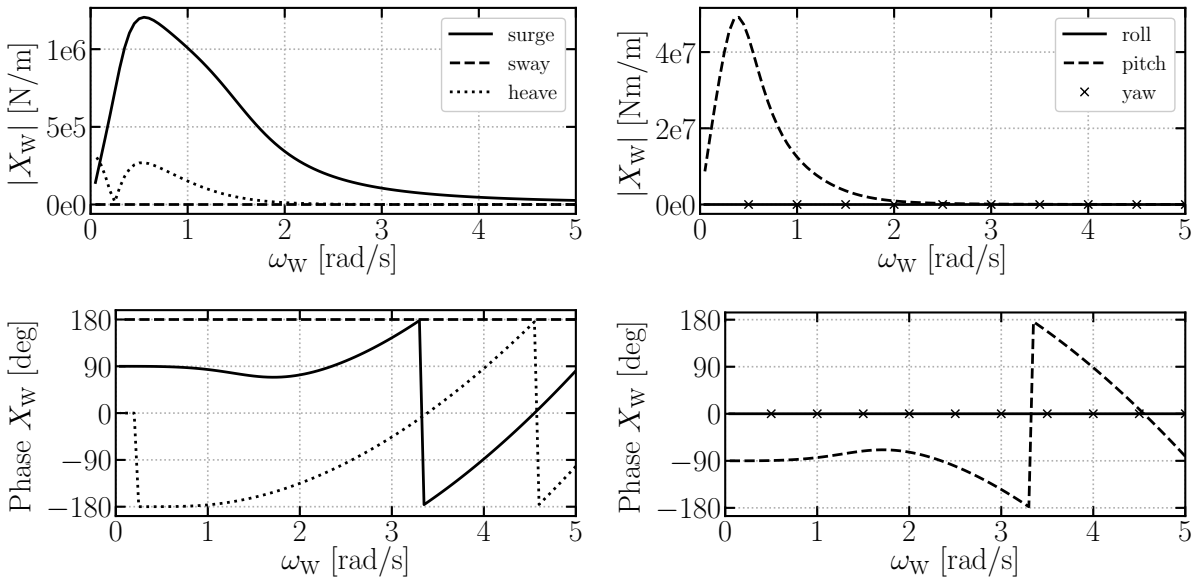

(a) Forces on platform.

(b) Moments on platform.

Figure 2.12: Wave force excitation coefficients. OC3 platform.

frequency domain representation $J(\omega)$:

$$\boldsymbol{F}_w(t, \beta_\mathrm{w}) = \mathcal{F}^{-1}\{W(\omega_\mathrm{w})J(\omega_\mathrm{w})X_\mathrm{w}(\omega_\mathrm{w}, \beta_\mathrm{w})\}, \tag{2.115}$$

where $\mathcal{F}^{-1}$ is the inverse Fourier transformation and $W(\omega_\mathrm{w})$ is a frequency-domain representation of a white noise that enables the generation of different non-deterministic realisations of the wave forces with a spectra close to the original one. This white noise is generated with the Box-Muller approach [178] as

$$W(\omega_\mathrm{w}) = \sqrt{-2\ln U_1}\left(\cos\left(2\pi U_2\right) + j\sin\left(2\pi U_2\right)\right), \tag{2.116}$$

for $\omega_\mathrm{w} \geq 0$ and $W(-\omega_\mathrm{w}) = W^*(\omega_\mathrm{w})$. U_1 and U_2 two independent random variables in $[0, 1)$. Sea states are usually represented by the 1-sided power spectral density S_1 of the wave elevation. For example, the JONSWAP [126] power spectral density is:

$$S_1(\omega_\mathrm{w}) = \frac{1}{2\pi}\frac{5}{16}h_s^2 T_p \left(\frac{\omega_\mathrm{w}T_p}{2\pi}\right)^{-5} e^{-\frac{5}{4}\left(\frac{\omega_\mathrm{w}T_p}{2\pi}\right)^{-4}} \left(1 - 0.287\ln\gamma_J\right)\gamma_J^{\exp\left(-0.5\left(\frac{\frac{\omega_\mathrm{w}T_p}{2\pi}-1}{\sigma_J}\right)^2\right)}, \tag{2.117}$$

for waves of characteristic height h_s, peak period T_p and $\gamma_J(\omega_\mathrm{w}, T_p, h_s)$ the peak shape parameter and $\sigma_J(\omega_\mathrm{w}, T_p)$ the scaling factor according to IEC 61400-3 [174]. The two-sided power spectral density is $S_2(\omega_\mathrm{w}) = 0.5 S_1(\omega_\mathrm{w})$ for positive frequencies and $S_2(-\omega_\mathrm{w}) = S_2(\omega_\mathrm{w})$ for negative ones. The discrete frequency-domain representation of the sea state is computed as:

$$J(\omega_\mathrm{w}) = \sqrt{\frac{N S_2}{\Delta t}}, \tag{2.118}$$

for a discrete time signal with N time steps of size Δt.

The implementation of the white noise has been validated by computing 100 realisations and comparing the average to the original JONSWAP spectrum (Equation (2.117)) in Figure 2.13 for $T_p = 14.656\,\mathrm{s}$ and $h_s = 5.49\,\mathrm{m}$ showing good agreement and a significant deviation of the realisations with respect to the average value.

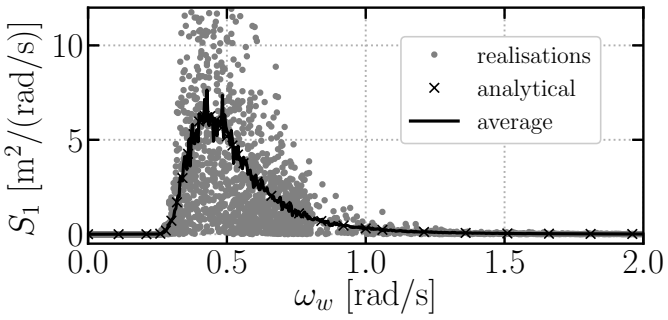

Figure 2.13: Different realisations, their average and analytical value of the JONSWAP spectrum.

2.3.4 Viscous drag

A dimensional analysis [120] for the forces in the interaction between platform and water shows that there are two dominant terms. The first term is associated to the inertia of displaced fluid and dominant in bluff bodies: $\rho_w c_m V_0 \dot{\boldsymbol{u}}_\mathrm{w}$, where ρ_w is the water density, c_m the apparent-mass force coefficient, V_0 is the volume of displaced fluid, $\boldsymbol{u}_\mathrm{w}$ is the relative solid-fluid velocity. The second term is related to drag forces and dominates for slender and small (with respect to the wave amplitude) structures:

$$\boldsymbol{F}_\mathrm{v} = \frac{1}{2} \rho_w c_d A_\mathrm{s} \boldsymbol{u}_\mathrm{w} |\boldsymbol{u}_\mathrm{w}|, \tag{2.119}$$

where $\boldsymbol{F}_{\mathrm{v}}$ is the hydrodynamic force, c_d the apparent-damping force coefficient, A_{s} is the solid area perpendicular to $\boldsymbol{u}_{\mathrm{w}}$. The addition of these two terms constitutes Morison's equation.

Section 2.3.3 assumes potential hydrodynamics which accurately capture the terms associated to inertia more accurately than Morison's equation. However, viscous forces are not accounted for and we consider that it is important to include them because they provide significant damping to the system. In our `SHARPy` implementation, the OC3 spar platform is modelled as a series of 2D independent cross sections that support a drag force computed though Equation (2.119). c_d is estimated as the drag coefficient of a infinite-span cylinder at high enough Reynolds number to be considered independent from it. We do not account for currents of wave velocities in the computation of the relative solid-fluid velocity.

2.4 Multiphysics integration

The concurrent simulation of the structural dynamics (Section 2.1), aerodynamics (Section 2.2) and floating dynamics (Section 2.3) generates dependencies and interactions between the different dynamics. In this section, we first describe the dependencies between the structural and the aerodynamic grid. Second, we present the exchange of information between the different dynamics. And, finally, we detail the control system. The single-body fluid-structure interaction (FSI) loop was already implemented in `SHARPy` at the beginning of this dissertation. However, the multibody and control dynamics are two of the author's main contributions.

The backbone of the aeroelastic system is the beam structure defined in Section 2.1. At the beginning of the simulation, the initial structural node coordinates together with a B frame of reference are defined at each node (Figure 2.14a). The X_B axis runs along the beam reference line and, in the most simple case, the airfoil chord is defined along the Y_B direction and discretised with aerodynamic nodes according to a user-defined distribution (Figure 2.14b). For more complex cases, such as cambered airfoils of swept blades, a curvilinear chord in other directions than Y_B is permitted. Assuming rigid airfoil chords, the aerodynamic grid is recomputed upon structural deformation (Figure 2.14d) and the velocities of the aerodynamic nodes are computed from the velocity of the structural nodes.

The aerodynamic theory (Section 2.2) computes the forces that wind generates on blades. In UVLM, in particular, these forces are computed at the aerodynamic grid vertices which are mapped onto the beam nodes assuming, again, rigid cross sections as described in Figure 2.15.

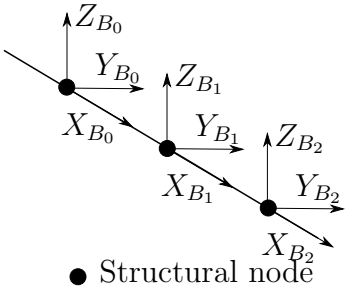

(a) Structural mesh.

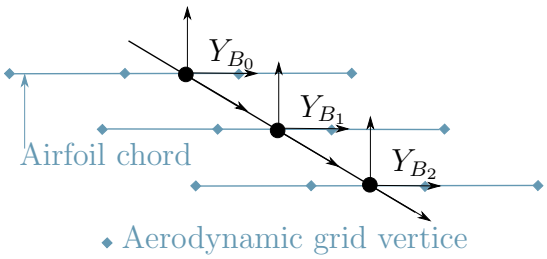

(b) Chordwise aerodynamic mesh discretisation.

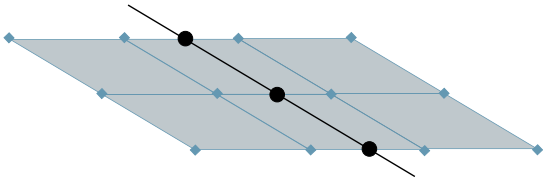

(c) Aerodynamic mesh.

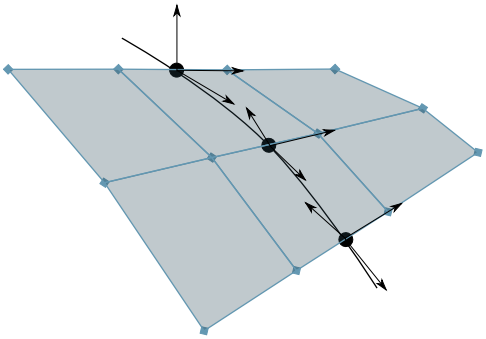

(d) Deformed aerodynamic mesh.

Figure 2.14: Scheme of the aeroelastic mesh.

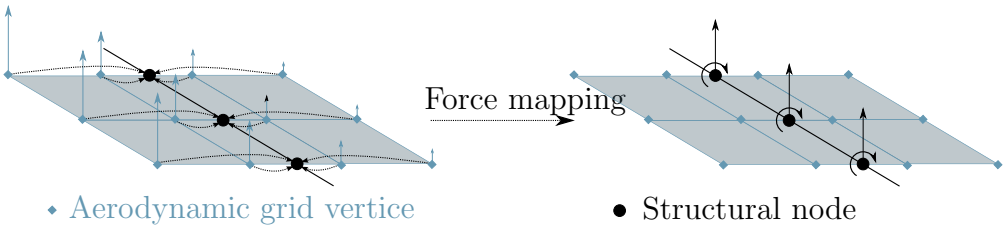

Figure 2.15: Scheme of the aerodynamic forces (left) mapping on the structural nodes (right).

Figure 2.16 describes the information exchange between the different physics. It shows the definition of the aerodynamic grid coordinates $\boldsymbol{\xi}$ and velocities $\dot{\boldsymbol{\xi}}$ from the structural node coordinates $\boldsymbol{R}_A$, orientation through the CRV $\boldsymbol{\Psi}$ and the linear $\boldsymbol{V}_B$ and angular velocities $\boldsymbol{\Omega}_B$. It also shows the mapping of aerodynamic forces on structural nodes and the interpolation of the wind velocity field on the aerodynamic grid to compute the aerodynamic forces.

The platform location $\boldsymbol{r}_G$, orientation $\boldsymbol{\varphi}$ and its linear $\boldsymbol{v}_A$ and angular $\boldsymbol{\omega}_A$ velocities are computed by the multibody structural solver. These variables are used by the hydrodynamic module to compute the reaction forces $\boldsymbol{F}_{\mathrm{p}}$ generated on the platform by the sea water and the mooring lines. These forces are transferred to the structural multibody solver.

This bidirectional dependency of the structural, aerodynamic and aerodynamic modules

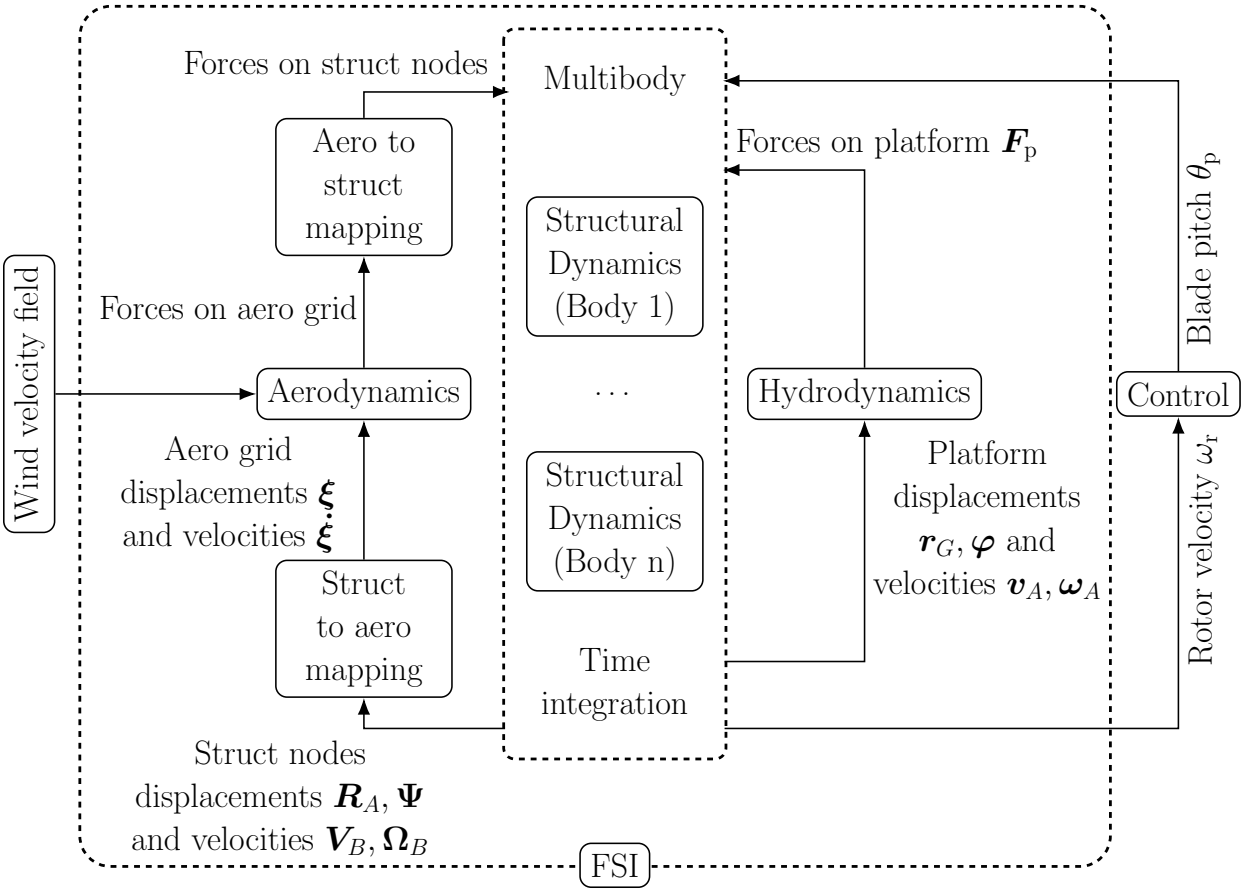

Figure 2.16: Scheme of the interactions between different dynamics.

generates a fluid-structure interaction (FSI) that is strongly enforced in the computations of the present work through a FSI iteration loop (indexed by f here). The error between iterations is computed as

$$\epsilon_{\mathrm{FSI}} = \frac{||\boldsymbol{q}^{f+1} - \boldsymbol{q}^{f}||}{||\boldsymbol{q}^{0}||}, \tag{2.120}$$

where $\boldsymbol{q}$ are the generalised coordinates computed by the structural solver as per Equation (2.17). The FSI iteration is terminated when the error is below a certain threshold. We also enforce the same criteria to the generalised velocities, such that, both need to be satisfied to terminate the iteration.

The multibody module (Figure 2.16) solves the structural dynamics equations for each body together with the constraints among them through Lagrange Multipliers (Section 2.1.3) and it performs the time integration of the system dynamics (Section 2.1.2). The constraint equations are algebraic equations and do not need to be time marched as opposed to the differential equations arising from GEBT (Section 2.1.2). These systems are named *Differ-*

ential algebraic equations and there is a wide theory on how to numerically compute their solutions [114, 115]. In particular, Equations (2.24) and (2.31) in the Newmark-β and the generalized-α time integration schemes, respectively, need to be modified. In the present work, a simple approach has been proved to be sufficient to converge the results:

$$\begin{bmatrix} M^* & \frac{\gamma_\mathrm{T}}{\beta_\mathrm{T}\Delta t} k_\mathrm{L} B^\top \\ k_\mathrm{L} B & 0 \end{bmatrix} \begin{Bmatrix} \boldsymbol{\Delta q} \\ \boldsymbol{\Delta \lambda} \end{Bmatrix} = \begin{Bmatrix} \boldsymbol{r}^* \\ -\boldsymbol{g}^* \end{Bmatrix} \tag{2.121}$$

Finally, the control module samples the rotor velocity ω_r from the structural multibody solver and computes a control command on the blade pitch θ_p. Next, we describe the control system in more detail.

2.4.1 Wind turbine control

This section describes the basics of the wind turbine control for power production [4, 179]. Other functions of the control system (start-up, stops, ...) are not of relevance in the present dissertation. Moreover, we focus on the aeroelasticity of the wind turbine, thus, we use a simplified model to simulate the drivetrain (Figure 2.17). The rotor is connected to the low speed shaft of a gearbox. Its high-speed shaft is connected to the generator which provides electric power E to the grid. Moreover, the generator speed ω_g is sampled, filtered ω_g^* and used as input to the collective (meaning that all blades operate at the same pitch angle) blade pitch θ_p controller.

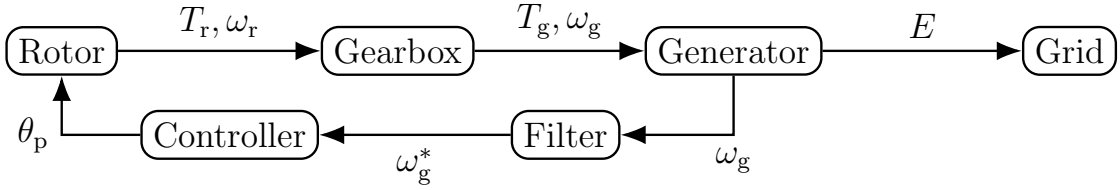

Figure 2.17: Scheme of the wind turbine drivetrain.

First, we describe the behaviour of the gearbox and the generator in a simplified manner that is convenient for aeroelastic simulations. The gearbox is modelled as a one-degree-of-freedom system in which the torque moment balance provides the rotor acceleration:

$$\dot{\omega}_\mathrm{r} = \frac{T_\mathrm{r} - G T_\mathrm{g}}{I_\mathrm{D}}, \tag{2.122}$$

where ω_r is the rotation velocity of the rotor, T_r and T_g are the rotor and generator torque

respectively, G is the gearbox ratio and I_{D} is the rotation inertia of the drive train. Moreover, the generator can operate in two simplified configurations. The first configuration consists of operation at constant power E by means of prescribing the generator torque T_{g} equal to

$$T_{\mathrm{g}} = E/\omega_{\mathrm{g}}. \tag{2.123}$$

The second configuration is operation at constant torque T_{g}. Operation at constant power is usually employed in onshore wind turbines because it provides more stable power output. However, in offshore wind turbines [180], the controller natural frequency should be reduced below the wind turbine pitch natural frequency to avoid the negative damping of this motion. This increases the rotation speed excursions from the nominal value which are reduced with a constant torque operation of the generator.

Next, we describe the control of variable-speed and variable-pitch wind turbines. The power generated by the wind turbine in quasi-steady operation and excluding losses is

$$E = \frac{1}{2}\rho U_{\infty}^3 \pi R^2 C_P, \tag{2.124}$$

where ρ is the air density, U_{∞} is the unperturbed air speed, R is the rotor radius and C_P is the power coefficient. The power coefficient C_P is the ratio between the power extracted by the wind turbine E and the available power in the wind stream that passes through the rotor sweep area $\frac{1}{2}\rho U_{\infty}^3 \pi R^2$. In steady-state, the power coefficient depends on the collective blade pitch angle θ_p and the tip-speed ratio $\lambda_{\mathrm{t}} = (\omega_r R)/U_{\infty}$, where ω_r is the rotor velocity, this is, $C_P\left(\lambda_{\mathrm{t}}, \theta_{\mathrm{p}}\right)$.

At wind speeds below rated production, the objective of the control is to maximise the power generation which is equivalent to maintaining the tip-speed ratio and the collective pitch angle that maximise the power coefficient and are known from the rotor design. In that situation, Equation (2.124), the tip-speed ratio definition and the gear-box ratio G lead to the relation between the generator torque T_g and velocity ω_g:

$$T_g = \frac{\rho \pi R^5}{2\lambda_{\mathrm{t_{max}}}^3 G^3}\omega_g^2. \tag{2.125}$$

In this operation regime, the collective blade pitch is set to the one that maximises the power coefficient and the generator measures its speed and sets the generator torque according to Equation (2.125). This configuration is able to track the optimum operation point through the torque balance in Equation (2.122) and is easily understood with the next example.

Consider the rotor operating at optimum power coefficient, that is, optimum collective blade pitch and tip-speed ratio (known for each rotor), an increase in rotor speed will increase the aerodynamic torque which will speed up the rotor and the generator. Under an increase of the generator velocity, the generator will generate an opposing torque such that the equilibrium is restored.

When the nominal power production has been reached, the controller objective changes to maintain nominal power production constant. To do so, a control loop is established between the generator velocity and the collective blade pitch. Next, we describe the behaviour of the closed loop system in Figure 2.17. In this operational regime, the generator maintains constant power and the aerodynamic torque depends on the collective pitch angle such that, in first approximation, we can write:

$$T_{\mathrm{g}}(G\omega_{\mathrm{r}}) = \frac{E_0}{G\omega_{\mathrm{r}}} \approx \frac{E_0}{G\omega_{\mathrm{r}}} - \frac{E_0}{G\omega_{\mathrm{r}}^2}\Delta\omega_{\mathrm{r}}, \tag{2.126a}$$

$$T_{\mathrm{r}}(\theta_p) = \frac{E(\theta_p, \omega_{\mathrm{r}})}{\omega_{\mathrm{r}}} \approx \frac{E}{\omega_{\mathrm{r}}} + \frac{1}{\omega_{\mathrm{r}}}\frac{\partial E}{\partial \theta_p}\Delta\theta_p. \tag{2.126b}$$

The controller is modelled with a PID equation with proportional K_P, integral K_I and derivative K_D gains between the generator velocity ω_{g} and the collective blade pitch angle θ_{p}:

$$\Delta\theta_p = K_P G\Delta\omega_{\mathrm{r}} + K_I \int_0^t G\Delta\omega_{\mathrm{r}}\,\mathrm{d}t + K_D G\Delta\dot{\omega}_{\mathrm{r}}. \tag{2.127}$$

Renaming $\dot{\theta} = \Delta\omega_{\mathrm{r}}$ a second order equation of motion is obtained:

$$\left(I + \frac{1}{\omega_{\mathrm{r}}}\left(-\frac{\partial E}{\partial \theta_{\mathrm{p}}}\right) GK_D\right)\ddot{\theta} + \left(\frac{1}{\omega_{\mathrm{r}}}\left(-\frac{\partial E}{\partial \theta_{\mathrm{p}}}\right) GK_P - \frac{E}{\omega_r^2}\right)\dot{\theta} + \left(\frac{1}{\omega_{\mathrm{r}}}\left(-\frac{\partial E}{\partial \theta_{\mathrm{p}}}\right) GK_I\right)\theta = 0. \tag{2.128}$$

This equation models the closed loop behaviour of the system in Figure 2.17 and it is useful because it allows the choice of the PID constants by the definition of the desired natural frequency and the damping ratio of the system [179]. The choice of PID constants is shown in Section 5.1. All the simulations in this dissertation are in the above-rated regime so only this control loop is currently implemented in `SHARPy`.

The input signal to the controller (generator velocity) can be filtered to eliminate high frequency oscillations. In this work, a first order low-pass filter has been implemented

$$\frac{\omega_{\mathrm{g}}^*}{\omega_{\mathrm{g}}} = \frac{\omega_{\mathrm{c}}}{s + \omega_{\mathrm{c}}}, \tag{2.129}$$

where ω_{g}^{*} is the filtered generator speed and ω_{c} the corner frequency of the low pass filter and s the Laplace variable.

In the floating environment, for the NREL 5 MW wind turbine on the OC3 platform, it has been proposed in literature [175] to use a generator that provides constant torque instead of constant power and to choose different PID constants to reduce the positive damping associated to the tower fore-after movement. This model is used in Sections 3.4.3 and 5.3.

In the multibody implementation (Section 2.1.3) we have discussed that the nacelle-rotor joint is characterised by a relative rotation between the tower top and the blade roots $\boldsymbol{\omega}_{A_1}^{*}$ (Equation (2.48)). This relative rotation velocity is composed by the rotor velocity ω_{r} from Equation (2.122) and the blade pitch velocity $\dot{\theta}_{\mathrm{p}}$ from Equation (2.127).

Chapter 3

Verification and validation

The aeroelastic theory presented in Sections 2.1.1 and 2.2.1 has been widely validated in the past for aircraft applications. The structural model has good performance under large deformations and rotations [98] and the estimation of aerodynamic forces generated in these largely-deformed unsteady cases has been found to be accurate [86, 181]. The range of application of linear and reduced order models has also been analysed in [182]. There are specific publications about the SHARPy implementation [154, 155] including some cases of wind turbine structural dynamics [101, 150] in previous versions of the code. The objective of this chapter is to verify and validate the author's new implementations and relevant phenomena to wind turbine aeroelasticity. First, multibody dynamics are validated in a double pendulum system, for which the performance of the time integration schemes (Newmark-β and the generalized-α) is also analysed. Second, the accuracy of Unsteady Vortex-Lattice Method (UVLM) to capture three-dimensional (sideslip and spanwise variations in inflow velocity) and unsteady aerodynamic effects is evaluated on a flat plate example. Third, a mesh convergence study is performed on the AVATAR 10 MW wind turbine rotor together with a comparison of UVLM and Blade-Element Momentum (BEM) loads in steady uniform wind. Finally, the floating dynamics, the influence of waves and the control implementation are validated on the NREL 5 MW OC3 wind turbine.

3.1 Double planar pendulum

The double pendulum is a multibody system composed by two beams and two constraints that has been widely studied in literature [85, 111]. In particular, the constraint between the two beams imposes equal linear velocity at both sides of the joint and the relative

rotation between them is only allowed around one predefined axis. This joint is numerically equivalent to the rotor-nacelle joint in wind turbines. Thus, a double pendulum constitutes a suitable verification case for the multibody dynamics described in Section 2.1.3. Moreover, the numerical solution of the double pendulum is very challenging [85], thus, we use it to study the performance of the time integration schemes described in Section 2.1.2.

3.1.1 Rigid multibody dynamics validation

The double pendulum described in [85] is employed to validate the present model. At the beginning of the simulation, the first beam is located horizontally along the X axis and the second one is vertically hanging along the negative Z axis (Figure 3.1). Both beams are one-meter long, rigid, massless, each one has a mass of one kilogram attached at the end point and they move in vacuum. Each beam is discretised with 10 elements. The reference [85] employs a Newmark-β time integration scheme with a $\Delta t = 0.01\,\mathrm{s}$ time step.

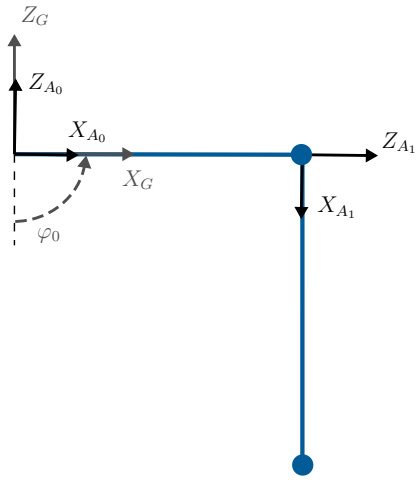

Figure 3.1: Initial position of the double pendulum.

The rotation angle of first node of the two beams (φ_0 and φ_1) is shown in Figure 3.2. The literature results [85] require a dissipation coefficient of $\alpha_\mathrm{N} = 0.015$ to stabilise the solution that fails otherwise. Our solution is stable for much smaller dissipation coefficients $\alpha_\mathrm{N} = 10^{-4}$. Moreover, our solution requires a dissipation coefficient ten times larger $\alpha_\mathrm{N} = 0.15$ to match the literature results. In summary, we can reproduce the available results in literature but our solution is less dissipative and, yet, more robust.

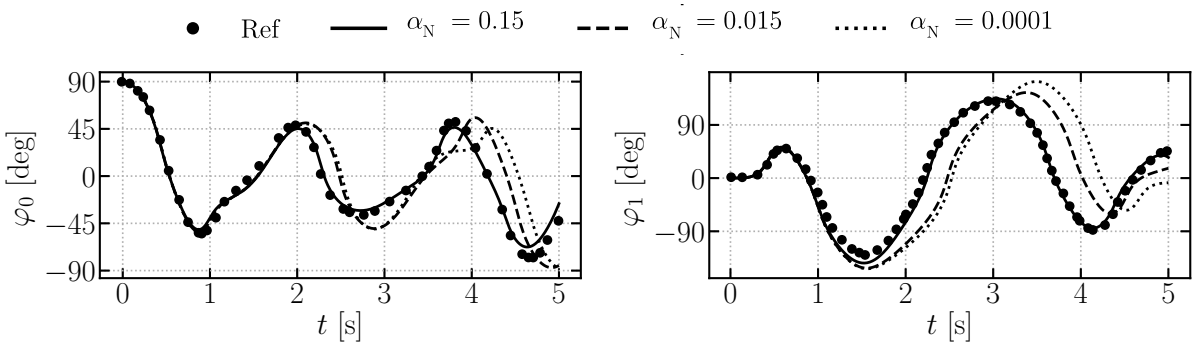

(a) First beam rotation angle.

(b) Second beam rotation angle.

Figure 3.2: Rigid double pendulum: multibody validation against Ref [85].

3.1.2 Performance of the time integration schemes

The double pendulum in Figure Figure 3.1 is considered again. Initially, the first beam is located horizontally along the X axis and the second one is hanging vertically along the negative Z axis, as in the previous Section 3.1.1. In this case, beams are considered flexible with the properties described in Table 3.1, no masses are attached to the end position of the beams and they also move in vacuum. Each beam is discretised with 20 elements. This case is interesting to analyse the time integration schemes because numerical dissipation plays a major role in the numerics due to the large and quick deformations of the beam.

Table 3.1: Flexible double pendulum structural properties.

Mass per unit length 1 [kg/m]	Mass inertia 10^{-5} [kgm]	Axial stiffness 1000 [N]	Shear stiffness 10^5 [N]	Torsional stiffness 10^5 [Nm^2]	Bending stiffness 1 [Nm^2]

Simulations with the Newmark-β and the generalized-α are run and compared to results of a code based on intrinsic beam equations [183]. Two time steps $\Delta t = 10^{-4}$ s and $\Delta t = 10^{-5}$ s and several dissipation levels are computed: the Newmark-β computations include dissipation parameters equal to $\alpha_N \in [10^{-4}, 10^{-3}, 10^{-2}, 10^{-1}]$ and the generalized-α ones include spectral radius at infinite equal to $\rho_\infty \in [1, 0.75, 0.5, 0.25, 0]$. However, some of these computations are not stable due to the extreme flexibility of the system, which has very low natural frequencies that would require an extremely small time step to be captured. In the case of the Newmark-β algorithm only the cases with the smallest time step $\Delta t = 10^{-5}$ s converge. The generalized-α method converges for the smallest time step and for cases with time step $\Delta t = 10^{-4}$ s when the spectral radius at infinity is $\rho_\infty \leq 0.5$. Very small time steps

are required for convergence due to the very high flexibility of the beams (Table 3.1).

First, the results with the smallest time step $\Delta t = 10^{-5}\,\mathrm{s}$ and smallest dissipation are compared with the intrinsic beam results [183] in Figure 3.3. The smallest dissipation is achieved for $\alpha_\mathrm{N} = 10^{-4}$ in the Newmark-β and $\rho_\infty = 0$ in the generalized-α schemes. Figure 3.3a shows the global horizontal coordinate of the end of the first beam x_G. Moreover, Figures 3.3b and 3.3c show the power spectral density P of the bending displacement of the tip of the first z_{A_0} and second z_{A_1} beams, respectively. Both time integration schemes and the intrinsic beam results show similar time evolution of the coordinates and power spectral density of the tip displacement in bending.

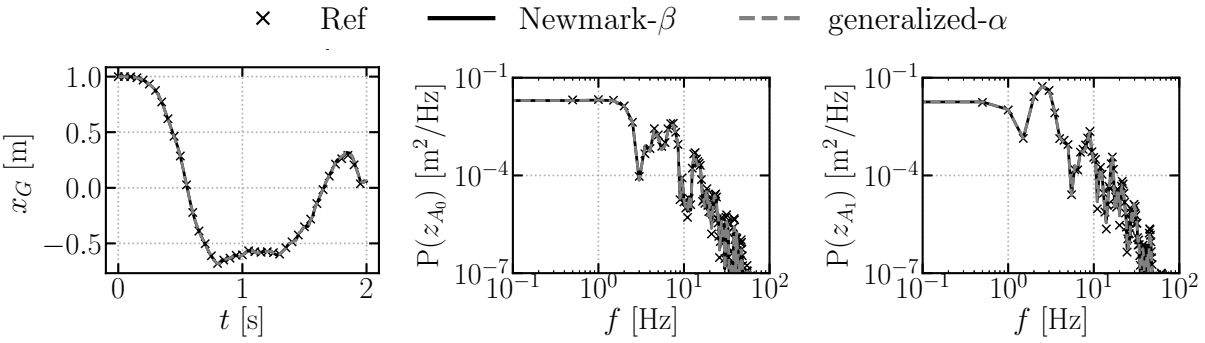

(a) First beam tip global horizontal coordinate.

(b) First beam tip bending displacement.

(c) Second beam tip bending displacement.

Figure 3.3: Flexible double pendulum: time integration scheme comparison. Ref [183].

The simulations of the flexible double pendulum with the Newmark-β time integration schemes at time step $\Delta t = 10^{-5}\,\mathrm{s}$ and two damping levels $\alpha_\mathrm{N} = 10^{-4}$ (less dissipative) and $\alpha_\mathrm{N} = 10^{-1}$ (more dissipative) are shown in Figure 3.4. The other dissipation levels ($\alpha_\mathrm{N} = 10^{-2}$, $\alpha_\mathrm{N} = 10^{-3}$) are not reported here for clarity but they provide intermediate results. Figure 3.4a shows the global horizontal coordinate of the end position of the first beam that has negligible difference for both dissipation levels. Figures 3.4b and 3.4c show that low frequencies are not affected by the numerical dissipation which only shows effects above $10^2\,\mathrm{Hz}$. Above that frequency, the energy content of the signal is six orders of magnitude below the zero-frequency value and, thus, negligible.

The performance of the generalized-α time integration scheme is presented next and shown in Figure 3.5. The two computations ($\Delta t = 10^{-5}\,\mathrm{s}$ and $\Delta t = 10^{-4}\,\mathrm{s}$) with the same dissipation level $\rho_\infty = 0.50$ show the same results for the time evolution of the position of the end of the first beam (Figure 3.5a). The energy content (Figures 3.5b and 3.5b)

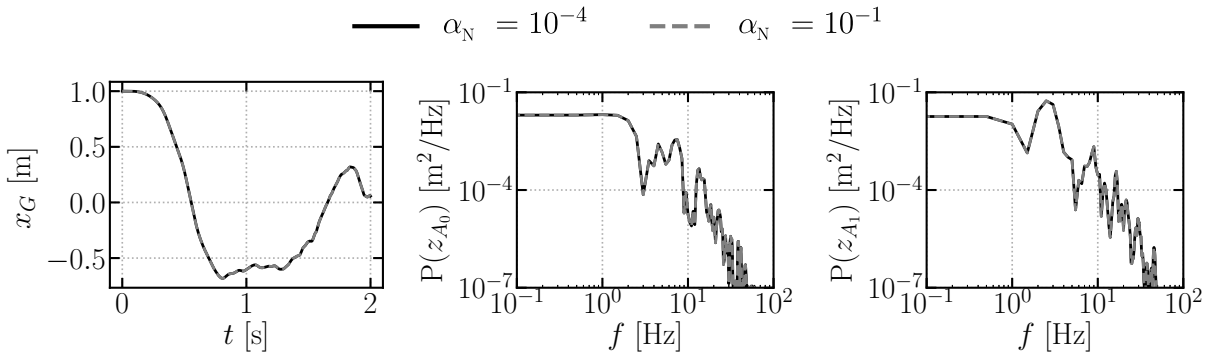

(a) First beam tip global horizontal coordinate.

(b) First beam tip bending displacement.

(c) Second beam tip bending displacement.

Figure 3.4: Flexible double pendulum: Newmark-β damping analysis.

in these two cases shows differences in dissipation for frequencies over 10^2 Hz where the amount of energy is negligible. The two simulations with the same time step $\Delta t = 10^{-5}$ s at two dissipation levels $\rho_\infty = 1.00$ (less dissipative) and $\rho_\infty = 0.50$ (more dissipative), show significant differences in the time evolution of the position (Figure 3.5a) associated with the dissipation at all frequencies (Figures 3.5b and 3.5c).

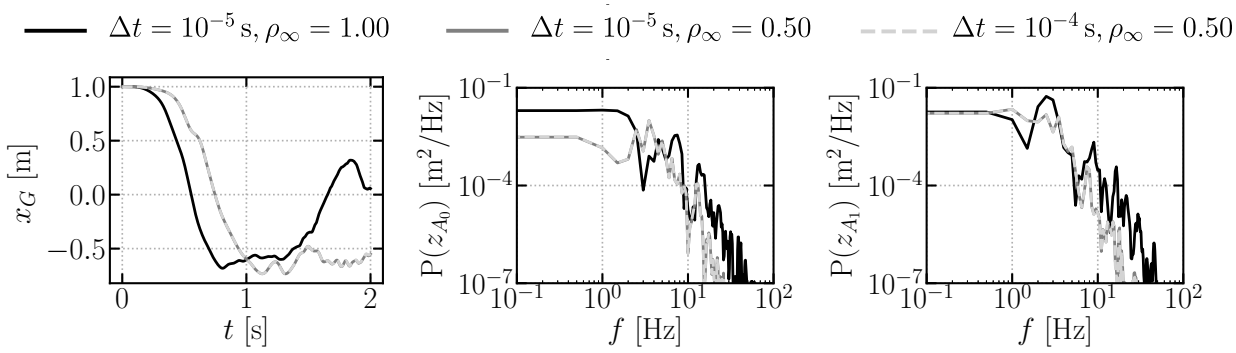

(a) First beam tip global horizontal coordinate.

(b) First beam tip bending displacement.

(c) Second beam tip bending displacement.

Figure 3.5: Flexible double pendulum: generalized-α analysis.

In summary, for stable results (small enough time step and dissipation) Newmark-β and generalized-α provide similar results. The generalized-α scheme provides stable solutions for larger time steps than the Newmark-β scheme when enough dissipation is applied. However, this dissipation affects all the frequency range, thus, modifying relevant physics of the problem and should be evaluated on a specific case base. No significant advantages of the

generalized-α were identified so the Newmark-β algorithm will be used in the rest of this report, unless specified otherwise.

3.2 Flat plate

Unsteady and three-dimensional aerodynamic effects under arbitrary kinematics are the main advantages of UVLM over other aerodynamic methods for wind turbines such as BEM. This section aims to validate and study these effects on a rigid flat plate where analytical solutions exist. First, we validate the unsteady capabilities of UVLM with the study of time-varying gusts on a flat plate in Section 3.2.1. Then, we validate the suitability of UVLM to compute three-dimensional effects with two examples, the study of sideslip flow (Section 3.2.2) and the study of inflow conditions that vary with the spanwise coordinate (Section 3.2.3) on a flat plate. This analysis was published by the authors in [184].

3.2.1 UVLM unsteady aerodynamics

Unsteadiness in wind turbine aerodynamics originates from a variety of sources such as aeroelastic couplings (flutter), wind fluctuations, separation or transition. BEM methods account for unsteadiness through dynamic wake models [12] and unsteady airfoil aerodynamics [48] but vortex methods can inherently account for most of them. The study of wing responses to incoming gusts [15] is the most common problem associated with unsteady aerodynamics. A suitable scale to measure the unsteady effects is the convective time scale which is generated using the airfoil semi-chord and the relative velocity

$$t^* = \frac{t u_r}{c/2}, \tag{3.1}$$

where t^* is the non-dimensional time, t is time, u_r is the relative velocity to the airfoil and c is the airfoil chord.

Small perturbation theory [15] provides the analytical lift response of 2D airfoils to different types of gusts. A Küssner gust is a sudden step in the vertical component of the inflow that is convected by the incoming wind velocity along the airfoil generating the following time history of the lift coefficient

$$c_L\left(t^*\right) = 2\pi\Delta\alpha(0)\psi_{\mathrm{K}}(t^*), \tag{3.2}$$

where c_L is the lift coefficient, t^* is the non-dimensional time, $\Delta\alpha$ is the effective change in angle of attack due to the gust and ψ_{K} is the Küssner function. On the other hand, a Wagner gust is a sudden change in the incoming velocity that applies to the whole flow field at the same time and generates the following lift response

$$c_L\left(t^*\right) = 2\pi\Delta\alpha_{3c/4}\phi_{\mathrm{W}}(t^*), \tag{3.3}$$

where c_L is the lift coefficient, t^* is the non-dimensional time, $\Delta\alpha_{3c/4}$ is the change in angle of attack measured at 3/4 of the chord and ϕ_{W} is the Wagner function.

The airfoil model based on thin-airfoil theory defines a linear dynamical system whose frequency response can be computed and approximated with a state-space representation of the system through rational function approximation. In this context, the Küssner and Wagner functions are obtained from the system response to a step in the incoming velocity or the airfoil pitch, respectively. In the present work, 10 states were enough to reach convergence and thus, this approximation of the system was used.

For validation, both Küssner and Wagner gusts have been computed for a flat plate ($\mathcal{AR} = 10^7$) at initially zero angle of attack and a gust step of 0.1 deg. The numerical solution is accurate for both gusts with an error below 1% after the noise in the first time steps (Figure 3.6). This noise is associated to the computation of the unsteady force Equation (2.75) which requires the approximation of the time derivative of the circulation which is infinite in the analytical solution.

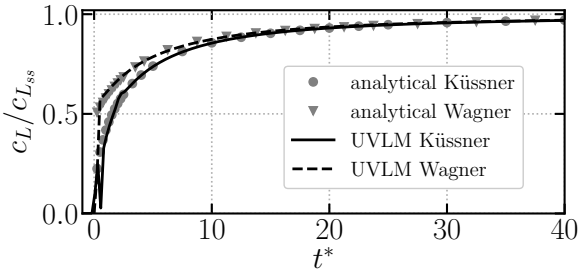

Figure 3.6: Küssner and Wagner gusts over an airfoil.

The computation of gusts on airfoils is the first step towards the characterisation of unsteady effects on full rotor configurations. For that reason, it is interesting to compute continuous varying velocity inflows. With that objective, a convolution integral can be applied to generate an analytical solution for continuous turbulence [15] based on the previous

solution for Küssner gusts in Equation (3.2)

$$c_L\left(t^*\right) = 2\pi\alpha(0)\psi_{\mathrm{K}}(t^*) + 2\pi\int_{0^+}^{t^*}\frac{\mathrm{d}\alpha}{\mathrm{d}\tau}\psi_{\mathrm{K}}(t^*-\tau)\,\mathrm{d}\tau, \tag{3.4}$$

where c_L is the lift coefficient, t^* is the non-dimensional time, α is the angle of attack and ψ_{K} is the Küssner function.

Continuous turbulence has been analysed on an airfoil ($\mathcal{R} = 10^7$) whose characteristics (twist $\beta_{\mathrm{t}} = 4.52\,\mathrm{deg}$, pitch $\theta_{\mathrm{p}} = 0\,\mathrm{deg}$, chord $c = 3.41$ m, blade velocity $\omega_{\mathrm{r}} r = 72.92\,\mathrm{m/s}$ and inflow velocity $U^\infty = 10.5\,\mathrm{m/s}$) have been obtained from the spanwise position $r = 0.75R$ of the AVATAR wind turbine that will be described in Section 3.3. The turbulence has been introduced in the system though the incoming wind velocity U^∞ which will generate a change in the angle of attack according to the geometric relationships in Figure 3.7a, this is,

$$\alpha + \Delta\alpha = \arctan\left(\frac{U^\infty + \Delta U^\infty}{\omega_{\mathrm{r}} r}\right) - \beta_{\mathrm{t}} - \theta_{\mathrm{p}}. \tag{3.5}$$

The time series of the inflow velocity has been obtained from the hub height probe of a turbulent field generated according to IEC-KAI level A with `Turbsim` [43]. The undisturbed relative velocity between the incident wind and the airfoil u_{r} is obtained as $\sqrt{(U^\infty)^2 + (\omega_{\mathrm{r}} r)^2}$.

Figure 3.7b shows good agreement between the numerical and the analytical solutions in Equation (3.4). Moreover, the importance of unsteadiness is revealed through the comparison between the previous solutions and the steady approximation. The unsteady signal is smoother and slightly delayed with respect to the steady approximation. This effects highlights the importance of having an adequate unsteady model to capture the flow unsteadiness in rotor aerodynamics. Cases of wind turbulence on full rotor configurations are studied in Section 4.2.3.

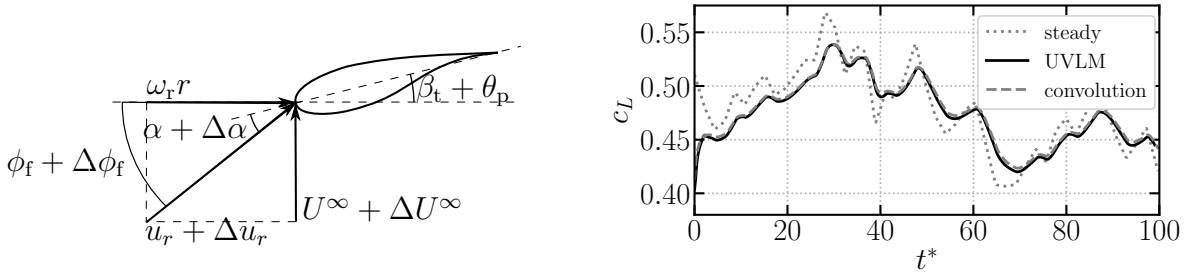

(a) Scheme.

(b) Lift response.

Figure 3.7: Turbulent inflow on an airfoil.

3.2.2 UVLM sideslip

Wind turbine blades are always subjected to spanwise flow due to the variations in loading along the span. In the root region, the dominant source of spanwise flow is separation and is usually corrected in BEM methods [185]. Spanwise flow is usually not addressed in the tip region where the behaviour is dominated by the tip-loss correction [4]. In yawed rotors, spanwise flow is of primary importance and cannot be tackled by the previous corrections, thus, it has to be further corrected by engineering approximations [35, 33]. On the other hand, vortex methods can inherently account for this effect. While this effect is very complex in three-dimensional wind turbine configurations, a first investigation to the problem can be done through flying wings under sideslip.

Lifting-line theory [18] provides the lift coefficient of elliptic wings under no sideslip for a certain aspect ratio AR. The extension of this theory for oblique wings [186] provides an approximation of the lift on wings under oblique inflow. For validation, an elliptic wing is used which has an analytical lift distribution given as

$$\begin{aligned}\frac{c_{L_a}}{8\cos(\Lambda)\alpha} =&\sqrt{1-y_l^2}\left(1-\frac{\pi}{2\mathit{AR}_l}\right)-\frac{\sin\Lambda}{\mathit{AR}_l}\sqrt{1-y_l^2}\sin^{-1}y_l+\\ &\frac{\sin\Lambda}{\mathit{AR}_l}y_l\left(\ln 8\mathit{AR}_l\sqrt{1-y_l^2}-(1-2a_\mathrm{s})-\csc\Lambda\left(\ln|1+\sin\Lambda|-(1-\sin\Lambda)\ln|\cos\Lambda|\right)\right),\end{aligned} \tag{3.6}$$

where c_{L_a} is the analytical lift coefficient, Λ is the sideslip, α in the angle of attack, y_l is the spanwise coordinate projected on the flow direction with AR_l associated aspect ratio and a_s is the straight axis location as a function of the chord.

The numerical estimation of lift with respect to the lift at zero sideslip (c_L/c_{L_0}) agrees very well with the theoretical solution in Equation (3.6) in value and maximum position (Figure 3.8a). A small difference occurs between both estimations towards the wing edges (Figure 3.8b), which can be explained from the lack of chordwise information in the lifting line model.

The effect of sideslip on wings is analysed through two variables: the maximum lift coefficient c_{Lmax} with respect to the maximum lift coefficient at zero side slip c_{Lmax_0} and its position along the span $y(c_{Lmax})/b$ where b is the semi-span. As pointed out by the validation case, the maximum lift coefficient decreases and displaces out of the mid position with the sideslip angle. Figure 3.9a shows how the decay of maximum lift coefficient is stronger the larger the sideslip angle and the weak influence of the aspect ratio. Moreover,

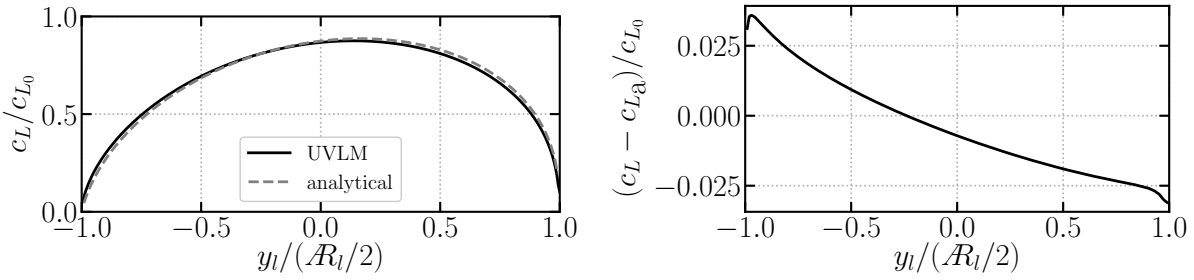

(a) Lift distribution along span.

(b) c_L difference between UVLM and the analytical solution.

Figure 3.8: Sectional lift on an elliptic wing with oblique inflow (45 deg).

Figure 3.9b shows the location of the maximum lift coefficient along the span: the smaller the aspect ratio the quicker the displacement of the maximum position with the sideslip angle. It is important to capture this effect because it will appear in wind turbines under yaw (Section 4.2.2). Furthermore, it will be complemented by the advancing/retreating and the skewed-wake three-dimensional effects.

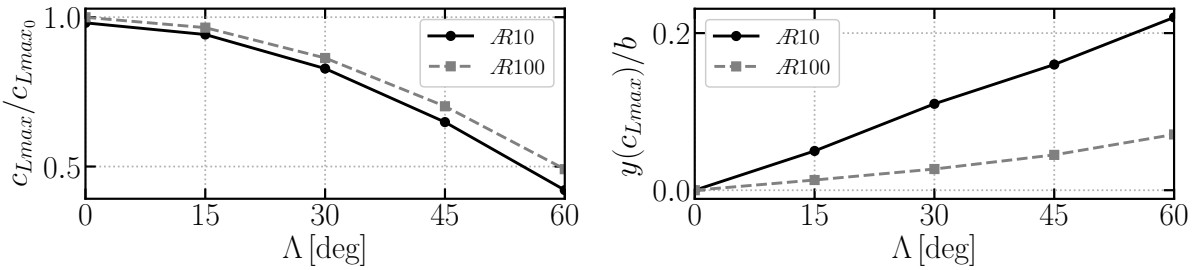

(a) Maximum lift coefficient with respect to the zero-sideslip case.

(b) Spanwise location of the maximum lift coefficient section.

Figure 3.9: Sideslip effect on sectional lift coefficient value and position.

3.2.3 UVLM spanwise variations

In cases of inflow turbulence there are spanwise variations of the incoming velocity that generate, consequently, spanwise varying loads. This scenario is against the fundamental hypothesis of BEM methods and is usually ignored. Vortex methods can inherently account for this effect and are used here to systematically study these cases on airfoil geometries before computing the full wind turbine configuration. In Section 4.2.3 this will be seen to have a huge effect for uncorrelated inflows on large rotors.

Lifting-line theory [25] provides, again, an analytical solution for the steady aerodynamics of finite-span wings under arbitrary incoming flow based on a spanwise parametrisation complying with the change of variable

$$y = b\cos\Theta, \tag{3.7}$$

where b is the semi-span, y is the coordinate along the span and Θ is the parameter of the change of variables. This solution consists of a Fourier series decomposition of the circulation along the airfoil whose coefficients should be resolved to meet the equilibrium between incoming and induced angles of attack

$$\frac{8b}{c_{L\alpha}(\Theta)c(\Theta)}\sum_{n=1}^{\infty}A_n\sin(n\Theta) + \sum_{n=1}^{\infty}nA_n\frac{\sin(n\Theta)}{\sin\Theta} = \alpha(\Theta) - \alpha_{L0}(\Theta), \tag{3.8}$$

where b is the semi-span, c_{L_α} is the lift vs. angle of attack curve slope, c is the airfoil chord, α is the angle of attack, α_{L0} is the angle of attack of zero lift and n and A_n are the index and coefficients of the Fourier series expansion, respectively.

The validation has been done for a wing of $\mathit{AR} = 100$, with $\lambda = 10c$ in a gust amplitude of 0.01 with respect to the average incoming velocity. In particular, 500 harmonics of the lifting line have been computed through a least squares approximation of 1500 sampling points. The difference between the UVLM and the lifting line solution (Figure 3.10b) is below 10% , yet, much more accurate than the 2D approximation (Figure 3.10a).

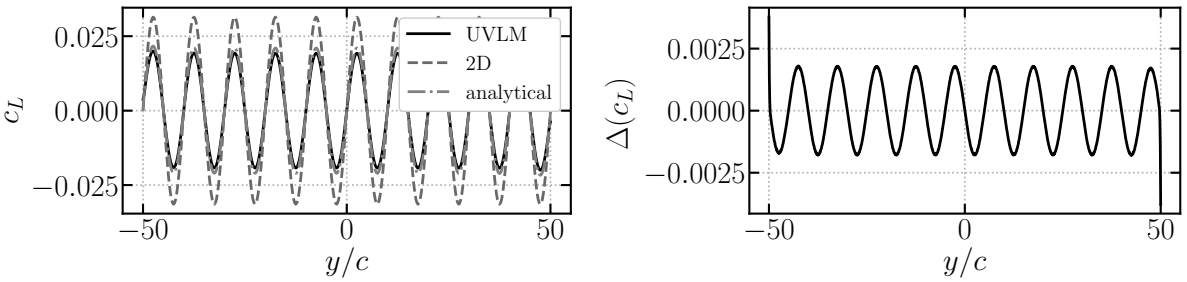

(a) Lift along the span.

(b) UVLM and lifting line c_L difference.

Figure 3.10: Sectional lift coefficient due to spanwise-varying incoming normal velocity on a slender wing ($\mathit{AR} = 100$).

3.3 Aerodynamic model of the AVATAR 10 MW wind turbine rotor

The AVATAR wind turbine is a benchmark case for large offshore wind turbines [187] which will be extensively used in this dissertation. Its main characteristics are: 10 MW of nominal power, $R = 102.88\,\text{m}$ rotor radius and 137.5 m hub height. In this dissertation no tilt, prebending or presweep are applied according to the wind turbine description in [188] and the structure is considered rigid. The operation point has been chosen at the end of the optimal production region of the power curve, namely an incoming wind speed of 10.5 m/s, a rotation velocity of 0.945 rad/s (tip-speed ratio equal to 9.26) and zero blade pitch.

For each airfoil, the out-of-plane $F_{\text{out}}(r)$ and in-plane $F_{\text{in}}(r)$ forces are computed from the airfoil lift $L(r)$ and drag $D(r)$ and the flow angle $\phi_{\text{f}}(r)$ are

$$F_{\text{out}} = L\cos\phi_{\text{f}} + D\sin\phi_{\text{f}}, \tag{3.9a}$$

$$F_{\text{in}} = L\sin\phi_{\text{f}} - D\cos\phi_{\text{f}}. \tag{3.9b}$$

The non-dimensional out-of-plane $c_{\text{out}}(r)$ and in-plane $c_{\text{in}}(r)$ force coefficients are computed by dividing $F_{\text{out}}(r)$ and $F_{\text{in}}(r)$, respectively, by $0.5\rho(U^{\infty})^2\pi R^2$ where ρ is the air density, U^{∞} is the average incoming wind velocity and R is the rotor radius. It is of interest to study the variation of the force coefficients along the normalised spanwise direction r/R. Finally, the integration of $c_{\text{out}}(r)$ and $c_{\text{in}}(r)r\omega_{\text{r}}$ along the span provides rotor thrust C_T and power C_P coefficients, that will be provided if required.

3.3.1 Steady UVLM mesh convergence

This section presents a mesh convergence study for the steady aerodynamics of the AVATAR 10 MW wind turbine, thus, it aims to find an adequate mesh of the aerodynamic surfaces and wakes yet computationally efficient. Steady-state UVLM solutions are directly obtained as described in Section 2.2.1. The baseline case consists of blades discretised with $N = 28$ spanwise panels, $M = 64$ chordwise panels and a wake able to account for the vorticity shed during 7 rotor revolutions. The wake discretisations in the spanwise direction matches the blade discretisation and it employs uniform size panels on the perpendicular direction (Figures 2.4 and 2.5). Each one of these variables is modified independently while the others are kept constant at the baseline value to evaluate the mesh convergence.

The wind turbine blade geometry and the flow circulation vary along the span. Thus,

the more spanwise panels, the more accurate the discretisation of the geometry and flow vorticity distribution. The baseline case has $N = 28$ spanwise panels following a half-sine distribution

$$r = \sin(\Theta)\, R, \tag{3.10}$$

with R the wind turbine radius and $0 \leq \Theta \leq 90\,\text{deg}$ a uniformly distributed set of $N + 1$ points. The case with 14 spanwise panels is obtained by removing every other point in the previous distribution. The case with 56 spanwise nodes adds one extra point at the middle of the original distribution.

The out-of-plane and the in-plane force coefficients along the span for the three spanwise discretisations are shown in Figures 3.11a and Figures 3.11b, respectively. The mid-span region ($0.2R < r < 0.8R$) has slow varying force coefficients and chords, thus, the sensitivity of the loads to the panels in that area is small. Near the root ($r < 0.2R$) and the tip ($r > 0.8R$) the force coefficients and the chords show larger variations with the span coordinate, hence the discretisation sensitivity. Table 3.2 shows the values of steady rotor thrust and power coefficients and the errors with respect to the case with 56 spanwise panels. The differences come from the root region where UVLM results are not trustworthy due to the significant thickness of the blade and the expected flow separation. The results for the cases of $N = 28$ and $N = 56$ spanwise panels are very close and, thus, a mesh with $N = 28$ spanwise panels is used in the rest of this work.

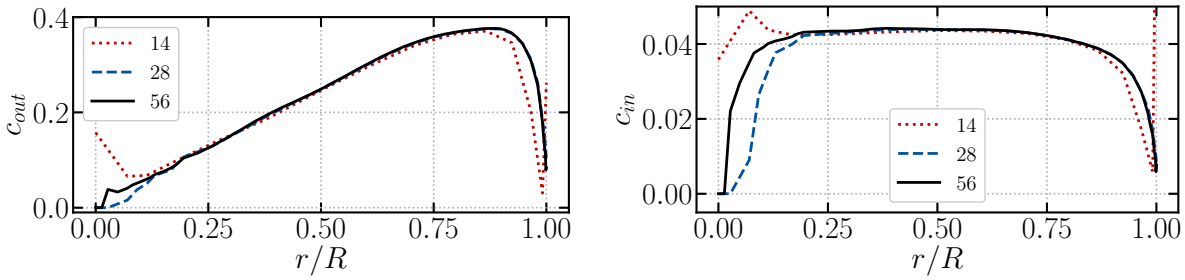

(a) Out-of-plane force coefficient.

(b) In-plane force coefficient.

Figure 3.11: Spanwise panels UVLM mesh convergence.

Wind turbine blades are curved along the camber line in the chordwise direction, thus, enough straight panels should be used to accurately reproduce this geometry. These panels are uniformly distributed along the camber line. The error in rotor thrust coefficient with respect to the case with $M = 128$ chordwise panels reduces significantly after $M = 64$ chordwise panels (Figure 3.12a). Figure 3.12b shows the spanwise distribution of in-plane

Table 3.2: Spanwise panels UVLM mesh convergence. Steady rotor thrust and power coefficients.

spanwise panels	C_T	C_P	$\epsilon(C_T)$	$\epsilon(C_P)$
14	0.676	0.540	-1.12 %	-1.86 %
28	0.676	0.546	-1.19 %	-0.69 %
56	0.684	0.550	0 %	0 %

force coefficient for the 4 discretisations. In this case, the mid-span region $0.2R < r < 0.8R$ is the most influenced by the discretisation because it includes cambered airfoils with large chords. Table 3.3 contains the numerical values of rotor thrust and power coefficients and the errors with respect to the case with $M = 128$. In the rest of this work, a mesh with $M = 64$ chordwise panels is used.

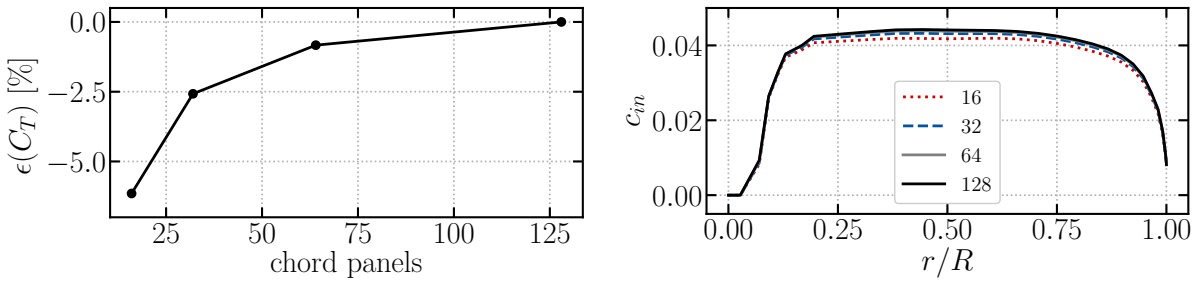

(a) Rotor thrust coefficient.

(b) In-plane force coefficient.

Figure 3.12: Chordwise panels UVLM mesh convergence.

Table 3.3: Chordwise panels UVLM mesh convergence. Steady rotor thrust and power coefficients.

chordwise panels	C_T	C_P	$\epsilon(C_T)$	$\epsilon(C_P)$
16	0.640	0.523	-6.15 %	-4.78 %
32	0.664	0.539	-2.58 %	-1.97 %
64	0.676	0.546	-0.83 %	-0.63 %
128	0.682	0.550	0 %	0 %

In vortex methods, the vorticity shed from solid surfaces to the wake should be accounted for throughout the simulation to capture unsteady effects. However, the influence of vorticity on solid surfaces decays with the inverse of the distance as per Equation (2.60). Thus, this mesh convergence study aims to find the distance behind the wind turbine above which the effects of the vorticity are negligible and can be ignored for computational efficiency.

The wake length is measured as the time (measured in rotor revolutions) that it can store information for. Figure 3.13a shows the changes in out-of-plane force coefficient for different discretisations which are more significant in the region $0.1R < r < 0.9R$ where the wake induction dominates the aerodynamic forces as opposed to the root and tip regions where the force are dominated by the three-dimensional effects. Figure 3.13b and Table 3.4 include the rotor thrust and power coefficients and the errors with respect to the case with a wake able to store 20 rotor revolutions of information. In the rest of this report, the tip-speed ratio does not change significantly and the rotor excursions in the cases of floating wind turbines are small compared with the wake length, thus, the case of 7 rotor revolutions stored in the wake (498112 wake panels) is considered to be converged in the rest of the report.

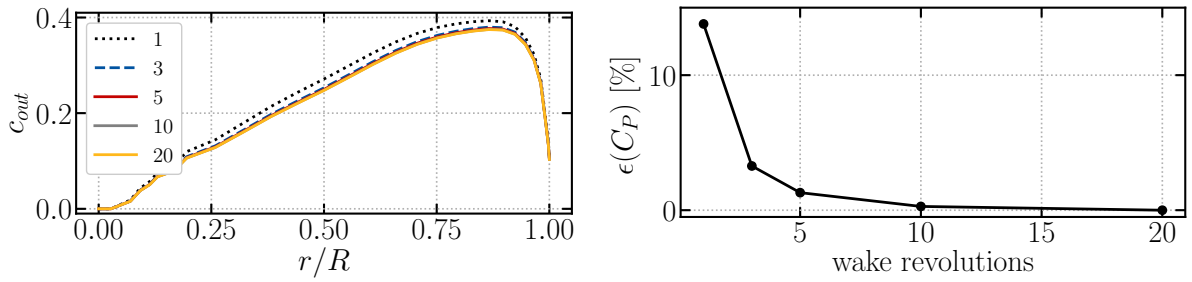

(a) Out-of-plane force coefficient.

(b) Rotor power coefficient.

Figure 3.13: Wake length UVLM mesh convergence.

Table 3.4: Wake length UVLM mesh convergence. Steady rotor thrust and power coefficients.

revolutions in wake	C_T	C_P	$\epsilon(C_T)$	$\epsilon(C_P)$
1	0.725	0.617	7.67 %	13.80 %
3	0.686	0.560	1.83 %	3.28 %
5	0.678	0.550	0.728 %	1.30 %
10	0.675	0.544	0.16 %	0.28 %
20	0.673	0.543	0 %	0 %

In wind turbine rotors, the time step Δt and the change in azimuthal angle $\Delta\theta$ of the rotor are related as

$$\omega_{\mathrm{r}}\Delta t = \Delta\theta, \tag{3.11}$$

with ω_{r} the rotor angular velocity. We believe that the use of the step in azimuthal angle $\Delta\theta$ is more intuitive and, thus, we use it from here on as the measure for the time step. Moreover, the time step and the wake panel size are linked through the Courant number as

we will explain in Section 4.1.2 and Equation (4.4). For now, it is enough with understanding that the time step influences the static solution because it defines the wake discretisation. This influence has been found to be small with a C_T and C_P difference of 0.2% and 0.3% when the time step is changed from $\Delta\theta = 8\,\text{deg}$ (0.145 s) to $\Delta\theta = 0.5\,\text{deg}$ (0.009 s). The usual time step employed in the rest of the report is below $\Delta\theta = 8\,\text{deg}$ so the influence of the time step on the steady wake discretisation is not the limiting factor. In the rest of the report, the time step will be adjusted to the dynamic physical phenomena that is studied.

3.3.2 UVLM wake modelling

There are two wake fidelities (prescribed and free) in UVLM to compute the wake convection as described in Section 2.2.1. The prescribed approximation assumes that the wake convects with the free-stream velocity. The free wake model includes the induced velocity generated by the shed vorticity and is substantially more computationally expensive.

Figures 3.14a and 3.14b show the out-of-plane and in-plane force coefficients, respectively, along the span for the AVATAR 10 MW wind turbine rotor in the steady-state case of inflow wind perpendicular to the rotor. In this case, all the BEM hypothesis hold (steady-state, low interaction between mid-span radial sections and use of Prandtl tip correction to model spanwise interactions at the blade root and tip regions), thus, BEM results are of reference [14] and two UVLM wake convection methods are compared against BEM. The estimation of out-of-plane force coefficient in Figure 3.14a is very similar in all the cases which shows the ability of all the solvers to capture the out-of-plane force coefficient. The reason is that, the flow angle ϕ_f is below 20 deg in regular wind turbine operation in the outermost part of the blade, thus, the out-of-plane coefficient is dominated by the blade lift as per Equation (3.9a). Lift is accurately captured by UVLM and BEM. The out-of-plane force is the main contributor to the system loads because it is around one order of magnitude larger than the in-plane force coefficient. On the other hand, Figure 3.14b shows the in-plane force coefficient which has significant contributions from both the blade lift and drag as per Equation (3.9b). This is very accurately captured by BEM in the steady uniform wind as it is computed from tabulated data but not by UVLM which estimates it from first principles (albeit without viscosity). In particular, the free wake approximation of UVLM is better than the prescribed wake approximation. The in-plane force coefficient is responsible for the power production which cannot be accurately predicted by UVLM. A correction for this difference in in-plane force coefficient is presented in Section 4.1.1.

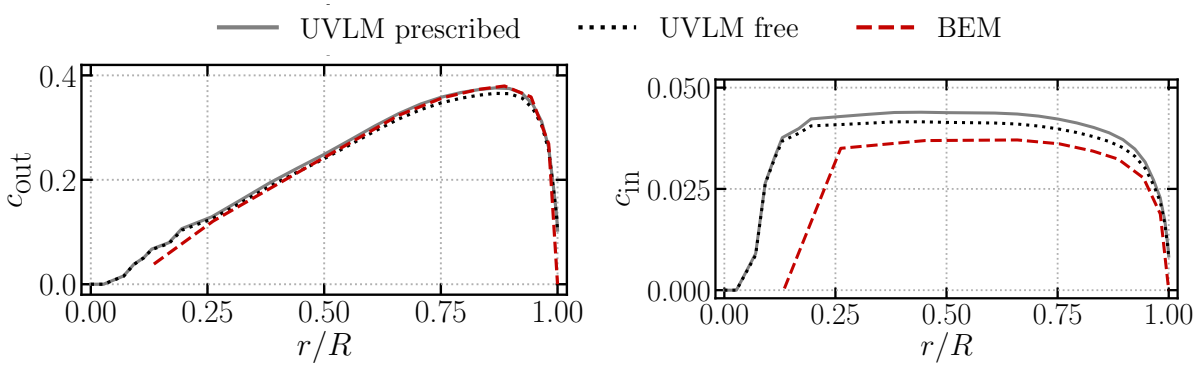

(a) Out-of-plane force coefficient.

(b) In-plane force coefficient.

Figure 3.14: UVLM wake model and BEM comparison. Uniform inflow. AVATAR 10 MW.

3.4 NREL 5 MW OC3 floating wind turbine

The NREL 5 MW [179] wind turbine including offshore platforms [175] has long been used by the wind energy research community. It has 5 MW nominal power and 63 m rotor radius. Two operation points have been used: 11.4 m/s and 18 m/s incoming wind speed with 0 deg and 15 deg pitch angle, respectively, with 12.1 rpm average rotation velocity in both cases. In particular, the floating OC3 spar structure has been used that leads to a hub height of 87 m. This platform is composed by an underwater vertical cylinder of $L_s = 120$ m and 6.5 m diameter, an underwater ballast and a base structure above sea water level (SWL) of $L_b = 10$ m on top of which the wind turbine is placed. The onshore and floating NREL 5 MW turbines have the same nacelle and rotor, however, the tower of the offshore wind turbine is lighter and more flexible [175]. We use this wind turbine for the validation of the floating forces due to the valuable open data available [176, 189]. There is some scatter between the different literature results, which is detailed in [176] and summarised next. Each contributor to the literature results detailed their modelling capabilities but some uncertainty remains about which of those capabilities were actually used in the analysis. As a general summary, all the contributors have BEM and Generalized Dynamic Wakes aerodynamic models and most of them include dynamic stall corrections. For the waves they all implement Airy theory and Morison's equation. Most of them have interfaces with external tools and some of them also include potential flow theory with radiation and diffraction. All of them used the same dynamic library as control module. In the structural models there are some that use modal, multibody or finite-element approximation. For the mooring dynamics, they show implementations with force-displacement relationships, quasi-steady catenary equations or

finite element methods. The objective of this section is not analysing those discrepancies but comparing our model to theirs.

The data about the spar structure is limited to the location of the centre of mass below sea water level z_{g}, the total mass of the platform M_{p}, the moments of inertia at the centre of gravity $I_y = I_z$ and I_x. We have generated two spar models that met the previous specifications. The first spar model (concentrated-spar) consists of the wind turbine base and a lumped mass (Figure 3.15a). The mass per unit length of the base has been assumed equal to the tower m_{T} and its stiffness has been set to 100 times that of the tower to model a rigid body. The lumped mass M_{L} is computed to keep the total mass of the platform

$$M_{\mathrm{L}} = M_{\mathrm{p}} - m_{\mathrm{T}} L_b. \tag{3.12}$$

The lumped mass location is such that the global centre of mass of the platform is kept to the provided z_{g} value

$$z_{\mathrm{L}} M_{\mathrm{L}} + m_{\mathrm{T}} L_b^2/2 = M_{\mathrm{p}} z_{\mathrm{g}}. \tag{3.13}$$

Finally, the moment of inertia around the I_{L_y} axis with respect to the sea water level is

$$I_{\mathrm{L}_y} = I_y + M_{\mathrm{P}} z_{\mathrm{g}}^2 - \frac{1}{3} m_{\mathrm{T}} L_b^3. \tag{3.14}$$

(a) Concentrated-spar model. (b) Full-spar model.

Figure 3.15: Floating platform models schemes.

The second model is referred to as full-spar and consist of two continuous uniform beams for the spar and the base, respectively and a ballast (Figure 3.15b). The spar stiffness is set as 100 times the tower stiffness and the base stiffness is linearly defined between the spar and the tower. The spar and the base have constant mass per unit length m_{s}, the ballast has mass M_{w} and is located z_{w} meters below sea water level. These properties are obtained

from the following system of equations

$$\begin{cases} M_{\mathrm{p}} = M_{\mathrm{w}} + m_{\mathrm{s}} \left(L_{\mathrm{b}} + L_{\mathrm{s}} \right), \\ z_{\mathrm{g}} M_{\mathrm{p}} = \dfrac{1}{2} m_{\mathrm{s}} \left(L_{\mathrm{s}}^2 - L_{\mathrm{b}}^2 \right) + M_{\mathrm{w}} z_{\mathrm{w}}, \\ I_y + M_{\mathrm{p}} z_{\mathrm{g}}^2 = M_{\mathrm{w}} z_{\mathrm{w}}^2 + \dfrac{1}{3} m_{\mathrm{s}} \left(L_{\mathrm{s}}^3 - L_{\mathrm{b}}^3 \right), \end{cases} \tag{3.15}$$

which guarantees that the global properties of the platform (mass, centre of mass and moments of inertia) are kept to the reported values.

In both cases, the symmetry of the system leads to the same moment of inertia in the y and x axis and the moment of inertia with respect to the z axis can be computed from the perpendicular axis theorem. In Section 3.4.1, some free decay simulations have been used to validate the floating dynamics as well as the mass distribution of the NREL 5 MW OC3 model set up in `SHARPy`. Results are shown for the platform displacements (surge r_{Gx}, sway r_{Gy} and heave r_{Gz}), rotations (roll φ_x, pitch φ_y and yaw φ_z), tower-top fore-aft movement x_{fa}, generator power E and rotor velocity ω_{r}. In some cases, the power spectral density P of the variables is used.

3.4.1 Floating dynamics: free decay tests

In each one of the simulations one of the platform degrees of freedom is displaced from the equilibrium position and the system is let to evolve. These cases do not include aerodynamics and assume a rigid structure. The literature results [176] ("Ref" in the next figures) include 10 different simulations (as explained in the introduction of this Section 3.4). Few results are considered not accurate in the original reference [176] because they lay clearly away from the majority of the results. We have removed those from the next plots to make a more clear explanation. From the heave free decay test (Figure 3.16), two literature results have been removed because one of them does not accurately capture the coupled motions and the other one has too much damping. In the case of the surge free decay test (Figure 3.17), one of the literature results shows less damping than the rest due to the lack of additional damping (Equation (2.113)) and has been removed. In the case of pitch free decay test (Figure 3.19), two literature results have been removed because one has too little damping and another one predicts the wrong coupling with the heave motion.

Consider an initial displacement along the heave direction and the following free decay movement of the platform (Figure 3.16). Our estimation of the time evolution of heave dis-

placement (Figure 3.16a) is in good agreement with the literature results. Despite the initial displacement of the platform along the heave direction, movements with smaller amplitudes appear on other directions. For example, the surge movement estimation (Figure 3.16b) the displacements are smaller than in the heave motion and, thus, numerical and modelling errors are more evident which makes literature results more scattered. In any case, our solution is in good agreement with the majority of them. Finally, there are movements, such as roll (Figure 3.16c), which are not excited at all in our case and most of the literature results but there is one of the literature results that reports small, yet non zero, values.

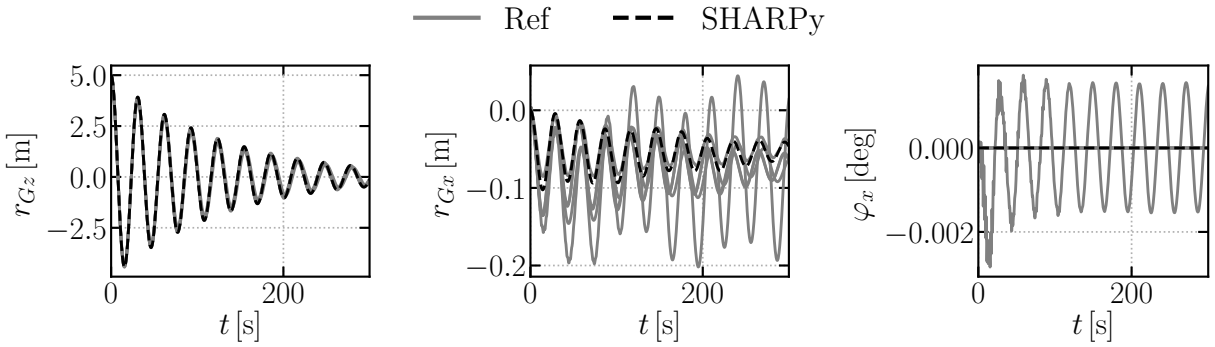

(a) Heave. (b) Surge. (c) Roll.

Figure 3.16: Platform movements in the heave free decay test. Comparison with Ref [176].

Our results for for surge decay (Figure 3.17a) the two spar models (concentrated and full spar) are identical and in agreement with the rest of the results obtained from the literature. This proves the possibility to simulate full spar cases, including, for example, spar flexibility. However, it comes to a cost of three times more computational resources due to the increased number of nodes and the poor conditioning of the structural stiffness matrix. Flexible spar structures are not considered here and, thus, the computational cost is not justified so the concentrated spar model is used from here on. In the pitch motion (Figure 3.17b), literature results are divided intro two groups and our results agree with the largest group in number. Finally, there is one outlier in the literature results in the estimation of the coupled sway motion (Figure 3.17c).

The case of free decay after an initial yaw perturbation (Figure 3.18) shows faster dynamics than the previous examples and it is still in good agreement with most of the literature results (Figure 3.18a) for the yaw motion. The surge displacement is very small compared to the system characteristic lengths and, thus, the numerical results show more scatter because small modelling or numerical errors are more relevant to the mean value (Figure 3.18b). Our

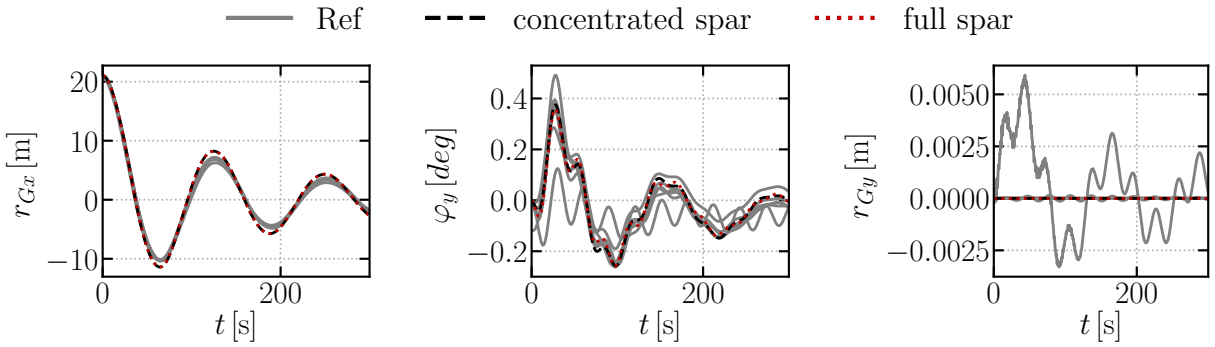

(a) Surge. (b) Pitch. (c) Sway.

Figure 3.17: Platform movements in the surge free decay test. Comparison with Ref [176].

results fall within the scatter of the literature results and agree with the majority of them. However, there is a small non-zero roll rotation (Figure 3.18c) which is not predicted by any of the literature results and is attributed to small asymmetries in our system.

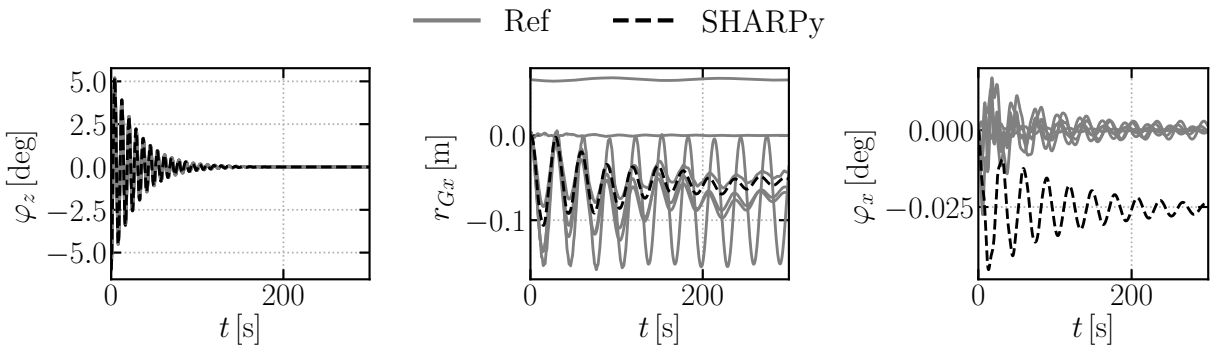

(a) Yaw. (b) Surge. (c) Roll.

Figure 3.18: Platform movements in the yaw free decay test. Comparison with Ref [176].

Our results are also in good agreement with most of the literature results for the free decay case after an initial pitch perturbation (Figure 3.19). Small differences appear in the yaw variable (Figure 3.19c) that is not excited in our simulations but shows a very small decaying movement in the literature results. We do not consider this is a concern because the values are very small and decaying to zero in short periods of time. A time step convergence study has been performed in this case that shows that a time step equivalent to 20 deg rotor azimuth is enough to achieve converged results due to the slow dynamics of the floating platform movements.

Consistent results have been obtained for the free decay tests associated with the pertur-

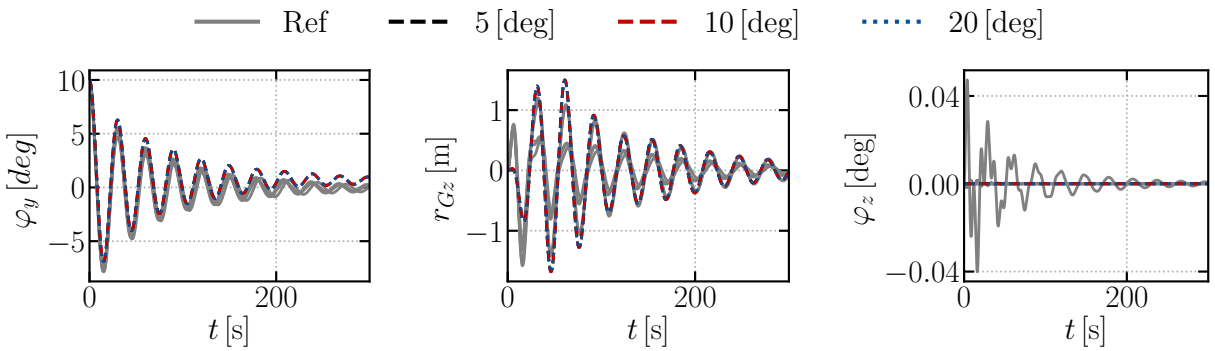

(a) Pitch. (b) Heave. (c) Yaw.

Figure 3.19: Platform movements in the pitch free decay test and time step convergence. Comparison with Ref [176].

bation of other degrees of freedom (sway and roll) and for the rest of variables but they are now shown for brevity.

3.4.2 Floating dynamics: waves

In this section, some examples of the dynamics of the NREL 5 MW OC3 platform under the effect of waves have been simulated. These cases do not include aerodynamics but they include structural flexibility. In particular, the results of the literature assume flexible tower and rigid blades. Our results include completely rigid cases and cases with flexible tower and blades.

The case of unidirectional regular waves with period 10 s, wave height 6 m and zero incidence $\beta_w = 0$ deg is shown in Figure 3.20. Our estimation of heave (Figure 3.20a) is in good agreement with the literature results in amplitude and period but it shows a very small constant positive value which comes from small modelling differences such as the system mass. Surge (Figure 3.20b) is the movement with the largest amplitude and our results fall within the scatter of the literature. In the pitch movement (not shown) our estimation of the movement amplitude is slightly larger than the literature results. Finally, the tower-top fore-aft displacement (Figure 3.20c) is twice as large in our case than in the literature results. We consider that the wave model we have implemented is introducing excessive energy in the system. However, this is not considered of concern in this validation case because the system behaves as expected. The platform displacements and rotations are the same for the rigid and the flexible models.

We generate a superposition of unidirectional (incidence $\beta_w = 0$ deg) waves according to

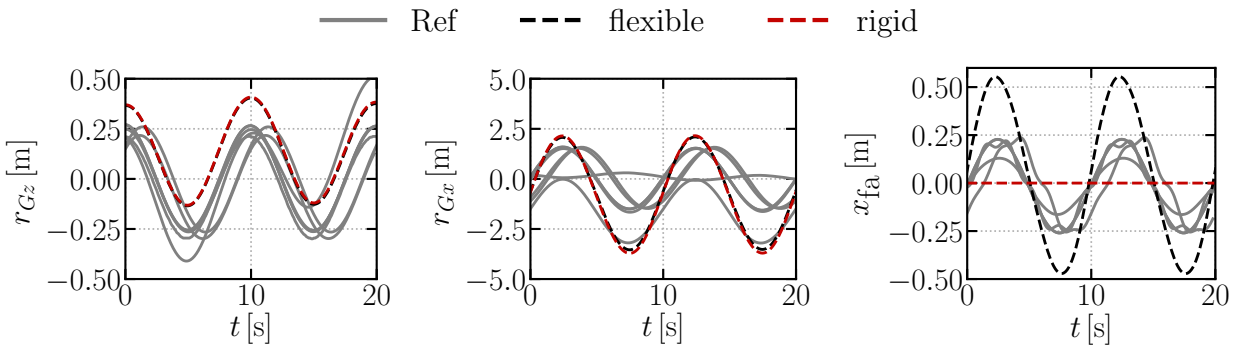

(a) Heave. (b) Surge. (c) Tower top fore-aft.

Figure 3.20: Platform movements and tower-top displacement under regular waves. Comparison with Ref [176].

the JONSWAP spectra described by Equation (2.117) with $T_p = 10\,\mathrm{s}$ and $h_s = 6\,\mathrm{m}$. The wave height spectrum is shown in Figure 3.21a with the maximum peak around $f_{\mathrm{w}} = 0.1\,\mathrm{Hz}$. Moreover, a detailed region of the spectrum is highlighted in Figure 3.21b because it shows some noise that may be a numerical artefact but that also has an impact on the system dynamics as shown in the following analysis. We do not have enough resolution to further analyse this noise, but we will highlight the two small frequency peaks (0.15 Hz and 0.17 Hz) in the next figures. These frequencies have been collected together with the system natural frequencies in Table 3.5 to facilitate the following analysis. In the following figures, relevant frequencies are marked with symbols that are also shown in Table 3.5. These cases have been run for 600 s starting from steady state scenario of calm sea and constant wind.

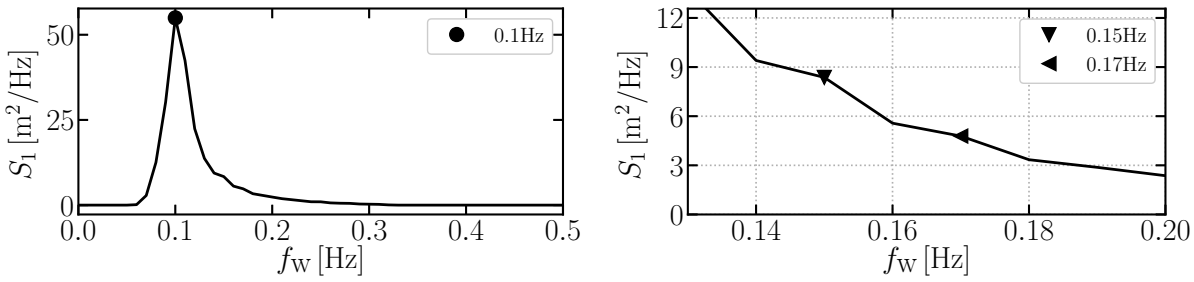

(a) Main view. (b) Zoom.

Figure 3.21: Wave height spectrum.

Figures 3.22a and 3.22b show the power spectral density of the surge and the tower-top fore-aft displacements, respectively, which are in good agreement with the literature. In par-

Table 3.5: NREL 5 MW OC3 natural frequencies and waves spectrum peaks for the JONSWAP waves validation case.

Platform	Movement	Surge and sway	Heave	Roll and pitch	Yaw
	Natural frequency [Hz]	$0.008^{\blacklozenge}$	0.032	$0.034^{\times}$	0.12
Tower	Movement	Side-to-side bending		Fore-aft bending	
	Natural frequency [Hz]	0.46		$0.47^{\blacksquare}$	
Blades	Movement	Collective flapwise bending		Edgewise bending	
	Natural frequency [Hz]	0.71		1.08	
Rotor	Movement	rotation frequency (1P)		Blade-passing (3P)	
	Natural frequency [Hz]	$0.2^{\bigstar}$		0.6^{+}	
Waves		Main peak		Minor peaks	
	Natural frequency [Hz]	$0.1^{\bullet}$		$0.15^{\blacktriangledown}$, $0.17^{\blacktriangleleft}$	

Symbols are used in figures to mark frequencies

ticular, the rigid and the flexible wind turbine models provide very close predictions of the platform degrees of freedom: surge (Figure 3.22a), heave (Figure 3.23a) and pitch (Figure 3.24a). The tower top fore-aft displacement (Figure 3.22b) is also in good agreement with the literature results. Major peaks in the spectrum are shown at the platform pitch natural frequency ($0.034^{\times}$ Hz) and the waves main spectral peak ($0.1^{\bullet}$ Hz). There is another important peak at twice the platform pitch natural frequency (0.07 Hz). Other small ones coming from the waves spectrum ($0.15^{\blacktriangledown}$ Hz and $0.17^{\blacktriangleleft}$ Hz) which do not appear in the literature results because their wave inflow spectrum was smoother. Finally, in the tower-top fore-aft displacement the peak of the tower fore-aft natural frequency ($0.47^{\blacksquare}$ Hz) shows significant resonance (Figure 3.22b). There is not a relevant peak in the surge spectrum (Figure 3.22a) at the surge natural frequency ($0.008^{\blacklozenge}$ Hz) because the simulations are not long enough to accurately capture this small frequency movement.

The influence of the Newmark-β dissipation parameter α_{N} is shown in Figures 3.23a and 3.23b for the heave movement and the tower top fore-aft displacement, respectively. There is a very small influence of the Newmark-β dissipation parameter at low frequencies which only show significant effect on higher order modes that are more damped for the largest values of the dissipation α_{N}. There is a local effect of the damping parameter around the platform natural pitching frequency (0.034 Hz) but all our simulations are within the range of the literature simulations. The location of the peaks in the spectra are similar to the ones explained above.

Finally, a time step analysis is shown in Figure 3.24 for the platform pitch (Figure 3.24a) and tower-top fore-aft displacement (Figure 3.24b). The differences between the reference

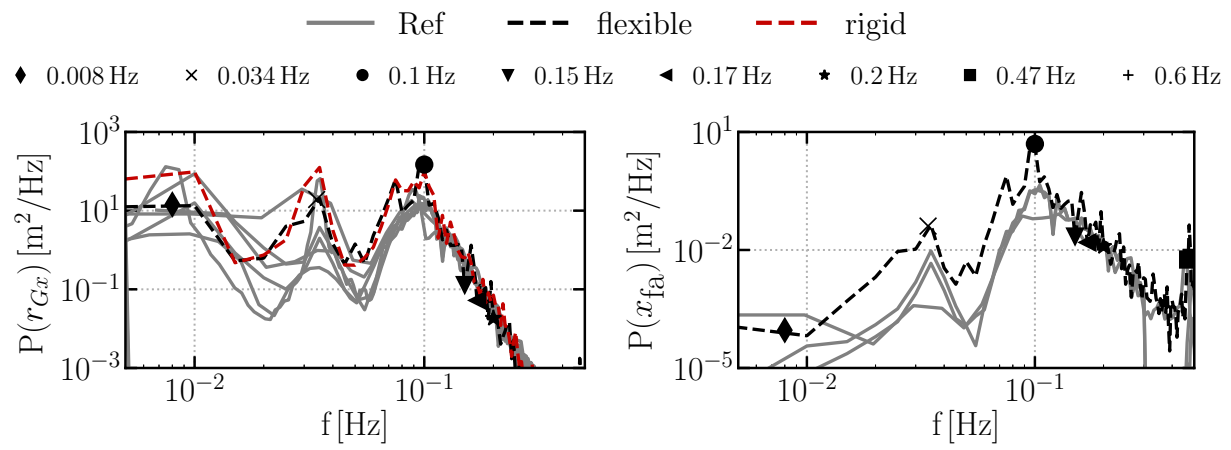

(a) Surge. (b) Tower top fore-aft.

Figure 3.22: Platform surge and tower-top fore-aft displacement under JONSWAP waves. Comparison with Ref [176].

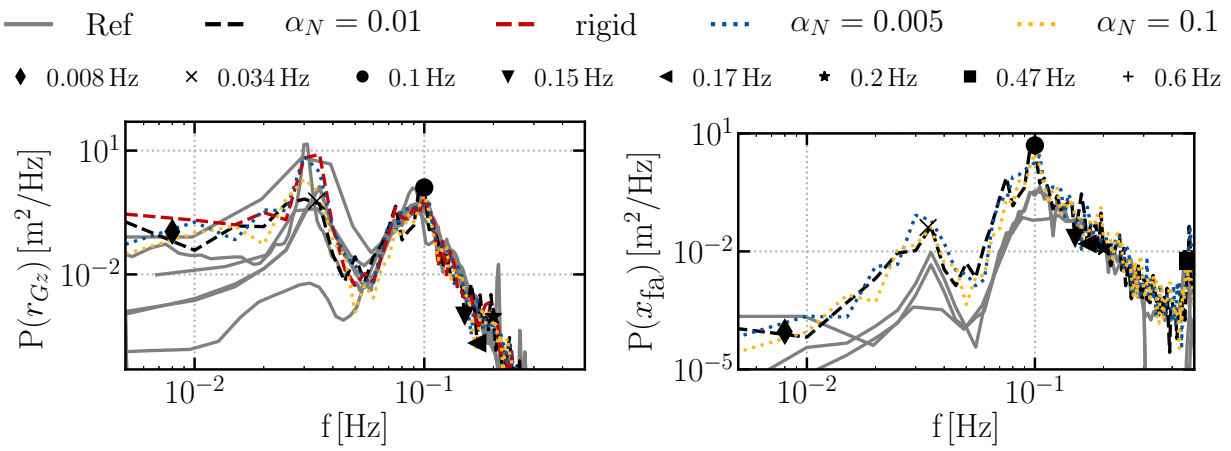

(a) Heave. (b) Tower top fore-aft.

Figure 3.23: Platform heave and tower-top fore-aft displacement under JONSWAP waves at different damping ratios. Comparison with Ref [176].

case $\Delta\theta = 5\,\text{deg}$ (0.07 s) and the case of $\Delta\theta = 10\,\text{deg}$ (0.14 s) are very small and very similar to the literature results. Thus, we can consider that the time step equivalent to $\Delta\theta = 10\,\text{deg}$ is small enough to capture the wave influence on floating dynamics. The location of the peaks in the spectra are similar to the ones explained above.

There is a general good agreement with the literature results. However, there is still some extra energy introduced in the system by the wave model, as discussed above, and some secondary peaks that come directly from the non-perfectly smooth wave spectrum that

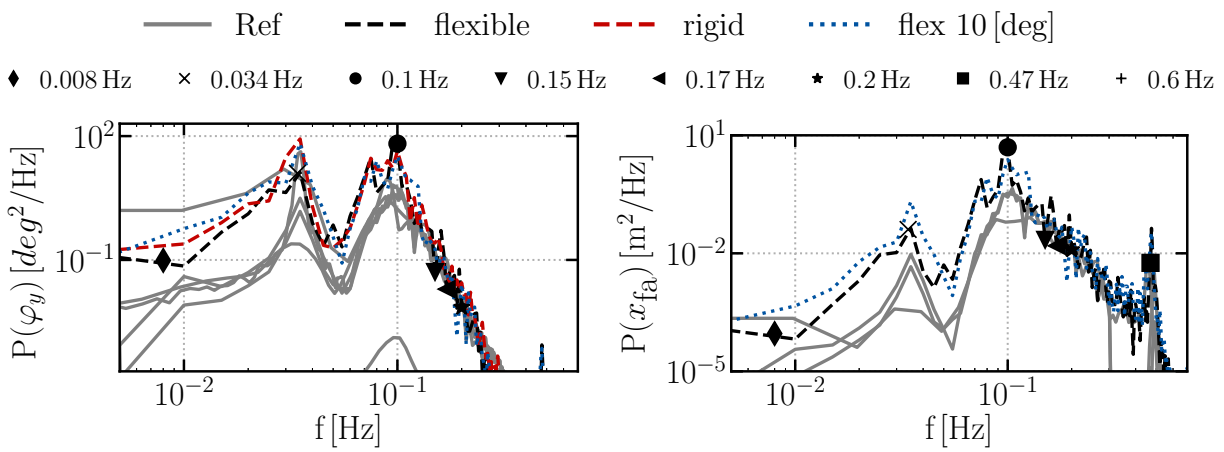

(a) Pitch.

(b) Tower top fore-aft.

Figure 3.24: Platform pitch and tower-top fore-aft displacement under JONSWAP waves for different time steps. Comparison with Ref [176].

is used as inflow. Nevertheless, these differences do not compromise the accuracy of the model.

3.4.3 Multiphysics validation

In Section 3.4.1 we have validated the radiation and diffraction phenomena and the mooring dynamics by using a rigid model and comparing with free decay tests available in the literature results. Then, in Section 3.4.2, we validated the wave forces on a flexible structure by comparing, again, with literature results. In this section, we use literature results that include all the physics described in Chapter 2: multibody structural dynamics, aerodynamics, hydrodynamics, mooring dynamics, irregular wave forcing and control.

Again, we use the NREL 5 MW OC3 wind turbine operating under a mean incoming wind speed of 18 m/s with a turbulence intensity $I_T = 11\,\%$. The longitudinal inflow velocity U_x^∞ and its power spectral density are shown in Figures 3.25a and 3.25b, respectively. The unidirectional wave spectrum follows a JONSWAP shape according to Equation (2.117) with a peak spectral period $T_\mathrm{p} = 10\,\mathrm{s}$, a significant wave height $h_\mathrm{s} = 6\,\mathrm{m}$ and a propagation direction along the positive x axis (Figure 2.6). We simulated 150 s with a time step equivalent to $\Delta\theta = 2\,\mathrm{deg}$ (0.028 s) but we do not have information about the simulation time used in the literature results [176]. The simulation begins at trimmed conditions under calm sea and constant wind. The wave height spectrum was already shown in Figure 3.21. The inflow wind velocity (Figure 3.25b) also shows small peaks at 0.02 Hz, 0.035 Hz, 0.06 Hz and even

smaller ones (0.1 Hz, 0.14 Hz, 0.17 Hz and 0.22 Hz) that are associated with the numerical generation of the turbulence field in the Mann box generator. These frequencies together with the system natural frequencies are included in Table 3.6 to facilitate the analysis below.

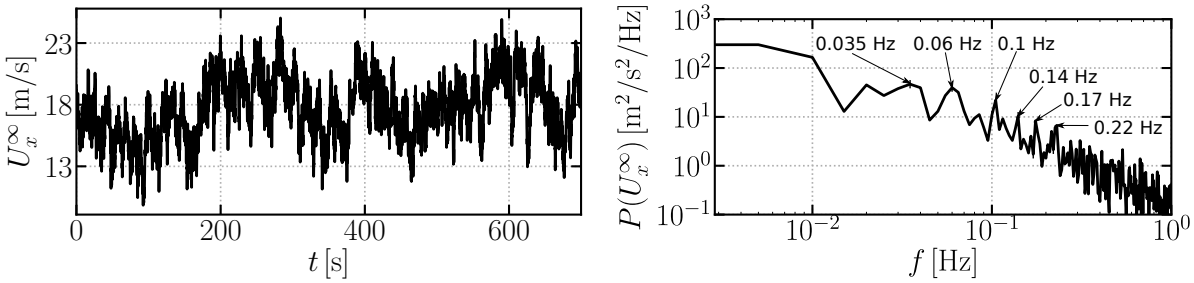

(a) Time evolution.

(b) Power spectral density.

Figure 3.25: Longitudinal wind velocity inflow.

Table 3.6: NREL 5 MW OC3 natural frequencies and waves spectrum peaks for the JONSWAP multiphysics validation case.

Platform	Movement	Surge and sway	Heave	Roll and pitch	Yaw
	Natural frequency [Hz]	$0.008^{\blacklozenge}$	0.032	$0.034^{\times}$	0.12
Tower	Movement	Side-to-side bending		Fore-aft bending	
	Natural frequency [Hz]	0.46		$0.47^{\blacksquare}$	
Blades	Movement	Collective flapwise bending		Edgewise bending	
	Natural frequency [Hz]	0.71		1.08	
Rotor	Movement	Rotation frequency (1P)		Blade-passing (3P)	
	Natural frequency [Hz]	$0.2^{\bigstar}$		0.6^{+}	
Waves		Main peak		Minor peaks	
	Natural frequency [Hz]	$0.1^{\bullet}$		$0.15^{\blacktriangledown}$, $0.17^{\blacktriangleleft}$	

Symbols are used in figures to mark frequencies

Figures 3.26 to 3.28 show the power spectral density of the platform displacements $\boldsymbol{r}_G$, rotations $\boldsymbol{\varphi}$, the first blade tip out-of-plane displacement x_{out}, the tower-top fore-aft movement x_{fa} and the rotor velocity ω_{r}. The largest platform movements are surge (Figure 3.26a), heave (Figure 3.26b) and pitch (Figure 3.26c) they all agree well with the literature results. However the zero-frequency value is slightly different in the case of surge and pitch. We can also see that the peak associated with the waves ($0.1^{\bullet}$ Hz) is larger in our case than in some literature results. There is also a small peak at the rotor rotating frequency ($0.2^{\bigstar}$ Hz) and a significant peak at the tower fore-aft bending frequency ($0.47^{\blacksquare}$ Hz) which overlaps with the blade passing frequency (0.6^{+} Hz). Our results show some peaks at the power spectral

that do not appear in the literature results. The most significant are one peak at twice the platform pitching natural frequency (0.07 Hz) and two peaks coming from the peaks in the wave and wind inflow spectra: 0.15$^{\blacktriangledown}$ Hz and 0.17$^{\blacktriangleleft}$ Hz. These peaks are shown at all Figures from 3.26 to 3.28.

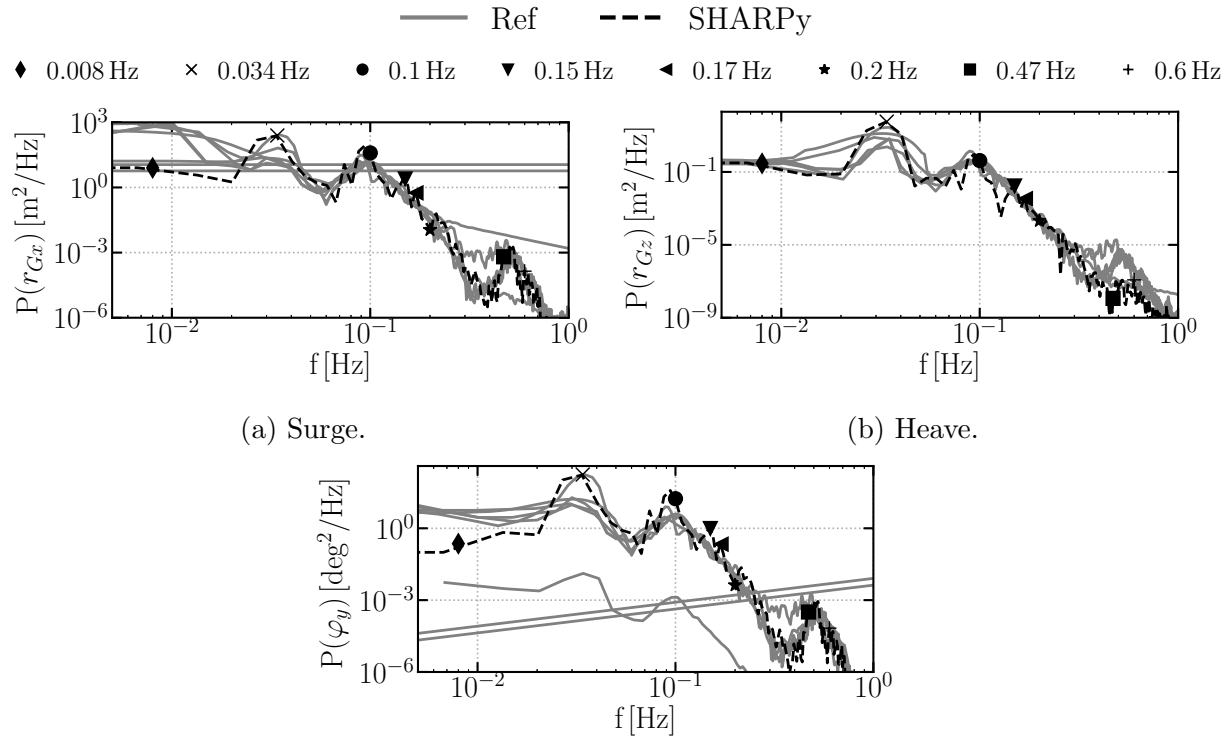

(a) Surge.

(b) Heave.

(c) Pitch.

Figure 3.26: Power spectral density of the larger platform movements under turbulent wind and JONSWAP waves with pitch control. Comparison with Ref [176].

We predict slightly smaller fluctuations in sway (Figure 3.27a) and roll (Figure 3.27b) movements around the platform natural pitch frequency (0.034$^{\times}$ Hz) and slightly larger fluctuations around the wave peak frequencies (0.1$^{\bullet}$, 0.15$^{\blacktriangledown}$ and 0.17$^{\blacktriangleleft}$ Hz) and 1P frequency (0.2$^{\bigstar}$ Hz). There is good agreement in the large peak in the spectrum associated to the tower fore-aft bending frequency (0.47$^{\blacksquare}$ Hz). The peak associated with the blade passing frequency (3P) is more noticeable than the peak at rotor frequency (1P) because in this simulation there is no shear or other input that can excite the rotor frequency. However, gravity excites the blade passing frequency (3P).

The tower-top fore-aft displacement (Figure 3.28a) shows similar tendencies between our solution and the literature: three peaks at platform pitch natural frequency (0.034$^{\times}$ Hz),

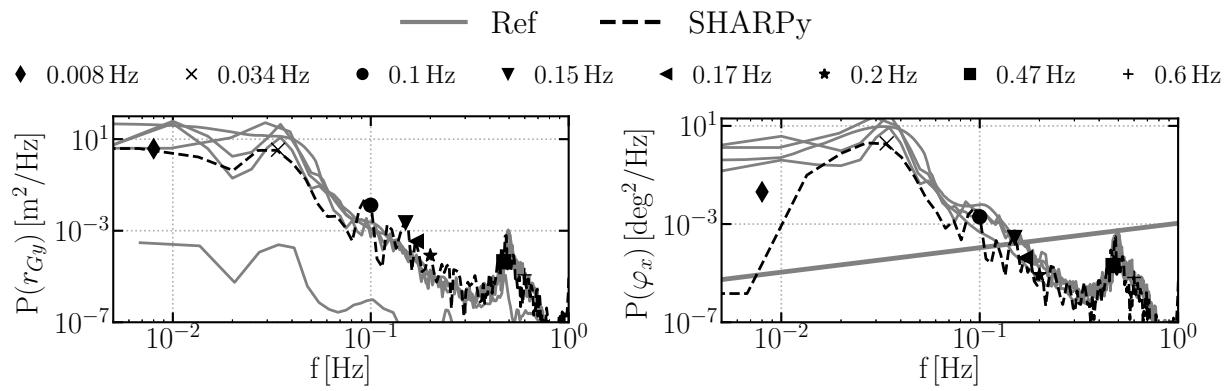

(a) Sway. (b) Roll.

Figure 3.27: Power spectral density of the smaller platform movements under turbulent wind and JONSWAP waves with pitch control. Comparison with Ref [176].

the waves peak period (0.1$^{\bullet}$ Hz) and tower fore-aft bending frequency (0.47$^{\blacksquare}$ Hz). We can appreciate again the small peaks that our wave spectrum has at 0.15$^{\blacktriangledown}$ and 0.17$^{\blacktriangleleft}$ Hz. However, the zero-frequency value is significantly smaller in out estimation, possibly related to the short simulation time and it shows again a larger peak around the wave peak frequency. This analysis is also valid for the out-of-plane blade-tip displacement in Figure 3.28b which shows more noisy spectrum at higher frequencies and a peak at the blade flapwise bending frequency 0.71 Hz.

The rotor velocity (Figure 3.28c) which is the variable stabilised by the controller shows a peak around the wave peak period (0.1$^{\bullet}$ Hz) which is significantly larger, again, in our prediction with respect to the literature value. The constant value is smaller which is related to the short simulation time because the average value of the rotor velocity is equal to the set-up value (12.1 rpm). Our results show the small peaks coming from the wave spectrum (0.15$^{\blacktriangledown}$ and 0.17$^{\blacktriangleleft}$ Hz) and there is a wide peak from the tower fore-aft bending frequency (0.47$^{\blacksquare}$ Hz) to the blade passing frequency (0.6^{+} Hz).

In summary, we have validated the mooring dynamics and the hydrodynamics with very accurate results when free-decay test are compared against the literature results. However, the waves model generates higher fluctuations on the platform that should come from higher forces. This requires an analysis of the wave model to match the forcing of the sea but it confirms the accuracy of the structural, aerodynamic, hydrodynamic and mooring dynamics.

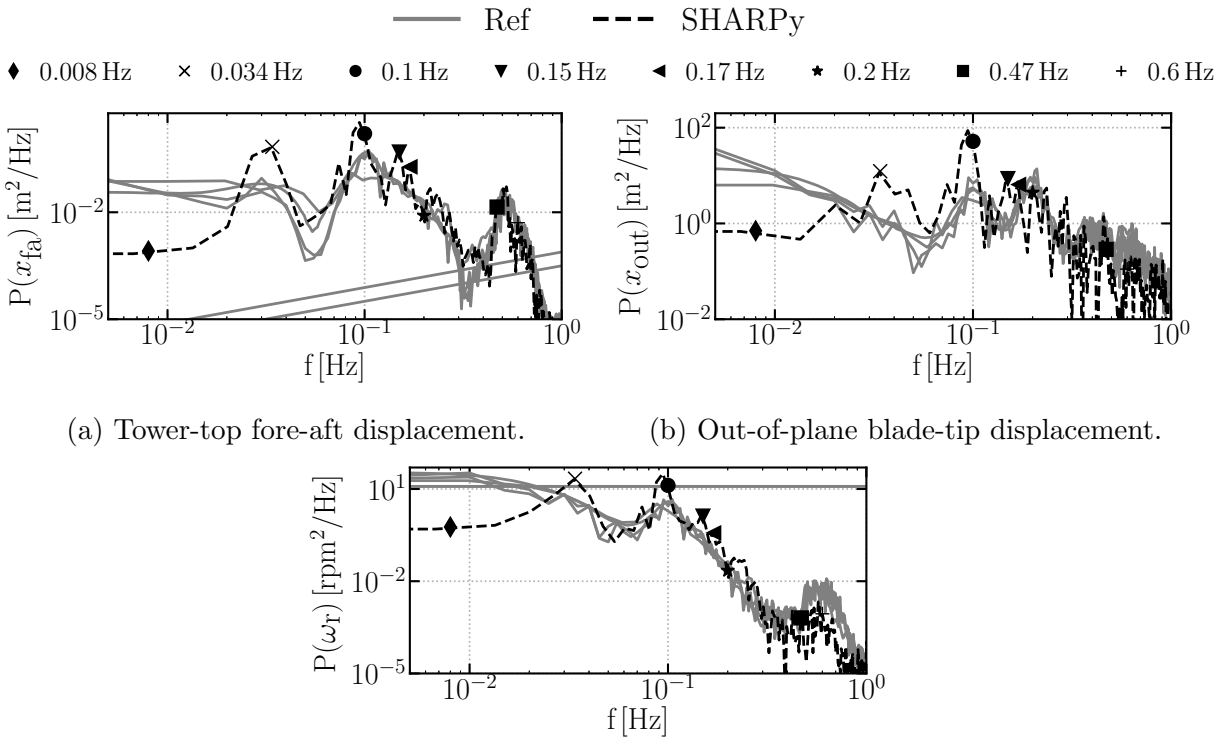

(a) Tower-top fore-aft displacement.

(b) Out-of-plane blade-tip displacement.

(c) Rotor speed.

Figure 3.28: Power spectral density of the tower-top fore-aft deformation, out-of-plane blade-tip displacement and rotor speed under turbulent wind and JONSWAP waves with pitch control. Comparison with Ref [176].

Chapter 4

Numerical improvements and benchmark of rigid wind turbine rotor aerodynamics

Experimental testing of current and future wind turbines is very challenging due to the large size of the designs [55] and the difficulty of coherently scaling the large number of physical phenomena involved [137, 190]. The most accurate numerical methods (fully-resolved CFD) are usually less expensive than experimental campaigns, however, they are still too time and resource consuming to be widely applied in wind turbine design [8]. Medium and low fidelity methods yield a balance between accuracy and efficiency and, as a result, are employed in most of the current industry analysis and design of wind turbines [8]. The basic theory behind each method (Chapter 2) defines the range of conditions for which the particular method is accurate. Unsteady and three-dimensional aerodynamic effects are gaining relevance in current designs due to the increasing length and flexibility of the tower and blades, the operation in floating platforms and the wake of other wind turbines. To account for these effects, the range of conditions in which numerical methods are accurate need to be usually expanded by semi-empirical corrections.

This chapter presents the analysis of rigid wind turbine rotor aerodynamics with three different numerical fidelities: Blade-Element Momentum (BEM), Unsteady Vortex-Lattice Method (UVLM) and Large-Eddy Simulation with Actuator Line (LES-AL). The first objective of this chapter is analysing the advantages and drawbacks of each numerical method and the inflow conditions under which they are accurate. A second objective is proposing improvements to increase the accuracy of some numerical methods under inflow conditions

that apriori cannot be captured by the basic methods described in Chapter 2. Thus, we benchmark the three fidelities and the proposed improvements under three common inflows. First, steady uniform inflow perpendicular to the rotor plane is a baseline for comparison. Second, the inherent capability of UVLM to describe the skewed-wake and unsteadiness of yawed inflow is shown and compared against LES-AL and BEM. Finally, the unsteadiness and interaction between spanwise sections of the blade in cases of turbulent inflow are analysed.

In this chapter, a rigid model of the AVATAR 10 MW wind turbine rotor described in Section 3.3 is analysed as an example of a future offshore wind turbine. Three numerical aerodynamic fidelities and their numerical implementation described in Section 2.2 are used: `OpenFAST v2.1.0` (BEM), `SHARPy v1.2` (UVLM) and `WInc3D` (LES-AL). Part of the results in this chapter have been published by the authors in [184, 191, 192].

4.1 Numerical improvements

This section describes some numerical improvements in the context of rigid rotor aerodynamics. We have already identified in Section 3.3.2 a significant in-plane force coefficient difference between UVLM and BEM associated to the absence of viscous drag estimation in UVLM. Thus, in Section 4.1.1, we propose a method to approximate viscous drag in UVLM following a methodology similar to BEM were the drag coefficient value is obtained from tabulated data. In Section 4.1.2, we tackle the high computational cost of UVLM through a new wake convection equation discretisation. In Section 4.1.3, we propose a method to account for spanwise-varying loads in BEM with the help of UVLM results. The turbulent inflow experience by the wind turbine in each modelling fidelity should be the same to reduce the uncertainty in the comparison. Thus, in Section 4.1.4, we present a method to generate turbulent fields that reduce the dissipation that takes place in the LES grid and not in the BEM and UVLM simulations.

4.1.1 Semi-empirical correction of UVLM viscous drag estimation

One of the drawbacks of UVLM arises from the assumption of inviscid flow, which implies an inability to account for viscous drag and, therefore, can lead to inaccurate force prediction. For this reason, we now propose a simple methodology to include viscous drag in the UVLM computation. This method is based on BEM philosophy in which forces are computed from look-up tables of steady lift, drag and moment force coefficients, parametrised by the

angle of attack, which is schematically shown in Figure 4.1a. These tables are obtained from steady two-dimensional wind tunnel experiments or Reynolds-Averaged Navier Stokes computations.

The velocity induced by the vortices in the UVLM discretisation becomes infinite at the vortex location (Section 2.2.1) generating singularities in the velocity field. Therefore, the computation of the angle of attack in UVLM is not well defined. Thus, we choose to determine the drag coefficient from the sectional lift coefficient c_L instead, computed from the UVLM forces in Equations (2.76) and (2.75), as input information (Figure 4.1b). The drag force is, then, computed from the non-dimensional coefficient using the relative velocity between the solid surface and the undisturbed incoming velocity and is added to the induced drag originally captured by UVLM. This approach is restricted to the region of the $c_L - \alpha$ curve between the maximum and the minimum lift coefficient so there is an unique value of drag associated to a certain lift. This is sufficient to capture the typical operational dynamics of wind turbines but it would require further development for other cases where the changes in lift-drag relation due to unsteady effects are not negligible. Moreover, operation at low angles of attack is considered so the lift does not need to be corrected due to viscous effects because the inviscid approximation is accurate. The effect of this improvement is shown in Section 4.2.1 on a full wind turbine rotor configuration.

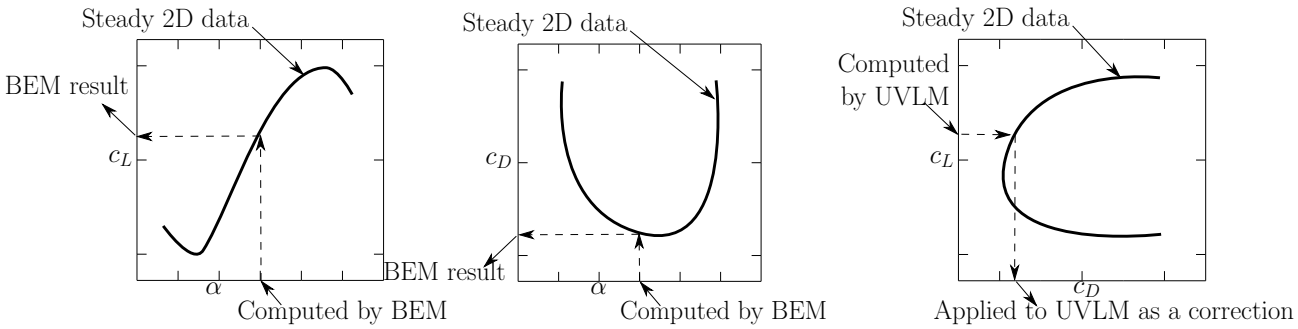

(a) BEM interpolation. (b) UVLM drag correction.

Figure 4.1: Scheme of the computation of force coefficients from tabulated data.

4.1.2 Generic discretisation of the UVLM wake convection equation

The vorticity shed by the solid surfaces $\partial\Omega_s$ at the trailing edge moves with the flow generating the wake $\partial\Omega_w$ (Figure 4.2). The circulation in the wake Γ_w in an arbitrary region

Σ with boundary $\partial\Sigma$ is related to the flow vorticity through Stokes' theorem

$$\Gamma_{\mathrm{w}} = \oint_{\partial\Sigma} \boldsymbol{u} \cdot \boldsymbol{dl} = \iint_{\Sigma} \boldsymbol{\nabla} \times \boldsymbol{u} \cdot \boldsymbol{d\sigma}. \tag{4.1}$$

The wake does not experiences any load, thus the pressure jump across the wake is zero $\Delta p = 0$, which implies that it convects with the flow such that a generic point $\boldsymbol{x} \in \partial\Omega_w$ initially located at $\boldsymbol{x}_0$ moves following the flow velocity $\boldsymbol{u}$ as

$$\boldsymbol{x}(t) = \boldsymbol{x}_0 + \int_0^t \boldsymbol{u}(\boldsymbol{x}(s), s) ds. \tag{2.69 revisited}$$

The flow velocity can be approximated either by the unperturbed upstream velocity $\boldsymbol{U}^{\infty}$ or, more accurately, by Equation (2.61), in which the unperturbed upstream velocity is combined with vortex-induced velocities. The former approximation is called prescribed-wake, since it implies that the wake shape is known a-priori. The latter choice is referred to as a free-wake model and leads to a more accurate computation of wake shape and, thus, more accurate values for axial induction and aerodynamic forces, as shown in Section 3.3.2 in the case of a wind turbine rotor.

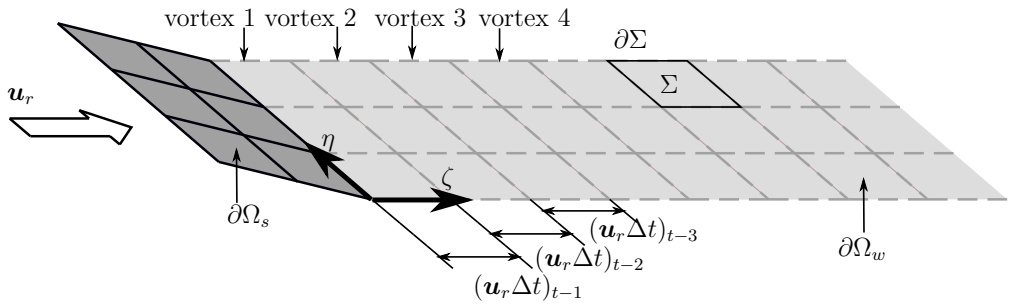

Figure 4.2: Solid and wake surfaces discretisation in UVLM.

In the wake, no external forces are applied and the fluid is ideal (a UVLM assumption), thus, Kelvin's theorem states that the flow circulation around a closed curve $\partial\Sigma$ does not change with time. In this scenario, the movement of the wake is simple and easily implemented via a Lagrangian description: displacement of the closed curves $\partial\Sigma$ with Equation (2.69) which retain their initial circulation.

However, aerodynamic problems are usually described with respect to frames of reference moving with solid surfaces because the influence of vorticity on the forces they experience decreases with the distance between them. This generates an effective convection of the wake circulation Γ_{w} away from solid surfaces that is convenient to describe with an Arbitrary

Lagrangian-Eulerian methodology. Two coordinates η and ζ parametrise the wake surface $\partial\Omega_w$ such that they run along the spanwise and streamwise directions, respectively. Therefore, curves along the streamwise direction ζ constitute streaklines and convection occurs only along them, such that, the convection equation for the circulation Γ_w can be applied independently for each streakline η:

$$\frac{\partial\Gamma_\mathrm{w}}{\partial t} + u_r\frac{\partial\Gamma_\mathrm{w}}{\partial\zeta} = 0, \tag{4.2}$$

where $\Gamma_\mathrm{w}(\zeta,\eta,t)$ is the flow circulation, the norm of the relative flow-solid velocity is computed as $u_r(\zeta,\eta,t) = \boldsymbol{u}(\zeta,\eta,t)\cdot\hat{\zeta}(\zeta,\eta,t) - \boldsymbol{u}_s(0,\eta,t)\cdot\hat{\zeta}(0,\eta,t)$ where $\boldsymbol{u}$ and $\boldsymbol{u}_s$ are the flow and known solid trailing edge velocities, respectively and $\hat{\zeta}$, the unit vector in the ζ direction. In general, the coupling of this equation with the vortex method described in Section 2.2.1 closes the problem. In practice, equations (2.59) and (4.2) are solved in a staggered manner such that the former provides the initial (i.e. $\Gamma_\mathrm{w}(\eta,\zeta,0)$) and boundary (i.e. $\Gamma_\mathrm{w}(0,\zeta,t)$) conditions for the latter.

The discretisation of the spanwise direction η is chosen at the beginning of the simulation while the discretisation in the streamwise direction ζ is generated automatically at each time step. This automatic generation is now described and is illustrated in Figure 4.3 which shows a side view (perpendicular to η) of the three-dimensional scheme in Figure 4.2. At the beginning of each time step (Figure 4.3b), solid surfaces have moved due to their velocity $\boldsymbol{u}_s$ and the wake has been convected by the local flow velocity $\boldsymbol{u}$. These movements have generated a gap between the trailing edge and the first wake node where a new segment of a vortex is created. This segment is equal to a vector $(\boldsymbol{u}-\boldsymbol{u}_s)\,\Delta t$ parallel to the streamwise direction ζ and the relative solid-fluid velocity ($\boldsymbol{u}_r = \boldsymbol{u}-\boldsymbol{u}_s$) by construction. The regions $\partial\Sigma$ generated with this discretisation (Figure 4.2) are called vortices and their corners are convected with Equation (2.69) to keep track of the wake surface.

Equation (4.2) is usually numerically solved on the mesh described in the previous paragraph and sketched in Figure 4.3. We denote $\Gamma^t_{\mathrm{w}\zeta} = \Gamma_\mathrm{w}(\zeta,\eta^p,t)$ for clarity. With this objective Equation (4.2) is discretised with a first order upwind scheme

$$\frac{\Gamma^{t+1}_{\mathrm{w}\zeta} - \Gamma^t_{\mathrm{w}\zeta}}{\Delta t} + u_r\frac{\Gamma^t_{\mathrm{w}\zeta} - \Gamma^t_{\mathrm{w}\zeta-1}}{\Delta\zeta} = 0, \tag{4.3}$$

with $\Delta\zeta$ the vortex size in the ζ direction. This equation can be rearranged and simplified

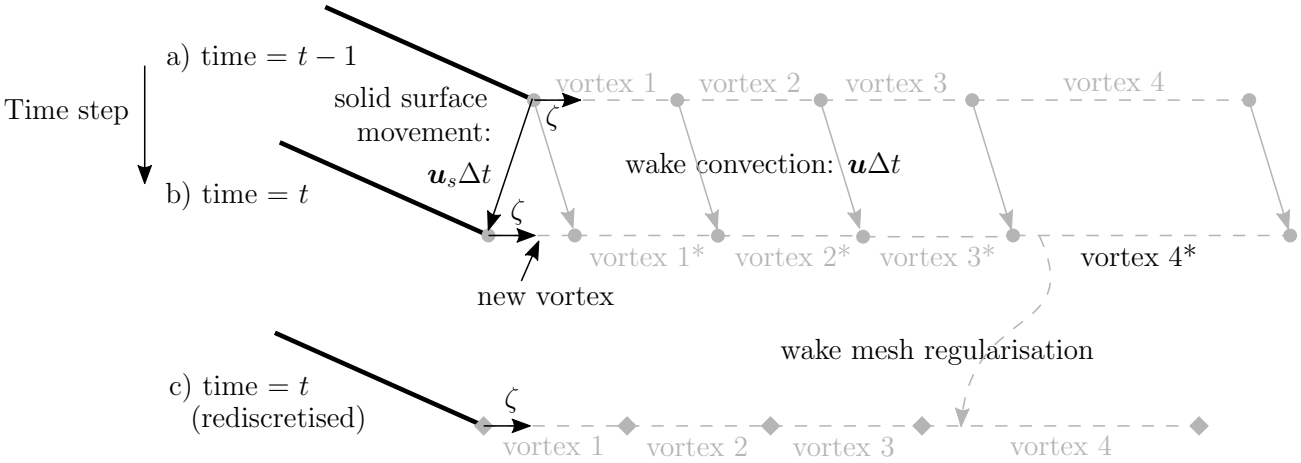

Figure 4.3: New non-uniform wake rediscretisation method.

by defining $C = u_r\Delta t/\Delta\zeta$ to give

$$\Gamma^{t+1}_{\mathrm{w}\zeta} = \left(1 - \frac{u_r\Delta t}{\Delta\zeta}\right)\Gamma^{t}_{\mathrm{w}\zeta} + \frac{u_r\Delta t}{\Delta\zeta}\Gamma^{t}_{\mathrm{w}\zeta-1} = (1-C)\cdot\Gamma^{t}_{\mathrm{w}\zeta} + C\cdot\Gamma^{t}_{\mathrm{w}\zeta-1}. \tag{4.4}$$

In most UVLM implementations [18], the wake discretisation is generated such that $\Delta\zeta = u_r\Delta t$, forcing $C = 1$ and simplifying the wake convection equation to displace the values from one discretisation element to the following:

$$\Gamma^{t+1}_{\mathrm{w}\zeta} = \Gamma^{t}_{\mathrm{w}\zeta-1}. \tag{4.5}$$

However, Equation (4.4) allows the discretisation of the wake surface to be performed with coarser vortices in regions where vorticity has less influence on the forces on solid surfaces (usually far away from them) such that $\Delta\zeta \neq u_r\Delta t$. This improves computational efficiency, which is of importance for the free wake model, since computation time grows as $\mathcal{O}(N_w^2)$ where N_w is the number of vortices that discretise the wake geometry.

To give a simple example, consider the airfoil in Figure 4.3 subjected to a step gust (Küssner gust) with horizontal relative velocity u_r. In particular, the airfoil is infinite in the spanwise direction, has a chord c and is initially placed at zero angle of attack. Figure 4.4a shows two wake discretisations, one complying with the traditional assumption of $C = 1$ and another employing a coarser wake discretisation using the method described above. It is clear that a large reduction in the number of vortices required to discretise the wake is achieved and, importantly, this does not lead to a decrease in accuracy. Indeed, the ratio between instantaneous lift coefficient c_L and its value in steady-state $c_{L_{\mathrm{ss}}}$ is shown in Figure

4.4b with respect to the reduced time

$$t^* = \frac{2tu_r}{c}. \qquad \text{(3.1 revisited)}$$

The results of both models are identical and equal to the analytical solution based on thin airfoil theory.

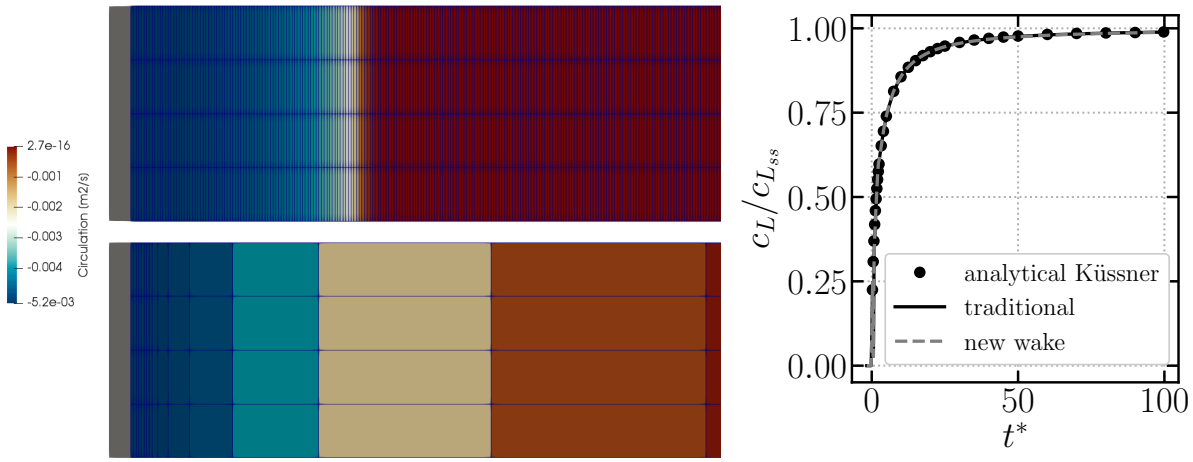

(a) Traditional (top) and new (bottom) wake discretisation.

(b) Lift coefficient.

Figure 4.4: Scheme and lift force in a Küssner gust with traditional and new wake discretisation schemes.

Resuming the analysis of Figure 4.3, at each time step, one vortex is created, while the last vortex is removed (vortex 4^* in Figure 4.3b) in order to keep the number of vortices constant for computational convenience. If the size of the vortices is not uniform (in the schematic example, vortex 4^* is larger than the new vortex created), the wake length is reduced at each time step which leads to reduced accuracy in the loads computation (Section 3.3.1). To avoid this shortening, an additional step of mesh regularisation is performed after the wake convection, as described in Figure 4.3c. The wake discretisation is updated along each streakline independently such that the distribution of distances from the solid trailing edge to each vortex corner matches the initial distribution at time $t = 0$ (Figure 4.3a). The remeshing algorithm conserves the total vorticity in the wake (zero-th moment of the distribution), which guarantees that the system complies with Kelvin's law. For straight wakes, a simple linear interpolation scheme in Cartesian coordinates is sufficiently accurate. For helicoidal wakes which are of importance to wind-energy applications, linear interpolation in Cartesian coordinates lead to a significant reduction of the wake radius. Figure 4.5a shows an example

of the error induced by the interpolation in Cartesian coordinates and the resulting non-physical reduction in wake radius between simulation time $\theta = 0\,\text{deg}$ and $\theta = 23\,\text{deg}$ in Figures 4.5b and 4.5c, respectively.

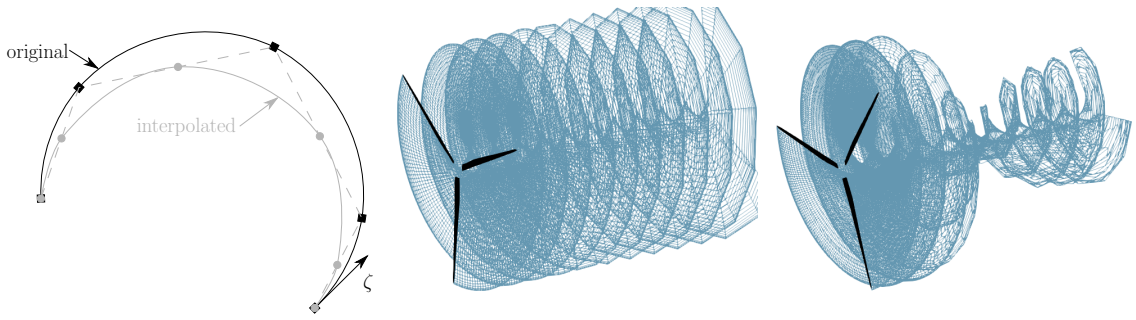

(a) Scheme. (b) $\theta = 0\,\text{deg}$. (c) $\theta = 23\,\text{deg}$.

Figure 4.5: Scheme and example of the failure of the linear interpolation in cartesian coordinates of helicoidal wakes.

This problem was overcome with a slerp interpolation scheme

$$\boldsymbol{a}_3 = \frac{\sin\left((1-q)\,\vartheta_\text{s}\right)}{\sin\left(\vartheta_\text{s}\right)}\boldsymbol{a}_1 + \frac{\sin\left(q\vartheta_\text{s}\right)}{\sin\left(\vartheta_\text{s}\right)}\boldsymbol{a}_2, \tag{4.6}$$

where $\boldsymbol{a}_3$ is the slerp-interpolated vector between $\boldsymbol{a}_1$ and $\boldsymbol{a}_2$ with q the interpolation parameter and ϑ_s the angle between $\boldsymbol{a_1}$ and $\boldsymbol{a_2}$. Equation (4.6) tends to the linear interpolation when $\vartheta_\text{s} \to 0$. This interpolation scheme represented in Figure 4.6 preserves the wake radius and does not need special treatment of the discontinuity at azimuth angle π radians as opposed to cylindrical coordinates. In the case of the real wind turbine studied in Section 4.2.1, the relative root-mean square error between the traditional UVLM and this new wake discretisation scheme is below 0.5% for rotor thrust and power coefficients. In the cases of inflow turbulence on a wind turbine rotor run in Section 4.2.3, the new wake convection equation reduces the computational time by 90% with respect to the standard UVLM implementation. Moreover, this new scheme does not modify the inherent capability of UVLM to capture the wake tip vortex roll-up, indeed, it just describes this vortex with a new discretisation.

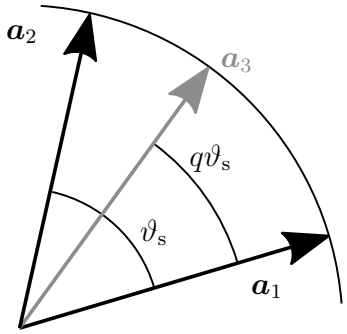

Figure 4.6: Slerp interpolation scheme.

Frequency-limited balanced truncation of the UVLM

The bespoke method for reduction of linear UVLM systems through frequency-limited balancing truncation briefly described in Section 2.2.1 from [171] assumes $C = 1$ in the wake convection Equation (4.4). The new wake convection equation described above allows discretisation such that $C \neq 1$. Again, each wake row η^p is independent of the others and convection only occurs along the ζ direction. The method in [171] requires the z-transform of Equation (4.4)

$$\overline{\Gamma}_{\mathrm{w}\zeta} = (1 - C_\zeta)\, z^{-1}\overline{\Gamma}_{\mathrm{w}\zeta} + C_\zeta z^{-1}\overline{\Gamma}_{\mathrm{w}\zeta-1}, \tag{4.7}$$

with $\overline{\bullet}$ the z-transform of the variable. Moreover, the method requires the explicit computation of the wake circulation at each vortex from the values at the bound vortices at previous time steps. With the new wake convection scheme, the first wake vortex $\zeta = 1$

$$\overline{\Gamma}_{\mathrm{w}1} = \frac{C_1 z^{-1}}{1 - (1 - C_1)\, z^{-1}}\overline{\Gamma}_M. \tag{4.8}$$

The circulation of the rest of the vortices can be recursively computed according to

$$\overline{\Gamma}_{\mathrm{w}\zeta} = \frac{C_\zeta z^{-1}}{1 - (1 - C_\zeta)\, z^{-1}}\overline{\Gamma}_{\mathrm{w}\zeta-1}, \qquad 1 < \zeta \leq M_w. \tag{4.9}$$

Finally, if Equations (4.8) and (4.9) are applied to every row η and the mapping

$$J(\eta, \zeta) \mapsto j, \tag{2.65 revisited}$$

is employed again to gather the bound $\Gamma(\zeta, \eta, t)$ and wake $\Gamma_\mathrm{w}(\zeta, \eta, t)$ distributions into the

$\mathbf{\Gamma}_j$ and $\mathbf{\Gamma}_{\mathrm{w}j}$ vectors, respectively. Thus, Equation (4.4) can be described in matrix form

$$\mathbf{\Gamma}_{\mathrm{w}}^{n+1} = \mathcal{C}_{\Gamma}\mathbf{\Gamma}^{n} + \mathcal{C}_{\Gamma_{\mathrm{w}}}\mathbf{\Gamma}_{\mathrm{w}}^{n}, \qquad \text{(2.73 revisited)}$$

In Section 2.2.1, the non-zero terms in the $\mathcal{C}_{\Gamma}$ and $\mathcal{C}_{\Gamma_{\mathrm{w}}}$ were ones that represented the shift operator in Equation (2.71). With the new wake convection equation, these non-zero terms are $(1-C)$ and C, according to Equation (4.4). C is computed from the distance between the centre of two vortices, thus, C_{ζ} is computed from the $(\zeta-1)^{th}$ to the ζ^{th} vortex. This is the only change that needs to be introduced in the frequency-limited balanced truncation method summarised in Section 2.2.1 and described in [171].

4.1.3 Spanwise sections interaction filter for BEM

Wind turbine blades under uniform inflow perpendicular to the rotor plane have nearly constant circulation except at the root and tip regions [4] and, in this case, the BEM hypothesis of independent 2D radial sections is reasonable. However, turbulent inflow cases generate spanwise-varying input velocities and forces that change significantly in distances comparable to the airfoil chord invalidating the hypothesis of constant circulation along the span and independent 2D radial sections. This is not accounted for by BEM, but can be described using, for example, strip theory as validated in Section 3.2.3 and expanded next.

The velocity distribution along the span under turbulent inflow can be formed by Fourier superposition of harmonic functions with a single wavelength. We study the wavelength dependence of this phenomena through the study of single wavelength signals. Consider a wing of infinite span, chord c and zero camber subject to an inflow velocity consisting of a constant horizontal component U_x^{∞} plus a span-varying vertical component, as shown in Figure 4.7. In particular, suppose that the vertical velocity has a sinusoidal distribution which varies with the spanwise coordinate y,

$$\boldsymbol{U} = U_x^{\infty}\hat{x} + \left(U_z^{\infty} + \Delta U_z^{\infty}\sin(2\pi y/\lambda)\right)\hat{z}, \qquad (4.10)$$

where U_z^{∞} is a constant, ΔU_z^{∞} the perturbation amplitude and λ its wavelength. The constant baseline angle of attack, α_0, the local angle of attack, $\alpha(y)$, and the peak-to-peak relative amplitude A are defined as

$$\alpha_0 = \arctan\left(\frac{U_z^{\infty}}{U_x^{\infty}}\right), \quad \alpha(y) = \arctan\left(\frac{U_z^{\infty} + \Delta U_z^{\infty}\sin(2\pi y/\lambda)}{U_x^{\infty}}\right) \quad \text{and} \quad A = \left(\frac{2\Delta U_z^{\infty}}{U_x^{\infty}}\right).$$

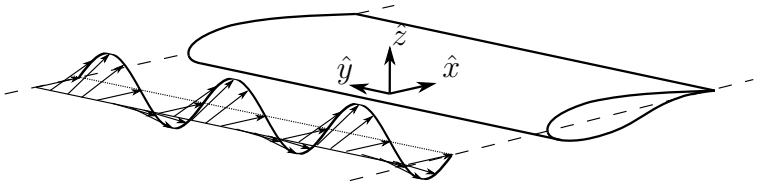

Figure 4.7: Spanwise-varying inflow velocity on airfoil.

BEM assigns a lift coefficient to every two-dimensional spanwise section according to the effective angle of attack α of the incoming velocity and disregards the interactions between spanwise sections. Similarly, in the 2D approximation of the studied case, the lift coefficient of each spanwise section is equal to $2\pi\alpha$. On the other hand, the lift predicted by UVLM inherently accounts for three-dimensional spanwise interactions. UVLM results are based on a three-dimensional implementation without periodic boundary conditions. The features of this process have been modelled through a convergence study on a very long blade with constant sections subjected to periodic inflow. In particular, at the centre of the UVLM blade a discretisation of 20 nodes per wavelength is used in the first 10 cycles of the inflow velocity. For computational efficiency, this discretisation is continuously coarsened towards the edges. Both models are now compared to demonstrate the disparity between three-dimensional and two-dimensional methods and to motivate a proposed correction to improve results based upon two-dimensional theory.

Figure 4.8 shows the force coefficients along the span for wavelength $\lambda = 10c$, baseline angle of attack $\alpha_0 = 4$ deg, and peak-to-peak relative amplitude $A = 0.1$. The mean values of lift c_L, moment c_M and spanwise c_s force coefficients are the same in the 2D and UVLM models (Figures 4.8a, 4.8c and 4.8d, respectively). However, a non-zero mean drag coefficient c_D is apparent in the 3D case (Figure 4.8b). The peak-to-peak values (which we subsequently denote using angled brackets $\langle\bullet\rangle$) of the lift coefficient are smaller in the UVLM case than in the 2D approximation (Figure 4.8a).

The previous example does not cover the wide range of characteristic spatial scales—ranging from the smallest spatial scale of atmospheric turbulence to blade-long eddies—that are of importance for wind turbines. For this reason, the effect of wavelength variation on the previous geometry (Figure 4.7) needs to be considered over a range of baseline angles of attack α_0 and peak-to-peak relative amplitudes A.

Previous qualitative analysis holds for all wavelengths, however there is an important quantitative influence of the inflow wavelength on the peak-to-peak value of the lift coefficient c_L. Figure 4.9 shows the ratio between the 3D model and the 2D approximation. The peak-to-peak lift coefficient c_L in the 3D model is reduced around 40% for inflow wavelength $\lambda =$

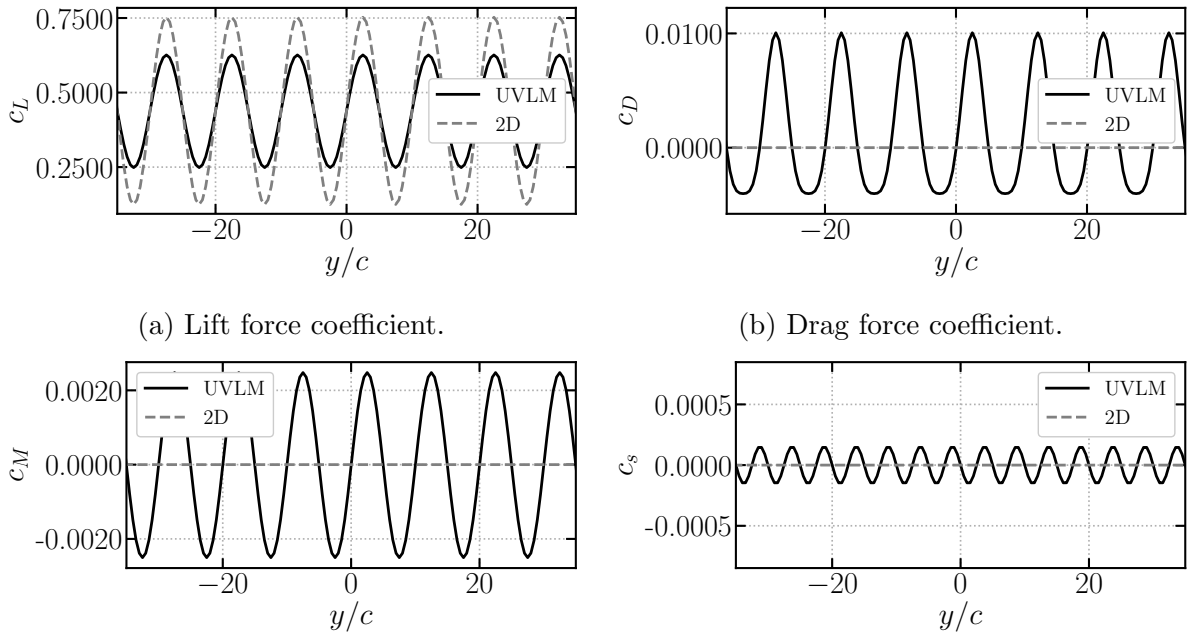

(a) Lift force coefficient.

(b) Drag force coefficient.

(c) Moment coefficient.

(d) Spanwise force coefficient.

Figure 4.8: Force coefficients under spanwise sine varying inflow. $\lambda = 10c$, $\alpha_0 = 4\,\text{deg}$ and $A = 0.1$ case.

$10c$ and by approximately 90% for wavelengths $\lambda = c$ with respect to the 2D approximation. Moreover, this effect is not influenced by the initial angle of attack (Figure 4.9a) or the inflow amplitude A (Figure 4.9b).

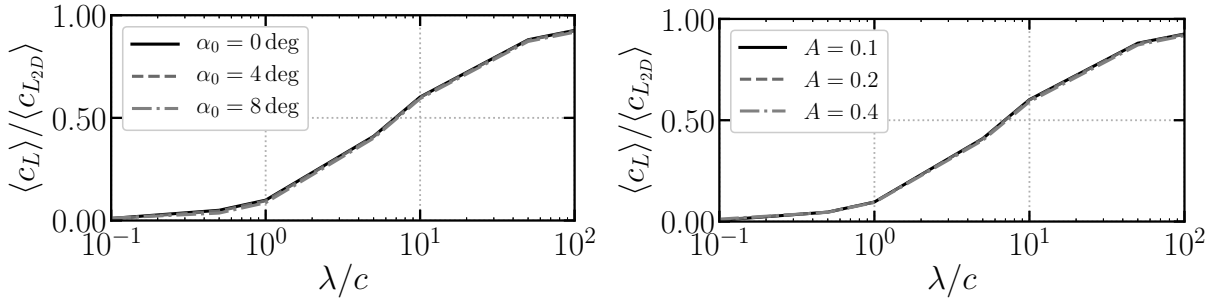

(a) Angle of attack effect. $A = 0.2$ case.

(b) Gust intensity effect. $\alpha_0 = 4\,\text{deg}$ case.

Figure 4.9: Peak-to-peak lift coefficient as a function of the spanwise sine varying inflow wavelength λ/c.

The numerical results in Figure 4.9 can be approximated by a second-order filter given

by a chord-normalised rational function H_c,

$$\frac{\mathfrak{c}_L(\lambda^{-1})}{\mathfrak{c}_{L_{2D}}(\lambda^{-1})} = H_c(\lambda^{-1}) = \frac{0.47}{(c\lambda^{-1})^2 + 3.3(c\lambda^{-1}) + 0.47}, \qquad \lambda > 0, \tag{4.11}$$

where

$$\mathfrak{c}_L(\lambda^{-1}) = \mathcal{F}\{c_L\}(\lambda^{-1}) = \int_{-\infty}^{\infty} c_L(y) e^{-2\pi i y \lambda^{-1}} dy, \qquad \lambda^{-1} > 0,$$

is the Fourier transform of c_L. This approximation has a root-mean square error of 9×10^{-3} and a maximum relative error of 7%. This suggests that the proposed spanwise filter can be applied to codes that assume 2D behaviour of blade sections (i.e. BEM). In particular, given the spanwise lift distribution $c_{L_{2D}}(y)$ computed with a 2D approximation, its filtered version $\tilde{c}_{L_{2D}}(y)$ is defined by

$$\tilde{c}_{L_{2D}}(y) = \mathcal{F}^{-1}\left\{H_c \mathcal{F}\{c_{L_{2D}}\}\right\}(y), \qquad y > 0.$$

In other words, the 2D approximation to the spanwise lift distribution is first transformed into instantaneous spatial frequencies, then filtered by $H_c(\lambda^{-1})$ and, finally, transformed back into the spatial domain. A numerical example on a full wind turbine rotor configuration is given in Section 4.2.3.

Some additional details of the implementation deserve some discussion. In particular, the filter function depends on the chord c which, in many applications, varies with span. It is possible to adapt the filter to this scenario by, first, computing the Fourier transformation of the lift distribution along the span. Then, for each of point y at which the filtered value of the lift distribution is to be obtained, the Fourier-transformed function is filtered using the chord at this location by using $H_{c(y)}$ in Equation (4.11). Afterwards, an inverse Fourier transformation is computed keeping only the value at the considered node and discarding the rest, that is $\mathcal{F}^{-1}\left\{H_{c(y)}\mathcal{F}\{c_{L_{2D}}\}\right\}(y)$. Usually, computational algorithms for the Fourier transformation require equi-spaced points. If known values of the lift distribution do not satisfy this property, then the lift distribution should be interpolated in a uniform grid at the beginning of the procedure, and subsequently interpolated back into the original grid.

A correction for the remaining force coefficients could be equally generated although their effect on loads would be less significant than lift. Moreover, higher fidelity simulations would be required to correct drag because UVLM does not provide a reference value. This exceeds the scope of this work but some results are shown next for completeness.

The average lift, moment and spanwise coefficients that appear on the UVLM approach

are zero for all wavelengths of the input (not shown). However, Figure 4.10 shows an average non-zero drag coefficient between 10^{-2} and 2×10^{-2} (100 and 200 drag counts, respectively), which is comparable to the usual drag value of airfoils. It reaches a maximum for wavelengths of the order of ten chords with larger value the larger the gust intensity (Figure 4.10b) but almost unaffected by the average angle of attack (Figure 4.10a).

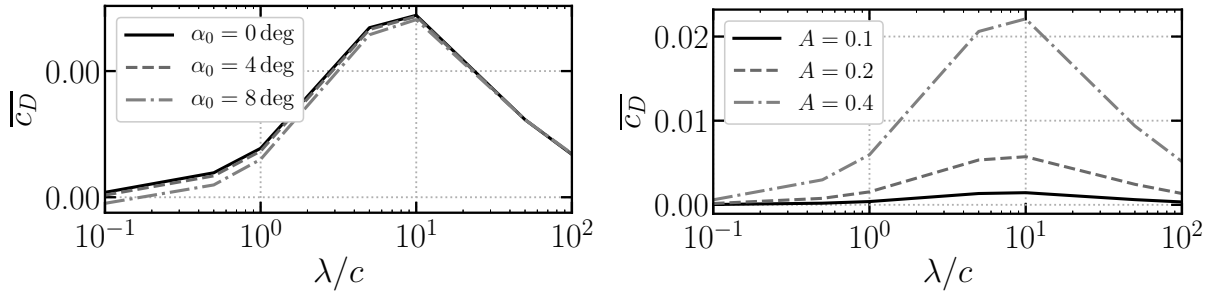

(a) Angle of attack effect. $A = 0.1$ case.

(b) Gust intensity effect. $\alpha_0 = 0\,\mathrm{deg}$ case.

Figure 4.10: Mean drag coefficient as a function of the spanwise sine varying inflow wavelength λ/c.

Similarly to Figure 4.9, the peak-to-peak drag, moment and spanwise coefficients are included in Figures 4.11, 4.12 and 4.13, respectively. The behaviour of the peak-to-peak drag coefficient is not well defined as a function of the wavelength because it depends on a balance between the average angle of attack (Figure 4.11a) and the gust intensity (Figure 4.11b). The peak-to-peak moment (Figures 4.12a and 4.12b) coefficient reaches the maximum for wavelengths of the order of 1 chord. The peak-to-peak spanwise (Figures 4.13a and 4.13b) coefficient decreases with the wavelength. These two coefficients are slightly affected by the initial angle of attack (Figures 4.12a and 4.13a) and they both increase with the gust intensity (Figures 4.12b and 4.13b). Their values are small but could be significant for certain airfoils.

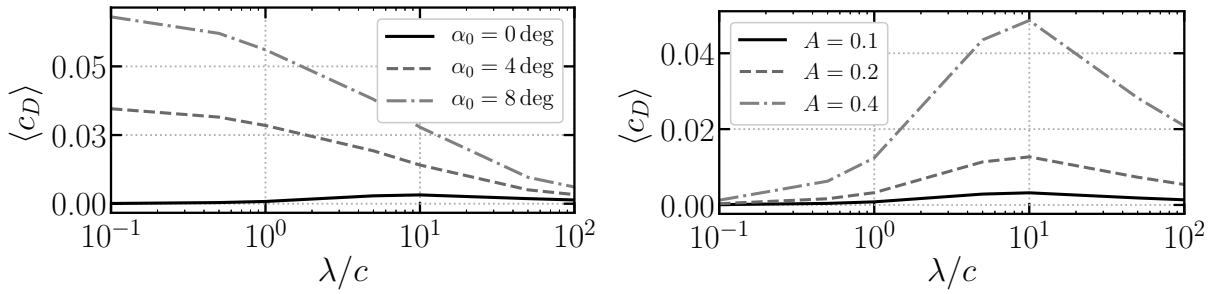

(a) Angle of attack effect. $A = 0.1$ case. (b) Gust intensity effect. $\alpha_0 = 0\,\mathrm{deg}$ case.

Figure 4.11: Peak-to-peak drag coefficient as a function of the spanwise sine varying inflow wavelength λ/c.

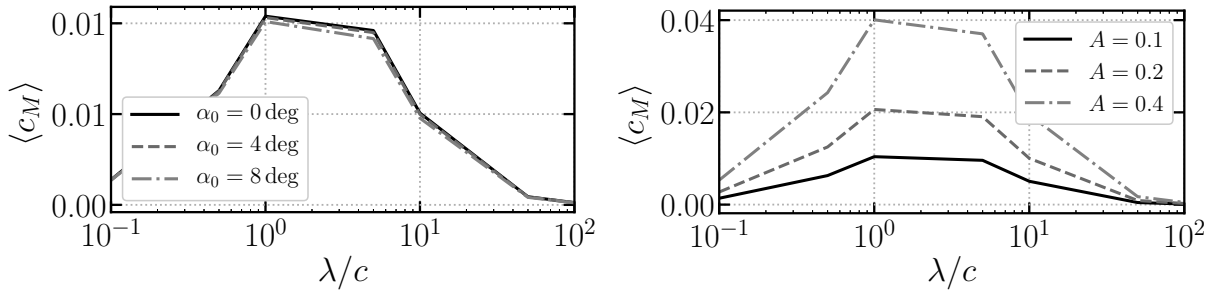

(a) Angle of attack effect. $A = 0.1$ case. (b) Gust intensity effect. $\alpha_0 = 0\,\mathrm{deg}$ case.

Figure 4.12: Peak-to-peak moment coefficient as a function of the spanwise sine varying inflow wavelength λ/c.

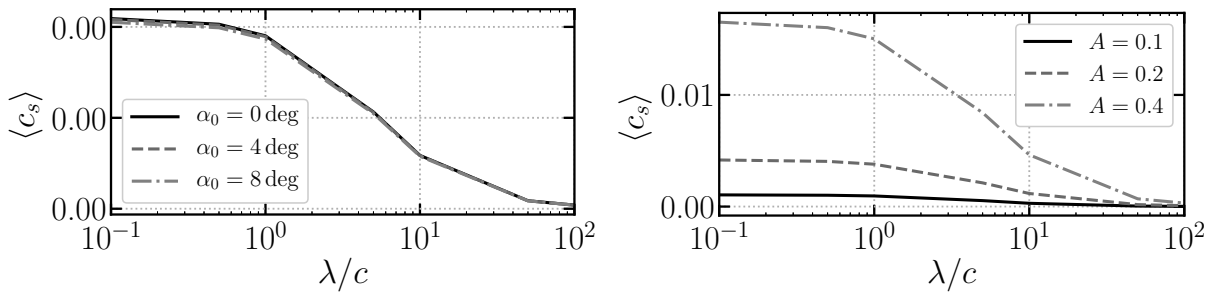

(a) Angle of attack effect. $A = 0.1$ case. (b) Gust intensity effect. $\alpha_0 = 0\,\mathrm{deg}$ case.

Figure 4.13: Peak-to-peak spanwise coefficient as a function of the spanwise sine varying inflow wavelength λ/c.

4.1.4 Turbulence generation

The three aerodynamic fidelities studied here treat the turbulent field differently: LES-AL fully simulates the most energetic scales of the turbulent field while BEM and UVLM rely

on the convection of a turbulence box based Taylor's hypothesis and not accounting for any interaction from the solid surfaces on the turbulence field. In Section 4.2.3, we benchmark the three aerodynamic fidelities under turbulent inflow. To achieve a fair comparison the turbulent field acting on the wind turbine in each fidelity has to be as similar as possible. Thus, in this section, we propose a procedure to generate turbulence boxes that reduce the uncertainty between different treatments of turbulence. The procedure combines the generation of turbulence from Mann boxes and the realistic turbulence fields of LES simulations. Two turbulence boxes, referred to as "higher turbulence" and "lower turbulence", generate the inflow for the three models (BEM, UVLM and LES-AL). The process to create these boxes is illustrated in Figure 4.15.

First, two random turbulence boxes are generated using the Mann box method [44], which controls the turbulence intensity. We use the numerical implementation of the Mann box method that comes as a pre-processing tool for the aeroelastic code `HAWC2` [161, 193, 55]. The input parameters are shown in Table 4.1 which are similar to other publications [59]. In particular, L_T is the largest characteristic length of turbulence. We use $L_\mathrm{T} = R$, being $R = 102.88\,\mathrm{m}$ the rotor radius of the wind turbine analysed in Section 4.2. Γ_T is the stretching parameter, N_x, N_y and N_z and Δx, Δy and Δz are the number of nodes and the grid size in the x, y and z directions, "seed" is the input for the random number generator and high frequency correction has been applied. The desired level of turbulence intensity I_T is defined through the combined parameter $\alpha_\mathrm{T}\epsilon^{2/3}$ where $\alpha_\mathrm{T} = 1.7$ is an empirical value and ϵ_T, the wind specific turbulence dissipation rate. This combined parameter is computed as

$$\alpha_\mathrm{T}\epsilon_\mathrm{T}^{2/3} = \frac{(U^\infty I_T)^2}{0.688 L^{2/3}}, \tag{4.12}$$

where U^∞ is the average wind speed perpendicular to the rotor.

Table 4.1: Mann box input parameters.

case name	$\alpha_\mathrm{T}\epsilon_\mathrm{T}^{2/3}$ [$\mathrm{m}^{1/3}\,\mathrm{s}^{-2}$]	L_T [m]	Γ_T	seed	N_x [-]	N_y [-]	N_z [-]	Δx [m]	Δy [m]	Δz [m]
higher turbulence	1.478	R	0	-100	1024	256	256	2	2	2
lower turbulence	0.894	R	0	-100	1024	256	256	2	2	2

Secondly, these Mann boxes have been separately used as input for an empty-box LES simulation (`WInc3D` [45]) with the objective of generating an energy spectrum closer to real flows. The empty LES box has a cell spacing of 2 m in a grid with dimensions $L_{e_x} = 4R$, $L_y = 8R$ and $L_z = 8R$.

The flow field statistics (mean, standard deviation, turbulence intensity and power spectrum $P(\boldsymbol{u})$ of the axial velocity $\boldsymbol{u}$) in each plane (characterised by the x coordinate) parallel to the rotor are computed at 17 points and averaged, i.e. the turbulence intensity at $x = 0\,\mathrm{m}$ is computed as

$$I_T\left(x=0\right) = \frac{1}{17}\sum_{i=1}^{17} I_T\left(x=0,i\right), \tag{4.13}$$

with i the index of the 17 points distributed in the $x = 0\,\mathrm{m}$ plane as described in Figure 4.14. The distribution of the 17 locations is as follows: one point in the rotation axis and 8 points each on the circumference of circles with radii $r = 0.5R$ and $r = R$ (with R the wind turbine rotor radius in Section 4.2.3) in azimuthal increments of 45 deg.

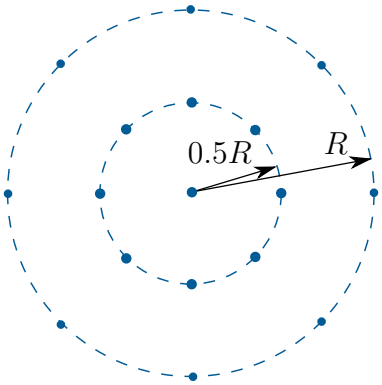

Figure 4.14: Distribution of points on a $y - z$ plane for the computation of flow statistics.

Simulations were run for 100 seconds, which was found to be sufficient to converge a moving average for the flow velocity and turbulence intensity at each plane, thus, to achieve steady state. After the transient period, 720 time steps (equivalent to one revolution in the example cases of Section 4.2.3) of the outflow were recorded and used as inflow for the following computations.

Due to the LES dissipation, the values of turbulence intensity are different at different x locations in the gird. Figure 4.16 shows the decay of turbulence within the empty LES grid. The $x = 0\,\mathrm{m}$ and $x = L_{e_x}$ locations show the power spectrum and turbulence intensity immediately after the Mann box and at the output of the LES domain, respectively. The latter represents the inflow for wind turbine rotor computations. Due to this turbulence decay, the desired turbulence intensity in Equation (4.12) has been increased by a factor of 2.5 obtained from preliminary studies.

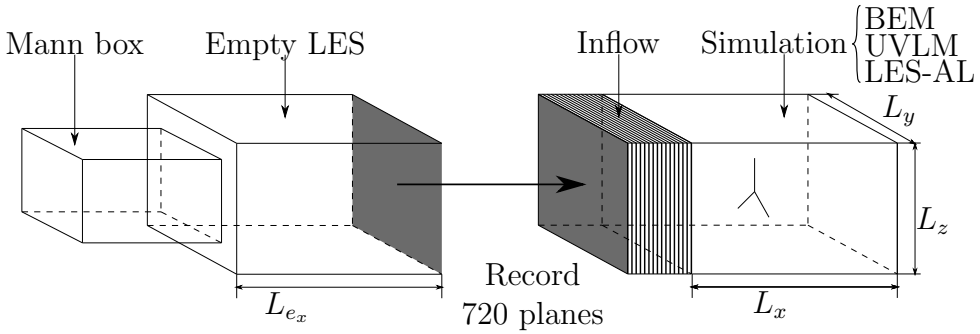

Figure 4.15: Scheme of the generation of the turbulent inflow for wind turbine simulations.

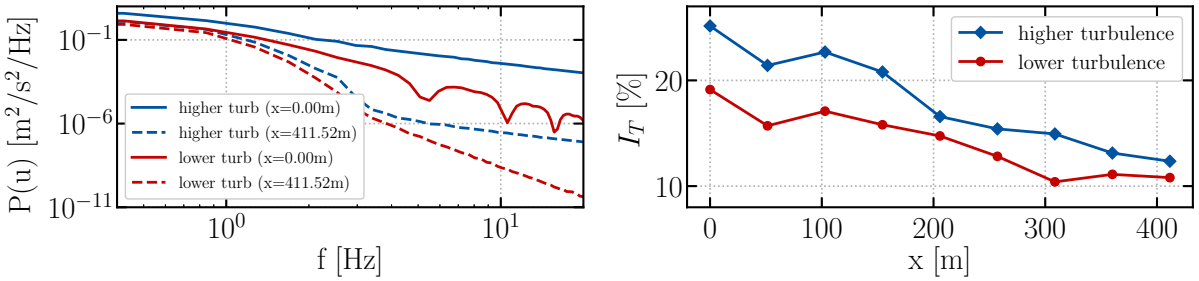

(a) Power spectral density.

(b) Turbulence intensity.

Figure 4.16: Turbulence decay along the first "empty" LES box.

Long turbulent inflow BEM and UVLM do not modify the inflow as it approaches the rotor, however, LES-AL does. The turbulent inflows generated before aimed to reduce these differences to perform a fair comparison among the three fidelities in the prediction of aerodynamic loads and to explain the physical reasons for the similarities and differences. Next, we describe the generation of a turbulent flow with a Mann box that is longer than the previous ones and aims to provide enough time to show statistically significant results. In this case, we choose the integral length scale of turbulence $L_\mathrm{T} = 29.4\,\mathrm{m}$ and the stretching parameter $\Gamma_\mathrm{T} = 3.9$ according to the IEC 61400 norm and a turbulence intensity of $I_T = 0.16$. The input parameters for the Mann turbulence box are gathered in Table 4.2. The wind axial velocity is shown in Figure 4.17.

Table 4.2: Mann box input parameters.

case name	$\alpha_\mathrm{T}\epsilon_\mathrm{T}^{2/3}$ [$\mathrm{m}^{1/3}\,\mathrm{s}^{-2}$]	L_T [m]	Γ_T	seed	N_x [-]	N_y [-]	N_z [-]	Δx [m]	Δy [m]	Δz [m]
long 01	0.431	29.4	3.9	-100	1024	128	128	2	2	2

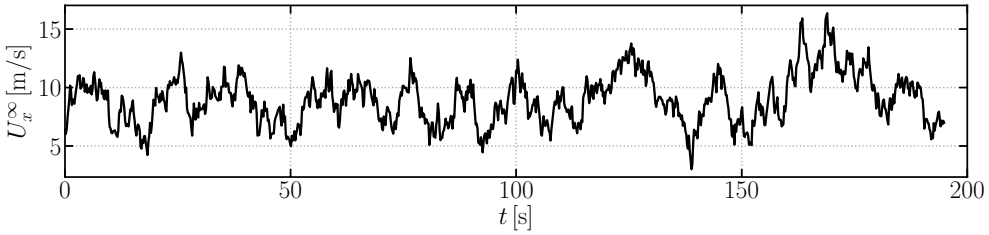

Figure 4.17: Wind axial component at hub height of the long turbulent inflow.

4.2 Benchmark of the three aerodynamic fidelities

In this section, the three aerodynamic fidelities (BEM, UVLM and LES-AL) are benchmarked on the AVATAR 10 MW rotor under three traditional inflow conditions: uniform inflow perpendicular to the rotor plane, yawed inflow and turbulent inflow. Moreover, the accuracy of the numerical improvements proposed in the previous Section 4.1 are evaluated. We evaluate the drag correction for UVLM and the free wake and prescribed wake models in UVLM under uniform flow perpendicular to the rotor plane (Section 4.2.1) where BEM is a very accurate reference case. We also describe the yaw aerodynamics and the accuracy of each fidelity under yawed inflow (Section 4.2.2). Finally, we use the turbulence generated in Section 4.1.4 to describe the unsteady character of the flow, to illustrate the effect of the spanwise filter we have generated for BEM and to benchmark the three aerodynamic models (BEM, UVLM and LES-AL) in Section 4.2.3. The average wind speed is $U^\infty = 10.5\,\mathrm{m/s}$, the rotor velocity is $\omega_\mathrm{r} = 0.945\,\mathrm{rad/s}$ and the collective blade pitch is zero. These cases do not include any control action to highlight the aerodynamic effects. We employ for the analysis the out-of-plane $F_\mathrm{out}(r)$ and in-plane $F_\mathrm{in}(r)$ forces along the spanwise direction r,

$$F_\mathrm{out} = L\cos\phi_\mathrm{f} + D\sin\phi_\mathrm{f}, \qquad \text{(3.9a revisited)}$$

$$F_\mathrm{in} = L\sin\phi_\mathrm{f} - D\cos\phi_\mathrm{f}. \qquad \text{(3.9b revisited)}$$

where $L(r)$ and $D(r)$ are the airfoil lift and drag forces, respectively and $\phi_\mathrm{f}(r)$ the flow angle. By dividing them by $\frac{1}{2}\rho\left(U^\infty\right)^2\pi R^2$ (ρ is the air density, U^∞ is the average inflow velocity and R is the wind turbine radius), we obtain the out-of-plane $c_\mathrm{out}(r)$ and in-plane $c_\mathrm{in}(r)$ force coefficients, respectively. The use of U^∞ instead of the relative wind velocity u_r makes the comparison between the three fidelities easier because the induced velocity is different in the three fidelities and very difficult to compute in UVLM and LES-AL. Their power spectral

densities $P(\bullet)$ are shown with respect to the reduced frequency

$$k = \frac{\omega c}{2u_r}, \tag{4.15}$$

where ω is the associated circular frequency, $c(r)$ is the airfoil chord and $u_r(r)$ is the local relative velocity between the flow and blade sections. As described in Section 3.3 we also employ the rotor thrust C_T and power C_P coefficients.

4.2.1 Uniform inflow

The ideal uniform steady wind perpendicular to the rotor plane generates steady loading along a revolution and is, therefore, an appropriate case with which to establish a baseline comparison. BEM is very accurate in this scenario [13, 14] because the flow is steady and there is low interaction between mid-span radial sections due to the blade optimally designed for this case. The spanwise interactions that appear at the blade root and tip regions are adequately corrected by the Prandtl tip correction. Thus, BEM will be considered as the reference in this section to evaluate the performance of UVLM and LES-AL. We start with an analysis of the UVLM modelling options and then we benchmark the three aerodynamic fidelities. In these simulations, the average wind speed is $U^\infty = 10.5\,\mathrm{m/s}$, the rotor velocity is $\omega_\mathrm{r} = 0.945\,\mathrm{rad/s}$ and the collective blade pitch is zero.

Effect of the UVLM drag correction and the UVLM wake models

In regular operation, the flow angle at the outboard section of the blade is not larger than 20 deg and lift is two orders of magnitude larger than drag. It follows that lift provides the dominant contribution to the out-of-plane force, while the in-plane force's behaviour is dependent upon both lift and drag contributions (Equation (3.9) revisited in Section 4.2).

We study the simulation results of the AVATAR wind turbine under uniform inflow. First, we describe the differences between the prescribed and free UVLM wake models in Figure 4.18 and Table 4.3. In general, there are very small differences in the out-of-plane force coefficient between all the cases (Figure 4.18a) with two exceptions. First, UVLM with both wake models overpredicts the out-of-plane force coefficient with respect to BEM in the blade root region ($r < 0.25R$) where UVLM is not valid due to the separated flow. Second, in the blade tip region ($r > 0.8R$) there is a very small difference between UVLM and BEM that is associated with the tip losses that are inherently captured by UVLM and modelled by BEM. The balance between these contributions results in a better agreement of

the rotor thrust coefficient between UVLM and BEM when the free wake is applied (Table 4.3). However, it is important to understand these effects separately. The free wake model reduces the rotor thrust and power coefficients in 3% and 5%, respectively, in comparison with the prescribed wake approximation. Then, it can be observed that the free wake agrees better with the BEM estimation.

The UVLM prescribed wake approximation slightly overpredicts the in-plane force coefficient. The viscous drag correction in UVLM explained in Section 4.1.1 does not significantly modify the out-of-plane force coefficient (Figure 4.18a) or the rotor thrust coefficient (Table 4.3). However, this drag correction significantly reduces the in-plane force coefficient (Figure 4.18b) and it reduces the rotor power coefficient, around 8% (Table 4.3). When the drag correction is included in free-wake UVLM, the agreement with BEM is very good especially in the span region $r > 0.6R$.

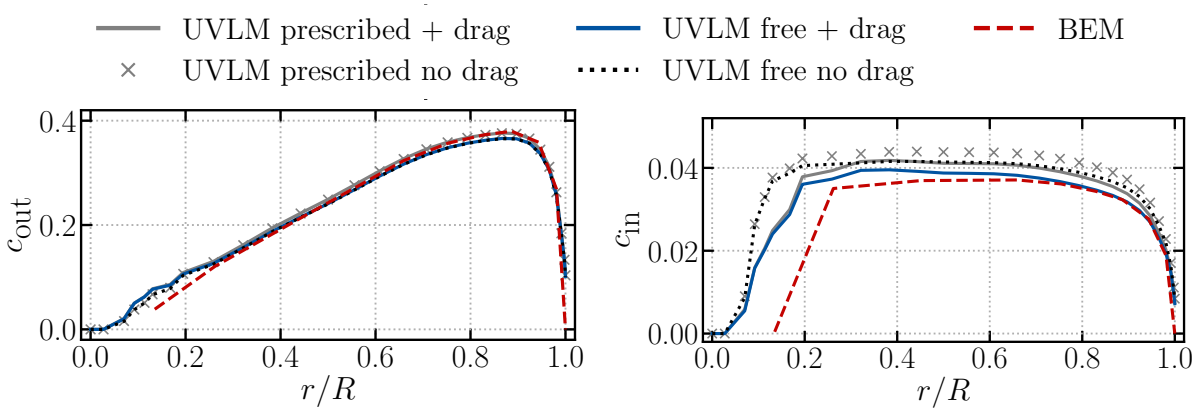

(a) Out-of-plane force coefficient.

(b) In-plane force coefficient.

Figure 4.18: Force coefficients along the span under uniform inflow. UVLM modelling options.

Table 4.3: Rotor thrust and power coefficients under uniform inflow.

aerodynamic model	wake model	drag accounted for	C_T	C_P
UVLM	free	No	0.66	0.52
UVLM	free	Yes	0.66	0.48
UVLM	prescribed	Yes	0.68	0.50
UVLM	prescribed	No	0.68	0.55
BEM	-	Yes	0.66	0.45
LES-AL	-	Yes	0.66	0.46

Benchmark

In conclusion, UVLM with a free wake and the drag correction described in Section 4.1.1 provides better agreement with BEM for cases of uniform flow perpendicular to the rotor plane than the other set-ups of UVLM. Thus, it is compared alone with the other two aerodynamic fidelities (BEM and LES-AL) in Figure 4.19. In general, the agreement between the fidelities is good. UVLM slightly overestimates the loads in the root region $r < 0.25R$ with respect to BEM and LES-AL, due to the separated flow. In the tip region $r > 0.8$, UVLM slightly underestimates the out-of-plane force coefficient with respect to BEM. In the tip region, three-dimensional effects appear that should be captured by UVLM and the Prandtl tip-correction in BEM, discerning which one is the accurate requires more precise studies, such as RANS. Nevertheless, this difference is very small. Finally, LES-AL agrees very well with BEM except in the tip region $r > 0.9R$ where it overestimates the force coefficients. This might be related to a lack of refinement of the LES grid in this region that was too computationally expensive to achieve because our LES solver uses uniform grids which imply meshing the whole domain with smaller cells. We considered that the computational cost was not justified due to the small differences observed.

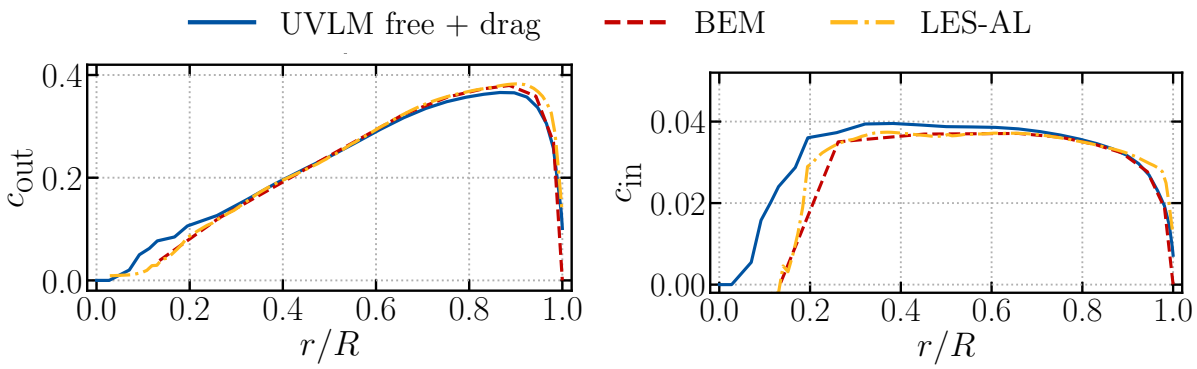

(a) Out-of-plane force coefficient

(b) In-plane force coefficient

Figure 4.19: Benchmark force coefficients along the span under uniform inflow.

4.2.2 Yawed inflow

Historically, misalignment between the rotation axis and the mean wind speed direction (yaw) was not expected in typical operation and only associated to small errors in the aligning mechanism (some certification load cases include large yaw error). However, larger yaw angles are expected in future wind turbines due to emerging wind farm control strategies

which attempt to voluntarily operate wind turbines in large yaw angles to reduce the influence of the wake on the downstream turbines [194].

The aerodynamic forces on wind turbine blades operating in yaw can be explained by addition of the skewed-wake and the advancing/retreating effects. These effects are studied first under a 30 deg yaw inflow. This yaw angle is large for traditional operation but is likely to be experienced in cases of wind farm control. Next, the aerodynamic fidelities are compared at smaller angles of attack to define a range of validity for each one of them. In the previous Section 4.2.1, BEM was considered the reference and we showed that also UVLM (with the drag correction) and LES-AL are accurate. However, in cases of yaw unsteady and three-dimensional aerodynamic effects are expected to be relevant, thus, UVLM and LES-AL are considered of reference because they inherently capture these effects.

Unsteady BEM models are used here because they are required to account for the blade loading unsteadiness. Moreover, the non-symmetry of the wake behind the wind turbine in cases of yaw is not accounted for by the basic BEM theory described in Section 2.2.2 (labelled as "BEM no skew" in the following analysis). There are empirical corrections to include these effects on BEM such as the Pitt and Peters model that will be employed here (labelled as "BEM skew"). The results in this section include the UVLM drag correction described in Section 4.1.1 which was not included in the original publication by the authors [191]. In these simulations, the average wind speed is $U^\infty = 10.5\,\mathrm{m/s}$, the rotor velocity is $\omega_\mathrm{r} = 0.945\,\mathrm{rad/s}$, the collective blade pitch is zero and the time step is equivalent to $\Delta\theta = 0.5\,\mathrm{deg}$ (0.0092 s).

Rotor aerodynamics in extreme yaw ($\gamma = 30\,\mathrm{deg}$)

The extreme case of $\gamma = 30\,\mathrm{deg}$ has been chosen to make the aerodynamic effects associated to the yaw inflow obvious. Figure 4.20a shows a top view of a turbine under a γ yaw angle (positive as shown on the image) between the rotation axis and the inflow wind velocity U^∞ on the horizontal plane. Moreover, Figure 4.20b shows a front view in which the azimuthal angle θ, the rotation velocity ω_r and the initial position are shown. The first blade (at $\theta = 0\,\mathrm{deg}$ in Figure 4.20b) is the blade whose forces are shown on the rest of this section.

In yaw cases, the forces along a revolution under uniform inflow are not constant and, thus, time series are shown below. However, we start with the average along a revolution $\bar{\bullet}$ of the out-of-plane and in-plane force coefficients in Figures 4.21a and 4.21b, respectively. There is a good agreement between UVLM and LES-AL for both coefficients. The agreement

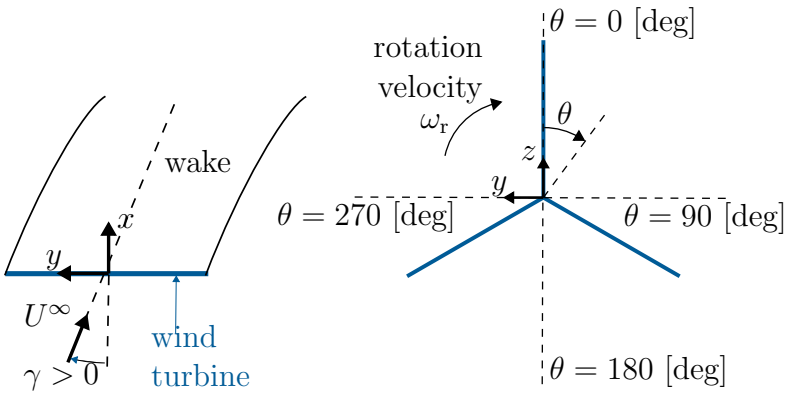

(a) Top view. (b) Front view.

Figure 4.20: Scheme of yawed inflow on a wind turbine.

of BEM with the other fidelities is good in the mean out-of-plane force coefficient (Figure 4.21a) but BEM underpredicts the in-plane force coefficient with respect to the other fidelities (Figure 4.21b). The mean force coefficients predicted by BEM with and without skewed-wake model are the same because the skewed-wake model assumes sinusoidal fluctuations around the average value, thus, the differences between these two models shown in the rest of this section average out along a revolution (Figure 4.21).

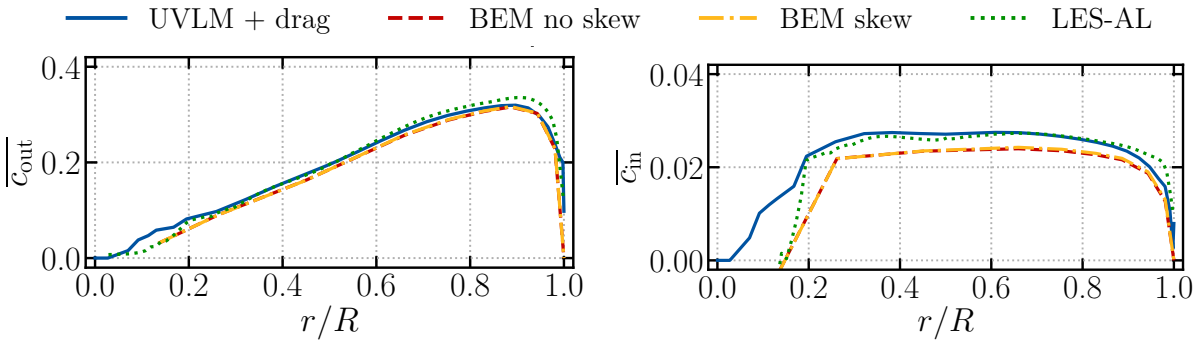

(a) Out-of-plane force coefficient. (b) In-plane force coefficient.

Figure 4.21: Mean force coefficients along the span ($\gamma = 30\,\text{deg}$).

The mean in-plane and out-of-plane force coefficients in the case of 30 deg yaw (Figure 4.21) are significantly smaller than those of the zero-yaw case (Figure 4.19). These differences are shown in Table 4.4 through the mean rotor thrust and power coefficients: the reduction in rotor thrust and power coefficients with the yaw angle predicted by UVLM and LES-AL are in good agreement and they are significantly smaller than those predicted by BEM *no*

skew and BEM *skew*.

Table 4.4: Differences in mean rotor thrust and power coefficients between the 30 deg yaw and the zero-yaw cases for each aerodynamic model.

	$\overline{C_T}$	$\overline{C_P}$
UVLM	-15%	-27%
BEM *no skew*	-20%	-35%
BEM *skew*	-20%	-35%
LES-AL	-16%	-27%

Yaw inflow has some unsteadiness associated to blade rotation because the relative orientation between the inflow and the blade changes along a revolution. In this case the reduced frequencies in Equation (4.15) for the airfoils at $r = 0.45R$ and $r = 0.75R$ are 0.055 and 0.022 (Table 4.5), respectively. Thereby, wind turbine loads under yaw can be reasonably approximated by a quasi-steady assumption and the Unsteady BEM model described in Section 4.2.2 does not predict significantly different loads to the BEM model in the studied cases. We keep using the dynamic corrections throughout this section.

Table 4.5: Reduced frequency associated to yaw at two spanwise positions. AVATAR 10 MW.

r/R	0.45	0.75
k	0.055	0.022

Yaw inflow also generates three dimensional effects (tip and root ends, azimuthal variations of induction and interaction between radial sections) which are only inherently accounted for by UVLM according to Section 2.2. LES-AL also accounts for some of these three dimensional effects, but it employs a two-dimensional approximation for the computation of aerodynamic loads. These three-dimensional effects generate varying loads along a revolution in yaw cases (as opposed to the $\gamma = 0$ deg case) that can be explained through the interaction between two effects [33]: the advancing/retreating effect and the skewed-wake effect. The best way to show these effects is by looking at different spanwise positions on the blade analysing how loads change along a revolution. This is done for two radial positions ($r = 0.75R$ and $r = 0.45R$) in Figures 4.22 and 4.24, respectively.

The skewed-wake effect accounts for the non-axisymmetric velocity deficit behind a wind turbine in yaw (Figure 4.20a). As a consequence, blades travel through regions of varying velocity deficit which generates oscillating induction along a revolution. In particular, the maximum loading is experienced when blades are in the upwind position ($\theta = 270$ deg),

and the minimum loading, when they are in the downwind position ($\theta = 90\,\text{deg}$). The oscillations along a revolution are stronger near the tips and thus this effect is more important in the outer part of the blade. We show the force coefficients at $r = 0.75R$ in Figure 4.22. First, BEM *no skew* lacks a wake model to capture the induction change along a revolution and, thus, it predicts incorrect locations of maximum and minimum loading which are incorrectly predicted at $\theta = 180\,\text{deg}$ and $\theta = 0\,\text{deg}$ azimuth locations. When the skewed-wake model is applied to BEM (BEM *skew*) it is able to reproduce the correct locations of the maxima and minima according to the previous explanation of the skewed-wake effect around $\theta = 270\,\text{deg}$ and $\theta = 90\,\text{deg}$ azimuth locations, respectively. However, BEM *skew* leads to larger fluctuations of the force coefficients compared to UVLM and LES-AL. UVLM can inherently account for unsteady and three-dimensional physics needed to capture the skewed-wake effect and LES-AL accounts for the flow unsteadiness and three-dimensional effects but it is not clear the influence of using steady-state tabulated data to retrieve the blade forces from the flow velocity. To quantify these fluctuations, we use the standard deviation along a revolution of the out-of-plane force coefficient at $r = 0.75R$ which is 52% and 23% smaller in UVLM and LES-AL, respectively, with respect to the BEM *skew* prediction.

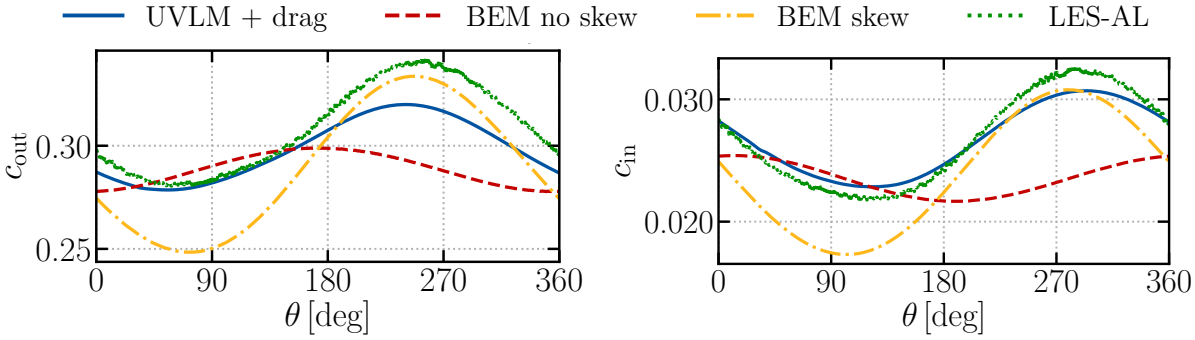

(a) Out-of-plane force coefficient.

(b) In-plane force coefficient.

Figure 4.22: Azimuthal variations of loads at $r = 0.75R$ ($\gamma = 30\,\text{deg}$).

The advancing/retreating effect accounts for the change in angle of attack along a revolution due to the change in relative orientation between the blade and the incoming wind. Figure 4.23 shows an scheme of this effect including the blade relative velocities for the zero-yaw case (Figure 4.23a) that do not change along a revolution and the blade relative velocities in a case of yaw for two blade azimuthal positions: $\theta = 0\,\text{deg}$ and $\theta = 180\,\text{deg}$ in Figures 4.23b and 4.23c, respectively. For example, at the top position (for positive yaw angles) the relative velocity due to blade rotation ($\omega_r r$) is in the opposite direction as the

in-plane component of the incoming wind $U^\infty \sin(\gamma)$ which increases the angle of attack (Figure 4.23b) with respect to the reference case (Figure 4.23a). At the bottom position $\theta = 180\,\text{deg}$ (Figure 4.23c), the effect is the opposite. The advancing/retreating effect generates maximum and minimum angle of attack at $\theta = 0\,\text{deg}$ and $\theta = 180\,\text{deg}$ with $\gamma > 0$. The advancing/retreating effect is less noticeable near the tip, since the velocity of the blade due to rotation is dominant there ($\omega_r r \gg U^\infty \sin(\gamma)$). However, this effect is dominant in the inboard region, thus, we show the out-of-plane and in-plane force coefficients at $r = 0.45R$ in Figure 4.24. UVLM, BEM *no skew* and LES-AL predict coherent locations of maxima and minima according to the previous theory for the in-plane force coefficient (Figure 4.24b) but not in the out-of-plane force coefficient (Figure 4.24a) whose variations are, nonetheless, very small.

The advancing/retreating effect is quasi-steady (Table 4.5) and should be captured by all the numerical methods. However, BEM *skew* does not capture it (Figure 4.24). The skewed-wake model was tuned to capture the effect near the tip and, inconveniently, this skewed-wake model extends beyond its real influence region (the outer part of the blade) leading to the incorrect location of the maximum and minimum loading predicted by the BEM *skew* model in the inboard region ($r = 0.45R$). Probably, this choice was made because the root-bending moments are the variable used for load design of wind turbines and, to accurately compute them, the contributions of the outer part of the blade force coefficients are more relevant than those of the root region.

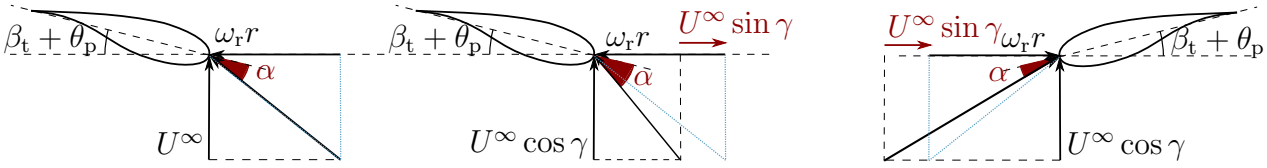

(a) Zero yaw (constant with θ).

(b) Yaw, top position ($\theta = 0\,\text{deg}$).

(c) Yaw, bottom position ($\theta = 180\,\text{deg}$).

Figure 4.23: Scheme of the advancing/retreating effect in yaw cases with respect to the zero yaw case.

Figures 4.22 and 4.24 have shown the aerodynamic force coefficients at local $r = 0.75R$ and $r = 0.45R$ spanwise positions, respectively, to investigate yaw aerodynamics in some detail. However, in load analysis it is more common to use the integration of these coefficients along the blade, namely the root-bending moments (M_{out} and M_{in}). In this integration, the tip region is the most important contributor and thus, the location of maximum and

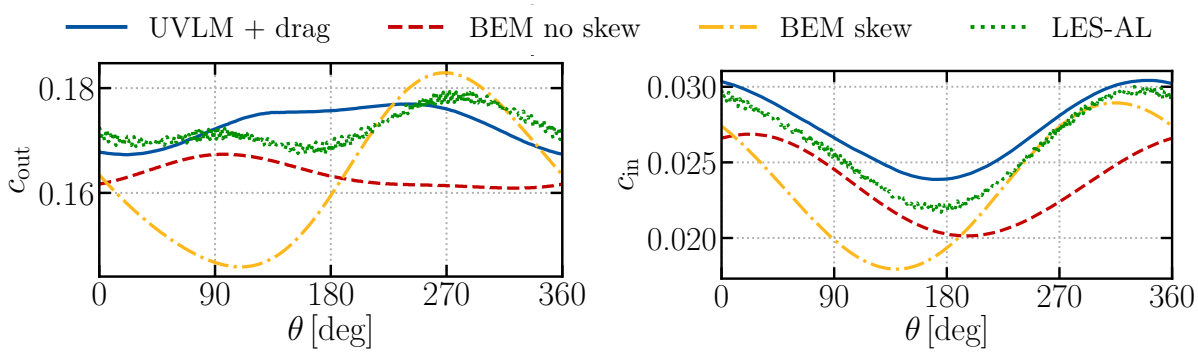

(a) Out-of-plane force coefficient.

(b) In-plane force coefficient.

Figure 4.24: Azimuthal variations of force coefficients at $r = 0.45R$ ($\gamma = 30\,\text{deg}$).

minimum root-bending moments along a revolution (Figure 4.25) follows a similar pattern as the force coefficients in the outboard region (Figure 4.22). Specifically, the minimum and maximum root-bending moments should appear at positions close to $\theta = 90\,\text{deg}$ and $\theta = 270\,\text{deg}$, respectively. Figure 4.25 shows that UVLM, BEM *skew* and LES-AL methods are able to capture these positions, however, the variations predicted by the BEM *skew* model are very large (Table 4.6). Finally, BEM *no skew* provides the wrong positions because it does not account for the skewed-wake effect that dominates in the outer part of the blade which is the main contributor to the root bending moments.

Table 4.6: Differences in root-bending moments' standard deviation between each fidelity and BEM *skew*.

	$\sigma\,(M_{\text{out}})$	$\sigma\,(M_{\text{in}})$
UVLM	−52%	−34%
BEM	−75%	−59%
BEM *skew*	0%	0%
LES-AL	−28%	−16%

Finally, the rotor integrated coefficients of thrust (C_T) and power (C_P) provide a simple metric to define the rotor operating state (Figure 4.26). The maximum difference in mean thrust coefficient between solvers has changed from 0.6% in the case of $\gamma = 0\,\text{deg}$ to 7% in the case of $\gamma = 30\,\text{deg}$ due to the differences in the yaw aerodynamic modelling explained in this section. Moreover, in the case of $\gamma = 0\,\text{deg}$ UVLM already predicts 3% higher mean C_P than the other solvers. However, in the case of $\gamma = 30\,\text{deg}$ yaw, UVLM and LES-AL predict even higher mean C_P than BEM (15%) due to the different modelling accuracy of yaw aerodynamics. This evidences that in cases of uniform inflow all fidelities

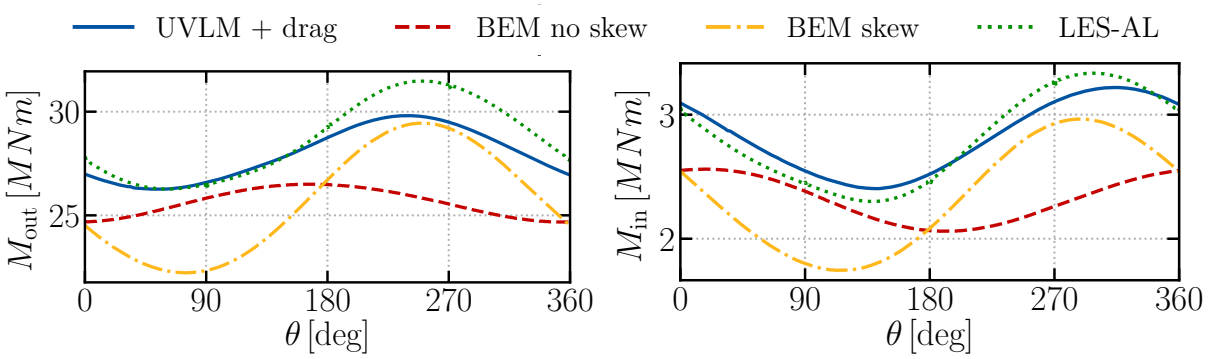

(a) Out-of-plane root-bending moment. (b) In-plane root-bending moment.

Figure 4.25: Azimuthal variations of root-bending moments ($\gamma = 30\,\text{deg}$).

perform well. However, in yaw cases more aerodynamic relevant effects appear, such as, the advancing/retreating and skewed-wake effects that require complex models to accurately capture them (UVLM and LES-AL). Finally, Figure 4.26 shows that the large fluctuations along a revolution of local force coefficients showed in Figures 4.24 and 4.22 have almost disappeared in the case of rotor coefficients due to the balancing effect between the three blades.

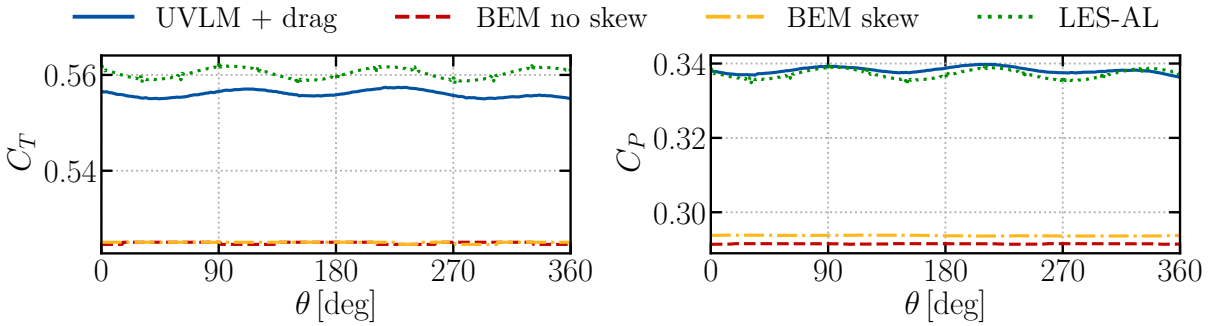

(a) Rotor thrust coefficient. (b) Rotor power coefficient.

Figure 4.26: Azimuthal variations of rotor thrust and power coefficients ($\gamma = 30\,\text{deg}$).

In this section we show that computational methods need to account for three dimensional effects to capture the local behaviour of loads under yaw, which is the case for UVLM and LES-AL. This behaviour is noticeable in the mean root-bending moments and rotor coefficients. It is also relevant in the oscillations of the root-bending moment coefficients but not in the oscillations of the rotor coefficients because they are significantly reduced by the balancing between the three blades.

Rotor aerodynamics as a function of the yaw angle ($0\,\text{deg} \leq \gamma \leq 30\,\text{deg}$)

In the previous section, the effect on loads of the extreme case of 30 deg yaw was analysed. This section aims to analyse the effect of milder yaw angles. To reduce the amount of data presented, this will be achieved via analysis of several statistics: the mean $\overline{\bullet}$ and standard deviation $\sigma(\bullet)$ of fluctuations and the position of maximum $\theta(\bullet)_{\max}$ and minimum $\theta(\bullet)_{\min}$ loading along a revolution. As in the previous section, loads at two spanwise positions ($r = 0.45R$ and $r = 0.75R$), root-bending moments and rotor coefficients are studied.

Figure 4.27 shows the statistics for the out-of-plane force coefficient at $r = 0.45R$ spanwise position. The small changes in out-of-plane coefficient at $r = 0.45R$ shown in Figure 4.24a make the minimum $\theta(c_{\text{out}})_{\min}$ and maximum locations $\theta(c_{\text{out}})_{\max}$ difficult to distinguish (Figures 4.27a and 4.27b, respectively). These small changes also lead to a good agreement of the methods in mean values of the out-of-plane force coefficient (Figure 4.27c). BEM *skew* model that predicts significantly larger standard deviation than the others (Figure 4.27d) due to the excessive influence of the skewed-wake model.

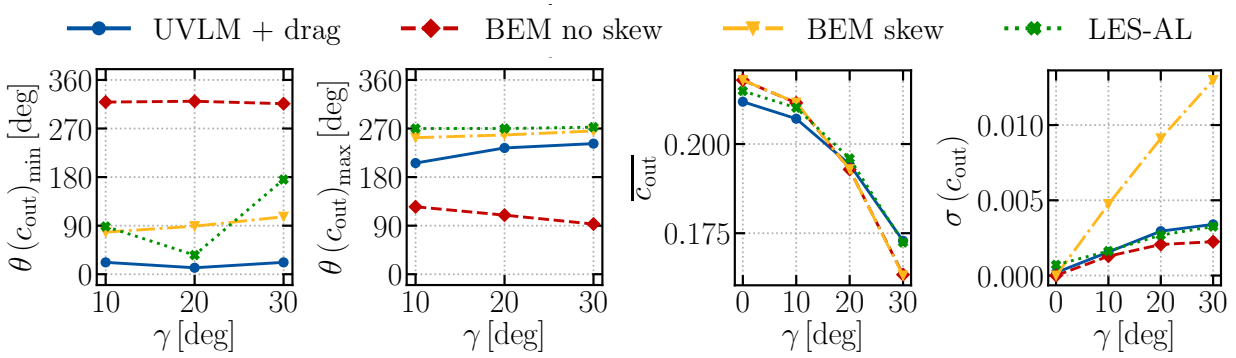

(a) Minimum position. (b) Maximum position. (c) Mean. (d) Standard deviation.

Figure 4.27: Yaw effect on the out-of-plane force coefficient at $r = 0.45R$.

Figure 4.28 shows the statistics for the in-plane force coefficient at $r = 0.45R$ spanwise position. In this region, the advancing/retreating effect is dominant, thus, the azimuthal location of the minimum and maximum in-plane force coefficient should be around $\theta = 180\,\text{deg}$ (Figure 4.28a) and $\theta = 360\,\text{deg}$ (Figure 4.28b), respectively. These locations are well captured by all the solvers. There is a difference in the mean in-plane force coefficient at zero-yaw (Figure 4.28c) between UVLM and the rest of the solvers of 3%. For larger yaw angles, the reduction of the mean in-plane force coefficient is stronger in both BEM estimations than in UVLM and LES-AL. The difference between the in-plane force coefficient at $\gamma = 30\,\text{deg}$ and $\gamma = 0\,\text{deg}$ is 29% in UVLM and LES-AL and 36% in both BEM models. Again, UVLM

and LES-AL agree well on the standard deviation but BEM *skew* overestimates the standard deviation (Figure 4.28d).

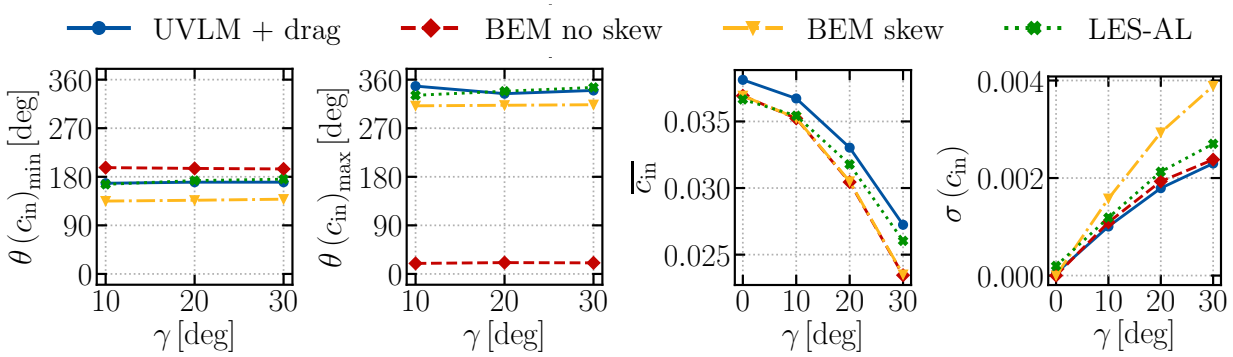

(a) Minimum position. (b) Maximum position. (c) Mean. (d) Standard deviation.

Figure 4.28: Yaw effect on the in-plane force coefficient at $r = 0.45R$.

Figures 4.29 and 4.30 show the out-of-plane and in-plane force coefficients at $r = 0.75R$. At this position, the skewed-wake effect is dominant over the advancing/retreating effect and the minimum and maximum location of the force coefficients (Figures 4.29a, 4.29b, 4.30a, 4.30b) are around $\theta = 90\,\text{deg}$ and $\theta = 270\,\text{deg}$, respectively, except from, BEM *no skew* that does not capture this effect. Again, we observe a decrease of the mean out-of-plane (Figure 4.29c) and in-plane (Figure 4.30c) force coefficients with the yaw angle which is stronger for both BEM than UVLM and LES-AL. Finally, BEM *skew* always predicts the largest fluctuations along a revolution of the out-of-plane (Figure 4.29d) and in-plane force coefficients (Figure 4.30d), and BEM *no skew* the smallest.

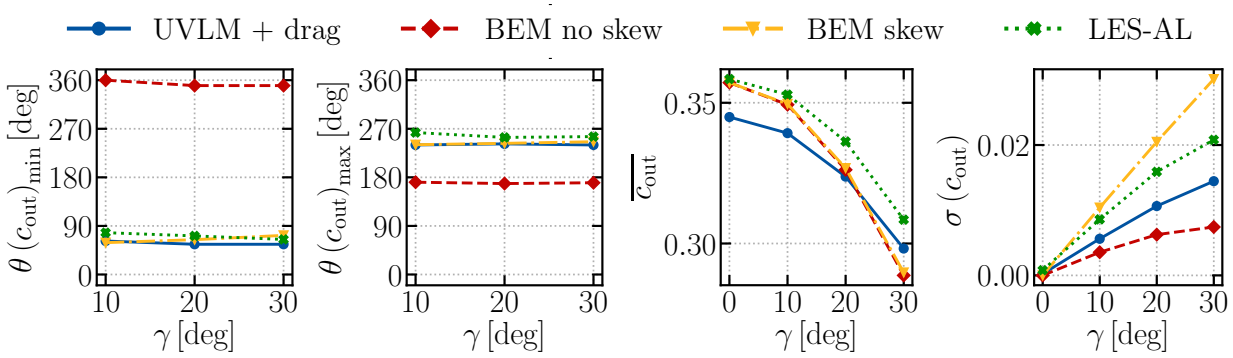

(a) Minimum position. (b) Maximum position. (c) Mean. (d) Standard deviation.

Figure 4.29: Yaw effect on the out-of-plane force coefficient at $r = 0.75R$.

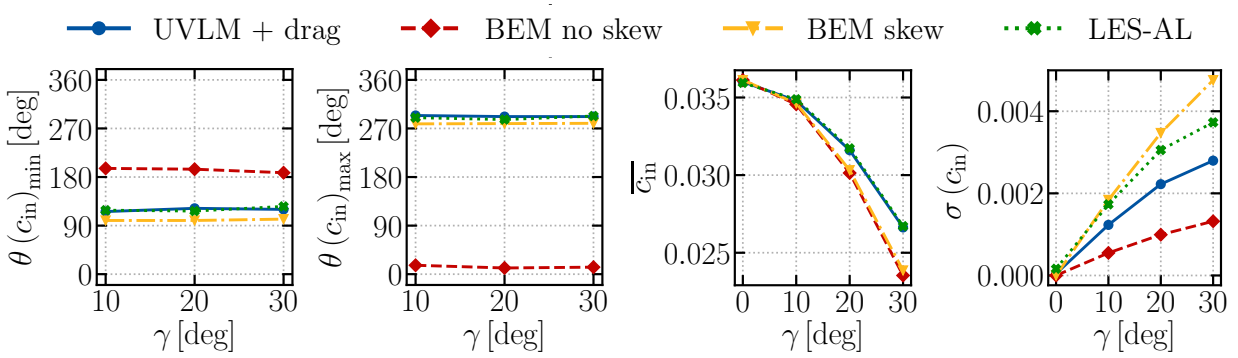

(a) Minimum position. (b) Maximum position. (c) Mean. (d) Standard deviation.

Figure 4.30: Yaw effect on the in-plane force coefficient at $r = 0.75R$.

The integration of the out-of-plane and in-plane force coefficients along the span give rise to the out-of-plane and in-plane root-bending moments shown in Figures 4.31 and 4.32, respectively. The minimum and maximum out-of-plane and in-plane force coefficient occur at $\theta = 90\,\mathrm{deg}$ (Figures 4.31a and 4.32a) and $\theta = 270\,\mathrm{deg}$ (Figures 4.31b and 4.32b), respectively, showing the dominance of the skewed-wake effect that generates maximum and minimum loading at these positions. The maximum and minimum do not occur exactly at these azimuthal locations because there are second-order effects (like the advancing/retreating effect) that slightly displace them. UVLM and LES-AL predict 3% and 6% higher mean out-of-plane root-bending moment (Figure 4.31c) than the two BEM models at zero-yaw angle. At 10 deg yaw angle, those differences are still similar. Moreover, at 30 deg yaw angle, those differences increase to 8% and 12%, respectively. This indicates that both BEM predict quicker reduction of the mean out-of-plane root-bending moment than UVLM and LES-AL which are more trustworthy because they capture the unsteady and three-dimensional effects associated to yaw. The mean in-plane root bending moment is smaller than the out-of-plane one and, thus, less important for wind turbine loading. It presents similar reduction with the yaw angle for all solvers (Figure 4.32c). Again, the largest fluctuations in out-of-plane (Figure 4.31d) and in-plane (Figure 4.32d) root-bending moments are predicted by BEM *skew* and the smallest by BEM *no skew*.

Finally, Figure 4.33 shows the effect of yaw on rotor coefficient. The agreement in the mean thrust coefficient (Figure 4.33a) for yaw angles below 10 deg is very good for all models. For larger yaw angles, the decrease of thrust predicted by both BEM methods is overly large compared to UVLM and LES-AL: at 30 deg yaw, both BEM models predict a decay of 20% with respect to the zero-yaw case while UVLM and LES-AL predict 15% and 16% decrease

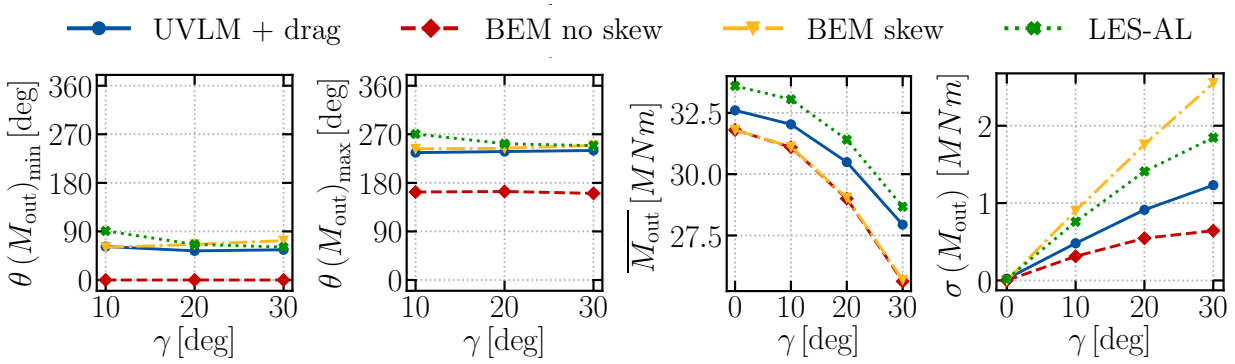

(a) Minimum position. (b) Maximum position. (c) Mean. (d) Standard deviation.

Figure 4.31: Yaw effect on the out-of-plane root-bending moments.

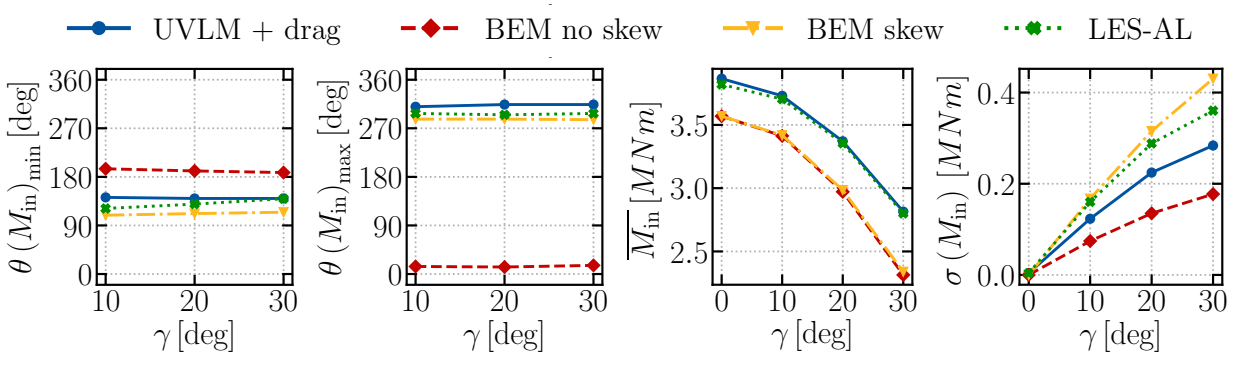

(a) Minimum position. (b) Maximum position. (c) Mean. (d) Standard deviation.

Figure 4.32: Yaw effect on the in-plane root-bending moments.

with respect to the zero-yaw case, respectively. In the case of the mean power coefficient (Figure 4.33c) below 10 deg of yaw, there is a small but constant difference between both BEM and UVLM and LES-AL. For larger yaw angles, the reduction predicted by BEM is again larger than UVLM and LES-AL. It is important to point out that these coefficients imply an important averaging effect and, consequently, their standard deviation is very small (Figures 4.33b and 4.33d). It is small enough to evidence the numerical noise in UVLM and LES-AL in the case of $\gamma = 0$ deg which should be exactly zero. It is interesting that, albeit small, UVLM and LES-AL predict larger fluctuations along a revolution. All the models agree on predicting a significant increase of the fluctuations for very high yaw angles ($\gamma \geq 20$ deg).

In this section we have described the aerodynamics of wind turbines in yaw through the skewed-wake and advancing/retreating effect. At zero-yaw we trust BEM models that have been calibrated for this case in the last few decades. In this scenario, we have shown small

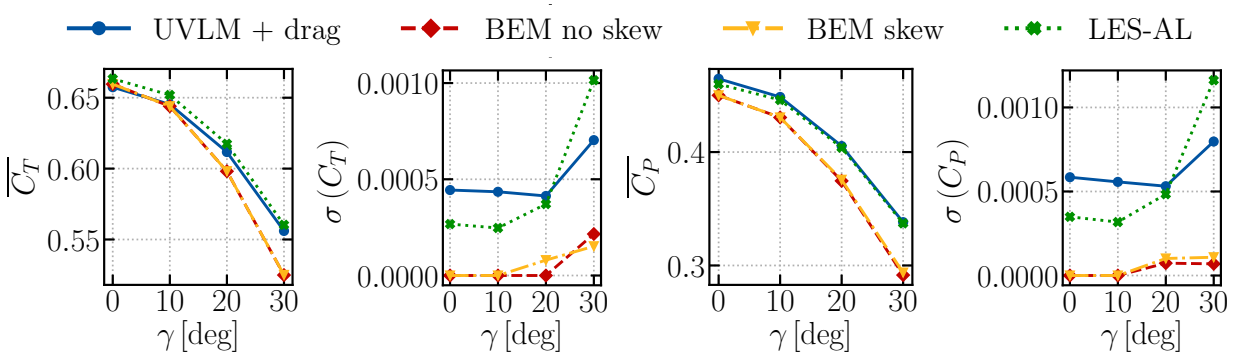

(a) Mean. (b) Standard deviation. (c) Mean. (d) Standard deviation.

Figure 4.33: Yaw effect on rotor thrust (C_T) and power (C_P) coefficients.

mismatches below 3% in the force and rotor coefficients with UVLM and LES-AL. These differences are kept constant for yaw angles below 10 deg. For yaw angles larger than 10 deg, the unsteady and three-dimensional effects are very significant and, thus, we trust more the decreases with the yaw angle of the force and rotor coefficients predicted with UVLM and LES-AL. For yaw angles larger than 10 deg, both BEM methods predict overly large fluctuations and power and thrust decrease with the yaw angle. Thus, the skewed-wake model in BEM performs well at angles of yaw below 10 deg, however, for larger yaw angles, it overestimates the effect of yaw on blade forces and rotor coefficients.

4.2.3 Turbulent inflow

The temporal and spatial scales of wind turbulence relevant for wind energy are very wide: from blade boundary layer fluctuations triggering laminar to turbulent transition to seasonal changes in wind direction and intensity. In this section, we use the turbulence box generated in Section 4.1.4 as inflow for BEM, UVLM and LES-AL. First, we quantify the level of unsteadiness present in the computations according to thin airfoil theory. Viscous drag corrections have been included into UVLM results according to Section 4.1.1 and labelled "UVLM + drag" in the following analysis. Next, we show the results of applying the spanwise filter to account for BEM spanwise sections interaction described in Section 4.1.3 (denoted "BEM + filter" in the next results). Finally, we compare the performance of the three aerodynamic fidelities in cases of turbulence. In these simulations, the average wind speed is $U^\infty = 10.5\,\mathrm{m/s}$, the rotor velocity is $\omega_\mathrm{r} = 0.945\,\mathrm{rad/s}$, the collective blade pitch is zero and the time step is equivalent to $\Delta\theta = 0.5\,\mathrm{deg}$ (0.0092 s).

Unsteady effects in turbulent inflow

This section assesses the non-stationary character of the flow over a rotor under turbulent atmospheric inflow and, therefore, the importance of employing unsteady aerodynamic models. First, the unsteadiness of different phenomena will be quantified according to the reduced frequency:

$$k = \frac{\omega c}{2u_r}, \qquad \text{(4.15 revisited)}$$

where ω is the associated circular frequency, $c(r)$ is the airfoil chord and $u_r(r)$ is the local relative velocity between the flow and blade sections. In attached flow conditions, thin airfoil theory defines processes with reduced frequencies below 0.05 as quasi-steady, and processes with reduced frequency over 0.6 as highly unsteady. Effects with reduced frequency between these two values are referred to as unsteady processes. This analysis is not valid for regions of separated flow such as the blade root region, which is intrinsically unsteady. Second, the unsteady aerodynamic models in BEM and UVLM will be analysed against their quasi-steady approximations.

Figure 4.34a shows the reduced frequency in Equation (4.15) of phenomena with characteristic frequency ω equal to rotor frequency (1P), for example, yaw or shear, and blade-passing frequency (3P). They change along the span r/R due to the varying local chord c and relative velocity $u_r^2 = (U^\infty)^2 + (\omega_{\mathrm{r}} r)^2$. Phenomena with characteristic frequencies 1P and 3P give rise to unsteady airfoil aerodynamics for spanwise positions $r < 0.5R$ and $r < 0.9R$, respectively. However, quasi-steady aerodynamics are observed from these spanwise positions to the tip. The picture is more complex for turbulent inflow in which the incoming velocity has its own frequency spectrum, Figure 4.34b shows the energy content of the higher turbulence inflow velocity generated in Section 4.1.4 at different radial positions. In the inner region ($r < 0.45R$) there is a large amount of energy in the unsteady and highly unsteady range. However, towards the tip, the term u_r in Equation (4.15) increases and the chord c decreases, thus, lowering the reduced frequencies. At the spanwise location $r = 0.75R$ the input turbulence velocity does not have significant energy beyond $k = 0.6$ and closer to the tip $r = 0.94R$ there is no significant energy content for $k > 0.07$.

It is therefore evident that non-stationary aerodynamics are of importance for a large part of the blade. Next, the effect of using quasi-steady or unsteady aerodynamic models is studied under the turbulent inflows described in Section 4.1.4. Simulations have just been run for one rotor revolution after steady state because it permits the detail analysis of the aerodynamic loads and the explanation of the physics behind. At the end of this section,

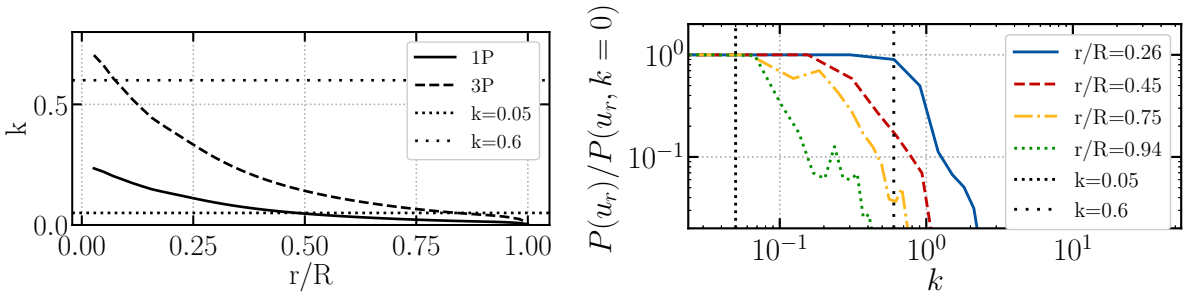

(a) Rotation frequencies.

(b) Relative velocity u_r. Higher turbulence case.

Figure 4.34: Reduced frequency values in the AVATAR rotor for different phenomena.

a longer simulation has been run to provide statistically significant results. On the one hand, BEM is originally a steady methodology ("BEM quasi-steady" label in next figures), although unsteady features are usually incorporated as sectional corrections as described in Section 2.2.2 ("BEM" label in next figures). BEM results are shown filtered according to Section 4.1.3 because it will be shown in Section 4.2.3 that it improves the accuracy of BEM. Thus, they are labelled "BEM + filter", however, it is irrelevant for this analysis. On the other hand, UVLM is inherently unsteady ("UVLM + drag" in next figures) but can be restricted to a quasi-steady solver by 1) neglecting the forces associated to time derivatives in Equation (2.75) and 2) completely convecting the shed vorticity to the end of the wake at each time step ("UVLM quasi-steady + drag" in next figures).

Figures 4.35a and 4.35b show the out-of-plane and in-plane force coefficients, respectively, along a revolution at an inner spanwise position $r = 0.45R$. The quasi-steady UVLM model predicts an increase in the standard deviation of the out-of-plane force coefficient by 19% with respect to the unsteady UVLM (Figure 4.35a) and a 27% increase for the in-plane force coefficient (Figure 4.35b). However, the quasi-steady BEM model predicts a decrease of both the out-of-plane (Figure 4.35a) and the in-plane (Figure 4.35b) force coefficients standard deviation by 17% and 8%, respectively, with respect to the unsteady BEM model. This evidences that the unsteady aerodynamic captured by UVLM act as a low-pass filter smoothing out the force coefficients along time (similar to the effect shown in Section 3.2.1) but the BEM model for unsteady aerodynamics fails to do so.

Figures 4.36a and 4.36b shows the out-of-plane and in-plane force coefficients, respectively, along a revolution at a spanwise outboard position $r = 0.75R$. Again, the quasi-steady UVLM model predicts increasing standard deviation with respect to the unsteady UVLM model, while the quasi-steady BEM model predicts smaller standard deviation with respect

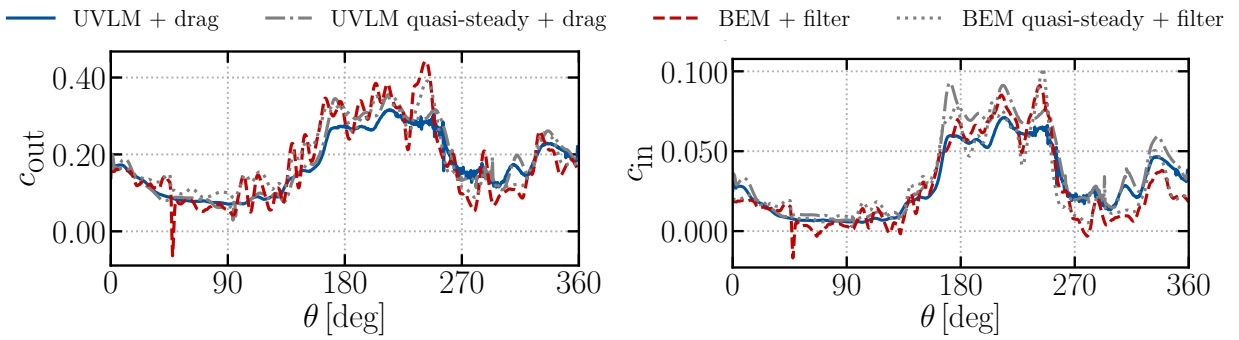

(a) Out-of-plane force coefficient. (b) In-plane force coefficient.

Figure 4.35: Time history of force coefficients predicted by both quasi-steady and unsteady UVLM and BEM at $r = 0.45R$. Higher turbulence case.

to the unsteady BEM model.

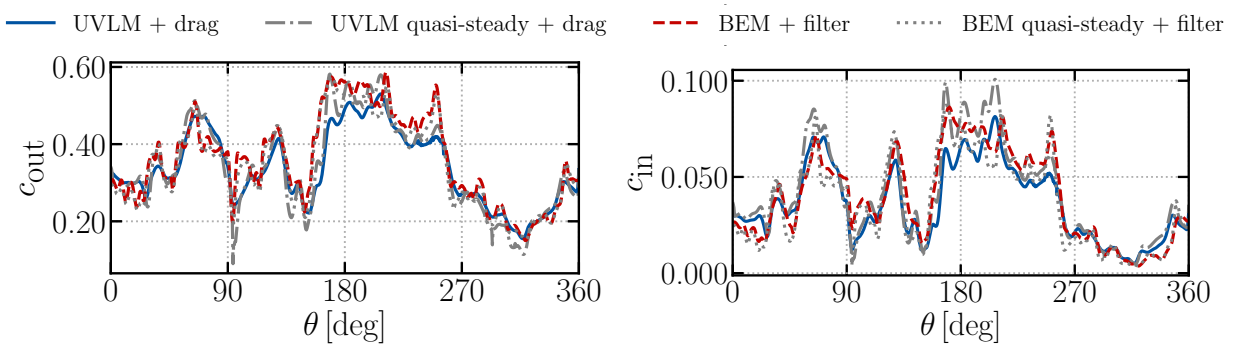

(a) Out-of-plane force coefficient. (b) In-plane force coefficient.

Figure 4.36: Time history of force coefficients predicted by both quasi-steady and unsteady UVLM and BEM at $r = 0.75R$. Higher turbulence case.

Figure 4.37 shows an example ($\theta = 90\,\text{deg}$) of the instantaneous force coefficients along the span. At this instant, quasi-steady UVLM at the outer part of the blade $r > 0.6R$ predicts slightly lower out-of-plane force coefficient than unsteady UVLM and there are not significant differences between both BEM models (Figure 4.37a). The in-plane force coefficient (Figure 4.37b) predictions are very similar for both UVLM models and the quasi-steady BEM, however, the unsteady BEM deviates from the rest.

Power spectral density of the force coefficients at different spanwise locations are shown in Figure 4.38. The quasi-steady approximation of UVLM predicts higher in-plane (Figures 4.38b and 4.38d) and out-of-plane (Figures 4.38a and 4.38c) power spectral density of the force coefficients than the unsteady UVLM model. This means that unsteady aerodynamics

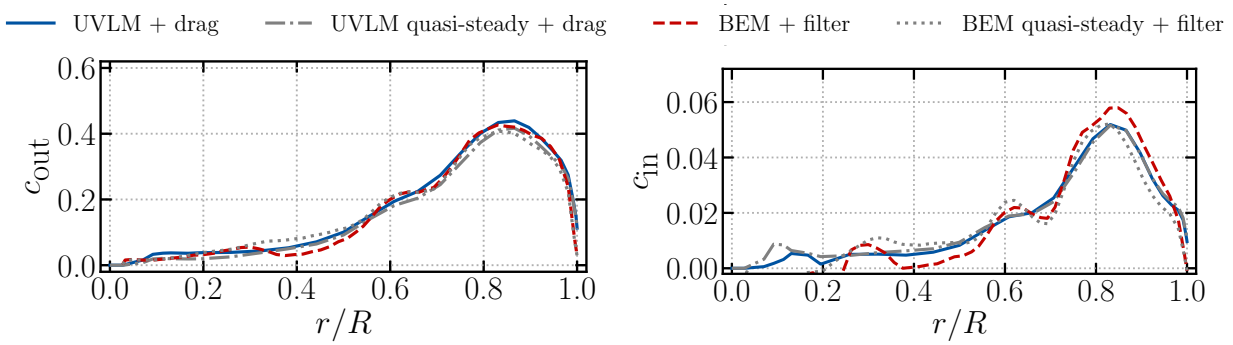

(a) Out-of-plane force coefficient. (b) In-plane force coefficient.

Figure 4.37: Instantaneous force coefficients along the span predicted by both quasi-steady and unsteady UVLM and BEM. Higher turbulence, $\theta = 90\,\text{deg}$.

have a damping or smoothing effect. On the contrary, quasi-steady BEM consistently predicts lower power spectral density of the force coefficients than the full model. In the inner region (Figures 4.38a and 4.38b) the unsteady aerodynamic models have a much stronger effect than at the tip region (Figures 4.38c and 4.38d) because of the smaller reduced frequencies near the tip explained before in Figure 4.34.

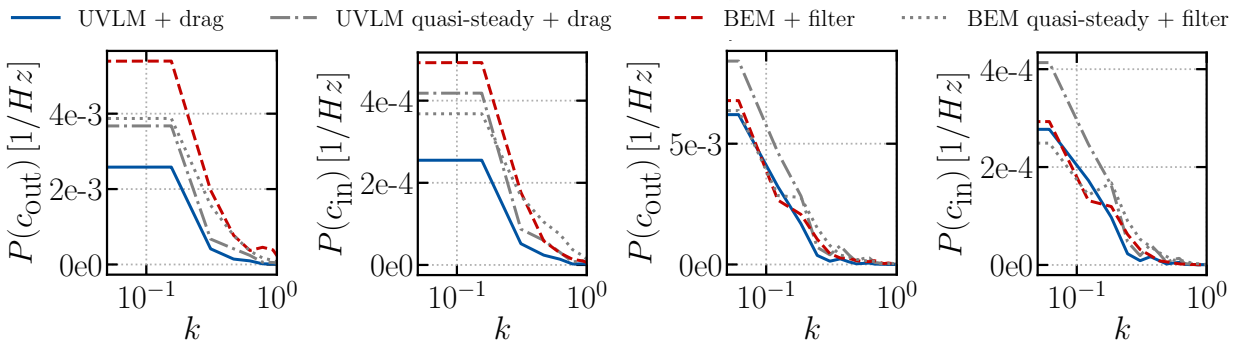

(a) c_{out} at $r = 0.45R$. (b) c_{in} at $r = 0.45R$. (c) c_{out} at $r = 0.75R$. (d) c_{in} at $r = 0.75R$.

Figure 4.38: Power spectral density of force coefficients predicted by both quasi-steady and unsteady UVLM and BEM. Higher turbulence.

To conclude, the mean and standard deviation along a revolution for the root-bending moments are shown in Table 4.7. It evidences that, the quasi-steady UVLM model predicts larger average loads and standard deviations with respect to the unsteady UVLM; while the quasi-steady BEM predicts smaller loads and standard deviations with respect to the unsteady BEM.

Table 4.7: Aerodynamic root-bending moments mean and standard deviation for unsteady and quasi-steady models.

	$\overline{M_{\text{out}}}$ [MNm]	$\sigma\,(M_{\text{out}})$ [MNm]	$\overline{M_{\text{in}}}$ [MNm]	$\sigma\,(M_{\text{in}})$ [MNm]
UVLM + drag	31.35	7.45	3.74	1.59
UVLM quasi-steady + drag	31.81	9.16	4.62	6.65
BEM + filter	31.63	9.17	3.66	1.93
BEM quasi-steady + filter	30.85	8.52	3.52	1.79

Long turbulent inflow We have just described the unsteadiness in turbulent flow and the behaviour of BEM and UVLM and their quasi-steady approximations. Here, we use the long turbulent inflow generated in Section 4.1.4 (Table 4.2 and Figure 4.17) to provide statistically significant values. Wake vortices in UVLM can eventually become close to other vortices experiencing a large induced velocity (Equation (2.63)) that is nonphysical. In this case, vortices experience a sudden displacement. If these vortices interact with the blades, the load estimation is not realistic. We have substituted those time steps by the interpolation of the contiguous ones. For clarity, the following figures show the last 7 rotor revolutions (47 s) of the computations, however, the average and standard deviation values are computed for 15 revolutions (93 s) after the steady-state has been reached.

Figures 4.39 and 4.40 show the time evolution of the out-of-plane and the in-plane root-bending moments, respectively. They confirm that the effect of the unsteady model in BEM barely modifies the results. However, the root-bending moments predicted by the unsteady UVLM model are significantly smoother than the quasi-steady UVLM predictions which can also be seen in the standard deviation included in Table 4.8. There are still some time steps in which the quasi-steady UVLM results show extremely large peaks that are considered non-realistic.

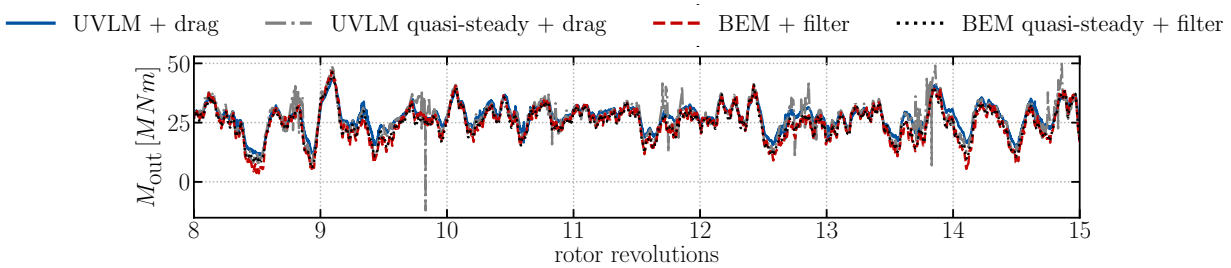

Figure 4.39: Time evolution of the out-of-plane root bending moment predicted by both quasi-steady and unsteady UVLM and BEM. Long turbulence case.

The average and standard deviation of the root-bending moments are shown in Table

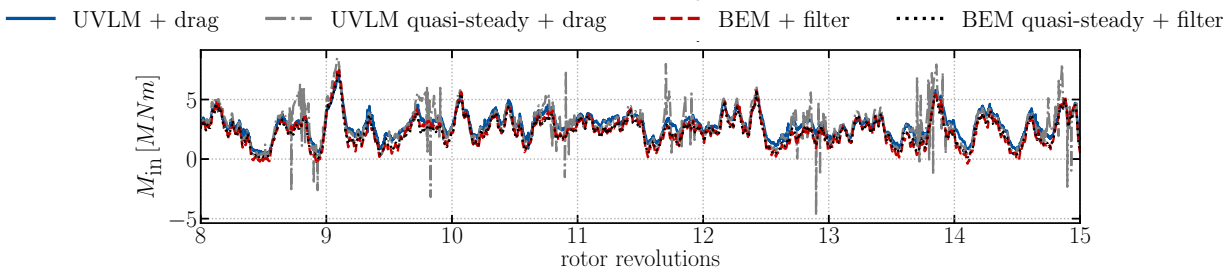

Figure 4.40: Time evolution of the in-plane root bending moment predicted by both quasi-steady and unsteady UVLM and BEM. Long turbulence case.

4.8. The average values are very similar between the unsteady and the quasi-steady approximations. UVLM predicts larger standard deviation of the root-bending moments when the quasi-steady model is used. This is coherent with airfoil theory (Section 3.2.1) because aerodynamic forces grow from zero to the steady-state value (Figures 3.6 and 3.7). However, the standard deviation predicted by the quasi-steady BEM model are smaller than those from the unsteady BEM approximation.

Table 4.8: Aerodynamic root-bending moments mean and standard deviation for unsteady and quasi-steady models.

	$\overline{M_{\text{out}}}$ [MNm]	$\sigma\,(M_{\text{out}})$ [MNm]	$\overline{M_{\text{in}}}$ [MNm]	$\sigma\,(M_{\text{in}})$ [MNm]
UVLM + drag	28.10	5.59	3.03	1.14
UVLM quasi-steady + drag	27.77	6.86	3.03	1.45
BEM + filter	25.69	7.39	2.52	1.37
BEM quasi-steady + filter	26.08	6.91	2.58	1.29

Figures 4.41 and 4.42 show the time evolution of the rotor thrust and power coefficients, respectively. Moreover, Table 4.9 shows the average and the standard deviation of these coefficients. The differences between the quasi-steady and the unsteady numerical models are very small in the prediction of these coefficients as explained before.

Table 4.9: Rotor coefficients mean and standard deviation for unsteady and quasi-steady models.

	$\overline{C_T}$	$\sigma\,(C_T)$	$\overline{C_P}$	$\sigma\,(C_P)$
UVLM + drag	0.54	0.073	0.36	0.091
UVLM quasi-steady + drag	0.55	0.071	0.37	0.081
BEM + filter	0.49	0.089	0.31	0.103
BEM quasi-steady + filter	0.50	0.086	0.31	0.103

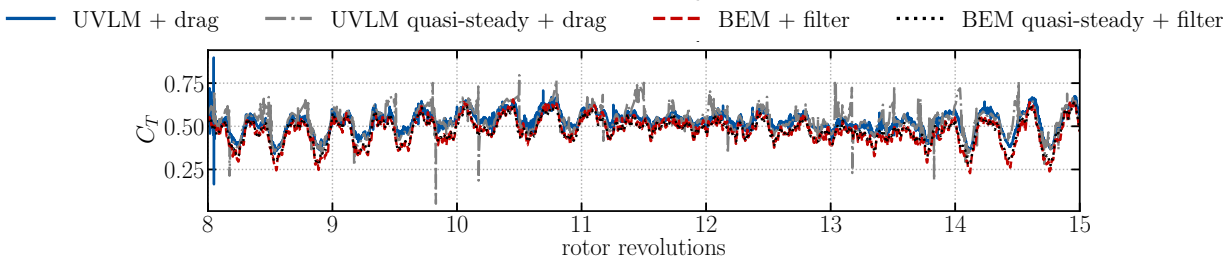

Figure 4.41: Time evolution of the rotor thrust coefficient predicted by both quasi-steady and unsteady UVLM and BEM. Long turbulence case.

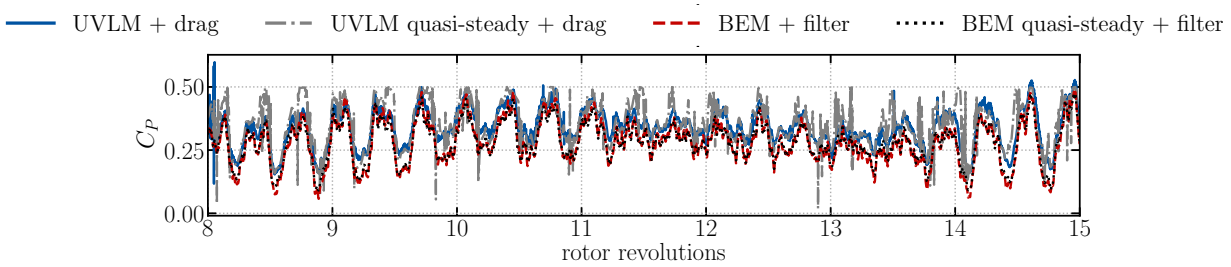

Figure 4.42: Time evolution of the rotor power coefficient predicted by both quasi-steady and unsteady UVLM and BEM. Long turbulence case.

Three-dimensional spanwise effects in turbulent inflow

In this section, we analyse the sectional force coefficients on wind turbine blades under the turbulent inflow generated in Section 4.1.4 in Figures 4.44 to 4.46. Simulations have just been run for one rotor revolution after steady state because it permits the detail analysis of the aerodynamic loads and the explanation of the physics behind. At the end of this section, a longer simulation has been run to provide statistical value to the results shown. We compare the original BEM prediction, the BEM prediction corrected for the three-dimensional effects for the interaction between spanwise sections according to Section 4.1.3 (labelled "BEM + filter" in figure legends). The prediction of UVLM (including the drag correction in Section 4.1.1) is also plotted in solid grey line as a reference in this section. The following figures do not include LES-AL data because, while achieved in literature [13], synchronising the LES-AL and the other signals is impractical because BEM and UVLM does not modify the upstream turbulence but, inevitably, LES-AL does.

Figure 4.43 shows the effect of the filter to account for spanwise interaction for the higher turbulence level at $\theta = 90\,\text{deg}$ as an example. The filter always smooths the spanwise results, and has the effect of modifying the BEM loads predictions to give a closer match to those provided by UVLM. There is a stronger effect of the filter on fluctuations with short

wavelengths which is coherent with the filter function shown in Figure 4.9.

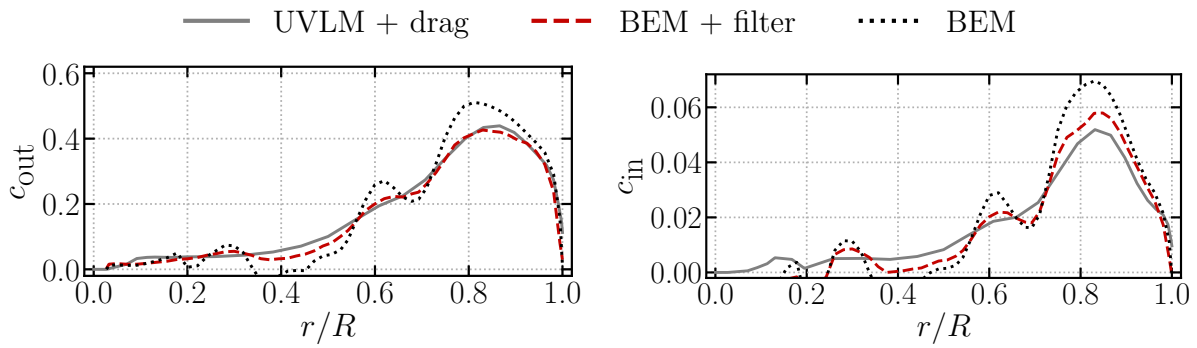

(a) Out-of-plane force coefficient. (b) In-plane force coefficient.

Figure 4.43: Instantaneous force coefficients along the span at $\theta = 90\,\text{deg}$. Higher turbulence case.

Figure 4.44 shows the same variables for the lower turbulence case. Depending on the specific time step and turbulent case, the filtered BEM loads fall slightly above (Figure 4.43) or below (Figure 4.44) the UVLM prediction.

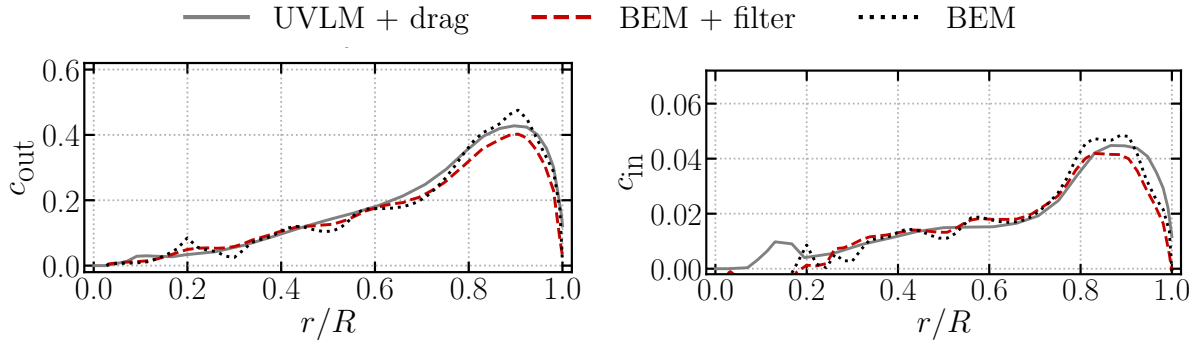

(a) Out-of-plane force coefficient. (b) In-plane force coefficient.

Figure 4.44: Instantaneous force coefficients along the span at $\theta = 90\,\text{deg}$. Lower turbulence case.

Figure 4.45 shows the force coefficients at an inner spanwise position $r = 0.45R$ in the higher turbulence case. The filter smooths also the time signal of the loads and improves the BEM approximation with respect to the UVLM one. The difference in standard deviation between BEM and UVLM is 82% and 47% for the out-of-plane (Figure 4.45a) and the in-plane (Figure 4.45b) force coefficients, respectively. When the filter is applied to BEM, these differences are reduced to 37% and 26%, respectively.

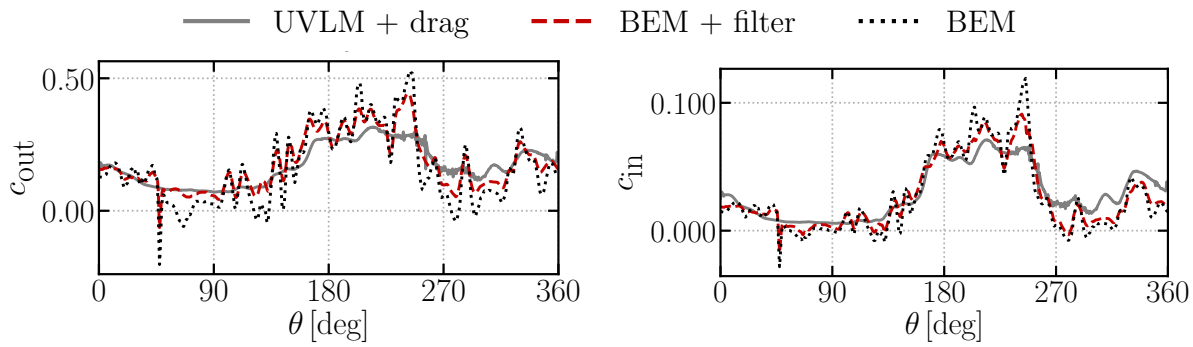

(a) Out-of-plane force coefficient. (b) In-plane force coefficient.

Figure 4.45: Time history of force coefficients at $r = 0.45R$. Higher turbulence case.

In the case of the force coefficients at an outboard location ($r = 0.75R$) shown in Figure 4.46 the filter also makes the BEM prediction closer to the UVLM one. However, the initial differences between BEM and UVLM predictions are not as large as in the inboard region: 44% and 30% for the out-of-plane (Figure 4.46a) and the in-plane (Figure 4.46b) force coefficients standard deviation, respectively. And the effect of the filter is smaller: it reduces the differences by 23% and 12% for the out-of-plane and the in-plane force coefficients standard deviation, respectively. The reason is that the chords near the tip are smaller, thus, for the same input wavelength, the force coefficients near the tip are less filtered (Figure 4.9).

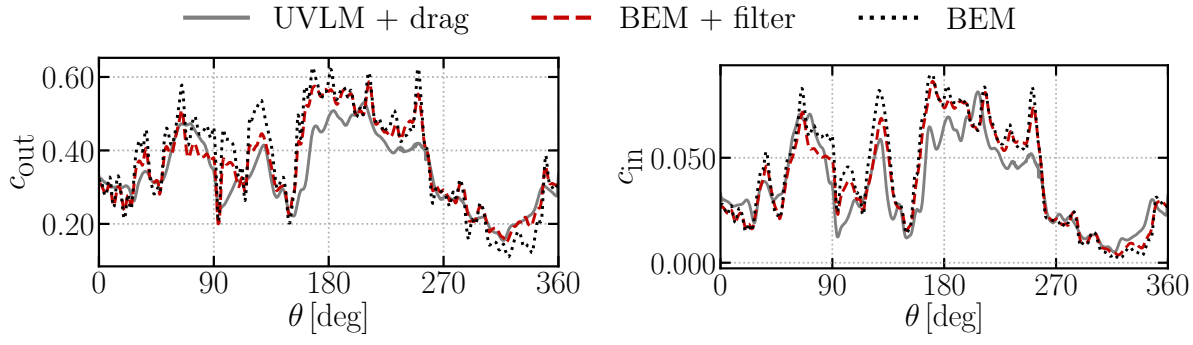

(a) Out-of-plane force coefficient. (b) In-plane force coefficient.

Figure 4.46: Time history of force coefficients at $r = 0.75R$. Higher turbulence case.

Figure 4.47 shows the mean force coefficients along a revolution as a function of the spanwise coordinate for the higher turbulence case. It evidences that the filter improves the agreement between BEM and UVLM.

Figure 4.48 shows the mean force coefficients as a function of the spanwise coordinate for the lower turbulence case with similar qualitative behaviour as the higher turbulence case

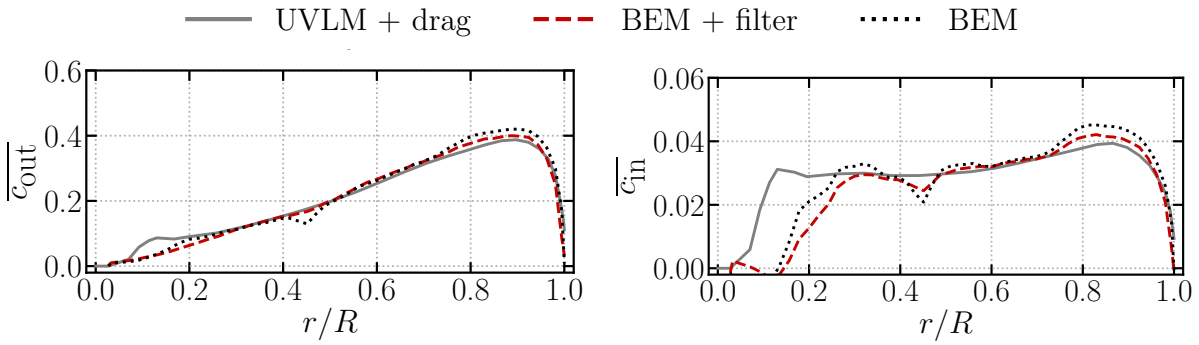

(a) Out-of-plane force coefficient.

(b) In-plane force coefficient.

Figure 4.47: Mean over one revolution of the force coefficients along the span. Higher turbulence case.

(Figure 4.47). Table 4.10 shows the qualitative differences of both BEM models with respect to UVLM in the estimation of the rotor thrust and power coefficients. There are small changes in the mean values but significant improvements in the estimation of the standard deviation when the spanwise filter is used.

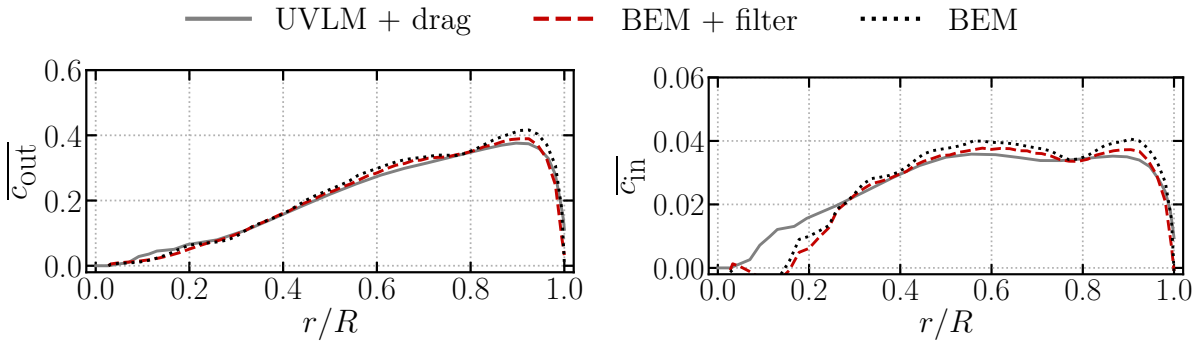

(a) Out-of-plane force coefficient.

(b) In-plane force coefficient.

Figure 4.48: Mean over one revolution of the force coefficients along the span. Lower turbulence case.

Table 4.10: Rotor coefficients mean and standard deviation differences for BEM with and without spanwise filter with respect to UVLM.

	$\overline{C_T}$	$\sigma(C_T)$	$\overline{C_P}$	$\sigma(C_P)$
BEM	1.57%	37.36%	5.59%	31.92%
BEM + filter	-1.25%	27.07%	-1.30%	18.21%
UVLM + drag	0.00%	0.00%	0.00%	0.00%

Long turbulent inflow We have just described the effect of the spanwise filter (Section 4.1.3) on the BEM computations. Here, we use the long turbulent inflow generated in Section 4.1.4 (Table 4.2 and Figure 4.17) to provide statistically significant values. For clarity, the following figures show the last 7 rotor revolutions (47 s) of the computations, however, the average and standard deviation values are computed for 15 revolutions (93 s) after the steady-state has been reached.

Figures 4.49a and 4.49b show the standard deviation of the out-of-plane and the in-plane force coefficients along the span. They show that the filter applied to BEM reduces the standard deviation of the force coefficients and makes BEM prediction closer to UVLM which is considered more accurate because it inherently accounts for the three-dimensional effect of interacting spanwise sections in turbulent inflow.

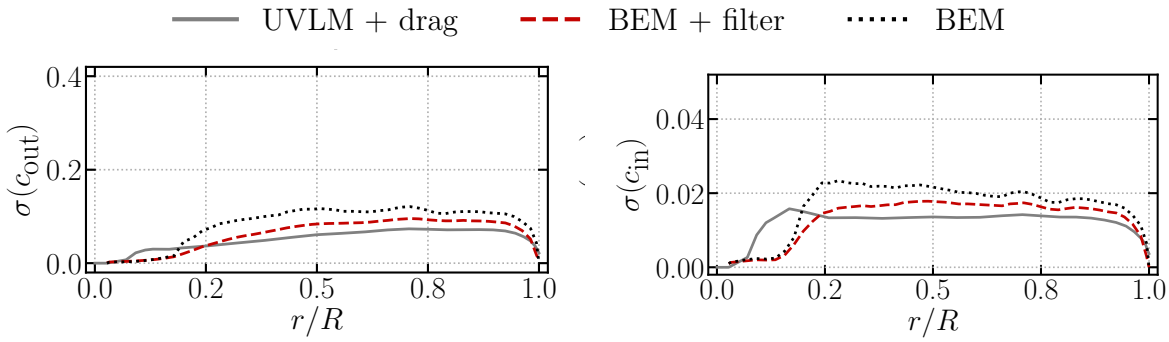

(a) Out-of-plane force coefficient.

(b) In-plane force coefficient.

Figure 4.49: Standard deviation of the force coefficients along the span. Long turbulence case.

Figures 4.50 and 4.51 show the time evolution of the out-of-plane and the in-plane root-bending moments, respectively. There are still some small differences between UVLM and BEM but the spanwise filter applied to BEM always makes the results closer to UVLM. The average and standard deviations are shown in Table 4.11.

Table 4.11: Aerodynamic root-bending moments mean and standard deviation.

	$\overline{M_{\text{out}}}$ [MNm]	$\sigma\left(M_{\text{out}}\right)$ [MNm]	$\overline{M_{\text{in}}}$ [MNm]	$\sigma\left(M_{\text{in}}\right)$ [MNm]
BEM	25.78	7.61	2.61	1.38
BEM + filter	25.69	7.39	2.52	1.37
UVLM + drag	28.10	5.59	3.03	1.14

Figures 4.52 and 4.53 show the time evolution of the rotor thrust and power coefficients,

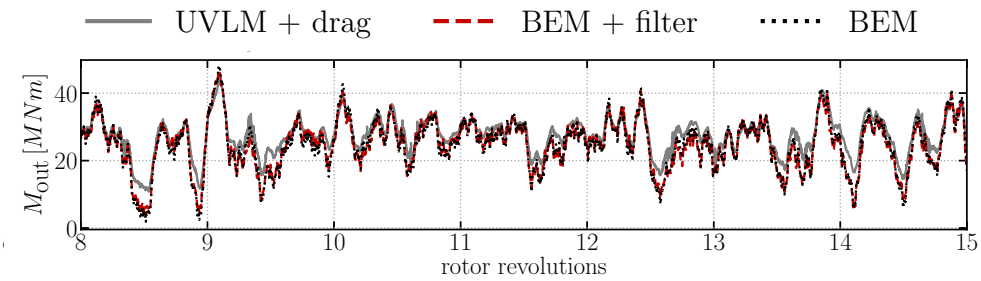

Figure 4.50: Time evolution of the out-of-plane root bending moment. Long turbulence case.

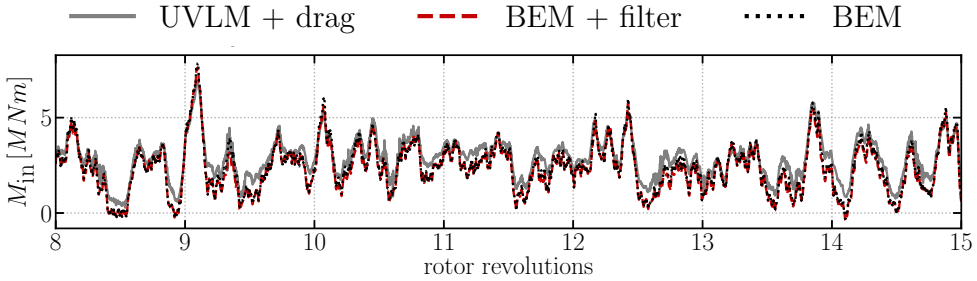

Figure 4.51: Time evolution of the in-plane root bending moment. Long turbulence case.

respectively, and Table 4.12 the average and standard deviation values. Again, they confirm that the filter applied to BEM makes the results closer to UVLM.

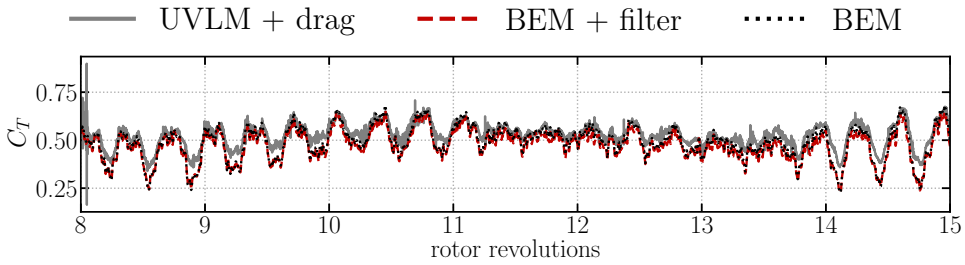

Figure 4.52: Time evolution of the rotor thrust coefficient. Long turbulence case.

Table 4.12: Rotor coefficients mean and standard deviation.

	$\overline{C_T}$	$\sigma\,(C_T)$	$\overline{C_P}$	$\sigma\,(C_P)$
BEM	0.51	0.096	0.33	0.109
BEM + filter	0.49	0.089	0.31	0.103
UVLM + drag	0.54	0.073	0.36	0.091

In summary, the use of the spanwise filter on BEM computations makes the aerodynamic

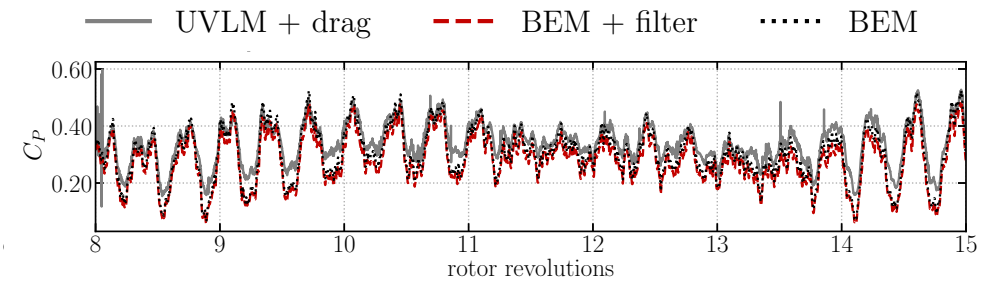

Figure 4.53: Time evolution of the rotor power coefficient. Long turbulence case.

loads of BEM more similar to UVLM in cases where significant interaction between spanwise sections are present. However, this filter could be improved with higher-fidelity methods.

Turbulent inflow benchmark

This section analyses the performance of the different fidelities with the proposed improvements in the computation of aerodynamic loads under the turbulent inflows generated in Section 4.1.4. Results are presented in terms of conventional statistics calculated over a short time window equivalent to one rotor revolution. The unsteady and three-dimensional aerodynamic effects that are of interest to this section have time scales shorter than one rotor revolution as shown in Section 4.2.3. However, this time would not be suitable to compute life-cycle performance indicators such as equivalent fatigue loads.

The average out-of-plane and in-plane force coefficients along a revolution for the higher turbulence case are shown in Figures 4.54a and 4.54b, respectively. In general, there is a very good agreement between UVLM and BEM for spanwise positions $r > 0.3R$. In the root region, UVLM is no longer valid because of the inapplicability of the thin-airfoil theory to this region of significant flow separation. LES-AL agrees well with the other solvers in the out-of-plane and in-plane force coefficients in the midspan region. However, it overpredicts the force coefficient near the tip probably because the grid refinement is not enough in that region where the chords become smaller. The LES-AL solver employs uniform grids so refining the mesh requires refining the whole domain which was computationally too expensive for this study.

Figure 4.55 also shows the out-of-plane and the in-plane force coefficients along the span for the lower turbulence case. The conclusions detailed for the higher turbulence case (Figure 4.54) are confirmed here. In the region $0.2R < r < 0.4R$ there is a significant disagreement between the LES-AL and the BEM predictions of the in-plane force coefficient in the higher

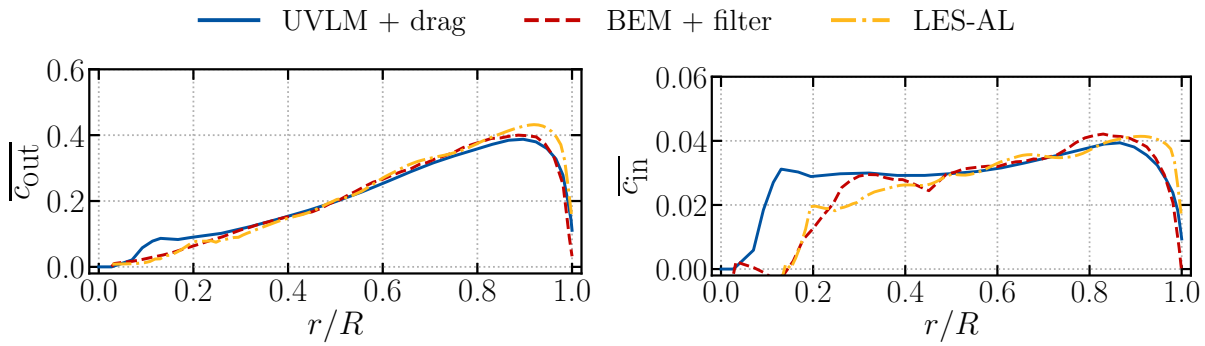

(a) Out-of-plane force coefficient.

(b) In-plane force coefficient.

Figure 4.54: Mean over one revolution of the force coefficients along the span. Higher turbulence case.

and lower turbulence cases (Figures 4.54b and 4.55b, respectively) and the out-of-plane foce coefficient in the lower turbulence case (Figure 4.55a). In this region, the flow is very unsteady and differences are expected because of the different treatment of unsteadiness by BEM and LES-AL.

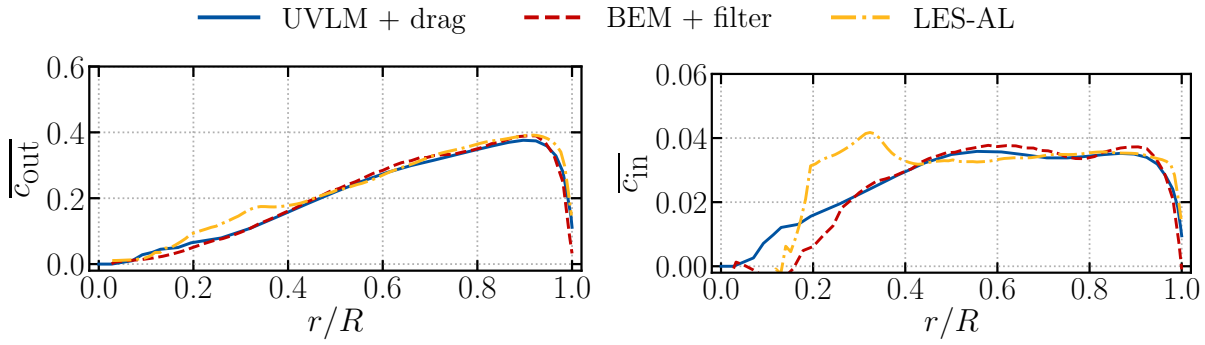

(a) Out-of-plane force coefficient.

(b) In-plane force coefficient.

Figure 4.55: Mean over one revolution of the force coefficients along the span. Lower turbulence case.

The standard deviation of the out-of-plane force coefficient in the higher and lower turbulence cases is shown in Figures 4.56a and 4.57a, respectively. The three methods are in good agreement. BEM slightly overpredicts the standard deviation of the in-plane force coefficients in the higher (Figure 4.56b) and the lower turbulence (Figure 4.57b) cases with respect to UVLM. In the prediction of the in-plane force coefficient, LES-AL agrees well with UVLM in the case of higher turbulence (Figure 4.56b) and LES-AL agrees better with BEM in the case of lower turbulence (Figure 4.57b). However, these differences in standard

deviation in the prediction of the in-plane force coefficients are small so we consider there is a general good agreement between the three numerical methods.

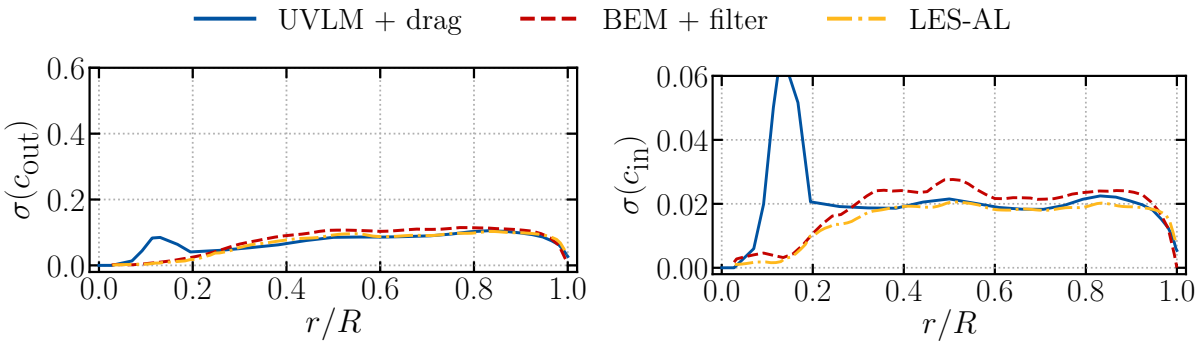

(a) Out-of-plane force coefficient.

(b) In-plane force coefficient.

Figure 4.56: Standard deviation over one revolution of the force coefficients along the span. Higher turbulence case.

The standard deviation of the in-plane force coefficients (Figures 4.56b and 4.57b) is around 50% the mean value of these coefficients (Figures 4.54b and 4.55b). However, in the case of the out-of-plane force coefficients, the standard deviation (Figures 4.56a and 4.57a) is around 25% of the mean values (Figures 4.54a and 4.55a). This indicates that the in-plane force coefficient is more sensitive to atmospheric turbulence than the out-of-plane force coefficient.

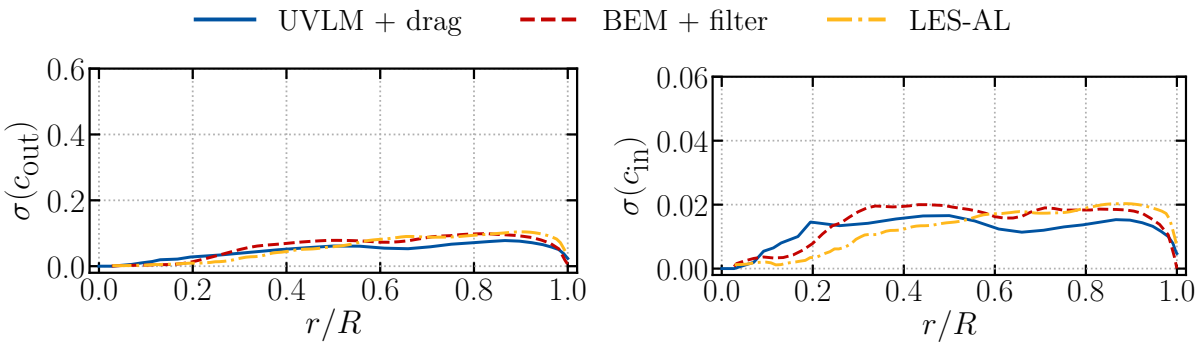

(a) Out-of-plane force coefficient.

(b) Lower turbulence.

Figure 4.57: Standard deviation over one revolution of the force coefficients along the span. Lower turbulence case.

Finally, Figure 4.58 shows the power spectral density of the out-of-plane and the in-plane force coefficients at two spanwise locations ($r = 0.45R$ and $r = 0.75R$) for the higher turbulence case. In the inner region $r = 0.45R$ (Figures 4.58a and 4.58b) there is a considerable

amount of energy in the highly unsteady range $k > 0.6$ which suggest that the flow behaviour is highly unsteady in the inner region. At the spanwise position $r = 0.75R$ (Figures 4.58c and 4.58d) the energy content in the highly unsteady range $k > 0.6$ is significantly smaller and the agreement of the three solvers has improved with respect to the inner region. For both spanwise positions and both force coefficients, BEM and LES-AL agree quite well in the power spectral density decay with increasing reduced frequency. However, UVLM predicts faster decay of power spectral density with the reduced frequency. It is likely that the unsteady BEM model and the computation of forces with steady-state data in LES-AL are not filtering enough these extremely high frequencies that are usually damped by aerodynamic effects (as described in Section 3.2.1).

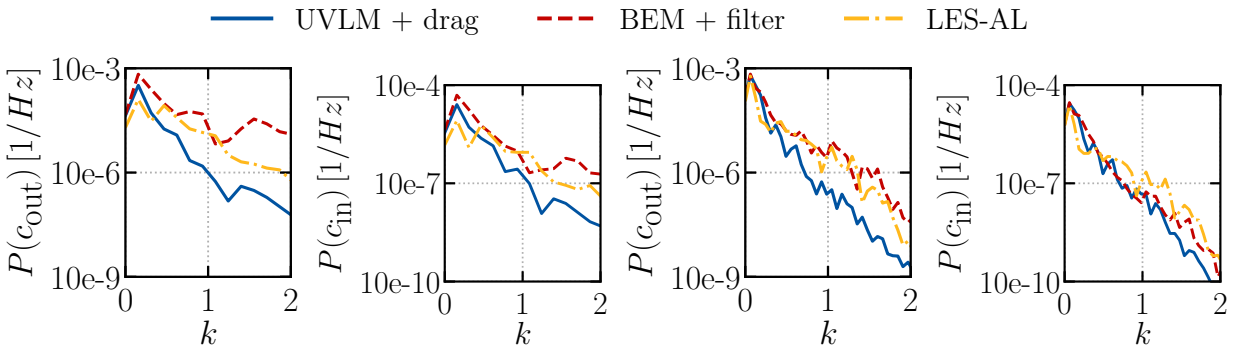

(a) c_{out} at $r = 0.45R$. (b) c_{in} at $r = 0.45R$. (c) c_{out} at $r = 0.75R$. (d) c_{in} at $r = 0.75R$.

Figure 4.58: Force coefficients power spectral density. Higher turbulence case.

In the lower turbulence case (Figure 4.59) the same trends are observed. The energy content in the inner region is smaller than in the higher turbulence case (Figure 4.58), however, at the spanwise position $r = 0.75R$ the energy is very similar between both turbulence levels because the relative velocity between the blade and the flow is dominated by the rotation velocity $\omega_{\text{r}} r$, instead of the freestream U^{∞} velocity.

In general, the three modelling methods for rotor aerodynamics (BEM, UVLM and LES-AL) agree well in the estimation of force coefficients along the span for cases of turbulent inflow when the improvements suggested in Section 4.1 are applied.

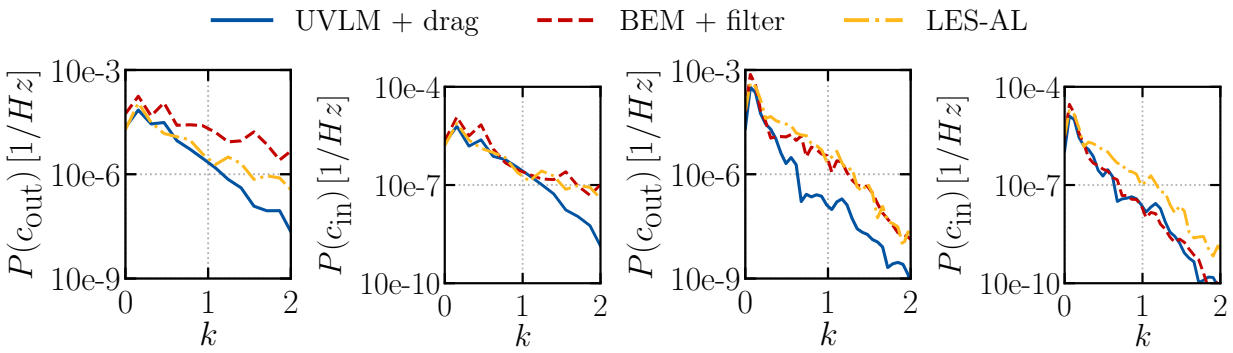

(a) c_{out} at $r = 0.45R$. (b) c_{in} at $r = 0.45R$. (c) c_{out} at $r = 0.75R$. (d) c_{in} at $r = 0.75R$.

Figure 4.59: Force coefficients power spectral density. Lower turbulence case.

Reduced order models

To conclude this chapter, we show a brief study on the accuracy of the reduced order models (ROM) of the linearised UVLM described in Section 2.2.1. The linearisation has been performed around steady-state conditions under uniform steady wind perpendicular to the rotor plane. In this case, the inflow is constant for any azimuthal position of the blades and the system becomes a time-invariant problem. The linear model includes 300000 states and the ROM only 72. In particular, the stability of this ROM was verified before running the computations. The $\mathcal{H}_\infty$ norm of the error of the frequency response is 10^{-3}. Figure 4.60 shows the frequency response between the inflow velocity perpendicular to the rotor and the aerodynamic force out-of-plane at $r = 0.75R$ as an example.

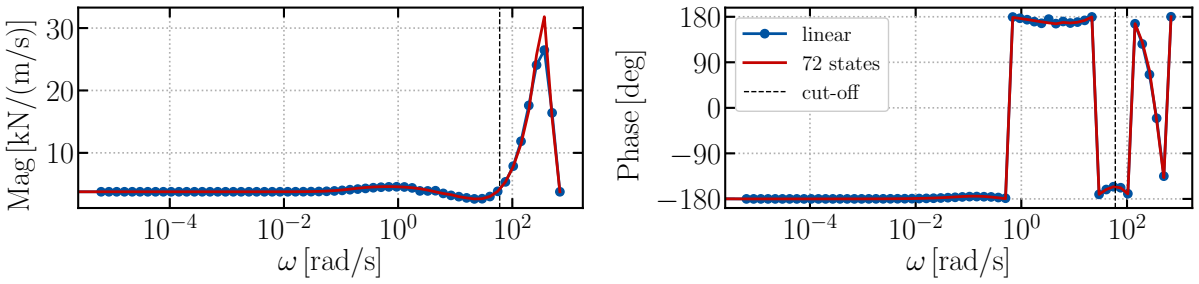

(a) Magnitude. (b) Phase.

Figure 4.60: Full linear and reduced order model frequency response.

The nonlinear UVLM, the linear UVLM and the reduced order model (UVLM ROM) have been tested under an idealised uniform turbulent inflow, this is, the wind velocity changes with time but at every instant the velocity is the same everywhere in the flow field.

This idealisation is required to reduce the input dimensions of the linear system such that the cost of the model order reduction is feasible. The time variation of the wind velocity has been generated as the hub height sampling of a turbulent field of turbulence intensity $I_T \approx 18\%$. Figure 4.61 shows the average out-of-plane and in-plane coefficients along the blade span. The three approximations provide very close results in every region of the blade.

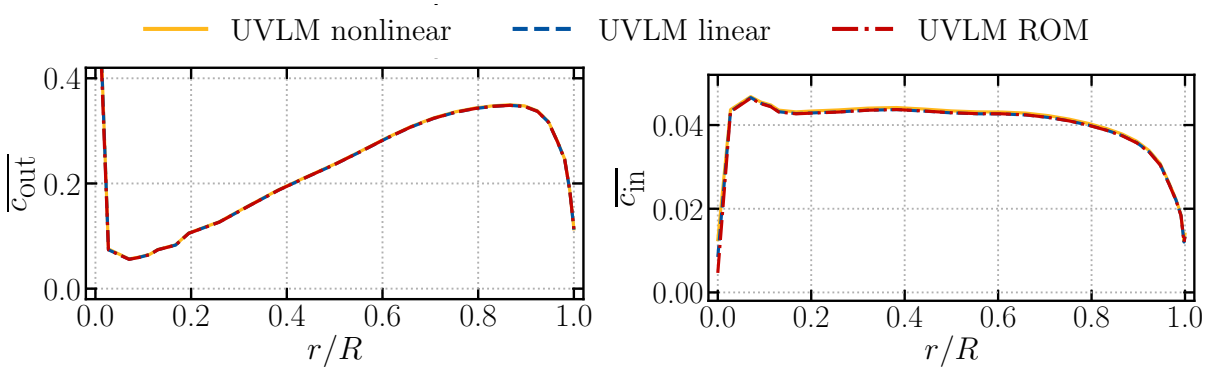

(a) Out-of-plane force coefficient. (b) In-plane force coefficient.

Figure 4.61: Force coefficients along the span. A-level turbulence.

Figure 4.62 shows the change of the force coefficients along a revolution at the span position $r = 0.75R$ showing very good agreement for all approximations. However, the nonlinear solution is slightly smoother and the linear and ROM solutions are slightly delayed. This is also observed in the rotor thrust and power coefficients (Figure 4.63).

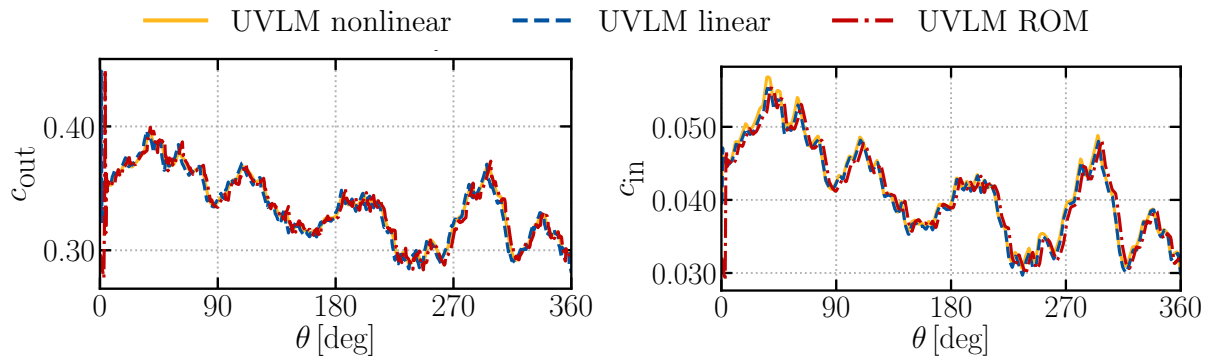

(a) Out-of-plane force coefficient. (b) In-plane force coefficient.

Figure 4.62: Time history of force coefficients at $r = 0.75R$. A-level turbulence.

Exploring the use of reduced order models could be a line of future research that has enormous potential to reduce the computational cost of aerodynamic modelling, especially, in combination with the new wake convection equation discretisation (Section 4.1.2).

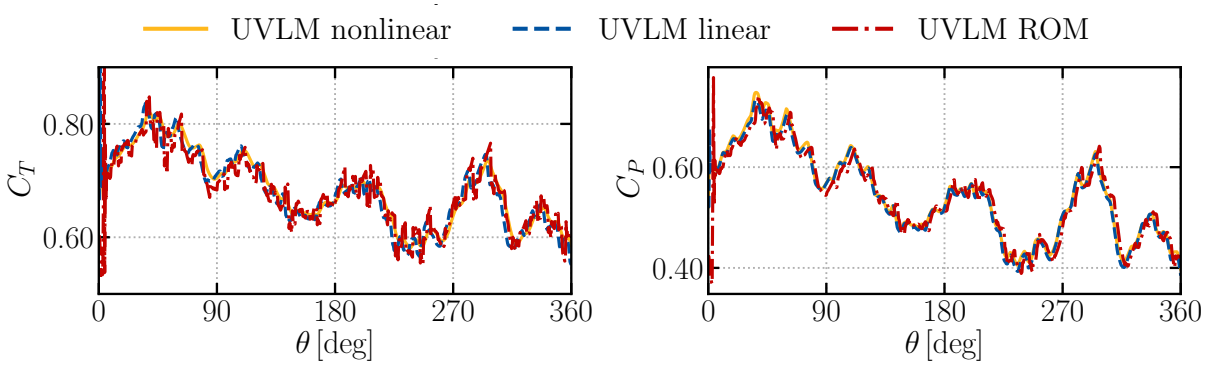

(a) Thrust coefficient.

(b) Power coefficient.

Figure 4.63: Time history of rotor coefficients. A-level turbulence.

Chapter 5

Floating wind turbine aeroelasticity and control

Chapter 4 has shown the suitability of vortex methods to capture unsteady and three-dimensional effects on rigid wind turbine rotors. However, offshore wind turbines have increasingly flexible blades and include tower and platform dynamics, which are studied in this chapter. First, we analyse the differences between a rigid and a flexible rotor, in Section 5.1. We describe the aeroelasticity of a flexible rotor under steady uniform inflow using Unsteady Vortex-Lattice Method (UVLM) for the aerodynamic computation (Section 2.2) and Geometrically-Exact Beam Theory (GEBT) for the nonlinear structural dynamics (Section 2.1.1). The combination of these two methods captures the dominant geometric changes of the aerodynamic surfaces associated to the structural deformation. Capturing blade twist has been shown to be of particular importance because it changes the angle of attack of the blade sections [195] and, therefore, wind turbine loads and power generation. This concurrent aeroelastic simulation is the basis to study complex phenomena like bend-twist coupling in composite structures [94] which are a promising tool for passive load alleviation [103].

In addition, floating platforms displace, rotate and are excited by forces with a wide range of characteristic frequencies from the wave and wind spectra, which can interact with the natural frequencies of tower, blades and rotor. In Section 5.2, a simplified set of cases including prescribed base movements provides insights on the influence of the platform motions on the system, in particular, the unsteady character of flow on the blades. The floating dynamics model (Section 2.3) includes quasi-steady mooring dynamics, linear hydrodynamics based on precomputed frequency response with vortex methods and viscous drag contribution from Morison's equation.

Finally, we have built a suitable model to study unsteady and three-dimensional aerodynamic effects with UVLM on large offshore wind turbines that require multibody nonlinear GEBT to capture the structural dynamics together with a model for the floating dynamics. In Section 5.3, we simulate the whole floating system subjected to a wide spectrum of waves and wind turbulence with a collective (all blades are pitched at the same angle) blade pitch control system as described in Section 2.4.1 which we redesign based on our complex model aiming to improve the wind turbine dynamics. As an initial study, we only consider operation in the above-rated regime because it has more influence on structural loads than the below-rated regime [141].

In this chapter, we analyse the NREL 5 MW wind turbine with the OC3 platform described in Section 3.4, due to the availability of an exhaustive description of the floating platform [175] and numerical data for validation [176, 189]. We perform prescribed wake UVLM simulations to reduce the computational cost at the expense of diminished accuracy in the computation of in-plane forces and, thus, power coefficient. The methodology to include viscous drag described in Section 4.1.1 does not provide improved results here because the baseline values on which the correction would be applied are not accurate due to the use of a prescribed wake model. However, the in-plane force is usually smaller than the out-of-plane force and less relevant for the system dynamics. Moreover, this chapter focuses on above-rated conditions where fatigue loads appear and the control algorithm has significant influence on their limitation.

5.1 Steady flexible rotor

In this section and the rest of this chapter, we analyse the NREL 5 MW wind turbine (Section 3.4). The blade discretisation includes 28 spanwise and 64 chordwise panels and a wake able to account for the vorticity shed during 7 rotor revolutions to obtain mesh converged results according to Section 3.3.1. The time step is equivalent to $\Delta\theta = 2\,\text{deg}$ (0.028 s). The wind turbine is mounted on the OC3 platform which is modelled with a concentrated-spar model according to Section 3.4.

Consider the rotor operating under steady uniform wind of $U^\infty = 18\,\text{m/s}$ which corresponds to operation in the above-rated regime. In this regime, operating at maximum efficiency (for power production) is not desirable anymore because it would imply extremely high loads. A reduction in loads (and efficiency) is achieved by pitching the blades with the intention to keep the power production to the nominal value ($E = 5.3\,\text{MW}$). At $U^\infty = 18\,\text{m/s}$

the collective pitch angle needed to generate nominal power is $\theta_{\mathrm{p}} = 15\,\mathrm{deg}$ according to [179]. In this section, we study the forces and deformations of blades though the out-of-plane $c_{\mathrm{out}}(r)$ and the in-plane $c_{\mathrm{in}}(r)$ force coefficients described in Equation (3.9) along the spanwise direction r with respect to the rotor radius $R = 63\,\mathrm{m}$. We also include blade deformations with respect to the unloaded state in the out-of-plane $x_{\mathrm{out}}(r)$ and the in-plane $x_{\mathrm{in}}(r)$ directions. The deformations of the tower-top are described along the x and y axis, that is, moving forward and backwards (fore-aft) and side-to-side, respectively.

The blade twist angle $\beta_{\mathrm{t}}(r)$ is the rotation around the local x axis (parallel to the blade reference line). According to GEBT, the blade twist coincides with the first of the Euler angles associated to the rotation $C^{B_{\mathrm{d}}B_0}$ [85] between the undeformed B_0 and the deformed B_{d} local frames of reference (Figure 2.1). We also compute the pitching moment coefficient around the pitch axis $c_M(r)$, which is computed as the moment per unit span length around this axis divided by $0.5\rho\left(U^{\infty}\right)^2\pi R^3$. Positive twist angles and moment coefficients twist the blade towards feather (when the airfoil chord is aligned with U^{∞}), otherwise, it would indicate a twist towards stall (when the airfoil chord is aligned with $\omega_{\mathrm{r}}r$) as shown in Figure 5.1. Notice that this is the usual sign convention in wind energy but is contrary to that used in traditional airfoil theory.

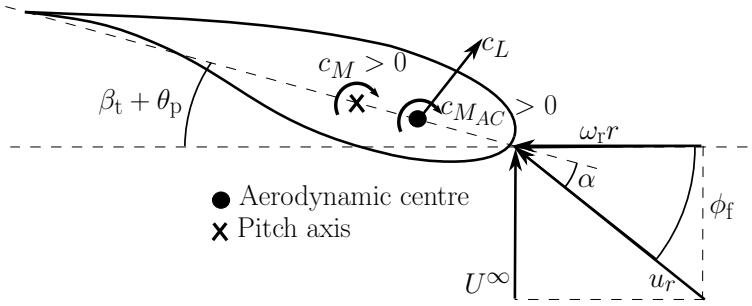

Figure 5.1: Blade pitching moment scheme.

We start the analysis with the rigid model. Figures 5.2a, 5.3a and 5.4a show the out-of-plane, in-plane forces and moment coefficients which, at the operation point ($\theta_{\mathrm{p}} = 15\,\mathrm{deg}$) are all small because the power available in the wind is much higher than required for nominal operation. At low pitch angles ($\theta_{\mathrm{p}} = 10\,\mathrm{deg}$), the angle of attack and, thus, the force coefficients increase. For high pitch angles ($\theta_{\mathrm{p}} = 20\,\mathrm{deg}$), the opposite behaviour is observed and, eventually, the in-plane force coefficient (associated with the power generation) becomes negative at the outer part of the blade $r > 0.6R$ as shown in Figure 5.3a, thus, opposing the

power generation in this part of the blade.

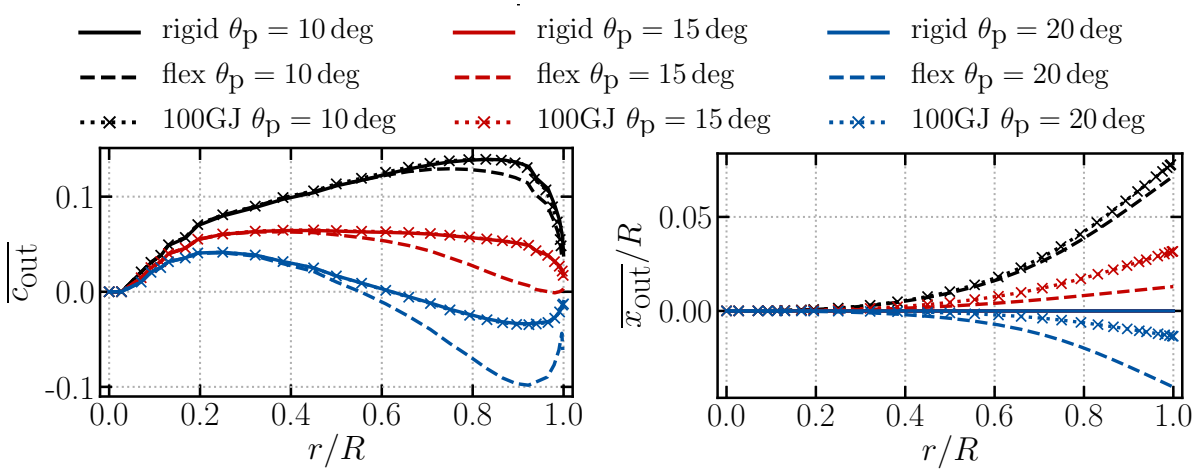

(a) Force coefficient.

(b) Displacement.

Figure 5.2: Out-of-plane force coefficient and displacement for different pitch angles and structural models.

The rigid and flexible models, labelled as "rigid" and "flex", respectively, in the figures of this chapter, have the true mass and stiffness distribution of the wind turbine [179]. The mean out-of-plane, in-plane and twist deformation are shown in Figures 5.2b, 5.3b and 5.4b, respectively. At the real operating point ($\theta_p = 15\,\mathrm{deg}$), the out-of-plane and the in-plane tip deformations are small: 1% and 0.5% of the blade radius, respectively. For smaller pitch angles ($\theta_p = 10\,\mathrm{deg}$), the blade is more heavily loaded and the out-of-plane and in-plane tip deformations are 6% and 2% of the blade radius, respectively. In the flexible blade estimation at pitch angles $\theta_p = 15\,\mathrm{deg}$ and $\theta_p = 20\,\mathrm{deg}$ the out-of-plane and the in-plane force coefficients decrease significantly in the outer part of the blade $r > 0.5R$ with respect to the rigid approximation (Figures 5.2a and 5.3a, respectively) and the pitching moment coefficient becomes more positive (Figure 5.4a). The case of $\theta_p = 20\,\mathrm{deg}$ shows the smaller loads, but still, the differences between the rigid and the flexible approximations are the largest. To explain this effect, we need to consider, first, that the pitch axis is behind aerodynamic centre and, second, that the pitching moment coefficient with respect to the pitch axis is composed by an approximately constant positive moment coefficient around the aerodynamic centre (remember the sign convention is opposite to traditional airfoil theory) plus a negative moment generated by the lift force as shown in Figure 5.1. The case of $\theta_p = 10\,\mathrm{deg}$ has the highest out-of-plane and in-plane force coefficients which are mainly related to the airfoil lift coefficient. In this cases, the negative and the positive contribution

to the moment coefficient balance out and thus, the blade twists less (Figure 5.4b). On the other hand, the case of $\theta_p = 20\,\text{deg}$, the lift coefficient is smaller and then it does not counteract the constant positive moment around the aerodynamic centre leading to larger twist angles.

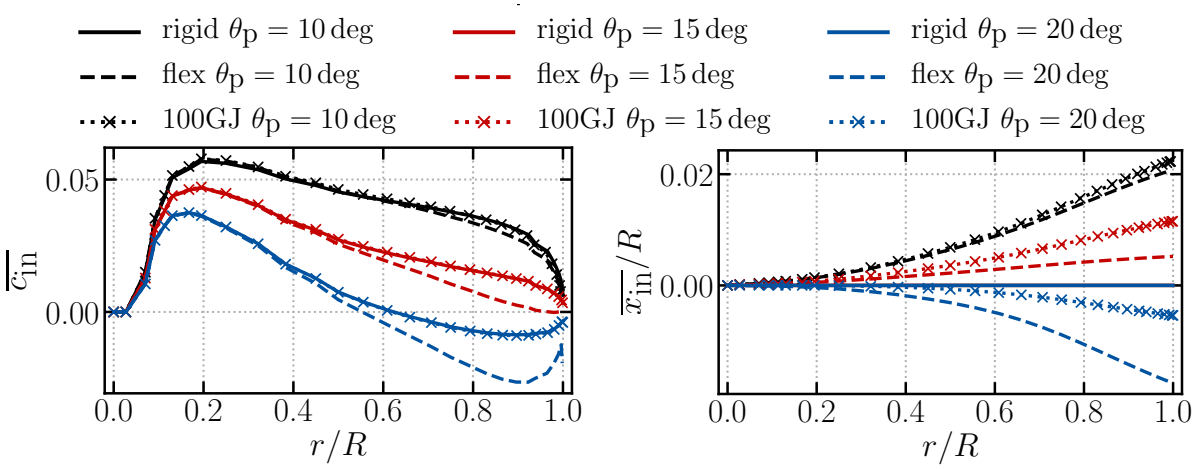

(a) Force coefficient.

(b) Displacement.

Figure 5.3: In-plane force coefficient and displacement for different pitch angles and structural models.

In the previous paragraph we have explained the significant decrease of in-plane and out-of-plane force coefficients of the flexible model with respect to the rigid one as a result of the blade twist. To corroborate this hypothesis, we have also created a fictitious wind turbine model in which the torsional stiffness has been increased by 100 times and it is labelled as "100GJ". If the decrease in in-plane and out-of-plane force coefficients is associated with the twist angle, as we proposed in the previous paragraph, this model should not display such behaviour. This change implies that the blade will not twist under these loads as shown in Figure 5.4b and it makes all the force coefficients (Figures 5.2a, 5.3a and 5.4a) equal to the rigid model. Notice that the blade does not twist (Figure 5.4b) but it bends in the out-of-plane (Figure 5.2b) and the in-plane (Figure 5.3b) directions. It actually bends more in those directions that the original flexible model because when the blade is not allowed to twist, the in-plane and out-of-plane force coefficients are the same as in the rigid case (larger than the flexible case) and, thus, the structure bends more.

In summary, a flexible model predicts significantly lower in-plane and out-of-plane force and pitching moment coefficients with respect to a rigid model. We measure this decrease in force coefficients through the integrated root-bending moments: in the true operation

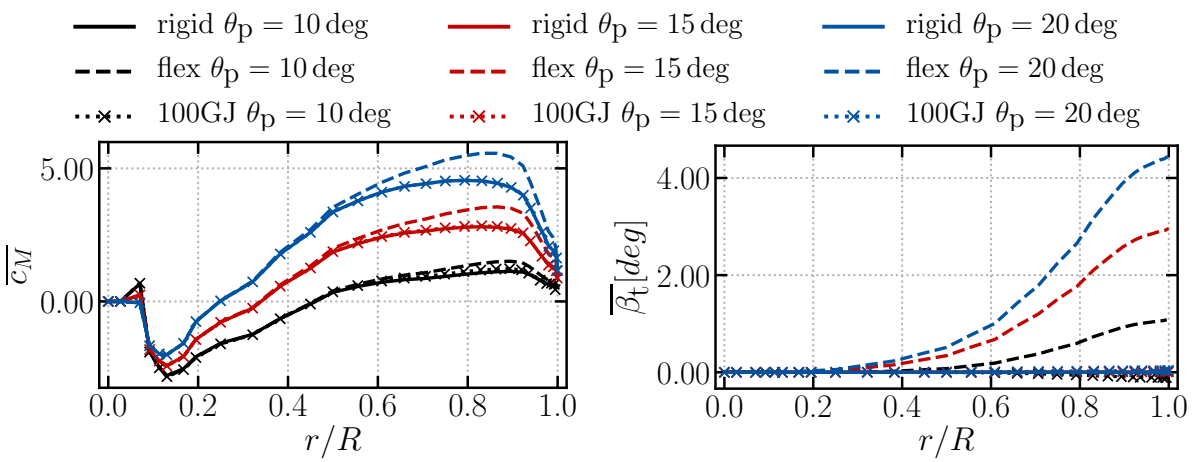

(a) Moment coefficient.

(b) Twist.

Figure 5.4: Moment force coefficient and twist for different pitch angles and structural models.

case of $\theta_p = 15$ deg, the out-of-plane and the in-plane root-bending moments computed with the flexible model are 35% and 24% lower than the rigid approximation. This constitutes a coupled interaction between the structural and the aerodynamic models in the sense that when the blade twists due to a positive pitching moment it deforms towards feather, this reduces the angle of attack and the lift coefficient, thus, the pitching moment becomes more positive and the blade deforms even further towards feather until an equilibrium is reached. This analysis shows the importance of accounting for the change in orientation of the aerodynamic surface due to structural deformation (in particular the twist rotation) to adequately capture forces and deformations.

The previous effect also influences the power production estimation. In the NREL 5 MW wind turbine description [179] the pitch angle at which the nominal power production $E = 5.3$ MW is generated in the above-rated regime is computed with BEM method and shown in Figure 5.5b. We use the collective blade pitch angle in Figure 5.5b to estimate the power based on UVLM for the rigid and the flexible (GEBT) models which is shown in Figure 5.5a. The inaccuracy of UVLM in the computation of the power production described in Section 4.1.1 is also evidenced here in the excess power generation with the rigid model with respect to the reference values. The power generation of the rigid and flexible models at wind speeds of 12 m/s is very similar (3% difference). As wind increases and the blade flexes, as described before in this section, the power generation decreases significantly in the flexible model with differences of 25% and 50% at $U^\infty = 18$ m/s and $U^\infty = 24$ m/s, respectively, with respect to

the rigid model. The decrease in loads associated with the blade twisting has already been reported for the NREL 5 MW wind turbine in aeroelastic simulations with BEM [195] and CFD [196].

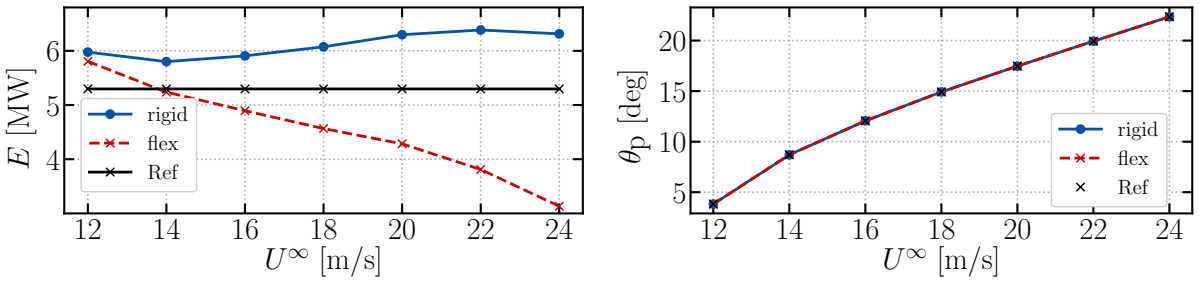

(a) Power generation. (b) Collective blade pitch angle.

Figure 5.5: Power production as a function of the freestream wind speed at blade pitch angle defined in Ref [133]. NREL 5 MW rotor.

Obviously, it is not desirable that the wind turbine generates power below nominal in the above-rated regime. Consequently, the collective pitch angle should be redefined for each wind speed such that the nominal power is achieved for each model. The rigid model should operate at higher pitch angles to reduce the angle of attack and, thus, the power generation. On the contrary, for the flexible model, the pitch should be decreased with respect to the reference approximation. The collective pitch angle that each model requires to generate nominal power is shown in Figure 5.6b and, for the ease of reading, we show how each model effectively generates nominal power in Figure 5.6a.

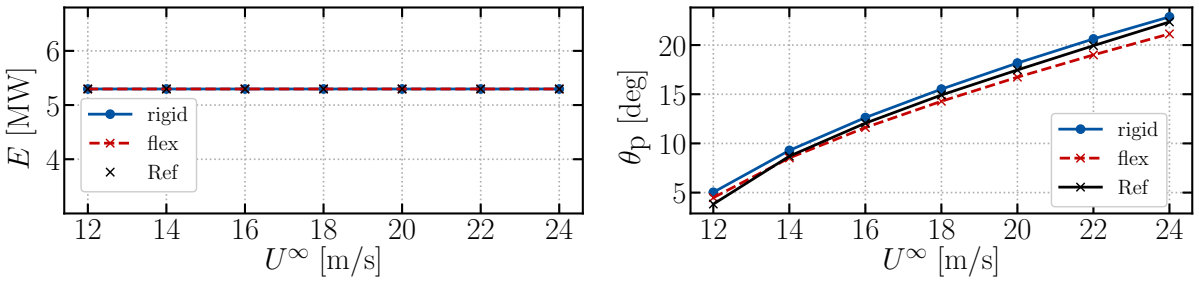

(a) Power generation. (b) Collective blade pitch angle.

Figure 5.6: Rotor collective pitch angle for nominal power production. NREL 5 MW rotor. Ref [133].

As we have seen, the blade pitch significantly modifies loads and power generation and it is currently the main actuation strategy for wind turbine control. Thus, an accurate

computation of the sensitivity of power to collective pitch angle is an important quantity to tune the control parameters according to

$$\left(I+\frac{1}{\omega_{\mathrm{r}}}\left(-\frac{\partial E}{\partial\theta_{\mathrm{p}}}\right)GK_D\right)\ddot{\theta}+\left(\frac{1}{\omega_{\mathrm{r}}}\left(-\frac{\partial E}{\partial\theta_{\mathrm{p}}}\right)GK_P-\frac{E}{\omega_r^2}\right)\dot{\theta}+\left(\frac{1}{\omega_{\mathrm{r}}}\left(-\frac{\partial E}{\partial\theta_{\mathrm{p}}}\right)GK_I\right)\theta=0, \tag{2.128 revisited}$$

to define the natural frequency and the damping ratio of the closed-loop system (Section 2.4.1). Figure 5.7 shows the power generation as a function of the blade pitch at different wind speeds around the pitch angle previously defined in Figure 5.6 at which we obtain nominal power generation.

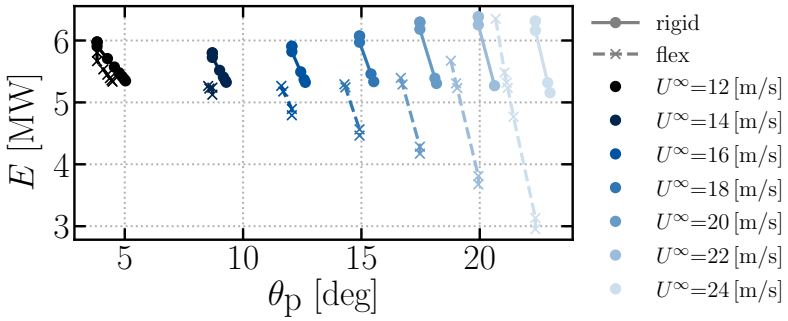

Figure 5.7: Power generation as a function of the collective blade pitch. NREL 5 MW rotor.

The slopes of the power-to-pitch curves in Figure 5.7, computed as the slope of the least squares fit of the points for each wind speed, provide the sensitivity $\mathrm{d}E/\,\mathrm{d}\theta_{\mathrm{p}}$ required to define the gains of the PID controller, such that, through the closed loop system (Equation (2.128)) has the damping and natural frequencies desired. This sensitivity is shown in Figure 5.8. The sensitivity of the flexible model is smaller than the rigid approximation. A better estimation of the sensitivity of power with respect to pitch leads to new PID gains that make the closed-loop natural frequencies and damping ratio closer to the desired ones.

Equation (2.128) describes the behaviour of an onshore wind turbine but the offshore wind turbine shows reduced aerodynamic damping due to platform pitching as we have already described in Section 1.1. To reduce the impact of this effect, it has been proposed in the literature [175] to reduce the P and I gains by 3 and 9 times, respectively, with respect to the onshore values. In the same way, we have computed the new P and I gains with the new power-to-pitch sensitivity and the new values are gathered in Table 5.1. Our model that includes flexibility and accounts for blade twist leads to P and I parameters 23% lower than those of the Reference [179]. We only consider operation in the above-rated regime because

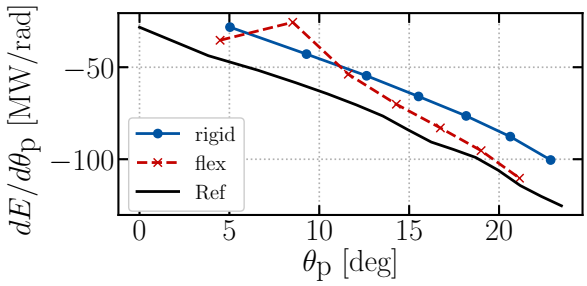

Figure 5.8: Change of the power generation with the pitch angle. NREL 5 MW rotor.

it has more influence on structural loads than the below-rated regime [141]. We will analyse the differences between the reference and the redesigned controllers in Section 5.3.

Table 5.1: PI values at $\theta_p = 0$ deg for the NREL 5 MW wind turbine.

	obtained from Ref [179]			computed from Figure 5.8	
	onshore	offshore	onshore/offshore	onshore	offshore
K_P	0.01883	0.006276	3	0.01455	0.004849
K_I	0.008069	0.0008965	9	0.006235	0.0006927

5.2 Prescribed platform movements

We prescribe sinusoidal motions at the base of the NREL 5 MW wind turbine mounted on the OC3 platform to study if these cases generate unsteady and three-dimensional aerodynamic and nonlinear structural effects. Computations are performed with flexible tower and blades, at incoming wind speed $U^\infty = 11.4$ m/s, rotor velocity $\omega_r = 12.1$ rpm (0.2 Hz) and fixed collective blade pitch angle $\theta_{\mathrm{p}} = 0$ deg. The system dynamics are closely related to the natural frequencies of the system, thus, the natural frequencies associated with platform motions and tower and blade flexibility are recorded in Tables 5.2 and 5.3, respectively. These natural frequencies were obtained in [179] assuming a rigid nacelle-rotor joint and zero rotation velocity.

Table 5.2: NREL 5 MW OC3 natural frequencies. Platform degrees of freedom.

Movement	Surge and sway	Heave	Roll and pitch	Yaw
Natural frequency [Hz]	0.008	0.032	0.034	0.12

Table 5.3: NREL 5 MW OC3 natural frequencies. Tower and blades deformations.

	Tower	Blade	
Movement	fore-aft bending	collective flapwise bending	edgewise bending
Natural frequency [Hz]	0.47	0.71	1.08

5.2.1 Platform pitch

First, we prescribe a pitching motion of the platform, according to

$$\varphi_y = \frac{A}{2}\cos\left(2\pi f_{\mathrm{p}} t\right), \tag{5.1}$$

where φ_y is the platform pitch angle, A is the peak-to-peak movement amplitude, f_{p} is the prescribed movement frequency and t is time. In particular, we have chosen the platform pitch natural frequency (0.034 Hz) for this motion because at this frequency large displacements are likely. We have also simulated twice that frequency (0.068 Hz). We have run the cases with amplitudes of $A = 4\,\mathrm{deg}$ and $A = 0.04\,\mathrm{deg}$. We use the zero-amplitude case ($A = 0\,\mathrm{deg}$) as a reference, that corresponds to an onshore wind turbine configuration.

All cases show negligible differences in mean out-of-plane and in-plane force coefficients as shown, along the spanwise direction r, in Figures 5.9a and 5.9b, respectively. However, each case generates significantly different fluctuations as measured by the standard deviation of these coefficients (Figure 5.10). To quantify these differences, both the out-of-plane and in-plane root-bending moments standard deviation increase by 2.5 times in the case with frequency equal to 0.034 Hz with respect to the fixed case. In the case of 0.068 Hz, the out-of-plane and the in-plane root-bending moments standard deviation increase by 6 and 5 times, respectively, with respect to the fixed case. Even the fixed case shows non-zero standard deviation of the force coefficients because of the gravity loads and the out-of-plane deformations.

The power spectral density of the tower-top displacements for the oscillation at pitching frequency 0.034 Hz has two large peaks of energy at the platform pitching frequency ($f_{\mathrm{p}} = 0.034\,\mathrm{Hz}$) and close to the tower fore-aft bending frequency (0.4 Hz) as shown in Figures 5.11a and 5.11b for the fore-aft and the side-to-side displacements. The peaks associated to the tower fore-aft bending appear at frequencies of around 0.4 Hz which is slightly below the tower bending frequency reported in literature [176] (0.47 Hz) because of a small mistake in the tower mass distribution. In the case of oscillation at 0.068 Hz, the first peak of the frequency spectrum is displaced to that frequency. The fore-aft displacement has the highest

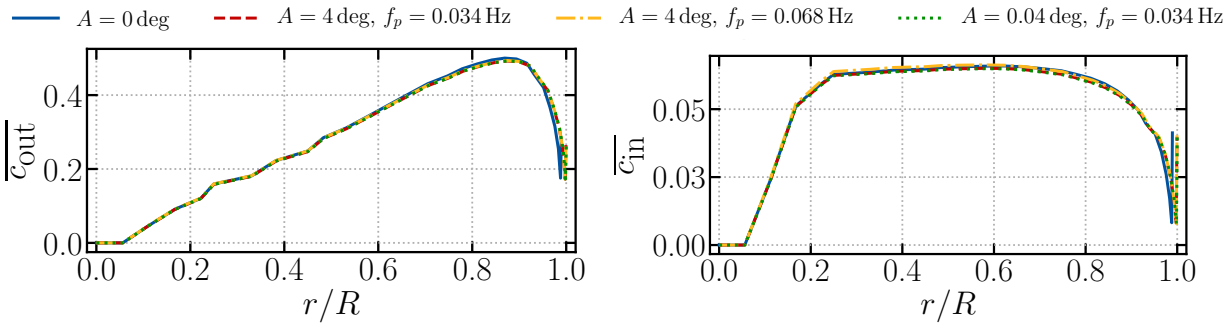

(a) Out-of-plane force coefficient. (b) In-plane force coefficient.

Figure 5.9: Prescribed platform pitch at different frequencies and amplitudes. Mean force coefficients.

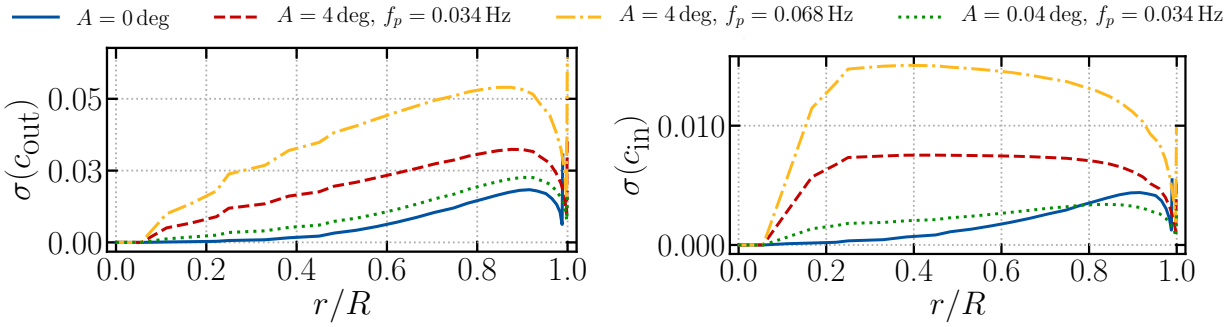

(a) Out-of-plane force coefficient. (b) In-plane force coefficient.

Figure 5.10: Prescribed platform pitch at different frequencies and amplitudes. Standard deviation of the force coefficients.

peak at the prescribed frequency because the platform pitching movement is aligned with the fore-aft displacement. On the other hand, the side-to-side energy content is smaller and centred around the tower bending frequency instead of the forced prescribed pitching frequency. It is important to highlight that the system is being excited at the platform natural frequencies because we consider that the critical case for operation. However, here we aimed to do a systematic analysis, thus, the platform movements are not free but prescribed (Equation (5.1)). Therefore, the platform is not free to move and, thus, cannot resonate at its natural frequencies. On the other hand, the tower and blades are resonating at their natural frequencies.

The tower-top displacements become an excitation at the blade root, thus, the blade forces and displacements show peaks at the previous frequencies (prescribed movement frequency f_{p} and tower bending frequency at 0.4 Hz). Additionally, there are peaks at the rotor

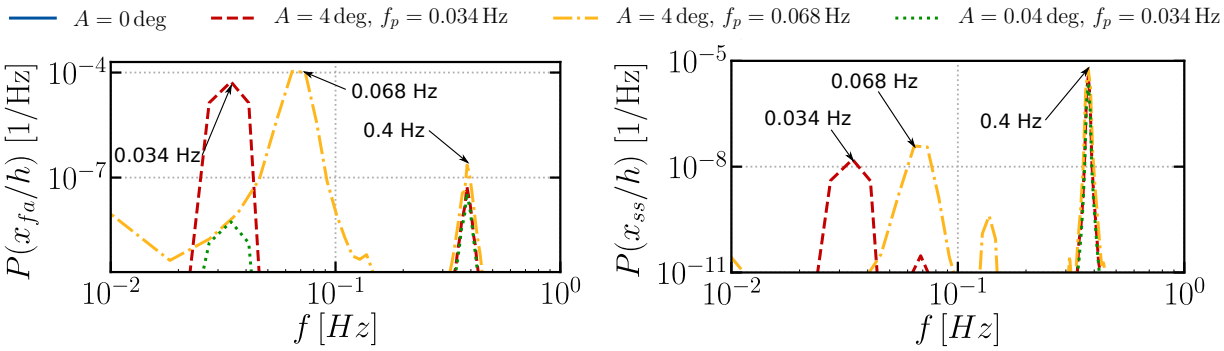

(a) Fore-aft tower top displacement. (b) Side-to-side tower top displacements.

Figure 5.11: Prescribed platform pitch at different frequencies and amplitudes. Tower-top displacements.

rotation frequency (0.2 Hz), the blade passing frequency (0.6 Hz), the tower fore-aft bending frequency (0.4 Hz). Moreover, there are two peaks that appear at 0.17 Hz and 0.23 Hz in the case of oscillation at 0.034 Hz and at 0.13 Hz and 0.27 Hz in the case of oscillation at 0.068 Hz. They do not correspond to any natural frequency of the system or external excitation and they do not appear in the case of small amplitude ($A = 0.04\,\text{deg}$). Thus, we can attribute them to nonlinear couplings in the system. The peak associated to the rotor rotation frequency (0.2 Hz) has, obviously, the same value regardless of the platform motion amplitude. However the peak associated with the platform motion value varies significantly with the movement amplitude. This makes the peak in the case of 0.04 deg almost imperceptible.

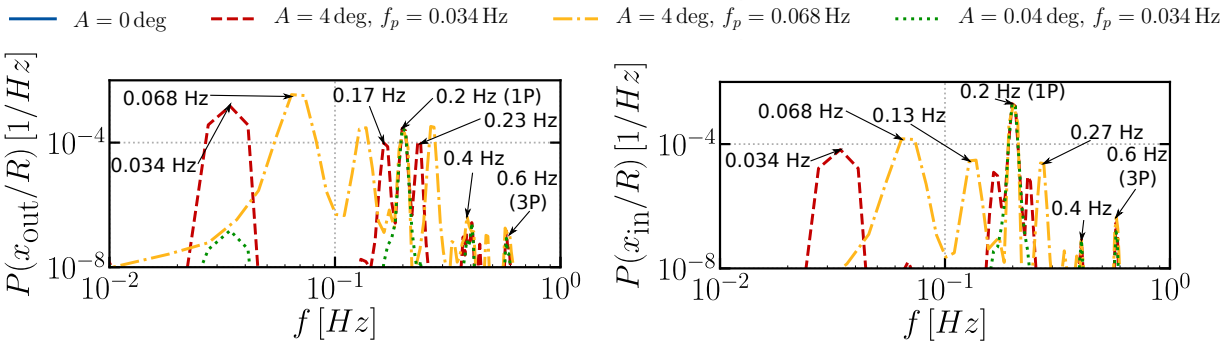

(a) Out-of-plane blade displacement. (b) In-plane blade displacements.

Figure 5.12: Prescribed platform pitch at different frequencies and amplitudes. Blade tip displacements.

Next, we analyse whether these displacements have triggered unsteady aerodynamics or if the quasi-steady approximation is accurate. As described in Section 4.2.3, the reduced

frequency in Equation (4.15) is a good measure of the aerodynamic unsteadiness of a process and is plotted here on the x axis, while the real frequency is shown for some peaks of the spectrum to identify them with natural frequencies. Figures 5.13a and 5.13b show the out-of-plane and the in-plane force coefficients' power spectral densities, respectively, at the spanwise position $r = 0.75R$. Processes with reduced order frequencies below $k < 0.05$ are considered quasi-steady which includes the peak associated with the pitching motion (0.034 Hz, $k \approx 0.005$). The rotor rotation frequency (0.2 Hz, $k \approx 0.03$) is also in the quasi-steady range. There is no relevant energy in the range of the spectrum considered highly unsteady $k > 0.6$.

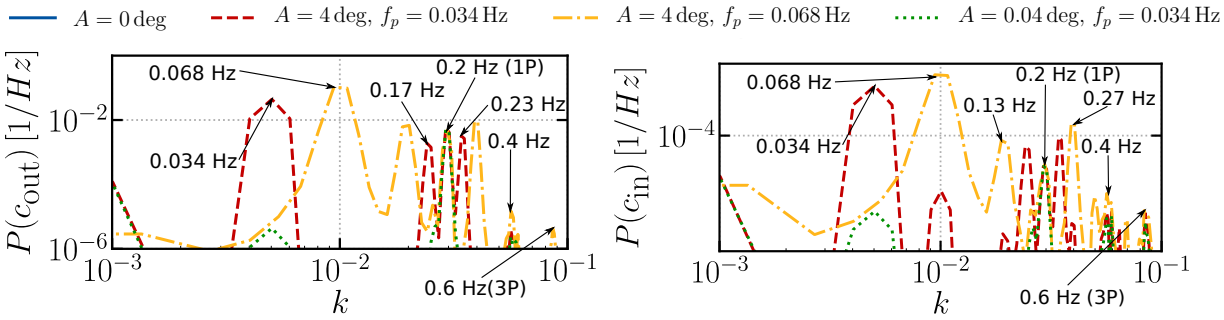

(a) Out-of-plane force coefficient.

(b) In-plane force coefficient.

Figure 5.13: Prescribed platform pitch at different frequencies and amplitudes. Force coefficients at spanwise location $r = 0.75R$.

We analyse the same variables at an inner spanwise position $r = 0.45R$ in Figure 5.14. The pitching motion is still in the quasi-steady range (0.034 Hz, $k \approx 0.01$). However, the rotor rotation (0.2 Hz, $k \approx 0.07$) and the tower and blades generate unsteady aerodynamic phenomena. These vibrations could be of concern for aerodynamic unsteadiness. Nevertheless, this region is usually unsteady due to blade stall [12].

In summary, prescribed pitch movements of the wind turbine base do not modify the average out-of-plane and in-plane force coefficients due to the symmetry of the movement. However, they significantly increase the standard deviation of these force coefficients which is relevant for fatigue load analysis. These movements at the platform natural pitching frequency and twice that frequency induce unsteady aerodynamic forces in the inner region of the blade but they are associated with quasi-steady effects in the outer part of the blade.

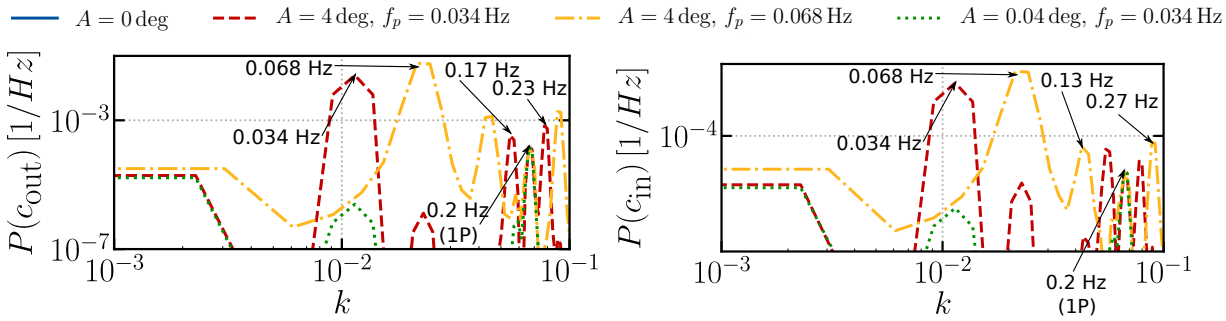

(a) Out-of-plane force coefficient. (b) In-plane force coefficient.

Figure 5.14: Prescribed platform pitch at different frequencies and amplitudes. Force coefficients at spanwise location $r = 0.45R$.

5.2.2 Platform roll

Similar to Equation (5.1) we now prescribe a rolling φ_x motion of the platform at the platform rolling natural frequency (0.034 Hz). Again the mean out-of-plane and in-plane force coefficients do not significantly change with the platform prescribed roll motion as shown in Figures 5.15a and 5.15b, respectively. The standard deviation of these coefficients increases when the motion is prescribed except for the in-plane force coefficient in the tip region $r > 0.8R$ (Figure 5.16b). The in-plane and out-of-plane root-bending moments standard deviation increases by 15% and 46%, respectively, with respect to the fixed case.

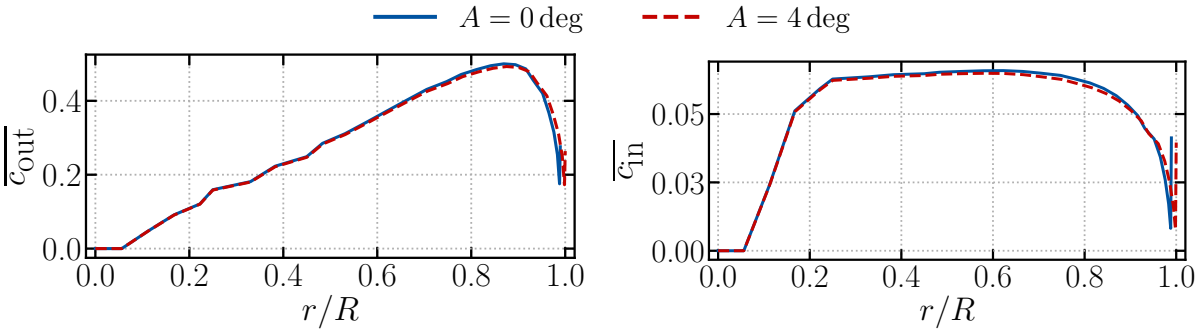

(a) Out-of-plane force coefficient. (b) In-plane force coefficient.

Figure 5.15: Fixed and prescribed platform roll. Mean force coefficients.

The tower-top fore-aft and side-to-side displacements are shown in Figures 5.17a and 5.17b, respectively. The peaks associated with the prescribed rolling frequency (0.034 Hz) and tower bending (0.4 Hz) are equally significant. These peaks are smaller than those found in the case of the prescribed pitching motion in previous Section 5.2.1 because the

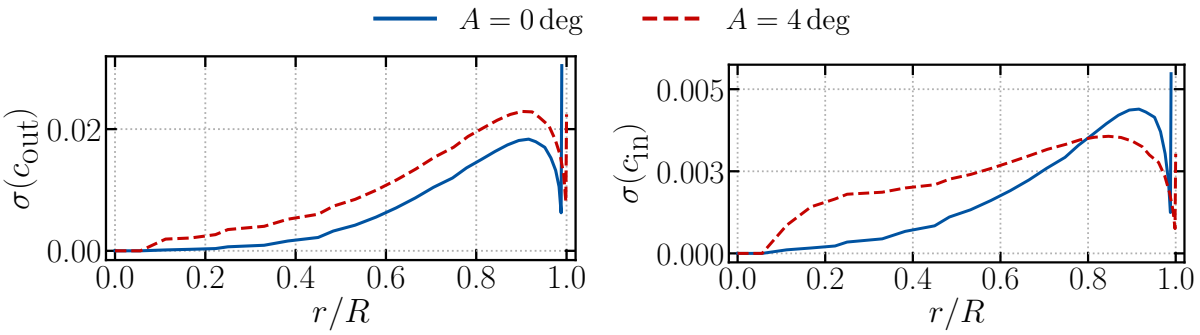

(a) Out-of-plane force coefficient. (b) In-plane force coefficient.

Figure 5.16: Fixed and prescribed platform roll. Force coefficients standard deviation.

interaction with the aerodynamics is not as strong as in the previous case. There are other interactions at twice the rolling frequency (0.07 Hz) and the blade passing frequency (0.6 Hz) in the fore-aft tower-top displacement (Figure 5.17a).

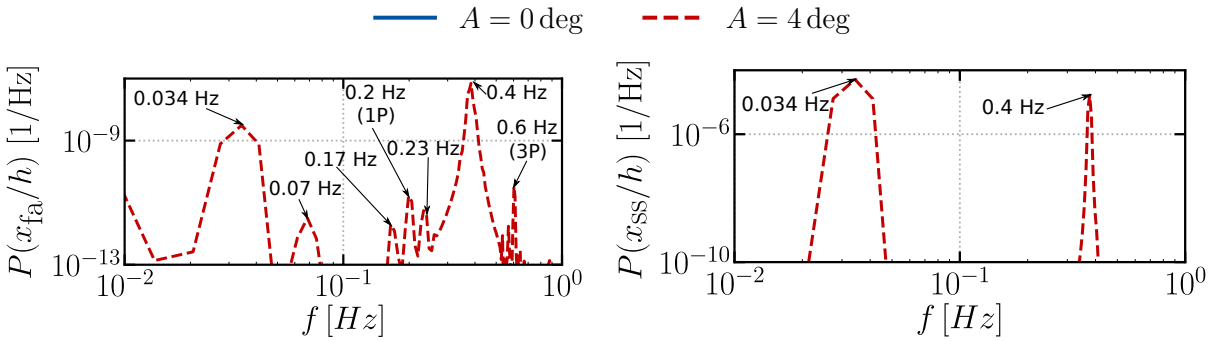

(a) Fore-aft tower top displacement. (b) Side-to-side tower top displacements.

Figure 5.17: Fixed and prescribed platform roll. Tower-top displacements.

In this case, the dominant peak at blade-tip out-of-plane (Figure 5.18a) and in-plane (Figure 5.18b) displacements appears at the rotor rotation frequency (0.2 Hz). However, the prescribed rolling frequency (0.034 Hz) is not significantly excited. There are two peaks in the tower-top fore-aft (Figure 5.17a) and the blade out-of-plane (Figure 5.18a) displacements spectra at frequencies 0.17 Hz and 0.23 linked to nonlinearities in the system.

In summary, the roll motion at the platform natural rolling frequency does not influence the mean out-of-plane and in-plane force coefficients but increases their standard deviation. The tower top displacements occur at the platform pitching motion and close to the tower bending frequency with similar energy content of both of them. This motion does not significantly affect the blade deformation that happens at the rotor frequency and close to

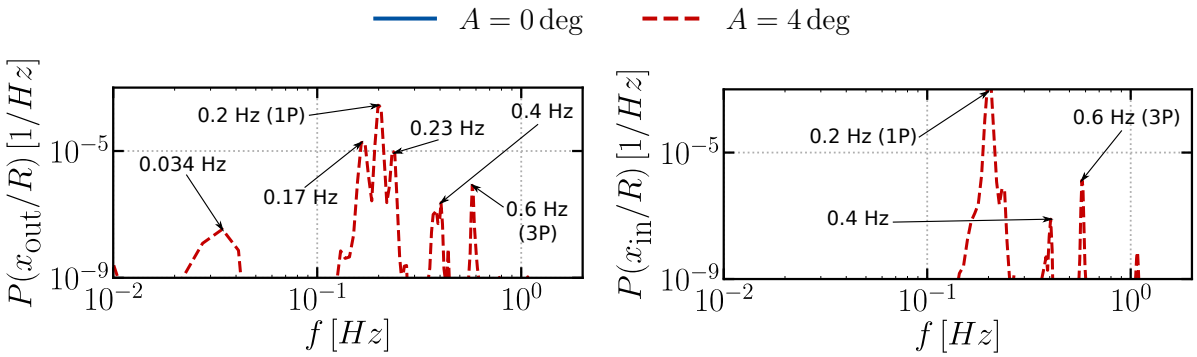

(a) Out-of-plane blade displacement.

(b) In-plane blade displacement.

Figure 5.18: Fixed and prescribed platform roll. Blade-tip displacements.

the blade bending frequencies.

5.3 Floating operation under turbulent wind and waves

Finally, we simulate the floating NREL 5 MW wind turbine with the OC3 platform under turbulent wind and an irregular wave spectrum excitation following the case description in [176]. Similar to Section 4.1.4, we generate a Mann box of turbulence to be convected to the wind turbine based on Taylor's hypothesis. The mean wind speed is $U^{\infty} = 18\,\mathrm{m/s}$ without wind shear and with a turbulence intensity of $I_T = 11\,\%$ using the parameters described in Table 5.4. The time evolution and the power spectral density of the wind velocity at hub height are shown in Figure 5.19. The mean wind speed and the wave spectrum are correlated under the assumption of fully-developed sea [120], in this case, the wave spectrum follows a JONSWAP shape according to Equation (2.117) with a peak spectral period $T_{\mathrm{p}} = 10\,\mathrm{s}$, a significant wave height $h_{\mathrm{s}} = 6\,\mathrm{m}$ and a unidirectional propagation direction along the positive x axis (Figure 2.6) which power spectral density is shown in Figure 5.20. These cases have been run for 150 s starting from steady state scenario of calm sea and constant wind with a time step equivalent to $\Delta\theta = 2\,\mathrm{deg}$ (0.028 s). The system natural frequencies and the characteristic peaks of the waves spectrum have been collected into Table 5.5 to facilitate the next analysis. We simulate the system in open-loop and closed-loop with the two sets of PI gains for offshore operation in Table 5.1 associated to the reference model [175] and the redesign model accounting for UVLM aerodynamics and GEBT structural dynamics (Section 5.1) to evaluate their performance.

Figures 5.21 to 5.24 show the mean value (diamond marker) and minimum-to-maximum

Table 5.4: Mann box input parameters. Floating NREL 5 MW OC3 simulation.

$\alpha_{\mathrm{T}}\epsilon_{\mathrm{T}}^{2/3}$ [m $^{1/3}$ s^{-2}]	L_{T} [m]	Γ_{T}	seed	N_x [-]	N_y [-]	N_z [-]	Δx [m]	Δy [m]	Δz [m]
0.33	29.4	3.9	7	8192	32	32	1.5381	4.6875	4.6875

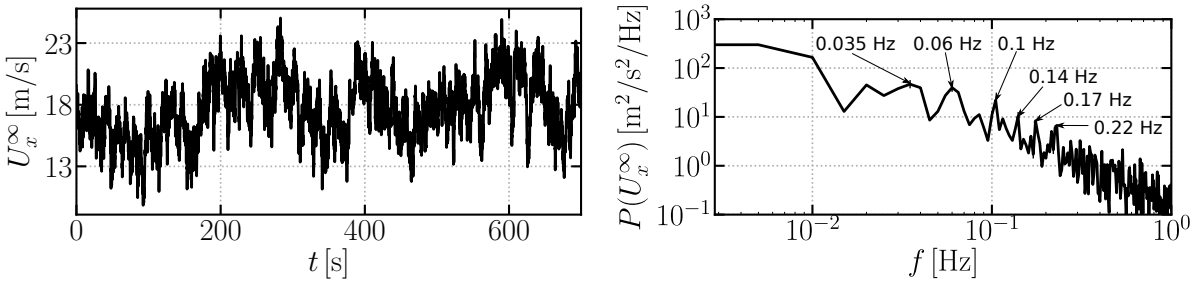

(a) Time evolution. (b) Power spectral density.

Figure 5.19: Longitudinal wind velocity inflow.

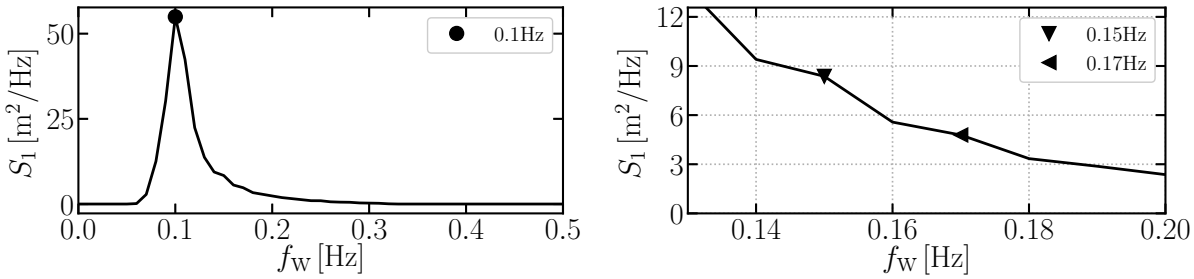

(a) Main view. (b) Zoom.

Figure 5.20: Wave height spectrum.

range (black horizontal lines) of some relevant variables. They also include a vertical dotted line at the equilibrium values, which are zero for all the variables except from the platform surge ($r_{Gx} = 11.6\,\mathrm{m}$), pitch ($\varphi_y = 2.3\,\mathrm{deg}$), blade pitch ($\theta_{\mathrm{p}} = 14.6\,\mathrm{deg}$), rotor velocity ($\omega_{\mathrm{r}} = 12.1\,\mathrm{rpm}$) and generator power ($E = 5.3\,\mathrm{MW}$).

In the open-loop case, the pitch is fixed at the equilibrium value but the rotor velocity can freely change based on the aerodynamic torque that it withstands. In this case, the effect of turbulent wind and waves reduces the system mean power generation by 10% with respect to the closed-loop reference case (Figure 5.24a), thus, the mean rotor speed is also 10% lower (Figure 5.24c) and the mean platform surge (Figure 5.21a) and pitch (Figure 5.21b) are both reduced by 16% with respect to the closed-loop reference case due to the

Table 5.5: NREL 5 MW OC3 natural frequencies and waves spectrum peaks for the JONSWAP multiphysics validation case.

Platform	Movement	Surge and sway	Heave	Roll and pitch	Yaw
	Natural frequency [Hz]	0.008♦	0.032	0.034×	0.12
Tower	Movement	Side-to-side bending		Fore-aft bending	
	Natural frequency [Hz]	0.46		0.47■	
Blades	Movement	Collective flapwise bending		Edgewise bending	
	Natural frequency [Hz]	0.71		1.08	
Rotor	Movement	Rotation frequency (1P)		Blade-passing (3P)	
	Natural frequency [Hz]	0.2★		0.6+	
Waves		Main peak		Minor peaks	
	Natural frequency [Hz]	0.1•		0.15▼, 0.17◀	

Symbols are used in figures to mark frequencies

reduction in thrust associated with the decreasing rotor velocity.

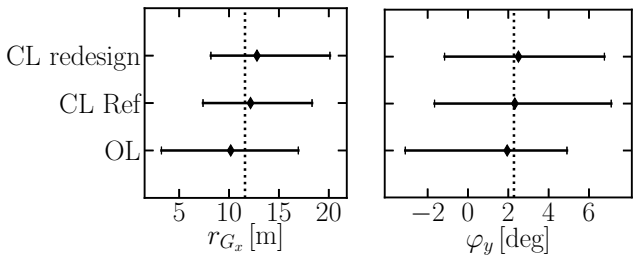

(a) Surge. (b) Pitch.

Figure 5.21: Open-loop (OL) and closed-loop (CL) mean ♦ and minimum-to-maximum range ⊢⊣ of platform motions.

Moreover, in the closed-loop case we can observe smaller maximum-to-minimum ranges in most of the variables with respect to the open-loop reference case because it actively reacts to external perturbations: 20% in surge (Figure 5.21a), 14% in both power (Figure 5.24a) and rotor velocity (Figure 5.24c) maximum-to-minimum range decrease. However, the closed-loop case shows larger ranges in the platform motions with almost zero average (Figure 5.22), a 5% decrease in tower-top fore-aft displacement standard deviation (Figure 5.23a) and a blade-tip out-of-plane deformation standard deviation increase of 8% (Figure 5.23b). In the closed-loop case, the mean out-of-plane and in-plane root bending moments increase by 20% and 2%, respectively, with respect to the open-loop reference case. The standard deviation of the out-of-plane root-bending moment also increases in 3% but the standard deviation of the in-plane force coefficient decreases by 12%, with respect to the

open-loop reference case. This increase in average loads is directly related to the larger power generation that the closed-loop controller achieves with respect to the open-loop.

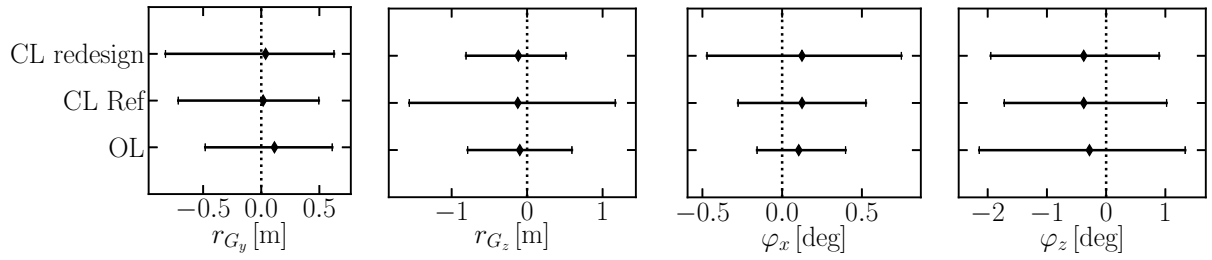

(a) Sway. (b) Heave. (c) Roll. (d) Yaw.

Figure 5.22: Open-loop (OL) and closed-loop (CL) mean ⧫ and minimum-to-maximum range ⊢⊣ of platform motions (continuation).

After the comparison of the reference controller to the open-loop dynamics in the previous paragraph, we now compare the closed-loop redesigned controller to the reference one [175] which is included in the same Figures 5.21 to 5.24. The redesign sets the average blade pitch angle 1% lower than the reference case (Figure 5.24b) but it still keeps the same average generator power and rotor velocity (Figure 5.24) by means of increasing the surge by 5% (Figure 5.21a) and the pitch (Figure 5.21b) by 8% with respect to the reference case. The redesigned controller accounts for the blade flexibility, and, thus, it performs better at keeping the rotor velocity constant than the reference controller based on BEM aerodynamics of rigid blades. The closed-loop redesign case increases the mean out-of-plane root-bending moment 3% with respect to the closed-loop reference case. However, it reduces the standard deviation of the out-of-plane and the in-plane root-bending moments in 8% and 11%, respectively, with respect to the closed-loop reference case which reduces the fatigue loads at blade root.

The platform surge standard deviation is 9% larger than the reference case (Figure 5.21a), however, the platform pitch standard deviation decreases by 9% (Figure 5.21b). Both the tower-top fore-aft and the out-of-plane blade-tip displacement standard deviation are reduced by 18% and 6%, respectively (Figure 5.23). Finally, an increase in blade pitch actuation of 23% in standard deviation achieves an 18% reduction in rotor speed standard deviation (Figure 5.24).

We additionally show the power spectral density of the platform displacements and rotations, the blade pitch, rotor velocity, generator power, the blade tip out-of-plane and the tower-top fore-aft displacement in Figures 5.25 to 5.29.

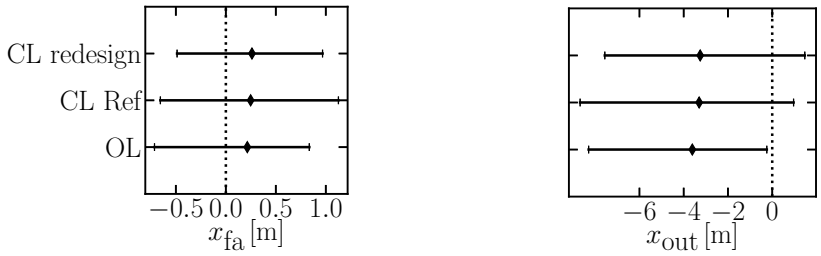

(a) Tower-top fore-aft deflection. (b) Blade-tip out-of-plane deflection.

Figure 5.23: Open-loop (OL) and closed-loop (CL) mean ⧫ and minimum-to-maximum range ⊢ of tower and blade displacements.

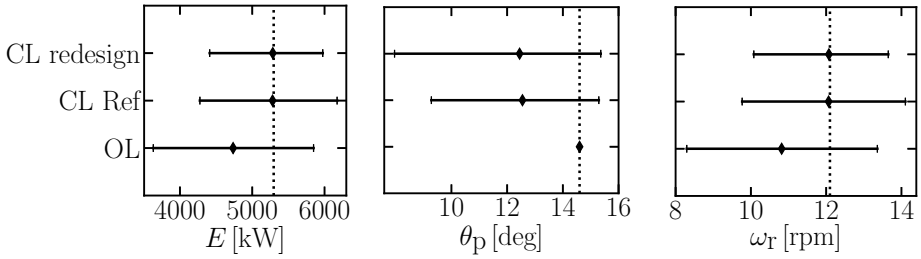

(a) Generator power. (b) Blade pitch. (c) Rotor speed.

Figure 5.24: Open-loop (OL) and closed-loop (CL) mean ⧫ and minimum-to-maximum range ⊢ of control-related variables.

The platform and wind turbine symmetry and the mean wind and waves propagation direction parallel to the positive x axis make surge r_{Gx} (Figure 5.25a) and pitch φ_y (Figure 5.25b) the largest movements of the platform. They show peaks at the platform natural frequencies (0.008$^{\blacklozenge}$ Hz and 0.034$^{\times}$ Hz respectively), the main peak spectral period (0.1$^{\bullet}$ Hz) and other minor peaks (0.15$^{\blacktriangledown}$ Hz and 0.17$^{\blacktriangleleft}$ Hz) of the waves (Figure 5.20). Both the open-loop system and the redesign of the controller based on the flexible aeroelastic model show significantly wider peaks around the wave peak spectral period than the reference controller. The open-loop system shows less energy around the platform natural frequencies and the redesigned closed-loop controller reduces the peak associated with the wave spectrum. The heave displacement (Figure 5.26b) also resonates with the waves showing a peak around 0.1$^{\bullet}$ Hz. However, this peak does not significantly appear in the sway (Figure 5.26a), roll (Figure 5.27a) or yaw (Figure 5.27b) motions because the waves' propagation direction is along the x axis. The two minor peaks in the wave spectrum (0.15$^{\blacktriangledown}$ Hz and 0.17$^{\blacktriangleleft}$ Hz) are significantly smoothed out in the open-loop and the redesigned closed-loop cases (Figures

5.25a and 5.26b).

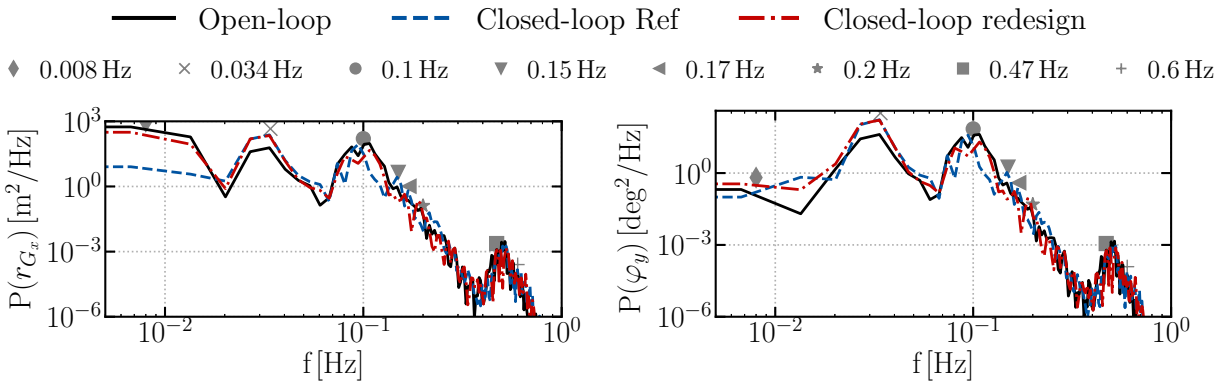

(a) Surge. (b) Pitch.

Figure 5.25: Waves and wind turbulence controlled case (I).

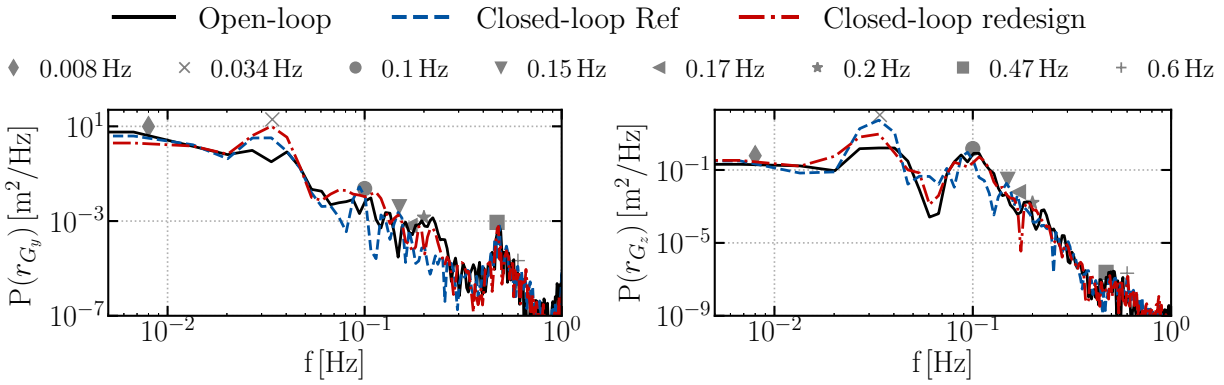

(a) Sway. (b) Heave.

Figure 5.26: Waves and wind turbulence controlled case (II).

Figure 5.28a shows the generator velocity ω_{g} which is the parameter that the controller tries to stabilise and is related to the rotor velocity ω_{r} and the gear-box ratio G as $\omega_g = G\omega_{\mathrm{r}}$. The main actuator strategy is to vary the collective blade pitch θ_{p} angle (Figure 5.28b) to stabilise the power generation of the wind turbine E. Again, the spectra of these variables show peaks at the platform natural frequencies (0.008$^{\blacklozenge}$ Hz and 0.034$^{\times}$ Hz) which are wider for the open-loop and the controller redesign. The latter reduces the highest peaks except in the case of the pitch actuation. The two minor peaks in the wave spectrum (0.15$^{\blacktriangledown}$ Hz and 0.17$^{\blacktriangleleft}$ Hz) are significant in the closed-loop reference case (Figure 5.28a).

Finally, the first blade tip displacement out of the rotor plane x_{out} (Figure 5.29a) has

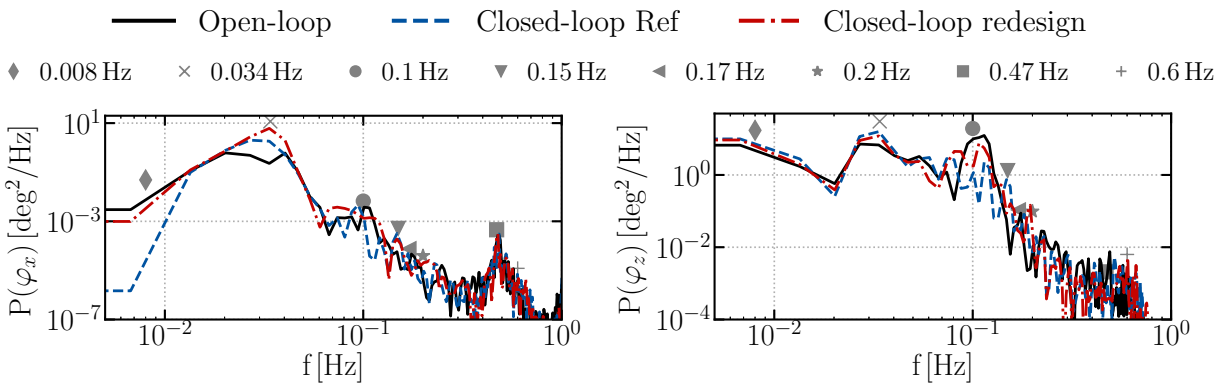

(a) Roll. (b) Yaw.

Figure 5.27: Waves and wind turbulence controlled case (III).

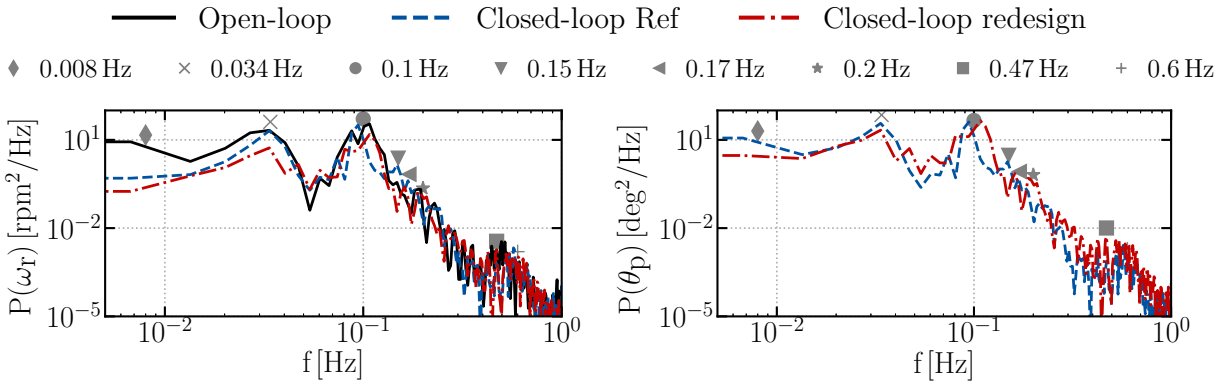

(a) Rotor speed. (b) Blade Pitch.

Figure 5.28: Waves and wind turbulence controlled case (IV).

the most significant peak around the wave spectrum peak but the energy content is quite evenly distributed in the frequency range $f < 0.4\,\text{Hz}$. In the case of the tower top fore-aft displacement x_{fa} (Figure 5.29b) there are three peaks associated to the platform motion ($0.034^{\times}\,\text{Hz}$), the wave peak ($0.1^{\bullet}\,\text{Hz}$) and the tower fore-aft bending frequency ($0.47^{\blacksquare}\,\text{Hz}$). The open-loop and the redesign controllers shift the maximum value of the highest peak but displace it to slightly higher frequencies and make it wider. The open-loop case clearly decreases the peak at platform natural frequencies.

In summary, the open-loop system is well designed to operate at the equilibrium point of a design state without perturbations. Perturbations to the system in form of wind turbulence and waves make the system less efficient with a reduction of power generation and rotor velocity with respect to the desired values. On the other hand, closed-loop controllers are

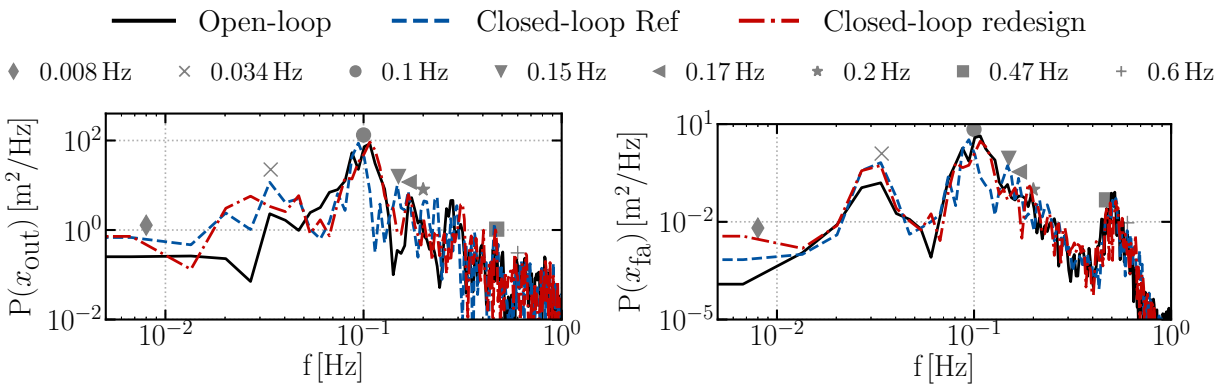

(a) Out of plane blade tip deflection.

(b) Tower top fore-aft deflection.

Figure 5.29: Waves and wind turbulence controlled case (V).

able to track the average rotor velocity and power generation. The controller redesign based on UVLM aerodynamics and GEBT structural dynamics is able to reduce fluctuations with respect to the original redesign. In this case, platform floating dynamics are dominated by motions at the platform natural frequencies and the wave spectrum forcing. The reference controller keeps the highest spectrum peaks narrower and the controller redesign including flexible behaviour slightly reduces this peak but makes it wider.

Chapter 6

Conclusions

We conclude this dissertation with a general overview of the work in Section 6.1, a highlight of the key contributions in Section 6.2 and a series of open questions as a starting point for future work in Section 6.3.

6.1 Summary

Over the last few decades, wind energy has revolutionised electricity generation as wind turbines have increased in height and blade length, become more flexible and are being operated under increasingly complex inflow conditions. All of this is forcing a review of the accuracy of computational methods to enable new designs, because physical phenomena of importance for wind turbine dynamics, such as unsteady and three-dimensional aerodynamics, can no longer be assumed to be negligible. Baseline Blade-Element Momentum (BEM) theory is based on steady assumptions and Large-Eddy Simulation with Actuator Line (LES-AL) employs steady tabulated data for the computation of forces, so these numerical methods are not adequate for problems in which unsteady and three-dimensional effects on blade aerodynamics are involved. Even so, BEM is the industry standard for wind turbine design due to its simplicity and LES-AL provides very useful information about wind turbine wakes and their interaction in the current problems of wind farm optimisation and control. Vortex methods, in particular Unsteady Vortex-Lattice Method (UVLM), inherently account for unsteady and three-dimensional effects which motivated our use of UVLM to gain understanding on these effects, decide if these effects are important and evaluate the range of validity of BEM and LES-AL when the semi-empirical corrections are applied.

Vortex methods have always been important in the research community to describe com-

plex aerodynamic phenomena like the change in induction along the azimuthal direction in wind turbines that resulted in the tip-loss correction for BEM. However, they have not been widely exploited by the wind energy industry. Therefore, in Chapter 3, we have thoroughly assessed the suitability of vortex methods for the computation of wind turbines, including a validation of their accuracy to capture unsteady and three-dimensional effects in comparison with classical airfoil theory. In Chapter 4, we have also compared UVLM against BEM and LES-AL, which evidenced that the main drawback of UVLM is the inability to capture viscous drag because it is based on potential flow theory. We have generated a correction for viscous drag inspired by BEM methodology that obtains forces from the interpolation of steady data (Section 4.1.1). In contrast to BEM, computing the angle of attack in UVLM is complex due to the singularities in the velocity field, thus, we decided to obtain the drag from the steady look-up tables by using the sectional lift provided by UVLM. This choice limited our method to cases where airfoils are in the region between the minimum and the maximum lift values. This is sufficient for the regular operation cases of wind turbines studied here. Regardless of the drag correction, UVLM is not an adequate theory to analyse extreme operation cases in which stall plays a significant role because UVLM assumes attached flow conditions.

In Section 4.2.2, we have analysed yaw cases characterised by significant three-dimensional aerodynamics that are described through the advancing/retreating and skewed-wake effects. The advancing/retreating effect is dominant at the inner region of the blade and we have shown that it is well captured by BEM, UVLM and LES-AL. The skewed-wake effect is dominant at the outer part of the blade and is captured by UVLM and LES-AL. However, this effect is not accounted for by basic BEM. We have shown that the skewed-wake corrections in BEM proposed before this dissertation improve the results where this effect is dominant (near the tip) but mask the advancing/retreating effect at inner spanwise positions. BEM provides accurate predictions of the mean loads along a revolution for yaw angles of less than ten degrees. Beyond this point, it overestimates the changes caused by yaw when compared to UVLM and LES-AL. BEM with the skewed-wake correction shows more severe fluctuations along a revolution than UVLM and LES-AL.

The skewed-wake effect in yaw cases is directly related with the wake shape. Therefore, UVLM requires a free-wake model to capture the wake shape, the skewed-wake effect and the associated loads. This model has medium computational cost (higher than BEM and lower than LES-AL) because it requires computing the influence of wake vorticity on the wake convection velocity which makes the computational cost grow as the number of wake panels

squared. Most implementations of the UVLM demand the same panel size near the wind turbine and far away from it which gives rise to the extremely high computational cost and does not significantly improve the accuracy of the results. In Section 4.1.2, we have proposed a new discretisation scheme for the wake convection equation that permits the use of coarser panels in regions of the flow that have a small influence on the aerodynamic forces and we have achieved a significant reduction of the computational time. In the cases of turbulence run in Section 4.2.3, the new wake convection equation reduces the computational time by 90% with respect to the standard UVLM implementation.

We have also exploited the suitability of UVLM to capture unsteady and three-dimensional effects triggered by turbulent wind that includes time and space velocity variations. Regarding flow unsteadiness, we have shown that the large velocity of the blade makes the reduced frequencies typically very small in the outer part of the blade, thus a large part of the loads spectrum generated by turbulent wind can be resolved by quasi-steady models. However, for the higher frequencies of the turbulent inflow or inboard sections of the blade, unsteady models are needed. In these cases, the unsteady corrections included in BEM perform reasonably well. Regarding the three-dimensional effects coming from the interaction between blade sections that is not accounted for by BEM but inherently accounted for by UVLM, we have discovered significant differences in the estimation of forces between BEM and UVLM. Thus, we have performed a systematic study of the interaction between blade sections for different inflow wavelengths with UVLM and we have generated a filter that turned the two-dimensional approximation of BEM into a three-dimensional prediction that accounts for these interactions. The application of this filter to BEM has led to very good agreement with the UVLM results in turbulent inflows. UVLM cannot account for drag so we could not correct this force and we could not apply this correction to LES-AL because it computes forces from two-dimensional data but it shows some interactions between the blades sections through the feedback of forces to the flow.

Throughout this project, we have relied on the comparison between different computational fidelities to learn about aerodynamics due to the lack of access to high-quality experimental data or high-fidelity CFD computations. In particular, for turbulent flows we needed to reduce the differences between the turbulence seen by BEM and UVLM, that do not interact with the incoming flow, and LES-AL, that modifies the upstream turbulence. In Section 4.1.4, we used a box of artificially generated turbulence as an inflow to an empty LES domain and we let it evolve until a realistic turbulent spectra was obtained to be used as inflow to all the models.

We have focused on studying the effect of increasing length and flexibility of wind turbines blades that is making deformations larger and might require substituting the traditional linear analysis for nonlinear ones. Moreover, the anisotropic behaviour of composite materials requires complex models able to capture all the degrees of freedom of the beam. For these reasons, we have coupled UVLM with a nonlinear geometrically-exact beam theory (GEBT) that is also able to model the tower-rotor joint through a multibody approach based on Lagrange multipliers. On top of that, the base movements of floating wind turbines generate rotor excursions that might reinforce the unsteady and three-dimensional aerodynamic effects. Thus, we have also included a quasi-steady mooring line model, a linear hydrodynamic model based on precomputed added-mass and damping matrices from potential theory and the addition of viscous drag from Morison's equation. We have shown that for increasingly longer and more flexible blades, it is particularly relevant to capture the twist degree of freedom because there is a coupling between the structural deformation in twist and the aerodynamic forces generated that is not routinely included in all the numerical methods. This leads to very significant loads and power overestimation of rigid models with respect to flexible ones. We have also shown that, for the cases we studied, the pitch and roll at platform natural frequencies do not generate significant unsteadiness on the blades away from the root region.

Overall, we have built a medium-fidelity framework for the analysis of aeroelastic phenomena in current and future offshore wind turbines that accounts for unsteady and three-dimensional aerodynamic effects and nonlinear deformations. In this environment, we have studied how to improve controller efficiency by taking advantage of the significant change in aerodynamic loads observed due to blade twist. We confirmed that the open-loop system was not able to maintain the rotor velocity and generated power when the system was perturbed from the equilibrium position by waves and turbulent inflow. We recomputed the PID controller gains based on a model (UVLM and GEBT) that accounts for changes in aerodynamic loading due to flexibility. This controller reduces the fluctuations of rotor velocity and generator power with respect to the controller designed based on the rigid model. Finally, we have briefly explored the possibility of computing wind turbine response to turbulent flows with reduced order models based on UVLM because control design and testing requires extremely efficient computational methods.

6.2 Key contributions

From the work summarised in previous Section 6.1 we highlight here the key contributions of this thesis. To begin with, we have described wind turbine aerodynamics in cases of uniform wind perpendicular to the rotor plane, yaw and turbulent inflows with three models: BEM, UVLM and LES-AL. Moreover, we have described aeroelastic phenomena and the effect of prescribed base movements. The main findings are:

- In cases of uniform inflow perpendicular to the rotor plane, BEM and LES-AL predict very accurate force coefficients along the span. The basic implementation of UVLM predicts the correct out-of-plane force coefficient but needs semiempirical corrections for the in-plane force coefficient due to the absence of viscous drag estimation.

- In yawed inflow, BEM, UVLM and LES-AL predict similar results of root-bending moments, rotor power and thrust coefficients up to yaw angles of approximately ten degrees. For larger yaw angles, BEM overpredicts the decay of forces with the increasing yaw angle and the fluctuations of the loads along a revolution. In the inner region of the blade, dominated by the advancing/retreating effect, the basic BEM, UVLM and LES-AL predict the correct locations of maximum and minimum loading. However, BEM with skewed-wake model fails to do so. In the tip region, dominated by a skewed-wake effect, BEM with a skewed-wake model, UVLM and LES-AL predict the true locations of maximum and minimum loading but the basic BEM fails.

- In cases of turbulent wind, UVLM, BEM with dynamic corrections and LES-AL perform well in the representation of the airfoil-level unsteady aerodynamics. The spanwise interaction between blade sections is relevant for characteristic wavelengths of the inflow smaller than 10 times the airfoil chord. The loads along the spanwise direction are smoother when the three-dimensional effects are accounted for. BEM does not inherently captures these effect but UVLM does.

- The structural twist is coupled to the aerodynamic loading such that models need to account for the twist degree of freedom to adequately predict the wind turbine loading. This effect is particularly relevant in current and future wind turbine blades. First, blades are becoming longer and more flexible which is leading to larger bending and twisting deformations. Moreover, the structural couplings of composite materials generate more blade twist from couplings with the bending deformations. Thus, it

is crucial that future models for wind turbine dynamic loading include aeroelastic behaviour which is not true for some current LES-AL simulations.

- The prescribed platform dynamics in pitch and roll motions at the platform natural frequencies do not trigger unsteady aerodynamic phenomena except from the root region of the blade which is usually already in the unsteady regime due to flow separation.

The knowledge about the physical processes evidenced by the previous analysis and the capabilities of the different aerodynamic fidelities were the foundation to propose numerical improvements to increase the accuracy or reduce the computational cost of some of the aerodynamic solvers. Our main contributions in this field are:

- We provide a methodology to include viscous drag in UVLM computations. The drag is computed from the lift coefficient predicted by UVLM and look-up tables with two-dimensional steady data similar to the BEM procedure.

- We have studied the three-dimensional interaction between blade sections with UVLM and the differences with the two-dimensional approximation. This has lead to a spatial filter to simulate the effect of the interaction between blade sections on the BEM computations.

- We have proposed a turbulence generation method based on two steps. First, a box of artificial turbulence is generated with linearised Navier-Stokes techniques. Second, this turbulence is convected through an LES grid that converges to a flow with realistic turbulence spectra. This method reduces the differences in the turbulence experienced by the wind turbine in LES-AL and BEM and UVLM simulation to reduce the uncertainty of benchmarking analysis.

We have demonstrated that having a model that accounts for the previously described effects is important for the design and analysis of control algorithms. We have illustrated it with a PI controller above rated wind speed whose gains have been adjusted based on the knowledge about the flexible behaviour of the blade. This controller is able to reduce the fluctuations around the target values of generator velocity and power generation.

Finally, we have implemented all of these contributions together with other minor ones required for the simulation of floating wind turbines in the aeroelastic code `SHARPy` which is available open-source [152]. These contributions include:

- Automatic generation of models from the usual available aerodynamic and structural data of wind turbines, that is, sectional data along the tower and blade span.

- Multibody dynamics through Lagrange multipliers for the tower-rotor joint and other constraints for testing and validation.
- A new module to simulate quasi-steady mooring dynamics, linear hydrodynamics from external precomputed damping and added-mass matrices and viscous drag from Morison's equation.
- Collective blade pitch PID control.
- Implementation of the viscous drag correction for UVLM.
- Reduced computational cost of UVLM based on the new wake convection equation and possibility to generate reduced order models.
- Turbulence field input from `TurbSim` and Mann box generators.

`SHARPy` is a state-of-the-art software package thanks to the collaboration with other members of the team. We have provided `SHARPy` with version control and a discussion forum open to everyone on `Github` and `Zenodo` [197], automatic testing of new code contributions with `unittest`, `Travis` and `Codecov` and a theory and user manual on `Read the Docs` [198].

6.3 Future work

We propose some recommendations for future work based on our analysis of offshore wind turbine aeroservoelasticity using low and medium fidelity computational methods. These recommendations arise from the critical view on our work as possible improvements, but also, from the certainty that our work can provide important advantages to solve wind energy problems.

Improve the accuracy of BEM in cases of yaw

In Section 4.2.2, we showed that the corrections applied to BEM to account for the skewed-wake effect provide accurate results up to 10 deg of yaw. Above that angle, they predict an overly large decay of loads and power in the wind turbines compared to UVLM. Until recently, wind turbines did not operate under large yaw angles, however, it is increasingly the case that large yaw angles are being explored as a wake steering mechanism for wind farm optimisation and control. The research community is mainly focusing on accurately

representing the complex wake behaviour but, the evidence presented in this thesis suggests that more effort should be put on the accurate computation of aerodynamic loads under yaw.

Improve the spanwise filter for BEM including drag forces and feedback to the aerodynamics

We have proposed a spanwise filter for BEM loads to account for the spanwise interaction of blade sections based on the analysis of this effect with UVLM in Section 4.1.3. UVLM does not provide an accurate drag estimation so it is not adequate to study three-dimensional effects on the drag force. For this reason, our method does not modify the drag prediction. An analysis with Reynolds-Averaged Navier Stokes simulations should be able to provide this information. Second, our methodology corrects the forces applied on the blade but does not account for the feedback effect that it has on the aerodynamics: the correction modifies the forces on the blade but we do not recompute the new equilibrium between the wake induction and the applied forces. This can be easily implemented with adequate knowledge of a BEM implementation.

Improve the stability of vortex methods

The velocity field induced by vortices is singular in the sense that the velocity tends to infinity at the vortex position. When two vortices come too close together the model predicts high velocities and, thus, they suddenly displace very far away from their original position. This nonphysical behaviour compromises the accuracy and stability of the computation. There is an abundant literature about stabilising the solution through the vortex radius concept which, briefly, defines a distance below which the induced velocity is limited. The vortex radius has to be small enough to capture all the interactions between bound vortices, otherwise, the boundary conditions are not satisfied and the aerodynamic loads estimation is not accurate. Thus, the use of a vortex radius is often not very useful. However, we use a vortex radius for the wake convection because it becomes very unstable and it does not introduce the same problem as in bound vortices. This problem is difficult to tackle because the velocity field associated to a infinitesimal vortices is inherently singular.

Study the change of aerodynamic damping with rotor excursions based on UVLM

The aerodynamic forces generated on the rotor provide damping for the rotor excursions, especially, those in the direction of the hub axis. This damping varies with the relative wind-rotor velocity and, thus, it is strongly influenced by the platform motions of floating wind turbines or the tower deformation. Moreover, this damping is also modified when blades are pitched due to the change in rotor thrust. This damping helps in the stabilisation of the system and, therefore, needs to be accurately controlled. The blade pitch actuation needs to be informed of these phenomena to maximise the efficiency of the control and guarantee the system stability. We have generated an aeroservoelastic framework for the simulation of wind turbines that captures unsteady aerodynamics, coupled nonlinear deformations, platform dynamics and control of wind turbines. It constitutes a suitable environment to study these phenomena that have been reported in literature as a significant problem. This framework is also suitable for the analysis of smart rotors with distributed actuation (i.e. flaps) that can be useful to stabilise the future large offshore wind turbines through new control designs.

Exploit reduced order models based on UVLM aerodynamics

Extremely efficient computational methods are required to perform processes that involve a large number of computations like design or optimisation. They are also useful for controller design such as model predictive control. We believe that there is a significant potential for reduced order models based on UVLM aerodynamics to provide accurate and efficient results to support these processes of design and optimisation. We have performed a short study on the accuracy of UVLM reduced order models in Section 4.2.3 showing very promising results. The accuracy of reduced order models needs to be assessed against higher order models or experiments and our full simulation environment, that provided much information about the wind turbine aeroservoelasticity, could be used to assess the accuracy of the reduced order methods in the future.

Methods to estimate separated flow effects with UVLM

Viscous drag was introduced into UVLM computations in Section 4.1.1 through a procedure that is limited to the region between the minimum and the maximum airfoil lift coefficients where the drag-to-lift relationship is univocal. This limitation comes from the

difficulty of defining the angle of attack in UVLM due to the singularities of the velocity field, similarly to difficulties found in experiments and CFD computations. Overcoming this limitation and also correcting the lift coefficient due to stall would not only make the range of application of the viscous drag addition larger but also tackle other of the main drawbacks of UVLM which is the assumption of attached flow which does not hold for the root region of the blade in complex cases of operation. There are proposals in the literature to measure the angle of attack, other approaches to include viscous drag and options to account for separated flow. Despite the proposed solutions in literature, it not an easy task. On the one hand, including viscous drag and correcting the lift coefficient due to stall would improve the accuracy of UVLM. On the other hand, some of the proposed corrections might show the same problems as BEM: they are based on steady two-dimensional data, not accounting for unsteady and three-dimensional effects. These corrections should be performed carefully to avoid ruining the appealing unsteady and three-dimensional physics inherently provided by UVLM and avoid building a model which might behave like a computationally-expensive BEM.

References

[1] B. Owens. *The wind power story : a century of innovation that reshaped the global energy landscape*. Hoboken: Wiley-IEEE Press, 2019.

[2] G. van Kuik, J. Sørensen, and V. Okulov. "Rotor theories by Professor Joukowsky: Momentum theories". *Progress in Aerospace Sciences* 73 (Feb. 2015), pp. 1–18. DOI: 10.1016/j.paerosci.2014.10.001.

[3] M. R. Luhur, A. L. Manganhar, K. Solangi, A. Q. Jakhrani, K. C. Mukwana, and S. R. Samo. "A review of the state-of-the-art in aerodynamic performance of horizontal axis wind turbines". *Wind and Structures* 22.1 (Jan. 2016), pp. 1–16. DOI: 10.12989/was.2016.22.1.001.

[4] T. Burton, D. Sharpe, N. Jenkins, and E. Bossanyi. *Wind Energy Handbook*. Wiley, 2001.

[5] IEA. *Renewables 2020*. Tech. rep. IEA, 2020. URL: https://www.iea.org/reports/renewables-2020.

[6] V. L. Okulov, J. N. Sørensen, and D. H. Wood. "The rotor theories by Professor Joukowsky: Vortex theories". *Progress in Aerospace Sciences* 73 (Feb. 2015), pp. 19–46. DOI: 10.1016/j.paerosci.2014.10.002.

[7] V. L. Okulov and J. N. Sørensen. "Maximum efficiency of wind turbine rotors using Joukowsky and Betz approaches". *Journal of Fluid Mechanics* 649 (Apr. 2010), p. 497. DOI: 10.1017/s0022112010000509.

[8] G. A. M. van Kuik, J. Peinke, R. Nijssen, D. Lekou, J. Mann, J. N. Sørensen, C. Ferreira, J. W. van-Wingerden, D. Schlipf, et al. "Long-term research challenges in wind energy – a research agenda by the European Academy of Wind Energy". *Wind Energy Science* 1.1 (Feb. 2016), pp. 1–39. DOI: 10.5194/wes-1-1-2016.

[9] P. Veers, K. Dykes, E. Lantz, S. Barth, C. L. Bottasso, O. Carlson, A. Clifton, J. Green, P. Green, et al. "Grand challenges in the science of wind energy". *Science* 366.6464 (Oct. 2019), eaau2027. DOI: 10.1126/science.aau2027.

[10] M. Buhl and A. Manjock. "A Comparison of Wind Turbine Aeroelastic Codes Used for Certification". *44th AIAA Aerospace Sciences Meeting and Exhibit* (Jan. 2006). DOI: 10.2514/6.2006-786.

[11] S. Butterfield, W. Musial, J. Jonkman, and P. Sclavounos. "Engineering Challenges for Floating Offshore Wind Turbines" (Sept. 2007). URL: https://www.osti.gov/biblio/917212.

[12] M. Hansen, J. Sørensen, S. Voutsinas, N. Sørensen, and H. Madsen. "State of the art in wind turbine aerodynamics and aeroelasticity". *Progress in Aerospace Sciences* 42.4 (June 2006), pp. 285–330. DOI: 10.1016/j.paerosci.2006.10.002.

[13] F. Wenz, K. Boorsma, T. Lutz, and E. Krämer. "Cross-correlation-based approach to align turbulent inflow between CFD and lower-fidelity-codes in wind turbine simulations". *Journal of Physics: Conference Series* 1618 (Sept. 2020), p. 062005. DOI: 10.1088/1742-6596/1618/6/062005.

[14] J. Schepers, K. Boorsma, S. Gomez-Iradi, P. Schaffarczyk, H. Madsen, N. Sørensen, W. Shen, T. Lutz, C. Schulz, et al. *Final report of IEA Wind Task 29: Mexnext (Phase 2)*. Tech. rep. ECN-E–14-060. ECN, 2014.

[15] M. Drela. *Flight Vehicle Aerodynamics*. MIT Press Ltd, Feb. 7, 2014.

[16] S. G. Voutsinas. "Vortex methods in aeronautics: how to make things work". *International Journal of Computational Fluid Dynamics* 20.1 (Jan. 2006), pp. 3–18. DOI: 10.1080/10618560600566059.

[17] G.-H. Cottet and P. D. Koumoutsakos. *Vortex Methods*. Cambridge University Press, Jan. 29, 2008. ISBN: 0521061709.

[18] J. Katz and A. Plotkin. *Low-Speed Aerodynamics*. Cambridge University Press, 2001. DOI: 10.1017/cbo9780511810329.

[19] O. C. Yilmaz, O. Pires, X. Munduate, N. N. Sørensen, A. P. Schaffarczyk, T. Reichstein, K. Diakakis, G. Papadakis, E. Daniele, et al. "Summary of the Blind Test Campaign to predict the High Reynolds number performance of DU00-W-210 airfoil". *35th Wind Energy Symposium*. American Institute of Aeronautics and Astronautics, Jan. 2017. DOI: 10.2514/6.2017-0915.

[20] N. Ramos-García, J. N. Sørensen, and W. Z. Shen. "Validation of a three-dimensional viscous-inviscid interactive solver for wind turbine rotors". *Renewable Energy* 70 (Oct. 2014), pp. 78–92. DOI: 10.1016/j.renene.2014.04.001.

[21] F. J. Simoes and J. M. R. Graham. "Application of a free vortex wake model to a horizontal axis wind turbine". *Journal of Wind Engineering and Industrial Aerodynamics* 39.1-3 (Jan. 1992), pp. 129–138. DOI: 10.1016/0167-6105(92)90539-m.

[22] M. Parenteau, É. Laurendeau, and K. Sermeus. "VLM Coupled with 2.5D RANS Sectional Data for High-Lift Design". *2018 AIAA Aerospace Sciences Meeting* (Jan. 2018). DOI: 10.2514/6.2018-1049.

[23] Á. González and X. Munduate. "Unsteady modelling of the oscillating S809 aerofoil and NREL phase VI parked blade using the Beddoes-Leishman dynamic stall model". *Journal of Physics: Conference Series* 75 (July 2007), p. 012020. DOI: 10.1088/1742-6596/75/1/012020.

[24] R. C. Paul and A. Gopalarathnam. "Iteration schemes for rapid post-stall aerodynamic prediction of wings using a decambering approach". *International Journal for Numerical Methods in Fluids* 76.4 (July 2014), pp. 199–222. DOI: 10.1002/fld.3931.

[25] J. D. Anderson. *Fundamentals of Aerodynamics*. McGraw-Hill Science/Engineering/Math, 2001.

[26] B. T. Roesler and B. P. Epps. "Discretization Requirements for Vortex Lattice Methods to Match Unsteady Aerodynamics Theory". *AIAA Journal* 56.6 (June 2018), pp. 2478–2483. DOI: 10.2514/1.j056400.

[27] K. Boorsma, M. Hartvelt, and L. M. Orsi. "Application of the lifting line vortex wake method to dynamic load case simulations". *Journal of Physics: Conference Series* 753 (Sept. 2016), p. 022030. DOI: 10.1088/1742-6596/753/2/022030.

[28] R. J. S. Simpson, R. Palacios, and J. Murua. "Induced-Drag Calculations in the Unsteady Vortex Lattice Method". *AIAA Journal* 51.7 (July 2013), pp. 1775–1779. DOI: 10.2514/1.j052136.

[29] N. P. M. Werter, R. De Breuker, and M. M. Abdalla. "Continuous-Time State-Space Unsteady Aerodynamic Modeling for Efficient Loads Analysis". *AIAA Journal* 56.3 (Mar. 2018), pp. 905–916. DOI: 10.2514/1.j056068.

[30] M. Belessis, P. Chasapogiannis, and S. Voutsinas. "Free-wake modelling of rotor aerodynamics: recent developments and future perspectives". *EWEC 2001* (July 2001).

[31] A. B. Kebbie-Anthony, N. Gumerov, S. Preidikman, B. Balachandran, and S. Azarm. "Fast Multipole Method for Nonlinear, Unsteady Aerodynamic Simulations". *2018 AIAA Modeling and Simulation Technologies Conference* (Jan. 1, 2018). DOI: 10.2514/6.2018-1929.

[32] H. A. Madsen, V. Riziotis, F. Zahle, M. Hansen, H. Snel, F. Grasso, T. Larsen, E. Politis, and F. Rasmussen. "Blade element momentum modeling of inflow with shear in comparison with advanced model results". *Wind Energy* 15.1 (Oct. 2011), pp. 63–81. DOI: 10.1002/we.493.

[33] H. Snel and J. G. Schepers. *Joint investigation of dynamic inflow effects and implementation of an engineering method*. Tech. rep. ECN-C–94-107. ECN, 1995.

[34] H. M. A. Glauert. *A general theory of the autogyro*. Tech. rep. 1111. ARCR R&M, 1926.

[35] D. M. Pitt and D. A. Peters. "Theoretical prediction of dynamic infow derivatives". *Vertica* 5(1) (1983), pp. 21–34.

[36] J. Schepers. "An engineering model for yawed conditions, developed on basis of wind tunnel measurements". *37th Aerospace Sciences Meeting and Exhibit*. American Institute of Aeronautics and Astronautics, Jan. 1999. DOI: 10.2514/6.1999-39.

[37] H. Rahimi, A. Martinez Garcia, B. Stoevesandt, J. Peinke, and G. Schepers. "An engineering model for wind turbines under yawed conditions derived from high fidelity models". *Wind Energy* 21.8 (Mar. 2018), pp. 618–633. DOI: 10.1002/we.2182.

[38] C. Wang, A. Muñoz-Simón, G. Deskos, S. Laizet, R. Palacios, F. Campagnolo, and C. L. Bottasso. "Code-to-code-to-experiment validation of LES-ALM wind farm simulators". *Journal of Physics: Conference Series* 1618 (Sept. 2020), p. 062041. DOI: 10.1088/1742-6596/1618/6/062041.

[39] R. J. Stevens and C. Meneveau. "Flow Structure and Turbulence in Wind Farms". *Annual Review of Fluid Mechanics* 49.1 (Jan. 2017), pp. 311–339. DOI: 10.1146/annurev-fluid-010816-060206.

[40] P. Knebel, A. Kittel, and J. Peinke. "Atmospheric wind field conditions generated by active grids". *Experiments in Fluids* 51.2 (Mar. 2011), pp. 471–481. DOI: 10.1007/s00348-011-1056-8.

[41] H. Heißelmann, J. Peinke, and M. Hölling. "Experimental airfoil characterization under tailored turbulent conditions". *Journal of Physics: Conference Series* 753 (Sept. 2016), p. 072020. DOI: doi:10.1088/1742-6596/753/7/072020.

[42] H. Madsen, P. Fuglsang, J. Romblad, P. Enevoldsen, J. Laursen, L. Jensen, C. Bak, U. S. Paulsen, M. Gaunna, et al. "The DAN-AERO MW Experiments". *48th AIAA Aerospace Sciences Meeting Including the New Horizons Forum and Aerospace Exposition* (Jan. 2010). DOI: 10.2514/6.2010-645.

[43] B. J. Jonkman and L. Kilcher. *TurbSim User 's Guide: Version 1.06.00*. Tech. rep. Report. Sept. 19, 2012.

[44] J. Mann. "The spatial structure of neutral atmospheric surface-layer turbulence". *Journal of Fluid Mechanics* 273 (Aug. 1994), pp. 141–168. DOI: 10.1017/s0022112094001886.

[45] G. Deskos, S. Laizet, and R. Palacios. "WInc3D: A novel framework for turbulence-resolving simulations of wind farm wake interactions". *Wind Energy* 23.3 (Jan. 2020), pp. 779–794. DOI: 10.1002/we.2458.

[46] S. D. Pesmajoglou and J. M. R. Graham. "Prediction of aerodynamic forces on horizontal axis wind turbines in free yaw and turbulence". *Journal of Wind Engineering and Industrial Aerodynamics* 86.1 (May 2000), pp. 1–14. DOI: 10.1016/s0167-6105(99)00125-7.

[47] H. A. Madsen, N. N. Sørensen, and S. Schreck. "Yaw Aerodynamics Analyzed with Three Codes in Comparison with Experiment". *41st Aerospace Sciences Meeting and Exhibit*. American Institute of Aeronautics and Astronautics, Jan. 2003. DOI: 10.2514/6.2003-519.

[48] T. S. Beddoes. *Practical computation of unsteady lift*. Tech. rep. 2.3. Association aeronautique et astronautique de France, 1982.

[49] F. Berger and M. Kühn. "Experimental investigation of dynamic inflow effects with a scaled wind turbine in a controlled wind tunnel environment". *Journal of Physics: Conference Series* 1037 (Jan. 2018), p. 052017. DOI: 10.1088/1742-6596/1037/5/052017.

[50] F. W. Diederich and J. A. Drischler. *Effect of spanwise variations in gust intensity on the lift due to atmospheric turbulence*. Tech. rep. TN-3920. NACA, Apr. 1, 1957.

[51] G. Coupry. "Effect of Spanwise Variation of Gust Velocity on Airplane Response to Turbulence". *Journal of Aircraft* 9.8 (Aug. 1972), pp. 569–574. DOI: 10.2514/3.59037.

[52] G. R. Pirrung, H. A. Madsen, T. Kim, and J. Heinz. "A coupled near and far wake model for wind turbine aerodynamics". *Wind Energy* 19.11 (Mar. 2016), pp. 2053–2069. DOI: 10.1002/we.1969.

[53] J. N. Sørensen. "Aerodynamic Aspects of Wind Energy Conversion". *Annual Review of Fluid Mechanics* 43.1 (Jan. 2011), pp. 427–448. DOI: 10.1146/annurev-fluid-122109-160801.

[54] N. N. Sørensen, F. Zahle, K. Boorsma, and G. Schepers. "CFD computations of the second round of MEXICO rotor measurements". *Journal of Physics: Conference Series* 753 (Sept. 2016), p. 022054. DOI: 10.1088/1742-6596/753/2/022054.

[55] H. A. Madsen, N. N. Sørensen, C. Bak, N. Troldborg, and G. Pirrung. "Measured aerodynamic forces on a full scale 2MW turbine in comparison with EllipSys3D and HAWC2 simulations". *Journal of Physics: Conference Series* 1037 (June 2018), p. 022011. DOI: 10.1088/1742-6596/1037/2/022011.

[56] S. Ehrich, C. Schwarz, H. Rahimi, B. Stoevesandt, and J. Peinke. "Comparison of the Blade Element Momentum Theory with Computational Fluid Dynamics for Wind Turbine Simulations in Turbulent Inflow". *Applied Sciences* 8.12 (Dec. 2018), p. 2513. DOI: 10.3390/app8122513.

[57] K. Boorsma, F. Wenz, K. Lindenburg, M. Aman, and M. Kloosterman. "Validation and accommodation of vortex wake codes for wind turbine design load calculations". *Wind Energ. Sci. Discuss.* (Jan. 2020). DOI: https://doi.org/10.5194/wes-2020-6.

[58] S. Benjanirat, L. N. Sankar, and G. Xu. "Evaluation of Turbulence Models for the Prediction of Wind Turbine Aerodynamics". *ASME 2003 Wind Energy Symposium* (Jan. 1, 2003). DOI: 10.1115/wind2003-517.

[59] Y. Kim, T. Lutz, E. Jost, S. Gomez-Iradi, A. Muñoz-Simón, B. Méndez, N. Lampropoulos, S. N., N. N. Sørensen, et al. *AVATAR Deliverable D2.5: Effects of inflow turbulence on large wind turbines*. Tech. rep. ECN Wind Energy, Dec. 31, 2016.

[60] N. N. Sørensen, N. Ramos-García, S. Voutsinas, E. Jost, and T. Lutz. *Aerodynamics of Large Rotors: Effects of complex inflow for the AVATAR reference rotor and NM80 rotors*. Tech. rep. Stuttgart. Sept. 1, 2017. URL: http://www.eera-avatar.eu/publications-results-and-links/index.html.

[61] H. Rahimi, B. Dose, B. Stoevesandt, and J. Peinke. "Investigation of the validity of BEM for simulation of wind turbines in complex load cases and comparison with experiment and CFD". *Journal of Physics: Conference Series* 749 (Sept. 2016), p. 012015. DOI: 10.1088/1742-6596/749/1/012015.

[62] M. Carrión, M. Woodgate, R. Steijl, G. Barakos, S. Gómez-Iradi, and X. Munduate. "CFD and Aeroelastic Analysis of the MEXICO Wind Turbine". *Journal of Physics: Conference Series* 555 (Dec. 2014), p. 012006. DOI: 10.1088/1742-6596/555/1/012006.

[63] E. Jost, A. Fischer, G. Bangga, T. Lutz, and E. Krämer. "An investigation of unsteady 3D effects on trailing edge flaps". *Wind Energy Science Discussions* (Dec. 2016), pp. 1–21. DOI: 10.5194/wes-2016-48.

[64] S. Gupta and J. G. Leishman. "Comparison Of Momentum And Vortex Methods For The Aerodynamic Analysis Of Wind Turbines". *43rd AIAA Aerospace Sciences Meeting and Exhibit* (Jan. 2005). DOI: 10.2514/6.2005-594.

[65] N. Ramos-García, J. N. Sørensen, and Z. Shen. "Simulations of the Yawed MEXICO Rotor Using a Viscous-Inviscid Panel Method". *Journal of Physics: Conference Series* 524 (June 2018), p. 012026. DOI: 10.1088/1742-6596/524/1/012026.

[66] L. Greco and C. Testa. "Wind turbine unsteady aerodynamics and performance by a free-wake panel method". *Renewable Energy* 164 (Feb. 2021), pp. 444–459. DOI: 10.1016/j.renene.2020.08.002.

[67] M. Jeon, S. Lee, and S. Lee. "Unsteady vortex lattice method coupled with a linear aeroelastic model for horizontal axis wind turbine". *Journal of Renewable and Sustainable Energy* 6.4 (July 2014). ISSN: 1941-7012.

[68] N. Troldborg, J. N. Sørensen, and R. Mikkelsen. "Actuator Line Simulation of Wake of Wind Turbine Operating in Turbulent Inflow". *Journal of Physics: Conference Series* 75 (July 2007), p. 012063. DOI: 10.1088/1742-6596/75/1/012063.

[69] S.-P. Breton, J. Sumner, J. N. Sørensen, K. S. Hansen, S. Sarmast, and S. Ivanell. "A survey of modelling methods for high-fidelity wind farm simulations using large eddy simulation". *Philosophical Transactions of the Royal Society A: Mathematical, Physical and Engineering Sciences* 375.2091 (Mar. 2017), p. 20160097. DOI: 10.1098/rsta.2016.0097.

[70] G. Deskos, S. Laizet, and M. D. Piggott. "Turbulence-resolving simulations of wind turbine wakes". *Renewable Energy* 134 (Apr. 2019), pp. 989–1002. DOI: 10.1016/j.renene.2018.11.084.

[71] S.-P. Breton, W. Shen, and S. Ivanell. "Validation of the actuator disc and actuator line techniques for yawed rotor flows using the New MEXICO experimental data". *Journal of Physics: Conference Series* 854 (May 2017), p. 012005. DOI: 10.1088/1742-6596/854/1/012005.

[72] P. Zhang and S. Huang. "Review of aeroelasticity for wind turbine: Current status, research focus and future perspectives". *Frontiers in Energy* 5.4 (Dec. 2011), pp. 419–434. ISSN: 1673-7504. DOI: 10.1007/s11708-011-0166-6. URL: https://doi.org/10.1007/s11708-011-0166-6.

[73] M. Eder and R. Bitsche. "A qualitative analytical investigation of geometrically non-linear effects in wind turbine blade cross sections". *Thin-Walled Structures* 93 (Aug. 2015), pp. 1–9. DOI: 10.1016/j.tws.2015.03.007.

[74] R. Palacios and C. E. S. Cesnik. "Cross-Sectional Analysis of Nonhomogeneous Anisotropic Active Slender Structures". *AIAA Journal* 43.12 (Dec. 2005), pp. 2624–2638. DOI: 10.2514/1.12451.

[75] C. J. Faccio Júnior, A. C. Pegoraro Cardozo, V. Monteiro Júnior, and A. Gay Neto. "Modeling wind turbine blades by geometrically-exact beam and shell elements: A comparative approach". *Engineering Structures* 180 (Feb. 2019), pp. 357–378. DOI: 10.1016/j.engstruct.2018.09.032.

[76] C. E. S. Cesnik and D. H. Hodges. "VABS: A New Concept for Composite Rotor Blade Cross-Sectional Modeling". *Journal of the American Helicopter Society* 42.1 (Jan. 1997), pp. 27–38. DOI: 10.4050/jahs.42.27.

[77] D. H. Hodges. *Nonlinear Composite Beam Theory*. American Institute of Aeronautics and Astronautics, Apr. 2006. DOI: 10.2514/4.866821.

[78] J. M. Gere. *Mechanics of Materials*. Thomson-Engineering, 2003.

[79] A. R. S. Bramwell, G. Done, and D. Balmford. *Bramwell 's Helicopter Dynamics*. Butterworth-Heinemann, 2001.

[80] H. Hesse and R. Palacios. "Consistent structural linearisation in flexible-body dynamics with large rigid-body motion". *Computers & Structures* 110-111 (Nov. 2012), pp. 1–14. DOI: 10.1016/j.compstruc.2012.05.011.

[81] E. Reissner. "On one-dimensional finite-strain beam theory: The plane problem". *Zeitschrift für angewandte Mathematik und Physik ZAMP* 23.5 (Sept. 1972), pp. 795–804. DOI: 10.1007/bf01602645.

[82] J. Simo and L. Vu-Quoc. "On the dynamics in space of rods undergoing large motions — A geometrically exact approach". *Computer Methods in Applied Mechanics and Engineering* 66.2 (Feb. 1988), pp. 125–161. DOI: 10.1016/0045-7825(88)90073-4.

[83] O. A. Bauchau and C. Hong. "Nonlinear Composite Beam Theory". *Journal of Applied Mechanics* 55.1 (1988), p. 156. DOI: 10.1115/1.3173622.

[84] D. H. Hodges. *Finite rotation and nonlinear beam kinematics*. Tech. rep. NASA, 1987.

[85] M. Géradin and A. Cardona. *Flexible Multibody Dynamics: A Finite Element Approach*. Wiley, 2001.

[86] R. Palacios, J. Murua, and R. Cook. "Structural and Aerodynamic Models in Nonlinear Flight Dynamics of Very Flexible Aircraft". *AIAA Journal* 48.11 (Nov. 2010), pp. 2648–2659. DOI: 10.2514/1.j050513.

[87] D. H. Hodges. "A mixed variational formulation based on exact intrinsic equations for dynamics of moving beams". *International Journal of Solids and Structures* 26.11 (1990), pp. 1253–1273. DOI: 10.1016/0020-7683(90)90060-9.

[88] Q. Wang, M. A. Sprague, J. Jonkman, N. Johnson, and B. Jonkman. "BeamDyn: a high-fidelity wind turbine blade solver in the FAST modular framework". *Wind Energy* 20.8 (Mar. 2017), pp. 1439–1462. DOI: 10.1002/we.2101.

[89] W. Collier and J. M. Sanz. "Comparison of linear and non-linear blade model predictions in Bladed to measurement data from GE 6MW wind turbine". *Journal of Physics: Conference Series* 753 (Sept. 2016), p. 082004. DOI: 10.1088/1742-6596/753/8/082004.

[90] D. A. Danielson and D. H. Hodges. "Nonlinear Beam Kinematics by Decomposition of the Rotation Tensor". *Journal of Applied Mechanics* 54.2 (1987), p. 258. DOI: 10.1115/1.3173004.

[91] T. M. Wasfy and A. K. Noor. "Computational strategies for flexible multibody systems". *Applied Mechanics Reviews* 56.6 (Nov. 2003), pp. 553–613. DOI: https://doi.org/10.1115/1.1590354.

[92] K. Holm-Jørgensen and S. R. K. Nielsen. "System reduction in multibody dynamics of wind turbines". *Multibody System Dynamics* 21.2 (Oct. 2008), pp. 147–165. DOI: 10.1007/s11044-008-9132-4.

[93] C. Pavese, T. Kim, Q. Wang, J. Jonkman, and M. A. Sprague. "HAWC2 and BeamDyn: Comparison Between Beam Structural Models for Aero-Servo-Elastic Frameworks" (Aug. 2016). URL: https://www.osti.gov/biblio/1304572.

[94] V. Riziotis, S. Voutsinas, E. Politis, P. Chaviaropoulos, A. M. Hansen, H. Madsen, and F. Rasmussen. "Identification of structural non-linearities due to large deflections on a 5MW wind turbine blade". *EWEA 2008* (Mar. 2008).

[95] S. Guntur, J. M. Jonkman, B. Jonkman, Q. Wang, M. A. Sprague, M. Hind, R. Sievers, and S. J. Schreck. "FAST v8 Verification and Validation for a MW-scale Wind Turbine with Aeroelastically Tailored Blades". *34th Wind Energy Symposium*. American Institute of Aeronautics and Astronautics, Jan. 2016. DOI: 10.2514/6.2016-1008.

[96] J. Murua, R. Palacios, and J. M. R. Graham. "Applications of the unsteady vortex-lattice method in aircraft aeroelasticity and flight dynamics". *Progress in Aerospace Sciences* 55 (Nov. 2012), pp. 46–72. DOI: 10.1016/j.paerosci.2012.06.001.

[97] A. Del Carre and R. Palacios. "Efficient Time-Domain Simulations in Nonlinear Aeroelasticity". *AIAA Scitech 2019 Forum* (Jan. 2019). DOI: 10.2514/6.2019-2038.

[98] R. J. Simpson and R. Palacios. "Numerical aspects of nonlinear flexible aircraft flight dynamics modeling". *54th AIAA/ASME/ASCE/AHS/ASC Structures, Structural Dynamics, and Materials Conference* (Apr. 2013). DOI: 10.2514/6.2013-1634.

[99] V. Riziotis and S. Voutsinas. "Advanced aeroelastic modeling of complete wind turbine configurations in view of assessing stability characteristics". *European Wind Energy Conference and Exhibition 2006, EWEC 2006* 3.Athens (Feb. 2006).

[100] L. Wang, X. Liu, N. Renevier, M. Stables, and G. M. Hall. "Nonlinear aeroelastic modelling for wind turbine blades based on blade element momentum theory and geometrically exact beam theory". *Energy* 76 (Nov. 2014), pp. 487–501. DOI: 10.1016/j.energy.2014.08.046.

[101] B. F. Ng, H. Hesse, R. Palacios, J. M. R. Graham, and E. C. Kerrigan. "Aeroservoelastic state-space vortex lattice modeling and load alleviation of wind turbine blades". *Wind Energy* 18.7 (Apr. 2014), pp. 1317–1331. DOI: 10.1002/we.1752.

[102] B. F. Ng, R. Palacios, and J. M. R. Graham. "Model-based aeroelastic analysis and blade load alleviation of offshore wind turbines". *International Journal of Control* 90.1 (July 2017), pp. 15–36. DOI: 10.1080/00207179.2015.1068456.

[103] T. Kim, A. M. Hansen, and K. Branner. "Development of an anisotropic beam finite element for composite wind turbine blades in multibody system". *Renewable Energy* 59 (Nov. 2013), pp. 172–183. DOI: 10.1016/j.renene.2013.03.033.

[104] C. Pavese, C. Tibaldi, F. Zahle, and T. Kim. "Aeroelastic multidisciplinary design optimization of a swept wind turbine blade". *Wind Energy* 20.12 (Aug. 2017), pp. 1941–1953. DOI: https://doi.org/10.1002/we.2131.

[105] M. K. McWilliam, F. Zahle, A. Dicholkar, D. Verelst, and T. Kim. "Optimal Aero-Elastic Design of a Rotor with Bend-Twist Coupling". *Journal of Physics: Conference Series* 1037 (June 2018), p. 042009. DOI: 10.1088/1742-6596/1037/4/042009.

[106] M. H. Hansen. "Aeroelastic instability problems for wind turbines". *Wind Energy* 10.6 (2007), pp. 551–577. DOI: 10.1002/we.242.

[107] G. Bir and J. Jonkman. "Aeroelastic Instabilities of Large Offshore and Onshore Wind Turbines". *Journal of Physics: Conference Series* 75 (July 2007), p. 012069. DOI: 10.1088/1742-6596/75/1/012069.

[108] J. Chung and G. M. Hulbert. "A Time Integration Algorithm for Structural Dynamics With Improved Numerical Dissipation: The Generalized-α Method". *Journal of Applied Mechanics* 60.2 (June 1993), pp. 371–375. DOI: https://doi.org/10.1115/1.2900803.

[109] L. Wang and B. Sweetman. "Multibody dynamics of floating wind turbines with large-amplitude motion". *Applied Ocean Research* 43 (Oct. 2013), pp. 1–10. DOI: 10.1016/j.apor.2013.06.004.

[110] A. Ibrahimbegović and S. Mamouri. "On rigid components and joint constraints in nonlinear dynamics of flexible multibody systems employing 3D geometrically exact beam model". *Computer Methods in Applied Mechanics and Engineering* 188.4 (Aug. 2000), pp. 805–831. DOI: https://doi.org/10.1016/S0045-7825(99)00363-1.

[111] O. A. Bauchau. *Flexible multibody dynamics*. Solid mechanics and its applications, v. 176. Dordrecht: Springer, 2011.

[112] B. Simeon. *Computational Flexible Multibody Dynamics*. Springer-Verlag GmbH, 2013. ISBN: 9783642351570.

[113] O. A. Bauchau, C. L. Bottasso, and L. Trainelli. "Robust integration schemes for flexible multibody systems". *Computer Methods in Applied Mechanics and Engineering* 192.3-4 (Jan. 2003), pp. 395–420. DOI: https://doi.org/10.1016/S0045-7825(02)00519-4.

[114] C. L. Bottasso, O. A. Bauchau, and A. Cardona. "Time-Step-Size-Independent Conditioning and Sensitivity to Perturbations in the Numerical Solution of Index Three Differential Algebraic Equations". *SIAM Journal on Scientific Computing* 29.1 (Jan. 2007), pp. 397–414. DOI: 10.1137/050638503.

[115] C. L. Bottasso, D. Dopico, and L. Trainelli. "On the optimal scaling of index three DAEs in multibody dynamics". *Multibody System Dynamics* 19.1-2 (June 2007), pp. 3–20. DOI: 10.1007/s11044-007-9051-9.

[116] Y. Li, A. Castro, J. Martin, T. Sinokrot, W. Prescott, and P. Carrica. "Coupled computational fluid dynamics/multibody dynamics method for wind turbine aero-servo-elastic simulation including drivetrain dynamics". *Renewable Energy* 101 (Feb. 2017), pp. 1037–1051. DOI: 10.1016/j.renene.2016.09.070.

[117] N. Ramos-Garcıa, M. Sessarego, and S. González Horcas. "Aero-hydro-servo-elastic coupling of a multi-body finite-element solver and a multi-fidelity vortex method". *Wind Energy* 24.5 (Nov. 2020), pp. 481–501. DOI: https://doi.org/10.1002/we.2584.

[118] C. Bottasso, A. Croce, C. Riboldi, and Y. Nam. "Multi-layer control architecture for the reduction of deterministic and non-deterministic loads on wind turbines". *Renewable Energy* 51 (Mar. 2013), pp. 159–169. DOI: 10.1016/j.renene.2012.08.079.

[119] O. Bauchau, C. Bottasso, and Y. Nikishkov. "Modeling rotorcraft dynamics with finite element multibody procedures". *Mathematical and Computer Modelling* 33.10-11 (May 2001), pp. 1113–1137. DOI: 10.1016/s0895-7177(00)00303-4.

[120] J. N. Newman. *Marine Hydrodynamics*. Cambridge: The MIT Press, 2018.

[121] M. Borg and M. Collu. "Offshore floating vertical axis wind turbines, dynamics modelling state of the art. Part III: Hydrodynamics and coupled modelling approaches". *Renewable and Sustainable Energy Reviews* 46 (June 2015), pp. 296–310. DOI: http://dx.doi.org/10.1016/j.rser.2014.10.100.

[122] J. Azcona, D. Palacio, X. Munduate, L. González, and T. A. Nygaard. "Impact of mooring lines dynamics on the fatigue and ultimate loads of three offshore floating wind turbines computed with IEC 61400-3 guideline". *Wind Energy* 20.5 (Oct. 2016), pp. 797–813. DOI: 10.1002/we.2064.

[123] M. I. Kvittem, E. E. Bachynski, and T. Moan. "Effects of Hydrodynamic Modelling in Fully Coupled Simulations of a Semi-submersible Wind Turbine". *Energy Procedia* 24 (2012), pp. 351–362. DOI: 10.1016/j.egypro.2012.06.118.

[124] M. A. Chella, A. Tørum, and D. Myrhaug. "An Overview of Wave Impact Forces on Offshore Wind Turbine Substructures". *Energy Procedia* 20 (2012), pp. 217–226. DOI: 10.1016/j.egypro.2012.03.022.

[125] H. Baek and G. E. Karniadakis. "A convergence study of a new partitioned fluid–structure interaction algorithm based on fictitious mass and damping". *Journal of Computational Physics* 231.2 (Jan. 2012), pp. 629–652. DOI: 10.1016/j.jcp.2011.09.025.

[126] K. Hasselmann, T. Barnett, E. Bouws, H. Carlson, D. Cartwright, K. Enke, J. Ewing, H. Gienapp, D. Hasselmann, et al. *Measurements of wind-wave growth and swell decay during the Joint North Sea Wave Project (JONSWAP).* Tech. rep. Deutsches hydrographisches institut - Hamburg, 1973.

[127] J. N. Newman. "Second-order, Slowly-varying Forces on Vessels in Irregular Waves". *Symp, Dynamics of Marine Vehicles and Structures in Waves* (1974). Ed. by M. E. L. London, pp. 182–6.

[128] I. Bayati, J. Jonkman, A. Robertson, and A. Platt. "The effects of second-order hydrodynamics on a semisubmersible floating offshore wind turbine". *Journal of Physics: Conference Series* 524 (June 2014), p. 012094. DOI: 10.1088/1742-6596/524/1/012094.

[129] T. T. Tran and D.-H. Kim. "A CFD study of coupled aerodynamic-hydrodynamic loads on a semisubmersible floating offshore wind turbine". *Wind Energy* 21.1 (Nov. 2017), pp. 70–85. DOI: 10.1002/we.2145.

[130] Chakrabarti, ed. *Numerical Models in Fluid-Structure Interaction*. WIT PR, Sept. 1, 2000. ISBN: 1853128376. URL: https://www.ebook.de/de/product/21490354/numerical_models_in_fluid_structure_interaction.html.

[131] R. MacCamy and R. Fuchs. *Wave Forces on Piles: a Diffraction Theory*. Tech. rep. 69. US Army Corps of Engineers, Beach Erosion Board, 1954.

[132] J. Azcona Armendáriz. "Computational and Experimental Modelling of Mooring Lines Dynamics for Offshore Floating Wind Turbines". PhD thesis. Navales, 2015.

[133] J. M. Jonkman. "Dynamics of offshore floating wind turbines-model development and verification". *Wind Energy* 12.5 (July 2009), pp. 459–492. DOI: 10.1002/we.347.

[134] *Theory manual Map++*. Oct. 14, 2020. URL: https://map-plus-plus.readthedocs.io/en/latest/theory.html.

[135] D. Matha, M. Schlipf, A. Cordle, R. Pereira, and J. Jonkman. *Challenges in Simulation of Aerodynamics, Hydrodynamics, and Mooring-Line Dynamics of Floating Offshore Wind Turbines*. Tech. rep. NREL/CP-5000-50544. NREL, Oct. 1, 2011.

[136] J. M. Jonkman and D. Matha. "Dynamics of offshore floating wind turbines-analysis of three concepts". *Wind Energy* 14.4 (Jan. 2011), pp. 557–569. DOI: 10.1002/we.442.

[137] B. J. Koo, A. J. Goupee, R. W. Kimball, and K. F. Lambrakos. "Model Tests for a Floating Wind Turbine on Three Different Floaters". *Journal of Offshore Mechanics and Arctic Engineering* 136.2 (Mar. 2014). DOI: 10.1115/1.4024711.

[138] A. J. Goupee, R. W. Kimball, and H. J. Dagher. "Experimental observations of active blade pitch and generator control influence on floating wind turbine response". *Renewable Energy* 104 (Apr. 2017), pp. 9–19. DOI: 10.1016/j.renene.2016.11.062.

[139] H. M. Johlas, L. A. Martınez-Tossas, M. J. Churchfield, M. A. Lackner, and D. P. S. Schmidt. "Floating platform effects on power generation in spar and semisubmersible wind turbines". *Wind Energy* 24.8 (Jan. 2021), pp. 901–916. DOI: https://doi.org/10.1002/we.2608.

[140] C. Lienard, R. Boisard, and C. Daudin. "Aerodynamic behavior of a floating offshore wind turbine" (Jan. 2019). DOI: 10.2514/6.2019-1575.

[141] E. A. Bossanyi. "Wind Turbine Control for Load Reduction". *Wind Energy* 6.3 (2003), pp. 229–244. DOI: 10.1002/we.95.

[142] K. E. Johnson and N. Thomas. "Wind farm control: Addressing the aerodynamic interaction among wind turbines". *2009 American Control Conference* (2009). DOI: 10.1109/acc.2009.5160152.

[143] M. H. Mughal and L. Guojie. "Review of Pitch Control for Variable Speed Wind Turbine" (Aug. 2015). DOI: 10.1109/uic-atc-scalcom-cbdcom-iop.2015.148.

[144] D. Castaignet, T. Barlas, T. Buhl, N. K. Poulsen, J. J. Wedel-Heinen, N. A. Olesen, C. Bak, and T. Kim. "Full-scale test of trailing edge flaps on a Vestas V27 wind turbine: active load reduction and system identification". *Wind Energy* 17.4 (Jan. 2013), pp. 549–564. DOI: 10.1002/we.1589.

[145] F. G. Nielsen, T. D. Hanson, and B. Skaare. "Integrated Dynamic Analysis of Floating Offshore Wind Turbines" (2006). DOI: 10.1115/omae2006-92291.

[146] J. Jonkman. "Influence of Control on the Pitch Damping of a Floating Wind Turbine" (Jan. 2008). DOI: 10.2514/6.2008-1306.

[147] C. E. S. Souza, J. M. Hegseth, and E. E. Bachynski. "Frequency-Dependent Aerodynamic Damping and Inertia in Linearized Dynamic Analysis of Floating Wind Turbines". *Journal of Physics: Conference Series* 1452 (Jan. 2020), p. 012040. DOI: 10.1088/1742-6596/1452/1/012040.

[148] T. Barlas and G. van Kuik. "Review of state of the art in smart rotor control research for wind turbines". *Progress in Aerospace Sciences* 46.1 (Jan. 2010), pp. 1–27. DOI: https://doi.org/10.1016/j.paerosci.2009.08.002.

[149] T. Barlas, G. van der Veen, and G. van Kuik. "Model predictive control for wind turbines with distributed active flaps: incorporating inflow signals and actuator constraints". *Wind Energy* 15.5 (Nov. 2011), pp. 757–771. DOI: 10.1002/we.503.

[150] B. F. Ng, R. Palacios, E. C. Kerrigan, J. M. R. Graham, and H. Hesse. "Aerodynamic load control in horizontal axis wind turbines with combined aeroelastic tailoring and trailing-edge flaps". *Wind Energy* 19.2 (Feb. 2016), pp. 243–263. DOI: 10.1002/we.1830.

[151] K. O. Merz. "Basic controller tuning for large offshore wind turbines". *Wind Energy Science* 1.2 (Sept. 2016), pp. 153–175. DOI: 10.5194/wes-1-153-2016.

[152] *Github - Simulation of High Aspect Ratio Planes in Python [SHARPy]*. Imperial College of London. Jan. 2019. URL: https://github.com/ImperialCollegeLondon/sharpy.

[153] I. C. London, ed. *Simulation of High Aspect Ratio planes in Python [SHARPy]*. Aug. 27, 2021. URL: https://ic-sharpy.readthedocs.io/en/master/index.html.

[154] A. del Carre, A. Muñoz-Simón, N. Goizueta, and R. Palacios. "SHARPy: A dynamic aeroelastic simulation toolbox for very flexible aircraft and wind turbines". *Journal of Open Source Software* 4.44 (Dec. 2019), p. 1885. DOI: 10.21105/joss.01885.

[155] N. Goizueta, A. Drachinsky, A. Wynn, D. E. Raveh, and R. Palacios. "Flutter predictions for very flexible wing wind tunnel test" (Jan. 2021). DOI: 10.2514/6.2021-1711.

[156] A. del Carre and R. Palacios. "Simulation and Optimization of Takeoff Maneuvers of Very Flexible Aircraft". *Journal of Aircraft* 57.6 (Nov. 2020), pp. 1097–1110. DOI: 10.2514/1.C035901.

[157] *OpenFAST Documentation*. version 1.0. Jan. 2019. URL: https://openfast.readthedocs.io/en/latest/index.html.

[158] K. Shaler, E. Branlard, and A. Platt. *OLAF User's Guide and Theory Manual*. Tech. rep. TP-5000-75959. NREL, Aug. 27, 2021.

[159] DTU. *HAWC2*. Feb. 16, 2019. URL: http://www.hawc2.dk/HAWC2-info.

[160] J. Rinker, E. Gaertner, F. Zahle, W. Skrzypiński, N. Abbas, H. Bredmose, G. Barter, and K. Dykes. "Comparison of loads from HAWC2 and OpenFAST for the IEA Wind 15 MW Reference Wind Turbine". *Journal of Physics: Conference Series* 1618 (Sept. 2020), p. 052052. DOI: 10.1088/1742-6596/1618/5/052052.

[161] *HAWC2 pre-processing-tools*. Aug. 18, 2020. URL: https://www.hawc2.dk/download/pre-processing-tools.

[162] DNV-GL. *BLADED Engineering feature summary*. Tech. rep. DNV-GL.

[163] D. G. Opoku, D. G. Triantos, F. Nitzsche, and S. Voutsinas. "Rotorcraft aerodynamic and aeroacoustic modelling using vortex particle methods". Athens (2019).

[164] *WAMIT v7.3 user manual*. Tech. rep. WAMIT, Inc., 2019.

[165] D. I. Manolas, V. A. Riziotis, G. P. Papadakis, and S. G. Voutsinas. "Hydro-Servo-Aero-Elastic Analysis of Floating Offshore Wind Turbines". *Fluids* 5.4 (Nov. 2020), p. 200. DOI: 10.3390/fluids5040200.

[166] A. J. Hanson. *Visualizing Quaternions*. Elsevier LTD, Oxford, Jan. 11, 2006.

[167] S. Maraniello, R. J. S. Simpson, and R. Palacios. "Optimal manoeuvres with very flexible wings". *57th AIAA/ASCE/AHS/ASC Structures, Structural Dynamics, and Materials Conference*. American Institute of Aeronautics and Astronautics, Jan. 2016. DOI: 10.2514/6.2016-1223.

[168] M. Géradin and D. J. Rixen. *Mechanical vibrations : theory and application to structural dynamics*. John Wiley & Sons, 2015.

[169] M. R. Flannery. "The enigma of nonholonomic constraints". *American Journal of Physics* 73.3 (Mar. 2005), pp. 265–272. DOI: 10.1119/1.1830501.

[170] S. Maraniello and R. Palacios. "State-Space Realizations and Internal Balancing in Potential-Flow Aerodynamics with Arbitrary Kinematics". *AIAA Journal* 57.6 (June 2019), pp. 2308–2321. DOI: 10.2514/1.J058153.

[171] S. Maraniello and R. Palacios. "Parametric Reduced-Order Modeling of the Unsteady Vortex-Lattice Method". *AIAA Journal* 58.5 (May 2020), pp. 2206–2220. DOI: 10.2514/1.J058894.

[172] R. Lanzafame and M. Messina. "Fluid dynamics wind turbine design: Critical analysis, optimization and application of BEM theory". *Renewable Energy* 32.14 (Nov. 2007), pp. 2291–2305. DOI: 10.1016/j.renene.2006.12.010.

[173] J. N. Sørensen and W. Z. Shen. "Numerical Modeling of Wind Turbine Wakes". *Journal of Fluids Engineering* 124.2 (2002), p. 393. DOI: 10.1115/1.1471361.

[174] J. M. Jonkman. *Dynamics modeling and loads analysis of an offshore floating wind turbine*. Tech. rep. NREL/TP-500-41958. NREL, 2007.

[175] J. Jonkman. *Definition of the Floating System for Phase IV of OC3*. Tech. rep. TP-500-47535. NREL, May 1, 2021.

[176] J. Jonkman and W. Musial. *Offshore Code Comparison Collaboration (OC3) for IEA Wind Task 23 Offshore Wind Technology and Deployment*. Tech. rep. Dec. 2010. DOI: 10.2172/1004009.

[177] C. Hirsch. *Numerical Computation of Internal and External Flows: The Fundamentals of Computational Fluid Dynamics*. Elsevier, 2007. DOI: 10.1016/b978-0-7506-6594-0.x5037-1.

[178] R. Y. Rubinstein and D. P. Kroese. *Simulation and the Monte Carlo Method*. John Wiley & Sons, Inc., Nov. 2016, pp. 49–90. DOI: 10.1002/9781118631980.

[179] J. Jonkman, S. Butterfield, W. Musial, and G. Scott. *Definition of a 5-MW Reference Wind Turbine for Offshore System Development*. Tech. rep. NREL/TP-500-38060. NREL, 2009.

[180] T. J. Larsen and T. D. Hanson. "A method to avoid negative damped low frequent tower vibrations for a floating, pitch controlled wind turbine". *Journal of Physics: Conference Series* 75 (July 2007), p. 012073. DOI: 10.1088/1742-6596/75/1/012073.

[181] J. Murua, R. Palacios, and J. Peiró. "Camber effects in the dynamic aeroelasticity of compliant airfoils". *Journal of Fluids and Structures* 26.4 (May 2010), pp. 527–543. DOI: 10.1016/j.jfluidstructs.2010.01.009.

[182] H. Hesse and R. Palacios. "Reduced-Order Aeroelastic Models for Dynamics of Maneuvering Flexible Aircraft". *AIAA Journal* 52.8 (Aug. 2014), pp. 1717–1732. DOI: 10.2514/1.j052684.

[183] M. Artola, A. Wynn, and R. Palacios. "Modal-Based Nonlinear Model Predictive Control for 3D Very Flexible Structures". *IEEE Transactions on Automatic Control* (2021), pp. 1–1. DOI: 10.1109/TAC.2021.3071326.

[184] A. Muñoz-Simón, A. Wynn, and R. Palacios. "Unsteady and three-dimensional aerodynamic effects on wind turbine rotor loads". *AIAA Scitech 2020 Forum* (Jan. 2020). DOI: 10.2514/6.2020-0991.

[185] H. Snel, R. Houwink, and W. J. Piers. *Sectional predictions of 3D effects for separated flow on rotating blades*. Tech. rep. National aerospace Laboratory (The Netherlands), 1992.

[186] H. K. Cheng. "Lifting-Line Theory of Oblique Wings". *AIAA Journal* 16.11 (Nov. 1978), pp. 1211–1213. DOI: 10.2514/3.61033.

[187] J. Schepers, K. Boorsma, N. Sørensen, S. Voutsinas, G. Sieros, H. Rahimi, H. Heisselmann, E. Jost, T. Lutz, et al. "Final results from the EU project AVATAR: Aerodynamic modelling of 10 MW wind turbines". *Journal of Physics: Conference Series* 1037 (June 2018), p. 022013. DOI: 10.1088/1742-6596/1037/2/022013.

[188] G. Sieros. *Redesign of the AVATAR RWT rotor*. Tech. rep. NTUA, Aug. 31, 2017. URL: http://www.eera-avatar.eu/publications-results-and-links/index.html.

[189] A. Robertson. *Task 23 OC3 - Google drive*. [Online; accessed 6-July-2021]. Oct. 2015. URL: https://drive.google.com/drive/folders/0B0KGNSHvXXgCMmVsU3RkZ3FHVlE?resourcekey=0-wIA1FXpiYBnIVxichoo-3g.

[190] C. L. Bottasso, F. Campagnolo, and V. Petrović. "Wind tunnel testing of scaled wind turbine models: Beyond aerodynamics". *Journal of Wind Engineering and Industrial Aerodynamics* 127 (Apr. 2014), pp. 11–28. DOI: 10.1016/j.jweia.2014.01.009.

[191] A. Muñoz-Simón, R. Palacios, and A. Wynn. "Benchmarking different fidelities in wind turbine aerodynamics under yaw". *Journal of Physics: Conference Series* 1618 (Sept. 2020), p. 042017. DOI: 10.1088/1742-6596/1618/4/042017.

[192] A. Muñoz-Simón, R. Palacios, and A. Wynn. "Some modelling improvements for prediction of wind turbine rotor loads in turbulent wind". *Wind Energy* (Aug. 2021). DOI: http://doi.org/10.1002/we.2675.

[193] T. J. Larsen and A. M. Hansen. *How 2 HAWC2, the user 's manual*. EN. Tech. rep. 1597. Version 4.7. Risø, 2018.

[194] P. M. O. Gebraad, F. W. Teeuwisse, J. W. van Wingerden, P. A. Fleming, S. D. Ruben, J. R. Marden, and L. Y. Pao. "Wind plant power optimization through yaw control using a parametric model for wake effects-a CFD simulation study". *Wind Energy* 19.1 (Dec. 2014), pp. 95–114. DOI: 10.1002/we.1822.

[195] X. Zhu, J. Chen, X. Shen, and Z. Du. "Impact of Blade Flexibility on Wind Turbine Loads and Pitch Settings". *Journal of Solar Energy Engineering* 141.4 (Jan. 2019). DOI: 10.1115/1.4042315.

[196] D. O. Yu and O. J. Kwon. "A Coupled CFD-CSD Method for Predicting HAWT Rotor Blade Performance" (Jan. 2013). DOI: 10.2514/6.2013-911.

[197] A. Del Carre, N. Goizueta, A. Muñoz-Simón, S. Maraniello, R. Palacios, and K. Otsuka. *SHARPy: A dynamic aeroelastic simulation toolbox for very flexible aircraft and wind turbines*. 2021. DOI: 10.5281/zenodo.3531965.

[198] A. Del Carre, N. Goizueta, A. Muñoz-Simón, S. Maraniello, and R. Palacios. *Simulation of High Aspect Ratio planes in Python [SHARPy]*. Imperial College London. Sept. 27, 2021. URL: https://ic-sharpy.readthedocs.io/en/master/index.html.